

UNIVERSIDAD AUTONOMA DE MADRID  
Facultad de Ciencias  
Departamento de Física Teórica



# **A Theoretical Perspective on Galaxy Clusters: Physical Properties of the Dark Matter and Baryons**

Yago Ascasibar Sequeiros

Memoria de Tesis

Presentada en la Facultad de Ciencias  
de la Universidad Autónoma de Madrid  
para optar al grado de Doctor en Ciencias Físicas

Trabajo dirigido por  
Gustavo Yepes Alonso

Madrid, 26 de noviembre de 2002



A mis padres

... bueno, ¡y a mi hermano también!



# Contents

<b>List of Figures</b>	<b>iv</b>
<b>List of Tables</b>	<b>v</b>
<b>Agradecimientos</b>	<b>vii</b>
<b>Resumen</b>	<b>ix</b>
<b>1 Introduction</b>	<b>1</b>
1.1 The cosmological model . . . . .	4
1.1.1 Theory . . . . .	4
1.1.2 Observations . . . . .	8
<b>2 Numerical experiments</b>	<b>11</b>
2.1 Description of the codes . . . . .	14
2.1.1 YK <sup>3</sup> . . . . .	15
2.1.2 ART . . . . .	19
2.1.3 GADGET . . . . .	21
2.2 Analysis . . . . .	26
2.2.1 Resolution limit . . . . .	26
2.2.2 Object finding . . . . .	27
2.2.3 Radial profiles . . . . .	29
2.2.4 Global properties . . . . .	31
2.3 Description of the simulations . . . . .	31
2.3.1 Cluster sample . . . . .	32
2.3.2 Santa Barbara Cluster . . . . .	35
2.3.3 Star-forming clusters . . . . .	37
<b>3 Dark matter</b>	<b>39</b>
3.1 The case for a universal density profile . . . . .	40
3.1.1 Models . . . . .	41
3.1.2 Central density . . . . .	43
3.1.3 Phase-space structure . . . . .	46
3.2 Simulation Results . . . . .	47

3.2.1	Universality . . . . .	49
3.2.2	Phase-space structure . . . . .	55
3.3	On the physical origin of dark matter profiles . . . . .	59
3.3.1	Spherical collapse . . . . .	60
3.3.2	Initial conditions . . . . .	64
3.3.3	Angular momentum . . . . .	67
3.3.4	Comparison with simulations . . . . .	69
<b>4</b>	<b>Gas</b>	<b>73</b>
4.1	Numerical gasdynamics . . . . .	74
4.1.1	Santa Barbara cluster . . . . .	75
4.1.2	Cluster A . . . . .	78
4.2	Structure of the ICM gas . . . . .	79
4.2.1	Physical state . . . . .	80
4.2.2	Radial profiles . . . . .	83
4.3	Scaling relations . . . . .	91
4.3.1	Mass-temperature . . . . .	92
4.3.2	Luminosity-temperature . . . . .	101
<b>5</b>	<b>Stars</b>	<b>111</b>
5.1	The cosmic star formation history . . . . .	112
5.1.1	Observations . . . . .	113
5.1.2	Simulations . . . . .	117
5.2	Star formation in clusters of galaxies . . . . .	123
5.2.1	Observations . . . . .	124
5.2.2	Simulations . . . . .	125
<b>6</b>	<b>Conclusions and future prospects</b>	<b>129</b>
6.1	Conclusions . . . . .	129
6.1.1	Dark matter . . . . .	129
6.1.2	Gas . . . . .	131
6.1.3	Stars . . . . .	133
6.2	Future prospects . . . . .	133
6.3	Conclusiones y perspectivas futuras . . . . .	135
6.3.1	Materia oscura . . . . .	135
6.3.2	Gas . . . . .	136
6.3.3	Estrellas . . . . .	138
<b>A</b>	<b>Cluster Atlas</b>	<b>141</b>
A.1	Figure description . . . . .	141
A.2	Individual clusters . . . . .	143
	<b>Bibliography</b>	<b>173</b>

# List of Figures

1.1	Cosmic triangle . . . . .	7
2.1	Mass refinement technique . . . . .	33
3.1	Comparison between ART and GADGET . . . . .	48
3.2	Dark matter density profiles . . . . .	51
3.3	Relation between NFW parameters . . . . .	53
3.4	Accuracy of NFW fit . . . . .	54
3.5	Phase space density profiles . . . . .	56
3.6	Anisotropy parameter . . . . .	57
3.7	Angular momentum in the simulated haloes . . . . .	58
3.8	Mass distribution expected from spherical collapse . . . . .	68
3.9	Accuracy of the spherical collapse prediction . . . . .	71
4.1	Simulations of the Santa Barbara Cluster . . . . .	76
4.2	Simulations of Cluster A . . . . .	78
4.3	Test of the hydrostatic equilibrium assumption . . . . .	81
4.4	Polytropic index as a function of $r$ . . . . .	82
4.5	Temperature normalisation . . . . .	85
4.6	Temperature profile . . . . .	86
4.7	Projected temperature . . . . .	87
4.8	Radial dependence of the local baryon fraction . . . . .	90
4.9	Average gas density profile . . . . .	91
4.10	Analytical $M - T$ normalisation . . . . .	94
4.11	$M - T$ relation for our sample . . . . .	100
4.12	Normalisation of the $L - T$ relation . . . . .	103
4.13	$L - T$ relation for our sample . . . . .	107
4.14	Deviations from the self-similar $L - T$ scaling law . . . . .	108
5.1	Conversion between SCDM and $\Lambda$ CDM star formation rates . . . . .	117
5.2	Evolution of the SFR density in different cosmologies . . . . .	118
5.3	Effects of stellar feedback . . . . .	119
5.4	Effects of resolution and volume . . . . .	121
5.5	Star formation rate densities in galaxy clusters . . . . .	126

A.1	Cluster A	143
A.2	Cluster B	145
A.3	Cluster C	147
A.4	Cluster D	149
A.5	Cluster E	151
A.6	Cluster F	153
A.7	Cluster G	155
A.8	Cluster H	157
A.9	Cluster I	159
A.10	Cluster $J_1$	161
A.11	Cluster $K_1$	163
A.12	Cluster L	165
A.13	Cluster M	167
A.14	Cluster $K_2$	169
A.15	Cluster $J_2$	171



# List of Tables

1.1	Possible energy densities in the universe . . . . .	6
2.1	GADGET simulation specifics . . . . .	33
2.2	Physical properties of the clusters at $z = 0$ . . . . .	34
2.3	Santa Barbara Cluster simulations . . . . .	36
2.4	Cosmological models . . . . .	37
2.5	Resolution and feedback parameters . . . . .	38
3.1	Best-fit values of NFW parameters . . . . .	50
3.2	Spherical collapse parameters . . . . .	70
4.1	Observed $M - T$ relation . . . . .	96
4.2	$M - T$ relation in previous simulations . . . . .	98
4.3	$M - T$ relation for our sample . . . . .	99
4.4	Observed $L - T$ relation . . . . .	104
4.5	$L - T$ relation in previous simulations . . . . .	105
4.6	$L - T$ relation for our sample . . . . .	106
5.1	Observational estimates of the cosmic SFR . . . . .	115
5.2	Cumulative star density . . . . .	122



# Agradecimientos

*What would you think if I sang out of tune?  
Would you stand up and walk out on me?  
Lend me your ears and I'll sing you a song  
and I'll try not to sing out of key*

– The Beatles : *With a little help of my friends* (1967) –

**H**a veremos a quien pongo... pero de momento, no pueden faltar

- Gustavo
- El Equipo
- Rafa y Pilar
- Y ar Natxo



# Resumen

*¿Qué son los agujeros negros?*

*¿Se expande el universo? ¿Es cóncavo o convexo?*

*¿Quiénes somos? ¿De dónde venimos? ¿A dónde vamos?*

*¿Estamos solos en la galaxia o acompañados?*

– Siniestro Total : *¿Quiénes somos? ¿De dónde venimos? ¿A dónde vamos?* (1984) –

**L**os cúmulos de galaxias ocupan una posición relevante en la jerarquía de la estructura cosmológica por muchas razones diferentes. Éstos, además de ser una de las estructuras limitadas más grandes en el universo, contienen cientos de galaxias y gas caliente que emite rayos X, por lo que pueden ser detectando por su alto corrimiento hacia el rojo. Por lo tanto, estos objetos nos permiten estudiar la estructura a gran escala del universo, comprobar las teorías de la formación de estructura así como extraer información cosmológica difícil de evaluar por otros métodos (ver v.g. Borgani y Guzzo, 2001; Rosati et al. 2002).

En el marco del modelo de jerarquías para la formación de estructuras a escala cósmica, se piensa que los cúmulos de galaxias se forman por acumulación de unidades más pequeñas (galaxias, grupos, etc.). Después de una época de agregación (que depende del modelo cosmológico), le sigue un proceso de relajación violenta que tiende a virializar los cúmulos produciendo sistemas regulares y quasi-esféricos, con suaves perfiles de densidad tipo King. Las recientes observaciones a bajo corrimiento al rojo basadas en las orientaciones relativas de las subestructuras dentro de los cúmulos, y en la relación entre el estado dinámico y el entorno a gran escala (Plionis y Basailakos, 2002) apoyan este escenario jerárquico.

En la pasada década, debido al incremento de la resolución espacial en las imágenes de rayos X (ROSAT/PSPC & HRI) y a la disponibilidad de las cámaras de gran campo, muchos de los cúmulos que anteriormente se pensaban que eran regulares presentan en realidad alguna subestructura. Esto ha sido evidente gracias a la aparición de los satélites Chandra (Weissjopf et al. 2000) y XMM (Jansen et al. 2001), un hecho que podría tener consecuencias importantes para las teorías de formación de estructuras. Las propiedades

físicas de los cúmulos de galaxias, tales como la fracción de cúmulos jóvenes, las funciones de luminosidad y temperatura, la estructura radial de la materia oscura y bariónica, así como las relaciones complejas entre todas estas magnitudes, constituyen un desafío para nuestro conocimiento actual sobre cómo esos objetos crecieron desde las fluctuaciones en la densidad primordial

Durante los últimos 20 años, el paradigma de la materia oscura fría (CDM) ideada por Peebles (1982), Blumenthal et al. (1984) and Davis et al. (1985) se ha convertido en el modelo estándar que explica la formación y evolución de la estructura cósmica. Éste supone que el contenido de materia de universo está dominado por una partícula masiva débilmente interactuante, que todavía no ha sido identificada, y cuyos efectos gravitacionales son los responsables de la dinámica de las galaxias y los cúmulos.

Un concepto clave en esta cosmogonía es la formación de los halos de la materia oscura. Estos sistemas casi en equilibrio de partículas de materia oscura se forman gracias a un colapso gravitacional no lineal que implica periodos de agregación estacionaria de masa, así como episodios de fusión violenta, en los cuales dos halos de masas comparables colisionan para dar lugar a un halo más grande.

Se piensa que las galaxias y otros objetos luminosos nacen por el enfriamiento y condensación de bariones dentro de pozos de potencial, creados por los halos de materia oscura (White and Rees 1978). En los cúmulos de galaxias, la mayor parte de los bariones se encuentran en un plasma caliente difuso e ionizado que constituye el medio intracumular (ICM).

La evolución dinámica de las galaxias y del gas ICM plantea un problema difícil para los modelos de formación y evolución de cúmulos (v.g. Kaiser 1986). Aunque la física asociada a los procesos hidrodinámicos (c.f. Sarazin 1988) es más complicada que un colapso gravitacional, los modelos simples pueden ser aplicados para relacionar el estado de los bariones con las condiciones particulares de la distribución subyacente de la materia oscura.. Incluso, se han encontrado algunas correlaciones en las propiedades de los rayos X en el medio intracumular, que sugiere que la estructura de densidad y temperatura de los cúmulos puede ser predicha por modelos teóricos autoconsistentes.

El presente trabajo intenta desvelar algunos de los mecanismos que dan lugar a las propiedades observadas en los cúmulos de galaxias. Nos hemos acercado al problema desde diferentes puntos de vista haciendo uso de aproximaciones analíticas y simulaciones numéricas, con el fin de comprender la compleja interacción entre las fuerzas gravitacionales a gran escala, que guía la formación de estructura, y la física bariónica, que domina la hidrodinámica sobre escalas locales.

En el capítulo uno describimos brevemente el modelo cosmológico asumido en nuestro estudio. La sección 1.1.1. ofrece una somera descripción de los conceptos matemáticos básicos necesarios para definir el escenario cosmológico. La sección 1.1.2 se centra en los valores concretos de los

parámetros que determinan la geometría del universo, su composición y su evolución temporal. La principal evidencia observacional que apoya el modelo  $\Lambda$ CDM también será descrita.

Hemos hecho una descripción detallada de los experimentos numéricos en el capítulo 2. Nuestras muestras de los cúmulos simulados son el resultado de tres códigos independientes basados en muy diferentes escenarios. La implementación de los procesos físicos en estos algoritmos es brevemente resumida, así como el procedimiento de análisis que ha sido seguido para obtener los resultados que se muestran. Finalmente damos una descripción de las muestras y explicamos los problemas que aparecen en cada uno de ellos.

El capítulo 3 está dedicado a la distribución de masas que esperamos encontrar en los cúmulos de galaxias. Especial incapié hacemos en la estructura radial de los halos de materia oscura, así como en su origen físico. Para ser más preciso: nos centraremos en los perfiles de densidad de nuestras simulaciones de los halos y en su dependencia con el estado dinámico. La densidad en el espacio de fases será también investigada, comparando los resultados numéricos con trabajos anteriores. El origen físico de la estructura de la materia oscura en los cúmulos será tratado en el marco del formalismo de colapso esférico (Gunn and Gott, 1972; Gunn 1977). Veremos los perfiles predichos por el modelo del colapso esférico que proporciona una descripción fiel de los experimentos numéricos realizados. Intentaremos entender las razones por las cuales se producen tal acuerdo, a pesar del hecho de que el crecimiento de los halos de materia oscura siga una serie de fusiones no lineales.

Las propiedades físicas del ICM serán investigadas en el capítulo 4. En primer lugar, comprobaremos la exactitud de las distintas implementaciones de la hidrodinámica del gas. Luego testaremos la validez de que los cúmulos de galaxias están en un equilibrio hidrodinámico soportado térmicamente, así como en una ecuación de estado apropiada (politrópica o isotérmica) que permite describir mejor la componente de gas difuso. Después, intentaremos predecir la densidad radial y los perfiles de temperatura en nuestras simulaciones de cúmulos, relacionando éstas con las formas fenomenológicas simples (v.g. Navarro et al. 1997; Moore et al. 1999) propuestas para describir los halos de materia oscura. La relación de escala entre las propiedades globales de los cúmulos, observados en diferentes densidades, son detalladas en una sección diferente. Intentaremos entender el origen de la relación masa-temperatura, así como analizaremos la discrepancia entre la relación de autosimilaridad en la luminosidad-temperatura y la que se observa (v.g. David et al. 1993; Ponman et al. 1996).

La formación estelar y los efectos de realimentación van a ser estudiados en el capítulo 5. Simulamos la historia de la formación estelar cosmológica para una serie de escenarios cosmológicos y los comparamos con las observaciones a diferentes frecuencias. Evaluamos los efectos de esta realimentación

en las explosiones de supernovas y la foto-ionización de las estrellas jóvenes, así como la variancia cósmica inducida cuando un pequeño volumen es considerado. Finalmente, tratamos la cuestión de cómo el entorno altera la actividad de la formación estelar en las galaxias individuales. La historia de la formación estelar de los cúmulos de galaxias es comparada con las de campos de galaxias, e incluimos una breve discusión de los mecanismos responsables para de la baja formación de estrellas halladas en esos ambientes tan densos.

Las principales conclusiones que pueden ser extraídas de nuestro resultados son expuestas en la sección 6. El apéndice A contiene un atlas de cúmulos. Éste enseña las características individuales de los 15 cúmulos que reúnen la principal característica analizada en este trabajo. También dibujamos algunas imágenes similares a las observadas, en las que la diferencia entre la cantidad de estructura en gas en materia oscura se muestra con claridad, así como el conjunto de figuras en el que las predicciones discutidas en el texto principal son aplicadas en una base de cúmulo a cúmulo.



# Chapter 1

## Introduction

*Exit light*

*Enter night*

*Take my hand*

*We're off to never-never land!*

– Metallica : *Enter Sandman* (1991) –

**G**alaxy clusters occupy a special position in the hierarchy of cosmic structure in many respects. Being the largest bound structures in the universe, they contain hundreds of galaxies and hot X-ray emitting gas and thus can be detected at large redshifts. Therefore, they appear to be ideal tools for studying large-scale structure, testing theories of structure formation and extracting invaluable cosmological information (see e.g. Borgani and Guzzo 2001; Rosati et al. 2002).

In the framework of the hierarchical model for the formation of cosmic structures, galaxy clusters are supposed to form by accretion of smaller units (galaxies, groups etc). After the epoch of aggregation (which depends on the cosmological model), violent relaxation processes will tend to virialise the clusters producing ‘regular’, quasi-spherical systems, with smooth King-like density profiles. Recent *low* – *z* observations based on the relative orientation of substructures within clusters (West et al. 1995) and on the relation between their dynamical state and the large-scale environment (Plionis and Basilakos 2002) do support the hierarchical scenario.

In the last decade, due to the increased spatial resolution in X-ray imaging (ROSAT/PSPC & HRI) and to the availability of wide-field cameras, many of the previously thought ‘regular’ clusters have shown to be clumpy to some level. This is even more so in the *Chandra* (Weisskopf et al. 2000) and *XMM* (Jansen et al. 2001) era, a fact that could have important consequences for structure formation theories. The physical properties of galaxy clusters, such as the fraction of dynamically young clusters, the luminosity

and temperature functions, the radial structure of both dark and baryonic components, as well as the complex relationships between all these quantities, constitute a challenging test for our current understanding of how these objects grow from primordial density fluctuations.

Over the last 20 years, the Cold Dark Matter (CDM) paradigm set out by Peebles (1982), Blumenthal et al. (1984) and Davis et al. (1985) has become the standard model to explain the formation and evolution of cosmic structures. It assumes that the matter content of the universe is dominated by an as yet unidentified, weakly interacting massive particle, whose gravitational effects are responsible for the dynamics of both galaxies and clusters.

A key concept in this cosmogony is the build-up of dark matter haloes. These quasi-equilibrium systems of dark matter particles are formed through non-linear gravitational collapse, involving both periods of steady accretion of mass, as well as violent merging episodes, in which two haloes of comparable mass collide to give birth to a larger halo.

Galaxies and other luminous objects are assumed to form by cooling and condensation of baryons within the gravitational potential wells created by the dark matter haloes (White and Rees 1978). In galaxy clusters, most baryons can be found in a hot, diffuse, ionised plasma that constitutes the intracluster medium (ICM).

The dynamical evolution of member galaxies and the ICM gas poses a difficult problem for models of cluster formation and evolution (e.g. Kaiser 1986). Nevertheless, although the physics associated to gasdynamical processes (c.f. Sarazin 1988a) is more complicated than pure gravitational collapse, simple models can be applied in order to relate the state of the baryons to the particular conditions of the underlying dark matter distribution. Indeed, several correlations have been observed in the X-ray properties of the intracluster medium, hinting that the density and temperature structure of clusters may be predicted by self-consistent theoretical models.

The present work attempts to unveil some of the mechanisms that give rise to the observed properties of galaxy clusters. We have approached the problem from different points of view, resorting to analytical approximations and direct numerical simulations in order to gain some understanding of the complex interplay between the large scale gravitational forces driving structure formation and the baryonic physics that dominates gas dynamics on local scales.

In this chapter, we briefly describe the cosmological model that will be assumed in our study. Section 1.1.1 offers an overview of the basic mathematical concepts required to define a cosmological scenario. Section 1.1.2 focuses on the actual values of the parameters that determine the geometry of the universe, its composition, and its temporal evolution. The main observational evidence supporting the  $\Lambda$ CDM model will be succinctly described.

A thorough discussion of the numerical experiments that have been per-

formed is given in Chapter 2. Our samples of simulated clusters are the outcome of three independent codes, based on very different integration schemes. The implementation of physical processes within these algorithms is briefly summarised, as well as the analysis procedure that has been followed in order to obtain the results reported here. Finally, a description of the samples themselves is given, explaining the problems that are to be addressed within each one of them.

Chapter 3 is devoted to the mass distribution that we expect to find in clusters of galaxies. Special emphasis is put in the radial structure of the dark matter haloes and its physical origin. To be more precise, we will study the density profiles of our simulated haloes and the dependence on their dynamical state. The phase-space density will also be investigated, comparing the numerical results with previous work. The physical origin of the structure of dark matter in clusters will be addressed within the framework of spherical collapse formalism (Gunn and Gott 1972; Gunn 1977). We will show that the profiles predicted by the spherical infall model provide an accurate description of those found in the numerical experiments. We will try to understand the reasons for such an agreement, albeit the fact that the growth of numerical dark matter haloes proceeds through a non-linear series of mergers.

The physical properties of the ICM will be investigated in Chapter 4. First of all, the reliability of current numerical implementations of gasdynamics will be assessed. Then, we will test the validity of the assumption that clusters of galaxies are in thermally-supported hydrostatic equilibrium, as well as the appropriate equation of state (polytropic or isothermal) that better describes the diffuse gas component. Then, we try to predict the radial density and temperature profiles of our simulated clusters, relating them to the simple phenomenological forms (e.g. Navarro et al. 1997; Moore et al. 1999b) proposed to describe the dark matter haloes. The scaling relation between the global properties of the clusters, observed at different overdensities, are dealt with in a separate section. We try to understand the origin of the mass-temperature relation, as well as of the reported discrepancy between the self-similar luminosity-temperature relation and the observed one (e.g. David et al. 1993; Ponman et al. 1996).

Star formation and feedback are studied in Chapter 5. The cosmic star formation history is computed for a variety of cosmological scenarios and compared with observational estimates based on different wavelengths. The effects of feedback from supernova explosions and photoionisation by young stars are evaluated, as well as the cosmic variance induced when a small volume is considered. Finally, we address the question of how does the environment alter the star formation activity of individual galaxies. The star formation history of clusters of galaxies is compared to that of field galaxies, and a brief discussion on the mechanisms responsible for the lower star formation found in dense environments is also included.

The main conclusions that can be drawn from our results are highlighted in Section 6. We also quote some of the aspects that in our opinion deserve a much deeper investigation than it is possible within the scope of the present thesis.

Appendix A contains a cluster atlas. It shows the individual characteristics of the 15 clusters that comprise the main sample analysed in this work. Mock observational images are plotted, in which the difference between the amount of structure in gas and dark matter is clearly seen, as well as a set of figures in which the prescriptions discussed in the main text are applied in a cluster-to-cluster basis.

## 1.1 The cosmological model

This work (as any other), relies on a series of axioms that it does not intend to verify. In our case, maybe the most important of them is the cosmological model that is assumed to describe the universe beyond the region of influence of our clusters of galaxies.

The consequences of the chosen cosmological scenario on the formation and evolution of galaxy clusters are twofold: On one hand, it sets the power spectrum of primordial fluctuations that give rise to cosmological structure. On the other, the expansion rate of the universe is largely determined by the contribution of its different components to the total energy density. The expansion factor, in turn, controls the density of cosmological objects, their accretion rate, or the probability that they undergo a merging event.

### 1.1.1 Theory

The basic tenet that governs our current view of the universe is the cosmological principle, which is a generalisation of the Copernican idea that the Earth does not necessarily have to play a central role in the solar system. In general terms, the cosmological principle states that the universe is homogeneous and isotropic on large scales, which seems to be corroborated by observations of the Large Scale Structure (LSS) or the Cosmic Microwave Background (CMB). Furthermore, we will assume that the evolution of the universe on such large scales is dominated by gravity, and therefore it can be described by the General Theory of Relativity.

Although it is evident that the universe is anything but homogeneous on small scales, the usual approach consists in separating the problem into two components: Cosmic structures are considered to grow as a perturbation field superimposed to an otherwise homogeneous and isotropic space-time fabric. The evolution of the universe as a whole is reduced, in this simple approximation, to the dynamics of cosmological expansion, which constitutes one of the most fundamental applications of General Relativity.

### Friedmann equations

It can be shown (e.g. Weinberg 1972) that the assumptions of homogeneity and isotropy are equivalent to the requirement that the metric tensor of the universe takes the form of the Robertson-Walker metric

$$ds^2 = dt^2 - a(t)^2 \left[ \frac{dr^2}{1 - kr^2} + r^2(d\theta^2 + \sin\theta d\phi) \right] \quad (1.1)$$

where the dimensionless function  $a(t)$  is the cosmic expansion factor.

According to General Relativity, the geometry of the space-time background is related to its matter-energy content by virtue of the Einstein field equations,

$$G_{\mu\nu} \equiv R_{\mu\nu} - \frac{1}{2}Rg_{\mu\nu} = 8\pi GT_{\mu\nu} + \Lambda g_{\mu\nu} \quad (1.2)$$

The stress-energy tensor of the universe is taken to be, also from the cosmological principle, that of a perfect fluid (such that a comoving observer would observe an isotropic universe),

$$T_{\mu\nu} = pg_{\mu\nu} + (p + \rho)u_\mu u_\nu \quad (1.3)$$

Inserting the perfect fluid tensor and the Robertson-Walker metric into the Einstein field equations above, we can apply the stress-energy conservation law ( $T_{;\nu}^{\mu\nu} = 0$ ) to get the Friedmann equations, which govern the dynamics of the cosmic scale factor  $a(t)$ :

$$\left(\frac{\dot{a}}{a}\right)^2 = \frac{8\pi G}{3}\rho + \frac{\Lambda}{3} - \frac{k}{a^2} \quad ; \quad \frac{\ddot{a}}{a} = -\frac{4\pi G}{3}(\rho + 3p) + \frac{\Lambda}{3} \quad (1.4)$$

The solutions of these equations are known as Lemaître-Friedmann-Robertson-Walker (LFRW) universes, and their characteristic properties vary greatly as a function of the several densities that can appear in (1.4) and their corresponding equations of state.

### Density parameters

Before the 1990's, little could be said about the matter-energy composition of the universe. The only points in which a general agreement existed were the validity of the cosmological principle, the finiteness of the age of the universe, and its expansion from a gas cloud of extremely high density and temperature.

This 'hot Big-Bang' scenario had been induced and confirmed by several independent observational evidences, namely the measurement of redshift in nearby galaxies (Hubble 1929), the relative abundances of light elements (explained through a primordial nucleosynthesis phase, Gamow 1946), and the detection of the CMB radiation by Penzias and Wilson (1965). With very

COMPONENT		DENSITY PAR.	STATE EQ.
Matter	Relativistic	$\Omega_\gamma + \Omega_{\text{HDM}}$	$p = 1/3\rho$
	Non-relativistic	$\Omega_b + \Omega_{\text{CDM}}$	$p = 0$
Space-time	Vacuum	$\Omega_\Lambda$	$p = -\rho$
	Curvature	$\Omega_k$	$p = -1/3\rho$

TABLE 1.1: Possible energy densities in the universe

few ingredients, this simple model was able to explain satisfactorily enough the main features of the observable universe from its very first seconds of existence.

Nevertheless, LFRW universes have a set of free parameters that only in the last decade has it been possible to bound. On one hand, the pressure and density terms that appear in (1.4) corresponding to the different types of energy density that may exist in the universe, and, on the other hand, the actual value of the expansion rate at the present time, usually known as Hubble constant and expressed as

$$H(t) \equiv \frac{\dot{a}(t)}{a(t)} ; H_0 \equiv H(t_0) \equiv 100 h \text{ (km s}^{-1}\text{Mpc}^{-1}) \quad (1.5)$$

It is useful, in order to classify the different terms contributing to the stress-energy tensor, to work with the density parameters, defined as fractions of the critical density required for the universe to have a spatially-flat geometry ( $k = 0$ ):

$$\Omega_i(t) \equiv \frac{\rho_i(t)}{\rho_c(t)} \equiv \frac{8\pi G}{3H^2(t)}\rho_i(t) \quad (1.6)$$

In analogy with ordinary matter, we define an effective density due to the curvature of space-time and to the cosmological constant term (which can be interpreted as a uniform vacuum energy density  $\rho_\Lambda = \Omega_\Lambda\rho_c$ ).

$$\Omega_k(t) \equiv \frac{-k}{a^2H^2(t)} ; \Omega_\Lambda(t) = \frac{\Lambda}{3H^2(t)} \quad (1.7)$$

With this definitions, the first Friedmann equation transforms into the following closure relation:

$$\sum_i \Omega_i(t) = 1 \quad (1.8)$$

Table 1.1 summarises a classification of the possible components that may contribute to the total energy density of the universe, according to the equation of state relating their density an pressure. These equations also define the relationship between the different densities and the cosmic scale

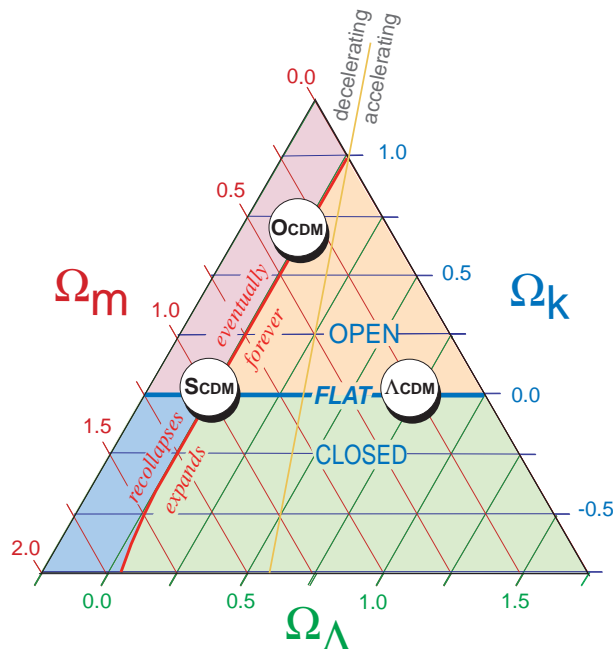


FIGURE 1.1: Cosmic triangle

factor  $a(t)$ . To obtain the time-dependence  $\Omega_i(a)$  we just have to insert the corresponding equation of state in (1.4):

$$p_i(t) = \omega_i \rho_i(t) \quad \Rightarrow \quad \rho_i(t) = \rho_i(t_0) a^{-3(1+\omega_i)} \quad (1.9)$$

As a result, the current values of the density parameters completely determine the solutions of the Friedmann equations. From now on, if there is no explicit time dependence of any density, we will take  $\Omega_i$  to denote the present-time value (unless otherwise noted). The first Friedmann equation may then be written as

$$\left(\frac{H}{H_0}\right)^2 = \Omega_r a^{-4} + \Omega_{nr} a^{-3} + \Omega_\Lambda + \Omega_k a^{-2} \quad (1.10)$$

where it becomes evident that the properties and evolution of a homogeneous and isotropic universe depend only on the four density parameters (subject to the closure relation 1.8) plus the Hubble constant.

This is very aesthetically summarised in Figure 1.1 (Bahcall et al. 1999), where the parameter space is represented by the position of the model universe in the 'cosmic triangle'. Each point within the triangle satisfies the closure relation (1.8). The horizontal line (marked 'flat') corresponds to  $k = 0$ , separating an open universe from a closed one. The red line, nearly along the  $\lambda = 0$  line, separates a universe that will expand forever (approximately  $\Lambda > 0$ ) from other that will eventually re-collapse (approximately

$\Lambda < 0$ ). And the yellow, nearly vertical line separates a universe with an expansion rate that is currently decelerating from one that is accelerating.

The locations of three key models are highlighted in the figure: The Standard Cold Dark Matter (SCDM) model, dominated by non-relativistic non-baryonic matter,  $(\Omega_m, \Omega_\Lambda) = (1, 0)$ ; an open universe with no cosmological constant,  $(\Omega_m, \Omega_\Lambda) = (0.3, 0)$ ; and a flat universe with a  $\Lambda$ -term, defined by  $(\Omega_m, \Omega_\Lambda) = (0.3, 0.7)$ .

### 1.1.2 Observations

From a theoretical point of view, there are no preferred values of the density parameters. Therefore, constraints on their actual values in the real universe must come from observational estimates. The last ten to fifteen years have witnessed a tremendous improvement in observational instrumentation. These novel technologies have opened a plethora of new possibilities to measure the contribution of the different types of energy densities to the total cosmological budget.

While in the 1960s Sandage's goal was to 'search for two numbers', it is now appreciated that even the basic cosmological model requires about a dozen or so parameters, which are linked in non-trivial ways. Combinations of several independent experiments must be used to break these degeneracies. In this section, we review some recent results aimed to find the values of the cosmic density parameters that best fit the whole set of available observations. As we shall see below, all observational evidence<sup>1</sup> seem to favour the so-called  $\Lambda$ CDM cosmological scenario.

### Baryon density

The standard theory of Big-Bang Nucleosynthesis (BBN) predicts the abundances of the light element nuclei H, D,  $^3\text{He}$ ,  $^4\text{He}$ , and  $^7\text{Li}$  as a function of the cosmological baryon-to-photon ratio,  $\eta = n_b/n_\gamma$  (see e.g. Kolb and Turner 1990). A measurement of the ratio of any two primordial abundances gives  $\eta$ , and hence the baryon density, while a second ratio tests the theory.

However, it is extremely difficult to measure primordial abundances because in most places gas ejected from stars has enriched the medium. Adams (1976) suggested that it might be possible to measure the primordial D/H ratio in absorption-line systems toward QSOs. Several estimations (e.g. Tytler et al. 1996; Burles and Tytler 1998a,b; O'Meara et al. 2001) have been made thereafter. The baryon density reported by O'Meara et al. (2001) amounts to

$$\Omega_b h^2 = 0.0205 \pm 0.0018 \quad (1.11)$$

---

<sup>1</sup>At the moment of writing this thesis.



### Hubble constant

In standard Big Bang cosmology, the universe expands uniformly; and locally, according to the Hubble law,  $v = H_0 d$ , where  $v$  is the recession velocity of a galaxy at a distance  $d$ , and  $H_0$  is the Hubble constant, the expansion rate at the current epoch. More than seven decades have now passed since Hubble (1929) initially published the correlation between the distances to galaxies and their recession velocities, thereby providing evidence for the expansion of the universe. But pinning down an accurate value for the Hubble constant has proved extremely challenging. There are many reasons for this difficulty, but primary among them is the basic difficulty of establishing accurate distances over cosmologically significant scales.

Measuring an accurate value of  $H_0$  was one of the motivating reasons for building the NASA/ESA *Hubble Space Telescope* (HST). The overall goal of the  $H_0$  Key Project was to measure the Hubble constant based on a Cepheid calibration of a number of independent secondary distance determination methods. To extend the distance scale beyond the range of the Cepheids, a number of methods that provide relative distances were chosen, including the Type Ia supernovae, the Tully-Fisher relation, the fundamental plane for elliptical galaxies, surface-brightness fluctuations, and Type II supernovae.

A recent paper by Mould et al. (2000a,b) combines the results of the HST with these secondary methods based on different standard candles. The final results of the  $H_0$  Key Project (Freedman et al. 2001) yield the following value:

$$H_0 = 72 \pm 8 \text{ km s}^{-1} \text{ Mpc}^{-1} \quad (1.12)$$

### Deceleration parameter

Just as large distance measurements on Earth show us the curvature on Earth's surface, so do large distance measurements in cosmology show us the geometry of the universe. Since the geometry of space-time is given by the values of the cosmic density parameters, measurements of the luminosity distance at high redshifts can be very help to constrain those values.

In these sense, observations of Type Ia supernovae at  $z \geq 3$  by the *Supernova Cosmology Project* (Perlmutter et al. 1999) and the *High-Z Supernova Search Team* (Riess et al. 1998; Schmidt et al. 1998) have provided an extremely useful benchmark to test the different cosmological scenarios. These measurements allowed for the first time an accurate determination of the deceleration parameter  $q_0 \equiv -a\ddot{a}/\dot{a}^2 = \Omega_m/2 - \Omega_\Lambda$ . The most striking conclusion drawn from these experiments was that the expansion of the universe is nowadays accelerating ( $q_0 < 0$ ), which hints the presence of a non-zero positive cosmological constant,

$$\Omega_m = 0.28_{-0.08}^{+0.09} \quad ; \quad \Omega_\Lambda = 0.72_{-0.08}^{+0.09} \quad (1.13)$$

## Curvature

One of the most promising techniques to determine the geometry of the universe is the study of the amplitude fluctuations in the cosmic microwave background. Early detection of a peak in the region of the so-called first acoustic peak (Netterfield et al. 1997), as well as the availability of fast codes to compute theoretical amplitudes (Seljak and Zaldarriaga 1996), have provided a first constraint on the value of  $\Omega_k$  (Lineweaver et al. 1997; Hancock et al. 1998).

The spectacular results of Boomerang and Maxima balloon experiments have firmly established that geometry of the universe is very close to flat (de Bernardis et al. 2000; Hanany et al. 2000; Balbi et al. 2000; Lange et al. 2001). Recently, Benoit et al. (2002) combined the anisotropies measured by the Archeops experiment with data from COBE (Tegmark 1996), Boomerang (Netterfield et al. 2002), Dasi (Halverson et al. 2002), Maxima (Lee et al. 2001), VSA (Scott et al. 2002) and CBI (Pearson et al. 2002). The combination of all these CMB experiments provides an estimation of the total energy density of the universe

$$\Omega_k = 1.04^{+0.12}_{-0.17} \quad (1.14)$$

as well as a measure of the baryon density completely independent (but consistent) with the nucleosynthesis estimate:

$$\Omega_b h^2 = 0.022^{+0.003}_{-0.004} \quad (1.15)$$

Adding other constraints, such as those imposed by the observed large scale structure (see e.g. the analysis based on the 2dF Galaxy Redshift Survey by Efstathiou et al. 2002) or the observed baryon fraction in galaxy clusters (e.g. Sadat and Blanchard 2001), the values of the density parameters are still compatible with those listed above. The so-called 'concordance' model emerges as an apparently solid observational measurement, confirmed by several independent methods.

Given the amount of observational evidence that currently supports the  $\Lambda$ CDM cosmology, we will base most of our study on the assumption that the space-time background is well described by a homogeneous and isotropic LFRW universe with  $\Omega_m = 0.3$ ,  $\Omega_\Lambda = 0.7$ ,  $\Omega_b = 0.04$  and  $h = 0.7$ . In those cases where some other cosmology is used, it will be explicitly noted.

## Chapter 2

# Numerical experiments

*One more, one more, one more, one more...  
Addict with an Apple Mac, megabyte maniac  
Moron with a mouse mat, a junky  
Distressed, you've guessed, obviously obsessed  
I, NEED MORE MEMORY!*

– Toy Dolls : *One More Megabyte* (1997) –

**N**umerical simulations of three-dimensional self-gravitating fluids have become an indispensable tool in cosmology. They are now routinely used to study the non-linear gravitational clustering of dark matter, the formation of galaxy clusters, the interactions of isolated galaxies, and the evolution of the intergalactic gas. Without numerical techniques the immense progress made in these fields would have been nearly impossible, since analytic calculations are often restricted to idealised problems of high symmetry, or to approximate treatments of inherently non-linear problems.

The advances in numerical simulations have become possible both by the rapid growth of computer performance and by the implementation of ever more sophisticated numerical algorithms. The development of powerful simulation codes, with high level of parallelism, still remains a primary task in order to take full advantage of new computer technologies.

Early simulations (e.g. White 1976; Fall 1978; Aarseth et al. 1979) largely employed the direct summation method for the gravitational N-body problem, which remains useful in collisional stellar dynamical systems, but it is inefficient for cosmological simulations with large  $N$  due to the rapid increase of its computational cost with  $N$  (see e.g. Yepes 2001, for a review on numerical methods for cosmological simulations).

In order to overcome the problems inherent to the direct summation N-body methods, a large number of groups have developed new techniques for collisionless dynamics that compute the large-scale gravitational field

in a (regular or irregular) grid. In the simplest implementation of grid-based N-body methods, the *Particle-Mesh*(PM) N-body technique (see e.g. Hockney and Eastwood 1981), the Poisson equation is solved using Fast Fourier Transform (FFT) in a regular grid of the density field, that is constructed by interpolation from the particle positions to the grid nodes. Newtonian forces are computed by differentiating the potential on the grid and interpolating back to the particle positions. The time for force computation scales as  $\mathcal{O}(N \log N)$  in these methods, which makes them able to treat a large amount of particles. In fact, this is the N-body method that can handle the largest number of particles, and it has been used widely to investigate the non-linear clustering of different cosmological models since the early 1980's (e.g. Klypin and Shandarin 1983; White et al. 1983).

The lack of resolution below the grid-size is one of the major problems of the PM model. Hockney et al. (1974) proposed an hybrid scheme to increase the numerical resolution of the PM method, consisting in the decomposition of the force acting on each particle into a long-range force, computed by the particle-mesh interaction, and a short-range force due to nearby particles. Modern versions of these codes use finer grids on highly clustered regions to recursively apply the P<sup>3</sup>M algorithm. Therefore, the number of neighbours per particle is considerably reduced, which makes the code much faster with respect to the original implementation. The publicly available *Adaptive* P<sup>3</sup>M (AP<sup>3</sup>M) code developed by Couchman (1991) is a good example of this technique and has helped the development of other codes based on this integration scheme.

Another approach to increase resolution of PM methods is to use non-uniform grids and algorithms to adapt the computational mesh to the structures formed by gravitational clustering. The Poisson equation can be solved on a hierarchically refined mesh by means of finite-difference relaxation methods, an approach taken in the Adaptive Refinement Tree (ART) code by Kravtsov et al. (1997), the MLAMP code (Knebe et al. 2001), and more recently by Teyssier (2002) in the RAMSES AMR code.

An alternative to these schemes are the so-called tree algorithms, pioneered by Colella and Woodward (1985). Tree algorithms arrange particles in a hierarchy of groups, and compute the gravitational field at a given point by summing over multipole expansions of these groups. In this way the computational cost of a complete force evaluation can be reduced to a  $\mathcal{O}(N \log N)$  scaling. The grouping itself can be achieved in various ways, for example with Eulerian subdivisions of space (Barnes and Hut 1986), or with nearest-neighbour pairings (Press et al. 1986; Jernigan and Porter 1989). A technique related to ordinary tree algorithms is the fast multipole-method (e.g. Greengard 1988), where multipole expansions are carried out for the gravitational field in a region of space.

While mesh-based codes are generally much faster for nearly homogeneous particle distributions, tree codes can adapt flexibly to any clustering

state without significant losses in speed. This Lagrangian nature is a great advantage if a large dynamic range in density needs to be covered. Here tree codes can outperform mesh based algorithms. In addition, tree codes are basically free from any geometrical restrictions, and they can be easily combined with integration schemes that advance particles on individual timesteps.

An independent way to speed up force computations for large number of particles, is to use efficient parallel algorithms to distribute the work load among many processors. A big effort has been done recently in developing parallel N-body codes, using either direct summation (Makino 2002), PM (Ricker et al. 2000), P<sup>3</sup>M (Macfarland et al. 1998) or tree methods (Dubinski 1996; Lia and Carraro 2001; Springel et al. 2001b). The advantage of parallel N-body codes is the portability. They can run from cheap Beowulf PC clusters to very expensive supercomputers.

In recent years, collisionless dynamics has also been coupled to gas dynamics, allowing a more direct link to observable quantities. Traditionally, hydrodynamical simulations have usually employed some kind of (Eulerian or Lagrangian) mesh to represent the dynamical quantities of the fluid. Modern grid-based computational fluid dynamical codes are based on Godunov methods: i.e. gasdynamical equations are integrated in each volume element of the computational mesh. The evolution of volume-averaged fluid quantities can be computed from fluxes through the cell boundaries, which are estimated from approximate Riemann solvers.

A particular strength of these codes is their ability to accurately resolve shocks without artificial viscosity terms that might introduce numerical dissipation. A regular mesh also imposes restrictions on the geometry of the problem, as well as onto the dynamic range of spatial scales that can be simulated. New adaptive mesh refinement codes (Norman and Bryan 1999; Kravtsov et al. 2002; Teyssier 2002) have been developed to provide a solution to this problem.

In cosmological applications, it is often sufficient to describe the gas by smoothed particle hydrodynamics (SPH), as invented by Lucy (1977) and Gingold and Monaghan (1977). The particle-based SPH is extremely flexible in its ability to adapt to any given geometry. Moreover, its Lagrangian nature allows a locally changing resolution that ‘automatically’ follows the local gas density. This convenient feature helps to save computing time by focusing the computational effort on those regions that have the largest gas concentrations. Furthermore, SPH ties naturally into the N-body approach for self-gravity, and can be easily implemented in three dimensions.

These advantages have led a number of authors to develop SPH codes for applications in cosmology in combination with different flavours of N-body codes, to the point that nowadays these hydrodynamic codes are by far the most numerous in cosmological simulations. A comparison study can be found in Frenk et al. (1999), where the major differences between SPH

and grid-based gasdynamical codes were found in the central part of the radial entropy and temperature profiles of the galaxy cluster used for the comparison. The AMR gasdynamical codes tend to produce an isentropic gas profile in the inner regions, while SPH codes predict an isothermal profile with a decreasing entropy towards the centre of cluster-size haloes. We will come back to this problem in Section 4.1, showing that results from SPH and grid-based codes can be reconciled when an appropriate treatment of entropy conservation in SPH codes is used (Springel and Hernquist 2002a; Serna et al. 2002).

The present chapter is devoted to the description of the numerical experiments reported in this thesis. First, the different codes that have been used are described in some detail, focusing on the specific merits of each one depending on the sort of problem that we wanted to tackle. The general procedure followed to analyse the results is discussed on a separate section, and finally a description of the actual numerical experiments is given.

## 2.1 Description of the codes

In order to study the internal structure of dark matter haloes, a high-performance N-body algorithm is required to accurately resolve their very central parts. For this purpose we used two independent state-of-the-art N-body codes; the parallel Tree-SPH code GADGET and the pure N-body implementation of the AMR code ART. Results based on these two integration schemes have been compared in order to assess the reliability of our conclusions (see Section 3.2).

Inclusion of gas dynamics in N-body simulations is even more demanding from the computational point of view, enforcing the use of efficient parallel codes for this purpose. The dynamical evolution of the gas component within dark matter haloes has been investigated by means of a series of simulations accomplished with GADGET. Because of the problems with entropy conservation in SPH codes, a new implementation of GADGET has been used in which the entropy (rather than energy) conservation equation is integrated (Springel and Hernquist 2002a). As a test of the consistency of our results, we have compared in Section 4.1 one of the galaxy clusters simulated by means of the SPH technique with an independent numerical experiment by Nagai and Kravtsov (2002) using the new hydrodynamical version of the ART code (Kravtsov et al. 2002).

Finally, to address the problem of star formation in different environments, it does not suffice to take into account only gravity and gasdynamics, but also all the complex physics related to star-gas interactions. In this regard, we have used a Particle-Mesh code for N-body coupled with an Eulerian hydrodynamical code based on the higher order Godunov *Piecewise Parabolic Method* (PPM). The code is supplemented with a model for

cooling, star formation and feedback from supernovae. From now on, we will refer to this code as YK<sup>3</sup>, which stands for the initials of the authors (Yepes et al. 1997).

All the codes employed in this work have been parallelised to run efficiently either in distributed (GADGET) or Shared Memory Processor systems (ART and YK<sup>3</sup>). Numerical experiments have been performed in a variety of supercomputers and centres:

- SGI Origin 2000 at the CEPBA (Barcelona, Spain)
- SGI Origin 2000 at the NCSA (Chicago, USA)
- SGI Origin 3800 at the CIEMAT (Madrid, Spain)
- Hitachi SVR at the AIP (Potsdam, Germany)
- Hitachi SVR at the LRZ (Munich, Germany)

### 2.1.1 YK<sup>3</sup>

This code implements the most complete treatment of the physical processes, at the expense of a much lower spatial resolution than that achieved by ART or GADGET.

The matter in the simulated Universe consists of four phases. 1) The dark matter (labelled by a subscript “dm”) in the form of weakly interacting collisionless particles is the main contribution to the mean density of the universe ( $\Omega_{\text{dm}} = 1 - \Omega_{\text{b}}$ ). The baryonic component is described as a medium consisting of three interacting phases: 2) hot gas (labelled by subscript h,  $T_{\text{h}} > 2 \times 10^4$  K), 3) gas in the form of cold dense clouds (subscript c, internal temperature  $T_{\text{c}} = 10^4$  K) resulting from cooling of the hot gas, and 4) “stars” (subscript \*), formed inside cold clouds and treated as collisionless particles. Thus, the total density ( $\rho$ ) is the sum of four components:

$$\rho = \rho_{\text{dm}} + \rho_{\text{h}} + \rho_{\text{c}} + \rho_{*}. \quad (2.1)$$

This picture is consistent with work on models of galaxy formation and evolution (see for example Nulsen 1986; Thomas, 1988a,b; Hensler and Burkert, 1990; Daines et al 1994; Nulsen & Fabian, 1995) and in this context appears to be superior to a treatment of the gas component as a one-phase medium.

### Gravity and Gas Dynamics

Gravity is described by the standard Particle-Mesh algorithm, i.e. density is computed at the grid points by *Cloud in Cell* interpolation from the particle positions. Poisson’s equation is solved on the grid by FFT and forces are

obtained by differentiating the potential in the grid. Forces acting on each particle are found by interpolation from the grid to the particle positions using the same kernel (CIC). Finally, Newton equations are integrated for each particle using a Leap-frog scheme, to advance them.

Gas dynamics is described by the high order Godunov PPM algorithm (Colella and Woodward 1984). As we said at the beginning of this section, the main advantage of this Eulerian code is that it does not involve an artificial viscosity, but still treats shocks very accurately. This method is very fast and highly parallelisable. This algorithm is applied to the gas-dynamical equations in one dimension at a time. Multiple dimensions are treated by directional timestep splitting, whereas local processes (heating, cooling, star formation, etc.), which involve various components of collisional matter, as well as self-gravitation and gravitational interaction with dark matter, are treated using process timestep splitting (Oran & Boris 1986).

### Additional physics

A proper treatment of cooling and star formation requires consideration of processes occurring on scales well below the numerical resolution of the code. Despite certain simplifications, the approach taken in YK<sup>3</sup> relies heavily on the picture of the interstellar medium by McKee & Ostriker (1977), who provided a detailed description of the physics in dense regions. This theory assumes the existence of cold clouds forming due to thermal instability in approximate pressure equilibrium with the surrounding hot gas.

Despite the existence of multiple phases with different temperatures, the cooling rate can still be computed from the mean parameters of the hot gas. Let us denote the *local* cooling rate of the plasma due to radiative processes by  $dE/dt = -\Lambda_r(\rho, T)$ , where  $\rho$  and  $T$  here represent the *true* local values of the gas density and temperature. According to the theory of McKee and Ostriker, the rate of energy loss expressed in terms of *average* gas density  $\rho_h$  and temperature  $T_h$  will be higher than the nominal rate  $-\Lambda_r(\rho_h, T_h)$  by a *cooling enhancement factor*  $C$ , which is taken to be  $C = 10$  to account for all the effects resulting from unresolved density inhomogeneities.

Cooling depends also on the chemical composition of the gas. In order to incorporate the effects of metallicity into the code, solar abundance is assumed in regions where either thermal instability is present or previous star formation has occurred. Otherwise, the region is considered not to be enriched by metals, and the cooling rate for a gas of primordial composition (Fall & Rees 1985) is used.

The ionisation of the intergalactic and interstellar medium by UV photons emitted by quasars, AGNs, and by nonlinear structures in the process of formation has two important consequences: First, gas outside dense regions ( $\rho_{\text{gas}} < 2\langle\rho_{\text{gas}}\rangle$ , where  $\langle\rho_{\text{gas}}\rangle$  is the mean cosmological gas density) is ionised and has a temperature of  $T = 10^{3.8}\text{K}$  (Giroux & Shapiro, 1996;



Petitjean, Mückel, & Kates, 1996; Mückel et al., 1996). Second, in low to moderate-density regions, heating due to the ionising flux suppresses the thermal instability (Mückel & Kates, 1996) and thus the formation of cold clouds and ultimately stars. Hence, cold clouds are allowed to form only if  $\rho_{\text{gas}}/\rho_{\text{cr}} > \mathcal{D} \cdot \Omega_{\text{bar}}$ , with  $\mathcal{D} \sim 50 - 100$ .

In addition to the above processes, energy loss due to Compton cooling is also included, given by  $\Lambda_{\text{Comp}} = 7 \times 10^{-36} n_H T_e a^{-4}$ , where  $n_H$  is the number density of hydrogen ions,  $T_e$  is the electron temperature, and  $a$  is the expansion parameter.

In this model, there are two mechanisms for gas to leave the hot phase and enter the cold phase. First, if the temperature of the hot gas drops below a threshold temperature  $T_{\text{lim}} = 2 \times 10^4$  K, and  $\rho_{\text{gas}}/\rho_{\text{cr}} > \mathcal{D} \cdot \Omega_{\text{bar}}$  all the hot gas is transferred immediately to the cold phase, thus making it available for star formation. This process gives the following terms in the continuity equations for the gas:

$$\left(\frac{d\rho_h}{dt}\right)_{\text{hot} \rightarrow \text{cold}} = -\frac{\rho_h}{t_{\text{cool}}}, \quad t_{\text{cool}} = \frac{\epsilon_h}{\partial\epsilon_h/\partial t}, \quad \frac{\rho_{\text{gas}}}{\rho_{\text{cr}}} > \mathcal{D} \cdot \Omega_{\text{bar}} \quad T < T_{\text{lim}}, \quad (2.2)$$

where  $t_{\text{cool}}$  is the cooling time, and  $\epsilon_h$  is the thermal energy per unit mass. The transfer may be treated as immediate if the cooling time is very short compared to a timestep, which typically happens at  $T \approx 2 \times 10^4$  K.

A second way of transferring gas to the cold phase is by sufficiently rapid thermal instability. The temperature range for creation of cold clouds depends in reality on the ionising flux and the local density (Mückel & Kates, 1996), but the simplified restriction  $T < T_{\text{inst}} = 2 \times 10^5$  is used in the code. To estimate the rate of growth of mass in cold clouds, the energy emitted by the hot gas is actually lost. If  $\epsilon_h$  and  $\epsilon_c$  are the internal thermal energies per unit mass of hot and cold gas, then the change of energy of the system due to radiative cooling is

$$\left(\frac{d(\rho_h\epsilon_h + \rho_c\epsilon_c)}{dt}\right)_{\text{cooling}} = -C\Lambda_r(\rho_h, T_h), \quad (2.3)$$

where  $C$  is the enhanced cooling factor due to unresolved clumpiness. We take  $\epsilon_c = \text{constant}$ , which means that the cold gas cannot cool below  $T_{\text{lim}}$ . For an ideal gas, these assumptions imply extra terms in the continuity equations:

$$\left(\frac{d\rho_h}{dt}\right)_{\text{therm.inst}} = -\left(\frac{d\rho_c}{dt}\right)_{\text{therm.inst}} = -\frac{C\Lambda_r(\rho_h, T_h)}{\gamma\epsilon_h - \epsilon_c}, \quad (2.4)$$

where  $\gamma$  is the ratio of specific heats.

Because of the frequent exchange of mass between the hot and cold gas phases, it is reasonable to consider the hot gas and cold clouds as *one* fluid

with rather complicated chemical reactions going on within it. Thus, only the motion of the hot component is computed in the code, integrating the change of the *total* density of the gas ( $\rho_{\text{gas}} = \rho_c + \rho_h$ ).

Both phases are assumed to be in pressure equilibrium,  $P_{\text{gas}} = P_c = P_h \equiv (\gamma - 1)u_h$ , where  $u_h = \rho_h \epsilon_h$  is the internal energy per unit volume. The velocity associated with the fluid involves an average over a cell size, but in a multiphase medium with supernovae, the hot gas is actually “windy”, and the cold clouds have a significant velocity dispersion (McKee & Ostriker, 1977; Cowie, et al., 1981; Hensler and Burkert, 1990.). Therefore, the code includes an effective pressure  $P_{\text{disp}} \propto \rho_c T_h$  associated with the cold gas component.

Star formation takes place in the cold clouds, leading to a decrease in the density given by

$$\left(\frac{d\rho_c}{dt}\right)_{\text{star-formation}} = -\frac{\rho_c}{t_*}, \quad (2.5)$$

where  $t_* \approx 10^8$  yr is a fixed characteristic star formation time. The actual time-scale for star formation can exceed  $t_*$  and will depend strongly on the rate of the conversion of hot gas to the cold phase. The lifetime of massive stars is about  $10^7$  yr or even shorter; thus most of stars with  $M_*$  heavier than  $(10 - 20)M_\odot$  will explode as supernovae during one timestep. Stars in the mass interval from  $(5-7)M_\odot$  to  $10M_\odot$  will explode on a longer time-scale, but they produce less energy, and therefore in view of the uncertainties in supernova energy, their energy input is neglected in the model. Due to the explosion of massive stars, the stellar growth rate is decreased by the fraction  $\beta$  of stars that explode as supernovae:

$$\frac{d\rho_*}{dt} = \frac{(1 - \beta)\rho_c}{t_*}. \quad (2.6)$$

The precise value of  $\beta$  is very sensitive to the form of the initial mass function (IMF), particularly its low-mass limit. The principal source of uncertainty is the dependence of the IMF on the abundance of heavy elements, which can be of critical importance at very early epochs of galaxy formation. In view of these uncertainties,  $\beta$  is taken to be constant in time. For a Salpeter IMF, the fraction of mass in stars with mass larger than  $10M_\odot$  is  $\beta = 0.12$ .

Evaporation of cold clouds is an important effect of supernovae on the interstellar medium (McKee & Ostriker 1977, Lada 1985). The total mass of cold gas heated and transferred back to the hot gas phase is assumed to be a factor  $A$  higher than that of the supernova itself. The *supernova feedback parameter*  $A$  could depend on, among other things, the energy of the supernovae, the cloud spectrum, and the ambient density. McKee and Ostriker (1977) give an estimate of the evaporated mass which scales with

the energy of the supernova  $E$  and the gas density as  $E^{6/5} \cdot n_h^{-4/5}$ . However, at present we do not include the dependence on the gas density, because here  $n_h$  refers to the local density, which is relevant for the propagation of the supernova shock, whereas our  $n_h$  is the mean density of the hot gas averaged over quite large a volume.

Assuming that the energy input due to supernovae is proportional to their total mass, we obtain for the evaporation rate

$$\left(\frac{d\rho_h}{dt}\right)_{\text{evap}} = -\left(\frac{d\rho_c}{dt}\right)_{\text{evap}} = \frac{A\beta\rho_c}{t_*} \quad (2.7)$$

Correspondingly, the net energy supplied to the hot gas phase by supernovae is:

$$\left(\frac{d\rho_h\epsilon_h}{dt}\right)_{\text{SN}} = \frac{\beta\rho_c}{t_*}[\epsilon_{\text{SN}} + A\epsilon_c]. \quad (2.8)$$

where  $\epsilon_{\text{SN}} = \langle E_{\text{SN}} \rangle / \langle M_{\text{SN}} \rangle$ ,  $\langle E_{\text{SN}} \rangle = 10^{51}$  erg, and  $\langle M_{\text{SN}} \rangle = 22M_{\odot}$  (Salpeter IMF). Admissible values of the supernova feedback parameter  $A$  are constrained by the condition that the energy of a supernova explosion must be larger than the energy required for the evaporation of cold clouds. This restriction leads to  $\epsilon_{\text{SN}} > A \cdot (\epsilon_h - \epsilon_c)$ . For the above supernova energy and mass and for hot gas temperature  $T_h \approx 10^6$  K, this condition implies the restriction  $1 \leq A < 250$ .

Therefore, for large values of  $A$ , cloud evaporation dominates over thermal re-heating, which translates into less pressure gradients and more mass transfer between cold and hot phases.

### 2.1.2 ART

The spatial resolution of particle-mesh codes like YK<sup>3</sup> can be substantially improved by means of adaptive grids that provide more resolution in the high density regions where galaxies form. The *Adaptive Mesh Refinement* (AMR) method increases the dynamical range with respect to YK<sup>3</sup> by about two orders of magnitude without loss of mass resolution or computational speed.

#### Gravity

The *Adaptive Refinement Tree* (ART) N-body code developed by Kravtsov et al. (1997) is based on this technique. The computational volume is covered by a cubic regular grid that defines the minimum resolution, where the Poisson equation is solved with a traditional *Fast Fourier Transform* (FFT) technique using periodic boundary conditions, as in the PM algorithm. The difference is that this grid is *refined* (i.e. its cells are divided) wherever the density exceeds a predefined threshold.

Any cell can be subject to further refinements; the local refinement process continues recursively until the density criterion is satisfied. Once constructed, the mesh is adjusted at each timestep to the evolving particle distribution. Finer meshes are built as collections of cubic, non-overlapping cells of various sizes organised in *octal threaded trees* (i.e. each node may be split in eight sub-cells).

This is the same construct used in standard Tree codes, but there is an important difference in that cells are connected to their 6 neighbours in a *Fully Threaded Tree* (FTT, Khokhlov 1998) on all levels of refinement. In addition, cells that belong to different trees are connected to each other across tree boundaries. We can consider all cells as belonging to a single threaded tree with a root being the entire computational domain and the base grid being one of the tree levels.

The refinement procedure can be used either to construct the mesh hierarchy from scratch or to modify the existing meshes. However, in the course of a simulation the structure is neither constructed nor destroyed. Instead, the existing meshes are modified every computational cycle to account for the changes in particle distribution. Therefore, the computational mesh is adapted automatically to the structures developed as clustering proceeds.

Poisson equation must be solved on every refinement level. Therefore, the value of the density must be computed for every cell regardless of whether or not it is a leaf. On each level, starting from the finest one and up to the zeroth level, the density is assigned using the standard CIC interpolation from the particle positions. For the zeroth level of the mesh hierarchy (regular grid of fixed resolution), Poisson equation is solved by the standard FFT method. In the refinement sub-meshes, the *relaxation* method (Hockney and Eastwood 1981; Press et al. 1986) is used. Masses and timesteps are independent for each particle.

## Gas dynamics

The ART code achieves high spatial resolution by adaptively refining regions of interest using an automated refinement algorithm. Due to the use of an Eulerian mesh hierarchy in the FTT algorithm, the inclusion of Eulerian gasdynamics is a natural extension to the pure N-body part.

As in YK<sup>3</sup>, the equations of gasdynamics and particle motion are integrated in 'supercomoving' variables Martel and Shapiro (1998); Yepes (2001). These variables are remarkable as their use almost completely (completely for ideal gas with  $\gamma = 5/3$ ) eliminates explicit dependence on cosmology in the model equations. The equations can therefore be integrated using standard solvers used in computational fluid dynamics, with no need for additional coefficients and corrections.

The main features of the gasdynamics implementation follow closely the algorithm used in YK<sup>3</sup>. A second-order Godunov-type solver (Colella and Woodward

1984) is used to compute numerical fluxes of gas variables through each cell interface, with 'left' and 'right' states estimated using piecewise linear reconstruction van Leer (1977). For cells that have neighbours at the same tree level, the entire integration procedure is formally second order accurate both in space and in time. For cells that have neighbouring leaves at different levels, the accuracy reduces to first order.

Gasdynamics is coupled to the dynamics of dark matter through the common potential, which is used to compute accelerations for both the DM particles and the gas. The code employs the same data structures and similar refinement strategy as the FTT used in the  $N$ -body part. However, in addition to the DM density criteria it also allows for additional refinement based on the local density of gas, as well as shock or sharp gradient indicators. The refinement criteria can be combined with different weights allowing for a flexible refinement strategy that can be tuned to solve the Euler equations for an inviscid flow according to the needs of a particular simulation.

### 2.1.3 GADGET

In recent years there has been considerable effort in developing tree codes that could run in parallel computers. This can alleviate the two most important drawbacks of these algorithms: Large memory requirements and long computations per timestep. In the present work we have extensively employed the Tree-SPH code GADGET (a rather strange acronym for *GA*laxies with *Dark* matter and *Gas* int*ERacT*), recently developed by Springel et al. (2001b) and publicly available from this Internet web page

<http://www.mpa-garching.mpg.de/gadget/>

GADGET computes gravitational forces with the hierarchical octal-tree algorithm proposed by Barnes and Hut (1986). The collisional fluid (gas) is represented by means of Smoothed Particle Hydrodynamics (SPH). The code is fully adaptive both in force computation and in time stepping (i.e. each particle has its individual mass and time step). Five different particle species can be defined by the user, each of them with its own gravitational smoothing, which is implemented as a spline-softened potential for point masses. Also, there are different criteria for selecting the optimal timestep. In what follows we will briefly describe how this code deals with gravity and gas dynamics.

#### Gravity

As we said above, gravity forces are computed by means of the BH tree algorithm. In this scheme, the particles are arranged in a hierarchy of groups according to their position in space. When the force on a particular particle is computed, the force exerted by distant groups is approximated by

their lowest multipole moments. In this way, the computational cost for a complete force evaluation can be reduced to order  $\mathcal{O}(N \log N)$ . The forces become more accurate if the multipole expansion is carried out to higher order, but eventually the increasing cost of evaluating higher moments makes it more efficient to terminate the multipole expansion and rather use a larger number of smaller tree nodes to achieve a desired force accuracy. As a compromise between accuracy and speed, the multipole expansion is terminated after the quadrupole moments have been included.

Force computation then proceeds by walking the tree, and summing up appropriate force contributions from tree nodes. In the standard BH tree walk, the multipole expansion of a node of size  $l$  is used only if

$$r > \frac{l}{\theta}, \quad (2.9)$$

where  $r$  is the distance of the point of reference to the centre-of-mass of the cell and  $\theta$  is a prescribed accuracy parameter. If a node fulfills the criterion (2.9), the tree walk along this branch can be terminated, otherwise it is ‘opened’, and the walk is continued with all its daughter nodes. For smaller values of the opening angle, the forces will in general become more accurate, but also more costly to compute.

The standard BH opening criterion tries to limit the relative error of every particle-node interaction by comparing a rough estimate of the size of the quadrupole term,  $\sim Ml^2/r^4$ , with the size of the monopole term,  $\sim M/r^2$ . The result is the purely geometrical criterion of equation (2.9). In the `GADGET` code, the acceleration of the previous timestep is used as a handy approximate value for the accuracy of force computation. Therefore, it is required that the estimated error of an acceptable multipole approximation is some small fraction of this  $\alpha$  total force.

The tree-construction can be considered very fast in both cases, because the time spent for it is negligible compared to a complete force walk for all particles. However, in the individual time integration scheme only a small fraction  $M$  of all particles may require a force walk at each given timestep, and hence the full tree is only reconstructed after a fixed number of timesteps has elapsed.

Time integration of Newton’s equations is a variant of the classical Leapfrog scheme in which an explicit prediction step is introduced to accommodate individual timesteps for particles. There are different possibilities for the choice of timestep size in `GADGET`. One is based on the second order displacement of the kinetic energy, assuming a typical velocity dispersion  $\sigma^2$  for all particles. This results is  $\Delta t = \alpha\sigma/|\mathbf{a}|$ . The other method is to constraint the second-order particle displacement ( $\Delta t \propto 1/\sqrt{|a|}$ ), or a more sophisticated one (and more computational expensive) based on an estimation of the local dynamical time ( $\Delta t \propto 1/\sqrt{G\rho}$ ). According to the convergence studies recently carried out by Power et al. (2002), we have cho-

sen the timestep criterion based on second order particle displacement, with the optimal parameters as given in that study.

### Gas dynamics

GADGET uses an implementation of SPH to estimate pressure forces acting on the collisional fluid. SPH is a powerful Lagrangian technique to solve hydrodynamical problems with an ease that is unmatched by grid based fluid solvers (see Monaghan 1992, for an excellent review). In particular, SPH is very well suited for three-dimensional astrophysical problems that do not crucially rely on accurately resolved shock fronts because, as we mentioned earlier, numerical artificial viscosity introduces some unphysical dissipation in the fluid.

Unlike other numerical approaches for hydrodynamics, the SPH equations do not take a unique form. Instead, many formally different versions of them can be derived. Furthermore, a large variety of recipes for specific implementations of force symmetrisation, determinations of smoothing lengths, and artificial viscosity, have been proposed.

Most of the SPH implementations integrate the standard mass, momentum and energy conservation equations for the fluid. The computation of the hydrodynamic force and the rate of change of internal energy proceeds in two phases. In the first phase, new smoothing lengths  $h_i$  are determined for the *active* particles (these are the ones that need a force update at the current timestep, see below), and for each of them, the neighbouring particles inside their respective smoothing radii are found. The Lagrangian nature of SPH arises when this number of neighbours is kept approximately constant. This is achieved by varying the smoothing length  $h_i$  of each particle accordingly, leading to a constant mass resolution independent of the density of the flow.

From the neighbours of each *active* particle, the density and the rest of quantities can be found using an spline interpolation kernel

$$\rho_i = \sum_{j=1}^N m_j W(\mathbf{r}_{ij}; h_i), \quad (2.10)$$

where  $\mathbf{r}_{ij} \equiv \mathbf{r}_i - \mathbf{r}_j$ . For the rest of the particles, values of for density, internal energy, and smoothing length are predicted at the current time based on the values of the last update of those particles. An equation of state for an ideal gas gives the pressure as a function of density and internal energy:  $P_i = (\gamma - 1)\rho_i u_i$ .

SPH is a slowly converging method with the number of particles. Theoretically, SPH equations will be exact in the limit  $N_{SPH} \rightarrow \infty$ . In cosmological problems, in which large volumes are often simulated, the mass resolution is rather coarse. Hernquist (1993) has shown that while integration of energy equation with SPH formalism results in rather good energy

conservation, the entropy is not conserved even for purely adiabatic flows. He also showed that the cause of the errors can be found in the use of variable smoothing and the neglect of relevant terms in the dynamical equations associated with the space dependence of  $h_i$ .

However, even if fixed smoothing is used in a simulation, simultaneous conservation of entropy and energy can only be achieved in the limit of large  $N_{SPH}$ . Most people believe that violation of entropy is a fair price to pay for energy conservation. Therefore, most of SPH codes developed so far do show this problem. As have been shown recently (Springel and Hernquist 2002a), integrating the thermal energy equation with SPH with not enough number of particles can lead to significant violations of entropy conservation in situations which are important for cosmological simulations of galaxy formation. As we will discuss in detail in Section 4.1, this problem with entropy dissipation of SPH codes could be the reason of the discrepancies that showed up in the Santa Barbara cluster comparison (Frenk et al. 1999).

Two possibilities have been proposed to overcome this problem: One is to include in the formulation of the dynamical equations for SPH particles the  $\nabla h$  terms associated with spatial derivatives of the smoothing length (e.g. the AP<sup>3</sup>M-SPH code DEVA Serna et al. 2002). The other solution, proposed by Springel and Hernquist (2002a), is an elegant formulation of SPH which employs variable smoothing lengths and explicitly conserve both energy and entropy. To this end, the equations of motion for the fluid particles were derived from the Lagrangian defined as:

$$L(\mathbf{q}, \dot{\mathbf{q}}) = \frac{1}{2} \sum_{i=1}^N m_i \dot{\mathbf{r}}_i^2 - \frac{1}{\gamma - 1} \sum_{i=1}^N m_i A_i \rho_i^{\gamma-1} \quad (2.11)$$

in the independent variables  $\mathbf{q} = (\mathbf{r}_1, \dots, \mathbf{r}_N, h_1, \dots, h_N)$ , where the thermal energy acts as the potential generating the motion of SPH particles. The densities  $\rho_i$  are functions of  $\mathbf{q}$  defined by the standard SPH kernel interpolation from particle positions. The internal energy is computed in terms of the specific entropy of fluid elements,  $A(s)$ , which for an ideal gas is  $u_i = \frac{A_i}{\gamma-1} \rho_i^{\gamma-1}$ . The quantities  $A_i$  are treated as constants (i.e. the flow is assumed to be strictly adiabatic).

The smoothing lengths  $h_i$  are selected by requiring that a fixed mass is contained within a smoothing volume, which provides  $N$  constraints

$$\phi_i(\mathbf{q}) \equiv \frac{4\pi}{3} h_i^3 \rho_i - M_{\text{sph}} = 0 \quad (2.12)$$

on the coordinates of the Lagrangian (note that, for SPH particles of the same mass, the requirement of constant  $M_{\text{sph}}$  is equivalent to a fixed number of neighbours). The equations of motion reduce thus to

$$\frac{d\mathbf{v}_i}{dt} = - \sum_{j=1}^N m_j \left[ f_i \frac{P_i}{\rho_i^2} \nabla_i W_{ij}(h_i) + f_j \frac{P_j}{\rho_j^2} \nabla_i W_{ij}(h_j) \right], \quad (2.13)$$



where the  $f_i$  are defined by  $f_i \equiv \left[1 + \frac{h_i}{3\rho_i} \frac{\partial \rho_i}{\partial h_i}\right]^{-1}$  and the abbreviated form  $W_{ij}(h) \equiv W(|\mathbf{r}_i - \mathbf{r}_j|, h)$  has been used.

Because the potential (thermal) energy of the Lagrangian depends only on coordinate differences, the pairwise force in equation (2.13) is automatically anti-symmetric. Total energy, entropy, momentum, and angular momentum are therefore all manifestly conserved, provided that the smoothing lengths are adjusted locally to ensure constant mass resolution as defined by equation (2.12). Moreover, the  $\nabla h$  terms are implicitly included in the equations through the  $f_i$  factors.

As in the standard (energy) implementation of SPH, artificial viscosity must be included to allow for the handling of shocks. A viscous force

$$\left. \frac{d\mathbf{v}_i}{dt} \right|_{\text{visc.}} = - \sum_{j=1}^N m_j \Pi_{ij} \nabla_i \bar{W}_{ij}, \quad (2.14)$$

is added to the acceleration given by equation (2.13). The resulting dissipation of kinetic energy is exactly balanced by a corresponding increase in thermal energy if the entropy is evolved according to

$$\frac{dA_i}{dt} = -\frac{\gamma-1}{\rho_i^\gamma} \mathcal{L}(\rho_i, u_i) + \frac{1}{2} \frac{\gamma-1}{\rho_i^{\gamma-1}} \sum_{j=1}^N m_j \Pi_{ij} \mathbf{v}_{ij} \cdot \nabla_i \bar{W}_{ij}, \quad (2.15)$$

which assumes that entropy is *only* generated by the artificial viscosity in shocks, and by possible external sources of heat ( $\mathcal{L}(\rho_i, u_i)$ ), if they are present (e.g. feedback from stars).

The modifications needed in the original GADGET code to account for this new version of SPH are not very important. A slight alteration is required for the algorithm which updates smoothing lengths, since it is now necessary to ensure that a ‘constant mass’ resides within a smoothing volume rather than a constant number of neighbours.

Tests performed by Springel and Hernquist (2002a) with this new implementation of SPH show that entropy is much better conserved, avoiding the substantial overcooling produced in poorly resolved haloes. In the standard SPH implementation based on the thermal energy equation, the lack of resolution can lead to insufficient compressional heating in the accretion flow, resulting in severe entropy losses.

For our numerical experiments of cluster formation we have used the new version of GADGET, based on the entropy-conserving implementation of SPH. Nevertheless, in order to check the differences with respect to the standard SPH technique, we have run several test simulations of cluster formation with both versions of the parallel code: The standard, public available, version and the entropy implementation of SPH, kindly provided by Volker Springel. Moreover, to compare SPH results with other numerical

integration schemes, some simulations of the same initial conditions have been rerun with the Eulerian gasdynamical code ART by Andrey Kravtsov (Kravtsov et al. 2002; Nagai and Kravtsov 2002). The outcome of this comparison is reported in Section 4.1.

## 2.2 Analysis

The output of a numerical experiment is a data file with the positions and velocities of dark matter and gas particles, gas densities and temperatures, and so on. In order to make a physical interpretation of these data, the analysis procedure is as important as the numerical simulation itself.

In this section, we describe the conventions followed in the analysis of the results of our numerical simulations. We address the questions of how to set the resolution limit, the definition of objects from particle data, and the computation of several magnitudes of physical interest, as well as their radial profiles. Throughout the present work, all magnitudes are expressed in units of  $H_0 \equiv 100h \text{ km s}^{-1} \text{ Mpc}^{-1}$ .

### 2.2.1 Resolution limit

Maybe the most common problem that must be faced by numerical simulations is the lack of mass and force resolution. Spurious effects arising from a low number of particles constitute a major source of uncertainty in any numerical experiment. In galaxy clusters, poor resolution leads to the so-called overmerging problem (see e.g. White et al. 1987; Klypin et al. 1999), namely the loss of substructure within the dark matter halo. Moreover, resolution is of critical importance in determining the radial profiles of both dark matter and baryons at very small radii.

It is not clear which numerical effects may determine the minimum scale above which the results of a given code can be trusted, but it is quite likely that this convergence scale is determined by a complex interplay of all possible numerical effects. Although there have been some recent attempts at unravelling the role of numerical parameters on the structure of simulated dark matter haloes (e.g. Moore et al. 1998a; Knebe et al. 2000; Klypin et al. 1999, 2001; Ghigna et al. 2000; Power et al. 2002), the conclusions from these works are still preliminary and, in some cases, even contradictory.

To cite an example, Moore et al. (1998a) argue that the smallest resolved scales correspond to about half the mean inter-particle separation within the virial radius, and conclude that many thousands of particles are needed to resolve the inner density profile of dark matter haloes. Klypin et al. (2001), on the other hand, conclude that the convergence scale is  $\sim 4$  times the formal force resolutions, or the radius containing 200 dark matter particles, whichever is larger. Ghigna et al. (2000) suggest a similar criterion based on the gravitational softening length, and argue that convergence is only

achieved on scales that contain many particles and that are larger than about  $\sim 3$  times the scale where pairwise forces become Newtonian.

Understanding the precise role of numerical parameters is clearly needed before a firm theoretical prediction for the structure of CDM haloes on  $\sim$ kpc scales may emerge. This question is particularly difficult because of the lack of a theory with which the true structure of dark haloes may be predicted analytically, so the best that can be done is to establish the conditions under which the structure of a simulated dark halo is independent of numerical parameters.

Furthermore, we note that most convergence criteria have been derived considering the minimum scale at which the density profiles of different resolution simulations are consistent among themselves. Other properties of dark matter haloes, such as their three-dimensional shape, their detailed orbital structure, or the mass function of substructure haloes, may require different resolution limits. For the radial profiles related to gasdynamical quantities, the convergence scale has been investigated in several studies (e.g. Borgani et al. 2002). The number of SPH neighbours plays a crucial role in the accuracy of results (see e.g. Power et al. 2002). In all our SPH simulations, this parameter has been set to 40 particles.

Having all these considerations into account, we adopted the following criteria to set the resolution limit of the numerical experiments using particle-based codes (GADGET) described in this chapter:

- 100 gas particles contained within  $r_{\min}$
- 200 dark matter particles
- $r_{\min} \geq 4\epsilon$ , where  $\epsilon$  is the gravitational softening length<sup>1</sup>

Usually, the first condition imposes the most stringent constraints on our resolution, since gas tends to be substantially less concentrated than the dark matter due to the repulsive pressure force. Hence, the radial profiles computed for GADGET feature an apparent lower spatial resolution than those of the N-body code ART, but this only reflects the presence of gas in the former simulations.

This resolution limit is only applied to the minimum scale that has been considered reliable in the radial profiles. Global quantities (see Section 2.2.4 below) have been computed from all the particles within the virial radius of the clusters.

### 2.2.2 Object finding

Obviously, the first step that must be taken to analyse a cluster of galaxies (or any other object) is to locate it. Identification of haloes in high density

---

<sup>1</sup>In GADGET, using a spline-based smoothing potential for point particles, pairwise force becomes Newtonian for  $r \sim 2.3\epsilon$

environments, such as groups and clusters of galaxies, is a challenging problem. Currently, there are several methods to accomplish this task, each one with its own merits and drawbacks. To mention some of the most popular, the *Friends Of Friends* (FOF, see e.g. Davis et al. 1985) algorithm connects those particles that are separated less than a given linking length. A hierarchical version of this method has been proposed (Klypin et al. 1999) to overcome the merging of apparently distinct haloes when the linking length is set too large and the missing of many particles when it is too small. An alternative is the 'spherical overdensity' scheme (e.g. Lacey and Cole 1994; Klypin et al. 1996), which looks for local maxima of the density field above some threshold defined as the 'virial' overdensity. Springel et al. (2001a) use a more elaborate algorithm that limits the objects by the isodensity contour that traverses a saddle point.

For our analysis, we have chosen the *Bound Density Maxima* (BDM, see e.g. Colín et al. 1999; Klypin et al. 1999) galaxy finding algorithm to identify bound structures from particle positions and velocities. This approach is based on the 'spherical density' outlined above, but particles that are not bound to the identified halo are removed recursively until a self-consistent definition of the object is found. The BDM algorithm proves extremely helpful in finding substructure within the dark matter haloes of galaxy clusters. As we discuss in Section 2.3.1 below, the presence of significant substructure within the virialised region of a cluster is used as an indicator of dynamical activity.

Another important issue is the determination of the centre of mass. This question is particularly relevant in those cases where the cluster halo is not exactly spherically symmetric, or when the study focuses on the detailed properties of the innermost regions of the simulated clusters.

We use as a first approximation the position given by the BDM algorithm, and then an iterative technique is employed in which the centre of mass is found for particles contained within a shrinking sphere. At each step of the iteration, the centre of the sphere is reset to the last computed barycenter (as a starting point, we use the BDM value) and its radius is reduced by 5%. The centre of mass is thus computed recursively until a convergence criterion is met. In our case, the iteration is stopped at the resolution limit described above, checking that the variation in the final centre of mass is less than  $1 h^{-1}$  kpc.

Halo centres identified with this procedure are quite independent of the parameters chosen to start the iteration, provided that the initial sphere is large enough to encompass a large fraction of the system. In a multi-component system, such as a dark halo with substructure, this algorithm isolates the densest region within the largest subcomponent. In more regular systems, the centre so obtained is in good agreement with centres obtained by weighing the centre of mass by the local density or gravitational potential of each particle.

### 2.2.3 Radial profiles

Throughout most part of this work, our analysis of the physical properties of galaxy clusters will focus on the spherically-averaged radial profiles of several quantities of physical interest. Although the detailed structure of clusters displays significant departures from spherical symmetry, radial profiles offer a simple description of the dynamical state of the system, providing a great deal of helpful information about both the dark and baryonic components.

This section is devoted to clarify those aspects of our analysis that are not straightforward. The spherically-averaged profiles are measured by binning the particles according to their distance from the centre of mass of the at  $z = 0$ . Logarithmic bins in steps of 0.05 dex are used in all cases, except in the computation of the radial profiles of projected quantities, for which a constant step of  $10 h^{-1}$  kpc is used. In this case, the cluster properties are computed within cylindrical shells oriented along the coordinate axes, truncated at a distance of  $3 h^{-1}$  Mpc. The final profile is taken to be the mean value of the three projections in order to reduce noise.

#### Dark matter

Density, cumulative mass and circular velocity ( $V_c^2(r) = GM(r)/r$ ) are computed the usual way. In order to study the kinetical structure of our clusters of galaxies, we have obtained several radial profiles related to the velocity of the particle with respect to the centre of mass. For each bin, the movement have been decomposed into the radial and tangential directions, as well as in bulk (i.e. average) and random motions ( $\sigma_i^2(r) = \langle v_i^2 \rangle - \langle v_i \rangle^2$ ). Angular momentum has been computed from the tangential component of the velocity, assuming that the radius is constant for all the particles in the bin. Ordered rotation is computed from  $\langle v_{tg} \rangle$ , while the contribution of random motions comes from the tangential velocity dispersion.

The orbits of individual particles have also been classified according to their apocentric radii (see Section 3.2.2). This is done by computing the gravitational potential  $\phi(r) - \phi_0 = \int_0^r GM(x)/x^2 dx$ , assuming spherical symmetry. This approximation incurs in some uncertainty due to the time variation in the mass distribution of the cluster. This effect is more important in the outer parts, where the cluster is still accreting a significant amount of matter at the present epoch.

Once the gravitational potential is known, the pericentric and apocentric radii that a particle reaches during its orbit are easily computed from its position and velocity. A useful quantity is the eccentricity, defined as  $e \equiv (r_{\max} - r_{\min}) / (r_{\max} + r_{\min})$ . It measures the depth that particles are able to penetrate into the cluster potential well; a value  $e = 0$  corresponds to perfectly circular orbits, whereas  $e = 1$  indicates that the particle trajectory goes through the centre.

## Gas

Gas density and mass are computed in an analogous manner as for the dark matter. We will use the notation  $F_b$  to denote the *global* baryon fraction,  $F_b \equiv M_g/M$ . The *local* baryon fraction will be referred to as  $f_b(r) \equiv \rho_g(r)/\rho_{dm}(r)$ . Note that the total mass is used in the definition of  $F_b$  while  $f_b$  is the ratio of the baryonic to the dark matter density. The difference, though, is quite small.

Temperature of gas particles is inferred from its internal energy. Bolometric X-ray luminosity is approximated by pure bremsstrahlung emission, where the emissivity is given by  $n_e^2 \Lambda(T)$ , that is, the square of the electron density  $n_e = \rho_g/(\mu m_p)$  times the cooling function  $\Lambda(T)$  ( $m_p$  is the proton mass and  $\mu = 0.65$  is the mean molecular weight of a fully ionised plasma). Following Navarro et al. (1995), we will assume that, at the temperatures relevant for galaxy clusters, the cooling function can be well approximated by

$$\Lambda(T) \simeq 1.2 \times 10^{-24} \left( \frac{T}{1 \text{ keV}} \right)^{1/2} \text{ erg s}^{-1} \text{ cm}^3 \quad (2.16)$$

and hence the luminosity of a set of SPH particles can be computed as

$$L_X = 1.2 \times 10^{-24} \sum_{i=1}^N \frac{m_i \rho_i}{(\mu m_p)^2} T_i^{1/2} \quad (2.17)$$

where  $m_i$ ,  $\rho_i$  and  $T_i$  are the mass, density and temperature of each gas particle.

Other quantities can be obtained from the radial density and temperature profiles, such as the polytropic index  $\gamma(r) = 1 + \frac{d \log(T)}{d \log(\rho)}$  or the gas entropy, defined as  $S(r) = T n_e^{-2/3}$ .

## Average profiles

A convenient way to represent our results is to combine the information obtained from a certain number of clusters into a single plot. Our approach is based on the following scheme:

1. Compute individual profiles
2. Define radial bins (points to plot)
3. For each bin, interpolate the value of every profile at that point
4. Compute mean value and standard deviation

Averaged profiles reported in the present work have been computed according to this simple prescription. The quoted error bars correspond to the standard deviation (note that, in some cases, this quantity can be dominated by Poisson noise due to the low number of clusters considered).

### 2.2.4 Global properties

In many occasions, we will be interested not only in the radial structure of galaxy clusters, but also in their bulk properties. Therefore, we must define their average value up to some radius that we define as the cluster limit.

As it happens in observations, there is no unambiguous prescription to define this limit. In a Standard Cold Dark Matter (SCDM) cosmology, spherical collapse theory predicts that dark matter haloes should be in virial equilibrium at densities of roughly  $200\rho_c$ . The radius at which the cumulative overdensity reaches 200 has often been used to mark the boundary of both observed and simulated objects. However, this estimate is a very simple approximation to the non-linear process of virial relaxation. As we will show in Section 4.2.1, the assumption that clusters of galaxies are in equilibrium at these large radii holds only marginally.

In a  $\Lambda$ CDM universe, this simple prescription based on spherical collapse yields an even lower density for virialisation ( $\sim 100\rho_c$ ). However, for historical reasons, it is not uncommon that the value corresponding to the SCDM model is used to define the limit of clusters. Since the difference in most physical quantities computed at  $r_{100}$  or  $r_{200}$  is not large, and the latter is most often quoted in observational studies, throughout this thesis we will use the term 'virial' to denote quantities defined at  $\Delta = 200$ , that is,

$$M_{200} \equiv \frac{4\pi}{3} 200\rho_c r_{200}^3 \quad (2.18)$$

In any case, the overdensity at which a magnitude is evaluated will always be indicated by a numerical subscript. For instance, in Section 4.3, the scaling relations between the total mass, luminosity and temperature are investigated at several values of the overdensity threshold  $\Delta$ , similar to those observed by the current generation of X-ray satellites.

In order to make a more consistent comparison with these observations, we compute the emission-weighted temperature of our galaxy clusters as

$$T_X = \frac{\sum_{i=1}^N \rho_i T_i^{3/2}}{\sum_{i=1}^N \rho_i T_i^{1/2}} \quad (2.19)$$

Unless stated otherwise, 'temperature' or ' $T$ ' will always refer to the mass-weighted temperature,  $T = \sum_{i=1}^N T_i/N$ . All other quantities are computed in the obvious way.

## 2.3 Description of the simulations

Most of the numerical analyses reported in this work is based on the study of a sample of 15 galaxy clusters simulated both with the adaptive Eulerian code ART (including only dark matter particles) and the explicit entropy-conserving implementation of the Lagrangian code GADGET (Springel and Hernquist

2002a), which uses a variant of the SPH technique to account for the gas-dynamics of the baryonic component of the intracluster medium.

In addition to this cluster sample, we have considered also the initial conditions used in the Santa Barbara Cluster Comparison Project (Frenk et al. 1999), as well as a different set of simulations (accomplished with the Eulerian YK<sup>3</sup>) that allow us to investigate the star formation and feedback effects in cluster and group environments.

### 2.3.1 Cluster sample

Our sample comprises a total number of 15 clusters of galaxies, selected from a low-resolution simulation with  $128^3$  dark matter particles. In total, we have performed 7 independent numerical experiments running GADGET on a SGI Origin 3800 parallel computer at CIEMAT (Spain), using 32 CPU simultaneously. The average computing time needed to run each simulation was  $\sim 8$  CPU days ( $6 \times 10^5$  s). The same clusters have also been simulated with the N-body version of ART on the Hitachi SVR at the LRZ (Germany).

The properties of the cluster sample are thoroughly discussed in Section 3.2, devoted to the dark matter distribution within the simulated haloes. In Chapter 4, the structure and scaling relations of the ICM gas for these clusters are investigated.

#### Initial conditions

In a cubic volume of  $80 h^{-1}$  Mpc on a side, an unconstrained realisation of the power spectrum of density fluctuations corresponding to the most favoured  $\Lambda$ CDM model ( $\Omega_m = 0.3$ ,  $\Omega_\Lambda = 0.7$ ,  $h = 0.7$  and  $\sigma_8 = 0.9$ ) was generated for a total of  $1024^3$  Fourier modes. The density field was then re-sampled to a grid of  $128^3$  particles which were displaced from their Lagrangian positions according to Zeldovich approximation up to  $z = 49$ . From this initial conditions, ART (dark matter only) and GADGET (dark and gas) codes were used to evolve the particles up to  $z = 0$ .

Selected clusters have been re-simulated with higher resolution by means of the multiple mass technique (see Klypin et al. 2001, for further details). For each one of them, we have computed the particles in a spherical region around the centre of mass of the  $128^3$  low-resolution counterpart at  $z = 0$ . Mass resolution is then increased by adding smaller particles in the Lagrangian volume depicted by these particles, including the additional small-scale waves from the  $\Lambda$ CDM power spectrum in the new initial conditions.

This is illustrated in Figure 2.1, where the colour code is used to indicate the refinement level. A buffer of medium-resolution particles (blue) avoids undesired two-body encounters between high-resolution (red) particles and the coarsest level (black) of refinement.



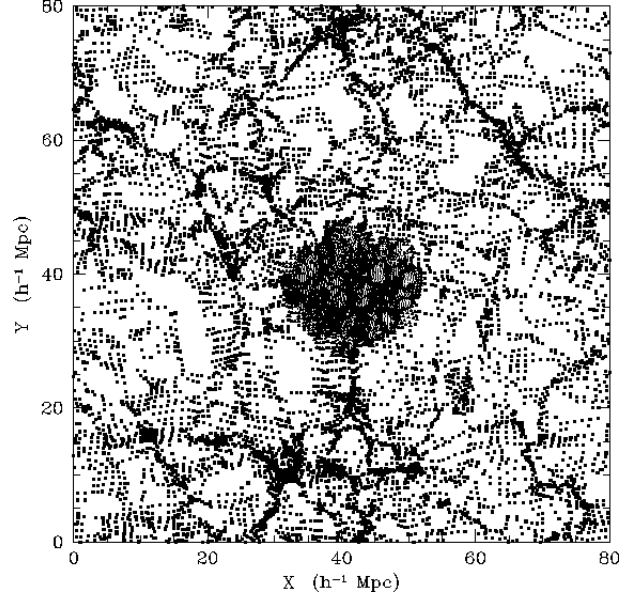


FIGURE 2.1: Mass refinement technique

Some of the clusters in the sample described in the present section were so close to each other that their Lagrangian spaces overlapped at high  $z$ . Hence, these objects have been simulated together and only 7 experiments have been necessary in order to re-simulate the full sample with high resolution. Individual images of every cluster can be found in Appendix A.

Parameters of these simulations are summarised in Table 2.1, where the first column indicates the clusters that were refined in that run. In the second column, the total number of particles in the  $80 h^{-1}$  Mpc box is given, and the third column states the number of high resolution particles for each type of matter (i.e.  $N_{hi}$  dark matter particles *and*  $N_{hi}$  gas particles

CLUSTERS	$N$	$N_{hi}$	$M_{DM}^{hi}$	$M_{gas}^{hi}$
A	4504797	1190016	29.6	2.12
B	4719315	1291008	29.6	2.12
C	5454182	1651648	29.8	2.01
D, H	4411785	1136064	29.6	2.12
E, L, M	4941262	1389440	30.0	1.80
F, G, K <sub>1</sub> , K <sub>2</sub>	4585734	1217088	29.6	2.12
I, J <sub>1</sub> , J <sub>2</sub>	5032957	1438848	29.6	2.12

TABLE 2.1: Total number of particles in each simulation, number of high resolution particles ( $N_{hi}$  dark matter +  $N_{hi}$  gas) and their mass in  $10^7 h^{-1} M_{\odot}$ .

CLUSTER	STATE	$r_{200}$	$M_{200}$	$L_{200}^X$	$T_{200}$	$T_{200}^X$
A	Minor	931	18.96	70.06	2.000	2.873
B	Minor	871	15.57	20.30	1.860	2.620
C	Relaxed	871	15.53	42.65	1.958	2.810
D	Minor	771	10.77	11.49	1.301	1.642
E	Relaxed	719	8.74	12.53	1.287	1.866
F	Major	661	6.79	12.47	1.059	1.195
G	Major	638	6.10	4.50	0.844	0.818
H	Relaxed	618	5.56	16.60	1.107	1.614
I	Major	581	4.60	2.34	0.666	0.666
J <sub>1</sub>	Relaxed	584	4.67	9.99	0.937	1.498
K <sub>1</sub>	Relaxed	557	4.06	4.98	0.690	1.043
L	Minor	547	3.84	1.21	0.624	0.779
M	Major	503	2.99	0.64	0.545	0.610
K <sub>2</sub>	Minor	497	2.89	3.08	0.470	0.808
J <sub>2</sub>	Relaxed	491	2.77	8.22	0.673	0.979

TABLE 2.2: Physical properties of the clusters at  $z = 0$ .  $r_{200}$  in  $h^{-1}$  kpc, enclosed mass in  $10^{13}h^{-1} M_{\odot}$ , bolometric X-ray luminosity in  $10^{25}h$  erg  $s^{-1}$  and average temperatures (mass and emission-weighted) in keV. One or two asterisks beside the cluster name indicate minor or major merging activity (see text).

have been used in each experiment). The last two columns show the mass resolution in units of  $10^7h^{-1} M_{\odot}$ , corresponding to the three levels of mass refinement that have been employed in all cases.

The gravitational softening length has been set to  $\epsilon = 2 - 5 h^{-1}$  kpc, depending on the number of particles within the virial radius of each individual cluster (Power et al. 2002). The minimum smoothing length for SPH was fixed to the same value as  $\epsilon$ .

### Physical properties

Table 2.2 displays the physical properties of the simulated clusters at  $z = 0$ . As discussed in Section 2.2.4, the subscript '200' refers to the overdensity with respect to the critical value  $\rho_c \simeq 2.8 \times 10^{11}h^2 M_{\odot} \text{Mpc}^{-3}$  (not to be confused with the mean density of the universe,  $\rho_m \equiv \Omega_m \rho_c$ ).

Clusters have been sorted (and named) in Table 2.2 according to their virial mass at the present day. Clusters J<sub>2</sub> and K<sub>2</sub> are an exception to this rule, since they are two small groups falling into J<sub>1</sub> and K<sub>1</sub> respectively. As a matter of fact, the smallest objects in the present sample could as well be considered rich groups instead of poor clusters. Not existing a clear-cut distinction between these categories, we will apply the term 'clusters' to all

the objects regardless of their virial mass.

In order to study the effect of mergers and close encounters, we labelled as *minor merger* any cluster in which we are able to identify a companion structure within  $r_{200}$  whose mass is greater than  $0.1 M_{200}$ ; if the mass of the companion is above  $0.5 M_{200}$ , then we classify the merger as *major*; otherwise, the cluster is assumed to be a *relaxed* system in virial equilibrium.

The results of this classification scheme are quoted in the second column of Table 2.2. Clusters named  $J_i$  and  $K_i$  are relatively close pairs, but they are separate enough ( $\sim 2 - 3$  Mpc) not to be considered as mergers. In any case, it is remarkable the amount of dynamical activity found in our sample, specially for low-mass systems. This is in agreement with the results of Gottlöber et al. (2001), who found that the typical merging rate in groups is much higher than in clusters, even for galaxies of the same mass.

Another interesting issue is that minor mergers tend not to show significant features in the X-ray images, although some of their physical properties can be noticeably affected (see Appendix A). High-resolution observation (such as those based on *XMM* or *Chandra* satellites) are required in order to detect asymmetries in the inner parts of most of our merging clusters. The consequences concerning observational results based on the assumption of hydrostatic equilibrium are difficult to evaluate.

### 2.3.2 Santa Barbara Cluster

The Santa Barbara Cluster Comparison Project (Frenk et al. 1999) was a compilation of the results of different hydrodynamical codes, applied to the formation of an X-ray cluster of galaxies in a SCDM universe. In order to test the two different formulations of SPH implemented in GADGET, we have used both versions of the code to carry out simulations with these initial conditions.

Numerical experiments described in this section have been carried out in the SGI Origin 2000 at the Centro Europeo de Paralelismo de Barcelona (CEPBA), the Astrophysicalisches Institut Potsdam (AIP) and the National Center for Supercomputing Applications (NCSA). Our findings are presented in Section 4.1.

#### Initial conditions

The initial conditions for the Santa Barbara cluster experiments have been supplied by the authors, both in Eulerian and Lagrangian format. They are publicly available on the Internet, at

<http://star-www.dur.ac.uk/~csf/clusdata/>

The initial fluctuation spectrum was taken to have an asymptotic spectral index  $n = 1$ , and shape parameter  $\Gamma = 0.25$ . The cosmological parameters are those of the SCDM model, that is  $\Omega_m = 1$ ,  $\Omega_\Lambda = 0$ ,  $h = 0.5$

VERSION	$N_{\text{eff}}$	MM	$\epsilon [h^{-1} \text{ kpc}]$
E	$64^3$	No	20
E	$128^3$	No	20
E	$128^3$	No	5
E	$128^3$	Yes	15
S	$128^3$	No	20
S	$128^3$	No	5
S	$128^3$	Yes	15
S	$256^3$	Yes	2

TABLE 2.3: Santa Barbara Cluster simulations

and  $\Omega_b = 0.1$ . The cluster perturbation was chosen to correspond to a  $3\sigma$  peak of the primordial density field smoothed with a Gaussian filter of radius  $r_0 = 10$  Mpc (in  $\exp[-0.5(r/r_0)^2]$ ). The perturbation was centred on a cubic region of side  $L = 64$  Mpc.

This cluster has been simulated several times, varying the formulation of SPH used in the integration of the gasdynamic equations, the total number of particles, and the gravitational softening length.

Table 2.3 summarises the values of these parameters. The implementation of SPH is quoted by the letter in the first column, where 'E' stands for 'energy', and 'S' for 'entropy'. In each case, the corresponding conservation equation is used to evolve the gas temperature in time. The second column quotes the effective resolution of the simulation, and the third, whether multi-mass techniques have been applied or not. When multiple masses have been used, the effective resolution correspond to the highest level of refinement; otherwise,  $N_{\text{eff}}$  equals the total number of particles in the simulated box (actually, one half, because there are as many gaseous as dark matter particles). The gravitational softening length is quoted in the last column.

### Physical properties

Quite expectedly, given that all the simulations correspond to the same cluster, the final global properties of the system are similar in all the experiments quoted in Table 2.3:  $r_{200} \simeq 1.35 h^{-1}$  Mpc,  $M_{200} \simeq 0.58 \times 10^{15} h^{-1}$  Mpc,  $T_{200} = 4.6$  keV,  $L_{200}^X \simeq 1.27 \times 10^{45} h$  erg  $s^{-1}$

These figures are consistent with the values reported in Frenk et al. (1999) for the average of all the numerical experiments presented in the Santa Barbara study. However, the detailed structure of the radial profiles of the diffuse gas component shows systematic trends as a function of the SPH implementation. A detailed discussion of this effect, as well as that of poor resolution, will be given in Section 4.1.

MODEL	$\Omega_{\text{DM}}$	$\Omega_{\text{b}}$	$\Omega_{\Lambda}$	$h$	$\sigma_8$
$\Lambda$ CDM	0.325	0.025	0.65	0.7	0.9
SCDM	0.95	0.05	0	0.5	1.2
BSI	0.95	0.05	0	0.5	0.6

TABLE 2.4: Cosmological models

### 2.3.3 Star-forming clusters

In order to investigate the formation of stars and the effects of the environment on the star formation rate (SFR) of the simulated galaxies, we have performed a series of numerical experiments with the code YK<sup>3</sup>, described in Section 2.1.1. The numerical code has been parallelised using OpenMP compiler directives. Therefore, it runs very efficiently in parallel computers with either Shared or Non Uniform Memory Access (NUMA) architectures. The simulations have been performed on a variety of machines.

These simulations were aimed in principle to a broader goal than the study of galaxy clusters, namely the evolution of the SFR density in different cosmologies and environments. Therefore, they include many small-volume numerical experiments in which no clusters of galaxies are formed. These experiments, however, offer interesting insights on the star formation history of the universe, as well as the dramatical changes that the star formation activity of a galaxy undergoes when it is accreted into a massive group or cluster of galaxies. These issues are covered in detail in Chapter 5.

#### Initial conditions

As has been discussed in Section 1.1, the  $\Lambda$ CDM model has proven to be very successful in describing most of the observational data at both low and high redshifts. However, in order to study the influence of cosmology on the global SFR, we have investigated two other scenarios: the standard CDM model (dominated by dark matter density), and the BSI model with a *Broken Scale Invariant* perturbation spectrum (as predicted by double inflation, see Gottlöber et al. 1991). The main parameters describing these cosmologies are summarised in Table 2.4.

The BSI model assumes a dark matter-dominated universe similar to the SCDM cosmology, but primordial fluctuations on small scales are significantly suppressed from its power spectrum (the overall normalisation, as in the other two models, is set by COBE data on large scales). The resulting  $P(k)$  is almost the same spectrum as in the  $\tau$ CDM model, in which the primordial perturbation spectrum has been changed due to the hypothetical decay of massive  $\tau$  neutrinos (Efstathiou et al. 1992).

All the experiments described in this section are based on completely in-

EXPERIMENT	$n_r$	$N$	$L_{\text{box}}$	$L_{\text{cell}}$	$M_{\text{DM}}$	$A$	$\mathcal{D}$
$\Lambda$ CDM1	1	$350^3$	30	85.7	28.1	200	100
$\Lambda$ CDM2	1	$270^3$	21.4	79.3	22.2	200	100
$\Lambda$ CDM3	1	$300^3$	12	40	2.85	200	100
$\Lambda$ CDM4	9	$128^3$	5	39.1	2.22	200	100,500,1000
$\Lambda$ CDM5	18	$128^3$	5	39.1	2.65	0,50,200	100
SCDM	18	$128^3$	5	39.1	3.96	0,50,200	100
BSI	18	$128^3$	5	39.1	3.96	0,50,200	100

TABLE 2.5: Resolution and feedback parameters. Number of realisations, total number of particles/cells, box length in  $h^{-1}$  Mpc, cell length in  $h^{-1}$  kpc, mass of dark matter particles in  $10^6 M_{\odot}$ , supernova feedback parameter and overdensity threshold for star formation.

dependent initial conditions (i.e. they do not belong to a consistent sample, as in Section 2.3.1). As will be discussed in more detail in Sections 5.1.2 and 5.2, the effects of cosmic variance due to a small simulated (or observed) volume are not negligible on the estimation of the mean star formation rate density.

### Physical properties

Table 2.5 summaries the set of experiments performed with YK<sup>3</sup>. In order to improve statistics, several realisations have been run when the number of particles was low enough ( $N = 128^3$ ), changing the random seeds used to generate the initial conditions. The number of realisations is given by  $n_r$  in the second column. Next 4 columns show, respectively, the number of particles, box size, cell size (which determines spatial resolution in these simulations) and mass of each dark matter particle (mass resolution). In the last two columns, we quote the values of the supernova feedback parameter  $A$  and the overdensity threshold  $\mathcal{D}$  required for star formation (details on the role of these parameters in YK<sup>3</sup> can be found in Section 2.1.1).

The comparison of experiments  $\Lambda$ CDM5, SCDM and BSI allows us to determine the effect of cosmology and feedback from supernovae on the global SFR history. The photoionisation prescription can be tested basing on the results of experiment  $\Lambda$ CDM4, and the dependence on resolution and volume will be thoroughly studied from the whole set of  $\Lambda$ CDM experiments.

Finally, experiments  $\Lambda$ CDM 1 and 2 simulate a volume large enough to contain a cluster of galaxies. We will use their results to investigated the star formation history of clusters in Section 5.2, focusing on the alterations of the star formation activity of galaxies when they fall into the potential well of the cluster.

## Chapter 3

# Dark matter

*If the sun refuse to shine  
I don't mind  
I don't mind*

– Jimi Hendrix : *If 6 was 9* (1968) –

**A**ccording to the current cosmological paradigm, most mass in the universe must be in the form of non-baryonic cold dark matter particles, whose nature is yet an unknown that has been puzzling both astronomers and particle physicists during the past few decades. As far as we are concerned, cold dark matter can be considered as a perfect fluid with negligible pressure, thus obeying the collisionless Boltzmann equation. Not being coupled to the electromagnetic field, CDM particles do not emit or absorb light, and hence (neglecting some form of self-interaction) gravity is the only physical process that must be accounted for.

In clusters of galaxies, the baryon fraction is expected to be close to the cosmic value (e.g. White and Frenk 1991), which implies that the amount of cold dark matter is higher by approximately one order of magnitude than the mass in baryonic form. Structure formation will be thus driven almost entirely by the CDM component. Galaxies and clusters are assumed to form by cooling and condensation of baryons into the potential wells created by dark matter haloes, which were able to collapse during the radiation-dominated epoch.

In this chapter, we will study the gravitational and kinetic structure of clusters of galaxies. The radial distribution of mass, density, velocity dispersion and angular momentum will be investigated in detail, focusing on the existence of common patterns usually known in the literature as 'universal profiles'. We will try to understand the physical origin of these patterns in the dark matter distribution by means of a simple analytical treatment based on the secondary infall model.

Most of the work refers to the cluster sample described in Section 2.3.1. Results concerning the density profiles of these haloes and the dependence on environment can be found in Ascasibar et al. (2002c). The orbital structure of galaxy clusters, as well as the numerical treatment of spherical collapse, are to going to be published in Ascasibar et al. (2002b).

### 3.1 The case for a universal density profile

One of the most interesting properties of the dark matter haloes found in numerical simulations is the apparent universality of their radial density profiles, valid over several orders of magnitude in mass.

Contrary to the early numerical work of Quinn et al. (1986) and Frenk et al. (1988), in which dark matter haloes showed an isothermal structure (i.e.  $\rho(r) \propto r^{-2}$ ), Dubinski and Carlberg (1991) and Crone et al. (1994) had enough resolution to detect the first evidence of non-power-law density profiles. Building upon these results, Navarro et al. (1996, 1997, hereafter NFW) found that haloes in their numerical simulations could be fitted by a simple analytical function with only two parameters (e.g. a characteristic density and radius).

The main result of NFW experiments was that the radial density profile was steeper than isothermal ( $\rho \propto r^{-3}$ ) for large radii, and shallower (but still diverging as  $\rho \propto r^{-1}$ ) near the centre. The corresponding logarithmic slope

$$\alpha(r) \equiv \frac{d \log \rho(r)}{d \log r} \quad (3.1)$$

varied smoothly between these two extreme values, being equal to isothermal ( $\alpha = -2$ ) at the characteristic radius only.

Navarro et al. (1997) further show that the characteristic parameters of a dark matter halo seem to correlate to a certain extent. Should this be true, the final mass distribution of objects of different mass could be described in terms of a one-parameter family of analytical profiles. This also implies that many relevant quantities, such as virial mass, central density, or formation time, must be correlated.

Similar results have been found in several independent studies, using much higher mass and force resolution than the original NFW paper. However, there is still some disagreement about the innermost value of the logarithmic slope  $\alpha$  and its dependence on resolution. Moore et al. (1998a, 1999b); Ghigna et al. (1998, 2000) and Fukushige and Makino (1997, 2001) find even steeper density profiles near the centre ( $\alpha \sim -1.5$ ), whereas other authors (Jing and Suto 2000; Klypin et al. 2001) claim that the actual value of  $\alpha$  may depend on halo mass, merger history and substructure.



### 3.1.1 Models

In order to investigate the existence and shape of a 'universal' density profile, we will compare the mass distribution of our simulated clusters with the functional forms advocated by NFW and Moore et al. (1999b). Although these are not the only profiles proposed in the literature<sup>1</sup>, they are by far the most widely referenced. Below, we describe the main features of both profiles, as well as some derived quantities that we will use in the comparison. Further details concerning these functions, such as the associated gravitational potential or the radial velocity dispersion can be easily computed analytically (see e.g. Łokas and Mamon 2001; Suto et al. 1998).

#### NFW

The radial density profile proposed by NFW

$$\rho(r) = \frac{\rho_s}{\frac{r}{r_s} \left(1 + \frac{r}{r_s}\right)^2} \quad (3.2)$$

depends on the characteristic density  $\rho_s$  and the scale radius  $r_s$  of the dark matter halo. This profile is often written in terms of the *concentration* parameter

$$c \equiv \frac{r_{200}}{r_s} \quad (3.3)$$

as

$$\rho(r) = \frac{200\rho_c c^2 g(c)/3}{s(1+cs)^2} \quad (3.4)$$

where we have used the definitions

$$s \equiv \frac{r}{r_{200}} \quad ; \quad g(c) \equiv \left[ \ln(1+c) - \frac{c}{1+c} \right]^{-1} \quad (3.5)$$

and  $r_{200}$  follows the convention given in Section 2.2.4 (i.e. 200 times the *critical* density of the universe).

This profile steepens monotonically with radius. The logarithmic slope is given by the expression

$$\alpha(r) = -1 - 2 \frac{\frac{r}{r_s}}{1 + \frac{r}{r_s}} = -1 - 2 \frac{cs}{1+cs} \quad (3.6)$$

The mass enclosed within radius  $r$  increases as

$$M(r) = 4\pi\rho_s r_s^3 \left[ \ln \left( 1 + \frac{r}{r_s} \right) - \frac{\frac{r}{r_s}}{1 + \frac{r}{r_s}} \right] \quad (3.7)$$

---

<sup>1</sup>For example, Jing and Suto (2000) use the expression  $\rho(r) \propto r^{-1.5}(r+r_s)^{-1.5}$ , very similar to that advocated by Moore et al.

or, equivalently,

$$M(r) = M_{200} g(c) \left[ \ln(1 + cs) - \frac{cs}{1 + cs} \right] \quad (3.8)$$

Instead of the logarithmic slope (3.6) of the radial density profile, in order to compare with the results of numerical simulations, we would rather use the corresponding value for the mass distribution

$$\alpha_M(r) \equiv \frac{d \log M(r)}{d \log r} \quad (3.9)$$

We decided to do so because the density profile is prone to significant Poisson noise when a narrow radial binning is set, and hence the number of particles in each bin is not very high ( $\leq 100$ ). Since the numerical evaluation of the derivative involved in the computation of  $\alpha$  is extremely sensitive to these errors, expression (3.9) constitutes a much more stable choice to be checked against the analytic results.

In the case of a pure power law,  $\alpha_M = \alpha + 3 = \text{constant}$ . However, the NFW profile (3.7) yields

$$\alpha_M(r) = \frac{\left( \frac{r}{r_s} \right)^2}{\ln \left( 1 + \frac{r}{r_s} \right) - \frac{r}{r_s}} \quad (3.10)$$

The limit of this expression as  $r \rightarrow 0$  is  $\alpha_M(0) = 2$ , i.e.  $M(r) \propto r^2$ . We see that, although density diverges as  $1/r$ , the enclosed mass has always a finite value, tending to zero when we choose a sphere of null radius.

### Moore et al.

Based on a set of high resolution simulations, Moore et al. (1999b) claim that the density profile of dark matter haloes can be fit by the function

$$\rho(r) = \frac{\rho_m}{(r/r_m)^{3/2} [1 + (r/r_m)^{3/2}]} \quad (3.11)$$

This expression is very similar to the form advocated by Jing and Suto (2000) for galaxy clusters. The logarithmic slope of this density profile is

$$\alpha(r) = -\frac{3}{2} \left[ 1 + \frac{(r/r_m)^{3/2}}{1 + (r/r_m)^{3/2}} \right] \quad (3.12)$$

reaching an asymptotic value  $\alpha = -1.5$  near the centre.

The cumulative mass is given by

$$M(r) = M_{200} \frac{\ln [1 + (r/r_m)^{3/2}]}{\ln [1 + (r_{200}/r_m)^{3/2}]} \quad (3.13)$$

whose logarithmic slope is

$$\alpha_M(r) = \frac{3}{2} \frac{(r/r_m)^{3/2}}{[1 + (r/r_m)^{3/2}] \ln [1 + (r/r_m)^{3/2}]} \quad (3.14)$$

implying a growth  $M(r) \propto r^{1.5}$  at small radii.

### 3.1.2 Central density

Obviously, every analytical fit to the mass distribution found in numerical simulations must have approximately the same shape. NFW and Moore et al. formulae are almost indistinguishable over most part of the halo ( $r > r_s$ ) as long as  $r_m \simeq 1.7r_s$ . The only difference between these two profiles is the asymptotic behaviour as  $r \rightarrow 0$ .

However, we would like to stress at this point that the density profile at such small radii is *not* a prediction of CDM simulations, as it is often stated in the literature. The finite number of particles used in numerical N-body experiments sets an upper limit to the depth of dark matter potential, and the mass distribution at  $r \rightarrow 0$  is completely dominated by numerical effects. Therefore, any extrapolation of the phenomenological fits to the density profile below the resolution limit must be taken with extreme caution, since there is no *a priori* reason why the profile should follow any of the proposed formulae at such small distances.

The minimum radius down to which the mass distribution can be reliably estimated in numerical simulations has been recently investigated by Moore et al. (1998a); Knebe et al. (2000); Ghigna et al. (2000); Klypin et al. (2001) and Power et al. (2002) as a function of particle number, softening length or time integration scheme. The first studies by Dubinski and Carlberg (1991) and NFW contained less than  $10^5$  particles within the virial radius, resolving scales  $\sim 0.1r_{200}$ . Nowadays, high-resolution numerical simulations of galaxy clusters attain particle numbers as high as  $\sim 2 \times 10^7$  (Springel et al. 2001a) inside the dark matter halo, which allows to probe the density profile at distances smaller than  $0.01r_{200}$ .

An important fact, pointed out by Power et al. (2002), is that the logarithmic slope becomes increasingly shallow inwards, with little sign of approaching an asymptotic value at the resolved radii. In that case, the precise value of  $\alpha$  at some definite cut-off scale (either a fixed physical distance or relative to  $r_{200}$ ) would not be particularly meaningful. A similar argument has been used by Klypin et al. (2001) to explain the different inner slopes found by Jing and Suto (2000) in terms of the  $c - M_{200}$  relation.

### Observational constraints at galactic scales

It is somewhat ironic to think that the cold dark matter scenario, originally proposed to explain the observed flat rotation curves of spiral galaxies, is

nowadays extremely successful in describing the large-scale structure of the universe and even the whole process of structure formation, but faces important problems when confronted with the shape of observed rotation curves at sub-galactic scales.

Although rotation curves of nearby galaxies have been routinely measured since the early 1970s (Rubin and Ford 1970; Rogstad and Shostak 1972), the analysis of observational data has continued to evolve as larger telescopes and improved detectors became available for optical, radio and millimetre wavelengths (see e.g. Sofue and Rubin 2001).

The gravitational mass can be easily inferred from the position-velocity diagram, just equating

$$\frac{GM(r)}{r} = \left[ \frac{v(r) - v_{sys}}{\sin i} \right]^2 \quad (3.15)$$

where  $i$  is the inclination angle and  $v_{sys}$  the systemic velocity of the galaxy.

Combined measurements of HI and H $\alpha$  or CO emission lines are the best tools to probe the dark matter content at galactic scales. Optical rotation curves provide high spatial resolution near the centre, while only the neutral Hydrogen gas extends far enough in radius to trace the outer parts.

Observed rotation curves of dwarf spiral and LSB galaxies (Flores and Primack 1994; Moore 1994; Burkert 1995; Kravtsov et al. 1998; Borriello and Salucci 2001; de Blok et al. 2001; de Blok and Bosma 2002; Marchesini et al. 2002) seem to indicate that the shape of the density profile at small scales is significantly shallower than the cusps predicted by both fitting models.

This discrepancy has been often signalled as a genuine crisis of the CDM scenario, and several alternatives, such as warm (Colín et al. 2000a; Sommer-Larsen and Dolgov 2001), repulsive (Goodman 2000), fluid (Peebles 2000), fuzzy (Hu et al. 2000), decaying (Cen 2001), annihilating (Kaplinghat et al. 2000) or self-interacting (Spergel and Steinhardt 2000; Yoshida et al. 2000; Davé et al. 2001) dark matter, have been invoked.

Unfortunately, it has been proved remarkably hard to establish the inner slope of the dark matter distribution observationally (see e.g. Swaters et al. 2002). Some authors (van den Bosch and Swaters 2001; Blais-Ouellette et al. 2001; Jimenez et al. 2002; Swaters et al. 2002) claim that a cuspy density profile with  $\alpha \leq 1$  is consistent with current observations, although a shallower mass distribution is able to explain them as well. Yet, a value as steep as  $\alpha = 1.5$  can be confidently ruled out in most cases.

### Observations of galaxy clusters

Historically, most estimates of the masses of clusters were made from optical studies of their galaxy dynamics, wherein the motions of individual galaxies were used to trace the cluster potentials by virtue of the virial

theorem (Zwicky 1937; Smith 1936). Nonetheless, these studies were sensitive to systematic uncertainties due to velocity anisotropies, substructure and projection effects (Lucey 1983; Frenk et al. 1990; van Haarlem et al. 1997). More recent work based on larger galaxy samples and employing careful selection techniques has led to significant progress (Carlberg et al. 1996; den Hartog and Katgert 1996; Fadda et al. 1996; Mazure et al. 1996; Borgani et al. 1999; Geller et al. 1999; Koranyi and Geller 2000).

Accurate measures of cluster masses are accomplished via X-ray observations of the hot intra-cluster gas and analysis of distortion of background galaxies due to gravitational lensing by the cluster mass.

X-ray mass measurements rely on the assumption that the emitting gas which pervades clusters is in hydrostatic equilibrium. Using spherical symmetry and considering purely thermal support,

$$\frac{1}{\rho} \frac{dP}{dr} = -\frac{GM}{r^2} \quad (3.16)$$

where the total mass profile is determined once the radial profiles of the gas density and temperature are known (see e.g. Sarazin (1988b)). The gas density can be directly obtained from X-ray images, while temperature requires detailed spatially-resolved spectroscopy. The advent of *Chandra* and *XMM-Newton* satellites allows, for the first time, sufficiently good spatial and spectral resolution for self-consistent determinations of the density, temperature and mass profiles of galaxy clusters.

In contrast to the aforementioned optical galaxy dispersion and X-ray techniques, gravitational lensing offers a method for measuring the projected surface density of matter along the line-of-sight which is essentially free from assumptions about the composition or dynamical state of the gravitating material (e.g. Mellier 1999). While strong lensing requires compact, dense cluster cores and thus probes their central mass distribution, weak lensing arclets can be found everywhere across clusters and allow their mass to be mapped even at clustercentric distances comparable to the virial radius.

Clearly, the best approach is to combine these three methods. The first analysis combining X-ray and lensing studies (Miralda-Escude and Babul 1995) suggested that strong lensing masses within 200 kpc of the cluster centre might be typically higher by a factor of  $\sim 2 - 3$  than the X-ray inferred mass. Later work (e.g. Allen 1998) highlighted that this discrepancy only occurs for non-cooling flow clusters, which typically appear to be more dynamically active than cooling-flow systems.

Both X-ray data (Ettori et al. 2002b; Pratt and Arnaud 2002; Schmidt et al. 2001; Allen et al. 2001a; Arabadjis et al. 2002; Lewis et al. 2002a), strong (Oguri et al. 2001) and weak lensing observations (Dahle et al. 2002) find steep slopes consistent with the CDM paradigm (i.e. NFW or Moore et al. profiles). However, some authors (Tyson et al. 1998; Sand et al. 2002) report evidence of soft cores based on lensing measurements, and some of

the X-ray derived profiles are not able to rule out the possibility of a shallow (or even null) inner slope. The size of a possible core is constrained to be less than  $\sim 50$  kpc, but, for the moment, it seems that current statistics do not allow any firm conclusion to be drawn on cluster scales.

### 3.1.3 Phase-space structure

Since CDM obeys the collisionless Boltzmann equation, the velocity dispersion is related to the density field by the Jeans equation. Assuming spherical symmetry and neglecting bulk velocities (i.e. infall and rotation), the Jeans equation reads (see e.g. Binney and Tremaine 1987)

$$\frac{1}{\rho} \frac{d}{dr} (\rho \sigma_r^2) + \frac{2\beta \sigma_r^2}{r} = -\frac{GM}{r^2} \quad (3.17)$$

where  $\sigma_r$  is the one-dimensional velocity dispersion and  $\beta$  is the anisotropy parameter, defined as  $\beta \equiv 1 - \sigma_\theta^2/\sigma_r^2$ . If random motions are considered to be isotropic ( $\beta = 0$ ), the radial velocity dispersion is entirely determined by the mass distribution. For a NFW profile,

$$\sigma_r^2(r) = -\frac{r}{r_s} \left(1 + \frac{r}{r_s}\right)^2 \int_0^{\frac{r}{r_s}} \frac{4\pi G \rho_s r_s^3}{x^3(1+x)^2} \left[ \ln(1+x) - \frac{x}{1+x} \right] dx \quad (3.18)$$

from which the corresponding 'universal' profile for  $\sigma_r$  can be obtained numerically.

Following a more empirical approach, Taylor and Navarro (2001) realised that the coarse-grained phase-space density of their galaxy-sized haloes followed a power law

$$\frac{\rho}{\sigma^3} \propto r^{-\alpha} \quad (3.19)$$

with  $\alpha \simeq 1.875$  over more than two and a half decades in radius. This statement is incompatible with a NFW profile and the Jeans equation, since (3.19), once substituted into the Jeans equation, fixes both the velocity dispersion and the mass distribution of the dark matter halo. The density profile thus obtained depends on the normalisation of the velocity dispersion, becoming unphysical (decreasing towards the centre) beyond a critical value. For this critical value, the density profile is very similar to NFW, although the asymptotic slope as  $r \rightarrow 0$  is  $\alpha = 0.7$  instead of  $\alpha = 1$ .

Concerning ordered motions, Barnes and Efstathiou (1987) found in their early work an indication for a 'universal' angular momentum profile, showing a rough proportionality between  $j$  (the specific angular momentum, computed in spherical shells) and the radial coordinate. More recently, Bullock et al. (2001) claimed that the cumulative mass with projected<sup>2</sup> an-

<sup>2</sup>When comparing the projected and total angular momentum in cells throughout the halo volume, the profiles were found to be very similar (within a factor of less than 2).

gular momentum less or equal to  $j$  can be described by the function

$$\frac{M(j)}{M_{200}} = \frac{\mu j}{j_0 + j} \quad (3.20)$$

where  $j$  reaches a maximum value  $j_{200} = j_0/(\mu - 1)$  and  $\mu > 1$  is a shape parameter. If the angular momentum distribution is assumed to be spherically symmetric and monotonically increasing with  $r$ , expression (3.20) yields

$$j(r) = \frac{j_0}{\mu M_{200}/M(r) - 1} \quad (3.21)$$

Although Bullock et al. (2001) claim that the specific angular momentum distribution in their sample of simulated dark matter haloes is closer to being cylindrically symmetric than spherically symmetric, they address the question of the behaviour of  $j(r)$  averaged over spherical shells, finding  $j \propto M^{1.3}$  or, equivalently,  $j \propto r^{1.1}$ .

## 3.2 Simulation Results

In order to study the mass distribution in cluster-size haloes, we ran a series of high-resolution numerical simulations, using two completely independent codes. Since dark matter is the main contributor to the mass budget of galaxy clusters, we used the N-body version of the adaptive mesh code ART (see Section 2.1.2), including dark matter only. Furthermore, we also simulated the same clusters of galaxies with the Tree-SPH code GADGET (Section 2.1.3), which allows us to

1. Test the consistency of both integration schemes.
2. Quantify the effects of a baryonic gas on the final density profiles.

The main properties of our sample of galaxy clusters is briefly summarised in Section 2.3.1 for both ART and GADGET simulations. Individual profiles of all clusters can be found in Appendix A.

### ART vs GADGET

Figure 3.1 shows the ratio between the cumulative dark matter masses found in ART and GADGET as a function of clustercentric distance (for details on the computation of the centre of mass and radial profiles, see Section 2.2). Due to the presence of baryons in GADGET, we must rescale the masses by the appropriate value of  $\Omega_{\text{CDM}} = \Omega_{\text{m}} - \Omega_{\text{b}}$  in order to compare results:

$$\frac{\Delta M}{M} \equiv \frac{M_{\text{ART}}}{M_{\text{Gadget}}} \left( 1 - \frac{\Omega_{\text{b}}}{\Omega_{\text{m}}} \right) - 1 \quad (3.22)$$

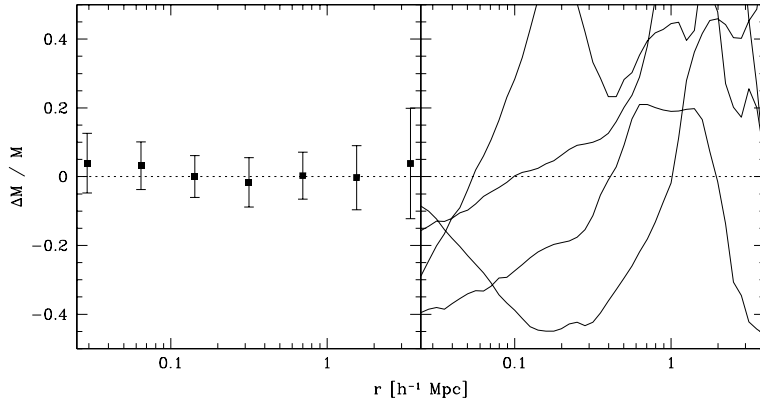


FIGURE 3.1: Comparison between ART and GADGET dark matter distributions. The relative difference in the cumulative mass is in most haloes (left panel) less than 15%. Clusters F, I, J and K (right panel) display bigger discrepancies (see text).

We compute this quantity for each cluster and average the individual profiles as discussed in Section 2.2.3. Clusters F, I, J<sub>1</sub> and K<sub>1</sub> are plotted separately on the right panel of Figure 3.1, and were not taken into account in the overall comparison. These clusters show discrepancies as high as 40% between both codes, but it cannot be attributed to inconsistencies in the simulation techniques but to slight differences in timing. Since all these clusters are undergoing major merging processes, small differences in the time of observation can have dramatic consequences on the morphology and dynamical state of the system. Indeed, clusters J<sub>2</sub> and K<sub>2</sub> are barely detectable in ART; in these simulations, we would simply have labelled clusters J and K as major mergers (obviously, clusters J<sub>2</sub> and K<sub>2</sub> have been excluded from these comparison, too).

As can be seen in the left panel of Figure 3.1, most individual profiles of our dark haloes are consistent within  $\sim 10\%$  accuracy. The mean deviation is null for most of the radial range, and it is only slightly biased towards larger masses in ART. However, this deviation is small compared to the scatter that it is quite likely to be a spurious effect. The fact that ART clusters appear to be a little bit heavier both near the centre and beyond the virial radius gives further support to this conclusion.

### Baryonic gas

Another interesting issue is whether baryons affect the shape of the dark matter distribution. Non-adiabatic baryonic processes such as cooling, star formation and feedback can change the phase-space distribution of the gas component, making it gravitationally dominant at the inner parts of galaxy-sized haloes. In fact, results from some gasdynamical simulations of galaxy



formation seem to indicate that galactic dark matter density profiles could be as steep as  $\rho(r) \propto r^{-2}$  for  $r \rightarrow 0$  (Tissera and Dominguez-Tenreiro 1998; Thacker and Couchman 2001).

However, most baryons in clusters of galaxies are in the form of a hot plasma and their dynamical effects on the host dark matter halo are less important even when cooling is considered (e.g. Loken et al. 2002). Our results seem to support this view, but a word of caution must be said here because our simulations take into account adiabatic physics only. In the central regions of clusters, the typical cooling times are less than a Hubble time, and hence a certain amount of cooling is expected to take place. Indeed, cooling flows (see Fabian (1994) for a recent review) have been observed in many clusters of galaxies<sup>3</sup>, as well as in numerical simulations including radiative cooling (e.g. Pearce et al. 2000).

If baryons played a significant role in the dynamics of the cluster, one would expect that they produced an adiabatic contraction of the dark matter halo, as it occurs on galactic scales, and hence the mass computed by GADGET should be appreciably smaller than that obtained by ART at small radii. Since we do not observe such a systematic trend in Figure 3.1, we conclude that the presence of a *hot* intracluster gas has no effect on the total mass distribution of the CDM component (or, at least, this effect is smaller than the 10% scatter we find between the results of simulating the same cluster with both codes).

### 3.2.1 Universality

In this section, we address the question of whether the radial dark matter density profile of our clusters follows a universal form, comparing the simulated mass distributions with the analytical profiles proposed by NFW and Moore et al. (1999b). If the clusters were described by a universal two-parameter function, then all the radial profiles should *exactly* overlap when they are properly rescaled. In the case of NFW formula (3.2), the scale factors are the characteristic density  $\rho_s$  in one axis and the characteristic radius  $r_s$  in the other.

#### Fitting procedure

The values of  $\rho_s$  and  $r_s$  are obtained by a  $\chi^2$  fit to the cumulative dark matter mass. As we discussed in Section 3.1.1, the density profile is much noisier than the cumulative mass, and hence much more sensitive to the chosen radial binning. We took equally-spaced logarithmic bins in order

---

<sup>3</sup>Nevertheless, high-resolution *Chandra* images and *XMM-Newton* spectra show that the physics of the ICM within the central 100 kpc can be extremely complex (Fabian 2002), and it is likely that some form of heating reduces the mass cooling rates by a factor up to ten.

CLUSTER	STATE	$\rho_s$	$r_s$	$c$	$\sqrt{\langle (\frac{\Delta M}{M})^2 \rangle}$
A	Minor	5.565	123.3	7.164	0.061
B	Minor	2.878	159.8	5.401	0.038
C	Relaxed	5.501	119.8	7.129	0.007
D	Minor	1.993	159.7	4.595	0.052
E	Relaxed	5.370	99.7	7.057	0.012
F	Major	1.718	155.5	4.301	0.042
G	Major	0.971	176.5	3.315	0.120
H	Relaxed	8.082	73.9	8.375	0.019
I	Major	0.661	183.3	2.766	0.178
J <sub>1</sub>	Relaxed	9.600	63.1	8.994	0.024
K <sub>1</sub>	Relaxed	7.366	64.9	8.058	0.037
L	Minor	2.622	97.1	5.186	0.072
M	Major	2.401	86.1	4.989	0.138
K <sub>2</sub>	Minor	9.871	49.9	9.098	0.061
J <sub>2</sub>	Relaxed	12.510	46.3	10.026	0.042

TABLE 3.1: Best-fit values of NFW parameters  $\rho_s$  ( $10^{15} h^2 M_\odot \text{Mpc}^{-3}$ ),  $r_s$  ( $h^{-1}$  kpc) and  $c \equiv r_{200}/r_s$ . Merging haloes are typically more extended than relaxed ones, and they are less accurately fit by a NFW profile.

to give more statistical weight to the inner regions, considering only radii between  $0.05 r_{200}$  and  $r_{200}$  to compute the r.m.s deviations from the fit. In the less massive haloes, our resolution limit of 200 dark matter particles (plus 100 gas particles in the case of GADGET simulations) placed a stronger constraint on the lower limit. In total, 26 points have been used for the fit in all clusters.

Actually, we fitted the mass distribution to expression (3.8) in terms of  $r_{200}$  and  $c$ , and then  $\rho_s$  and  $r_s$  were computed from the best values of these parameters. We imposed the physical constraints that  $c$  has been let to vary from  $c = 1$  to  $c = 15$ , while a first guess for  $r_{200}$  was obtained from the mass profile itself (see Table 2.2). The best-fit value of this quantity was allowed to fluctuate between 0.8 and 1.2 times the initial guess.

Table 3.1 summaries the values obtained by this method. The accuracy of each profile is expressed as the root mean square deviation of the numerical profiles from the analytical fit. For relaxed clusters, this quantity is always within a few percent, the quality of the fit being slightly better for more massive clusters. Minor mergers deviate about 6% and the discrepancy rises up to more than 10% in the major mergers.

At first sight, the well known  $c - M_{200}$  relation (e.g. Navarro et al. 1997) is not apparent in this table. The scatter in the concentration parameter

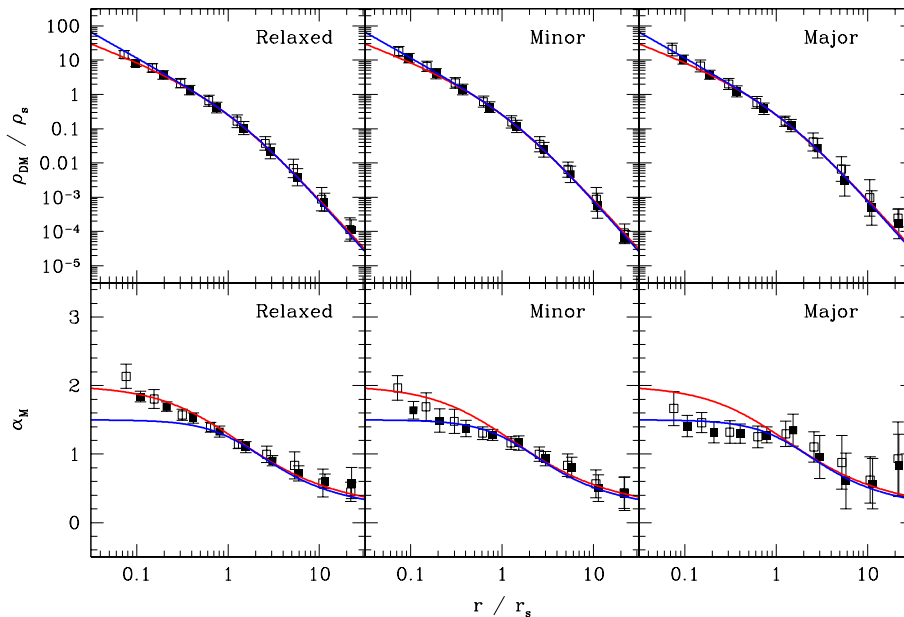


FIGURE 3.2: Top panel: dark matter density profiles (squares) scaled by the characteristic density and radius of each halo. Red lines indicate NFW fit; blue is used for Moore et al. Bottom panel: logarithmic slope  $\alpha_M$  of the mass profile. Merging clusters display a pure power-law behaviour near the centre, while the slope of relaxed structures decreases gently with radius.

seems to be quite large in the mass range covered by our sample (see also Jing 2000). However, there is a trend in the sense that  $c$  seems to be correlated with the dynamical state of the cluster. A more detailed discussion on this issue is given below, in connection with the effects of merging and environment.

### Mass profiles

We plot the radial density profiles of our clusters in the top panel of Figure 3.2, rescaled by the best-fit values of  $\rho_s$  and  $r_s$  given in Table 3.1. The phenomenological formulae proposed by NFW (red) and Moore et al. (blue) are also shown for comparison. Since we have fitted our dark matter haloes to the NFW form, we have assumed  $r_m = 1.7r_s$  and  $\rho_m = 6\rho_s$  to represent the Moore et al. 'universal' profile in the figure.

We have plotted ART/GADGET data as empty/solid squares, respectively, and the innermost bin is set by the constraints explained in Section 2.2.1. The formal resolution is similar in both codes: the finest grid level in ART and the gravitational softening length in GADGET were set to  $2 h^{-1}$  kpc.

From the top panel of Figure 3.2, we learn that most of the clusters of

galaxies in the present sample can be reasonably described by either NFW or Moore et al. analytical fits, although some of them (specially major mergers) display strong deviations from the 'universal' profile for  $r \geq r_{200}$  (a few times  $r_s$ ; see table 3.1).

Nevertheless, a log-log plot of the density profile offers very limited information about the subtleties of the radial distribution (in fact, any deviation smaller than a factor of 2 is not easily perceived, given the scale of the figure). In order to study the shape of the mass distribution in the innermost regions, we plot the local value of the logarithmic slope of the cumulative mass profile  $\alpha_M \equiv d \log M / d \log r$  as a function of radius (bottom panel of Figure 3.2). The difference in the logarithmic slopes predicted by NFW and Moore et al. is mostly evident for  $r \leq r_s$ .

We see that relaxed and merging clusters show a remarkably different behaviour near the origin. Focusing only on the relaxed subset of the sample, we find that NFW provides a good fit to our data. The steeper slope predicted by Moore et al. formula can be confidently ruled out at radii as large as one order of magnitude above our resolution limit.

However, in agreement with the results of Power et al. (2002), we find that  $\alpha_M$  does not tend to any asymptotic value at all, but steadily increases towards the centre. Even more resolution is required in order to reach smaller radii (at the kpc scale) and test whether the logarithmic slope stabilises at a constant value of 2 (as in NFW fit) or, on the contrary, it still increases until  $M \propto r^3$  (i.e. a constant density core).

This seems indeed to be the case when the simulated profiles are plotted slightly beyond the resolution limit. Yet, we would like to stress that the increasing slope at  $r \leq 0.1r_s$  may well be a numerical artifact induced by poor resolution. At this point, we prefer to be conservative and wait for higher-resolution data before reaching any conclusion.

### Dependence on environment

Relaxed clusters seem to follow indeed a universal profile dependent on two scale parameters only (albeit a small scatter exists for  $r > r_{200}$ ). This profile can be described with reasonable accuracy by NFW expression up to our resolution limit, being the innermost values of the logarithmic slope  $\alpha_M$  clearly inconsistent with the proposal of Moore et al.

However, the situation is quite different for merging clusters. Minor mergers feature logarithmic slopes systematically steeper than those of relaxed systems. The shape of their radial density profiles is not exactly NFW or Moore et al.-like, but lies somewhere in between both fits, in many occasions closer to the latter ( $\alpha_M = 1.5$ ) and sometimes even steeper.

Major mergers are an extreme case. Although they can be roughly approximated by NFW or Moore et al. formulae, significant deviations occur throughout the whole cluster. Nevertheless, our results hint that these re-

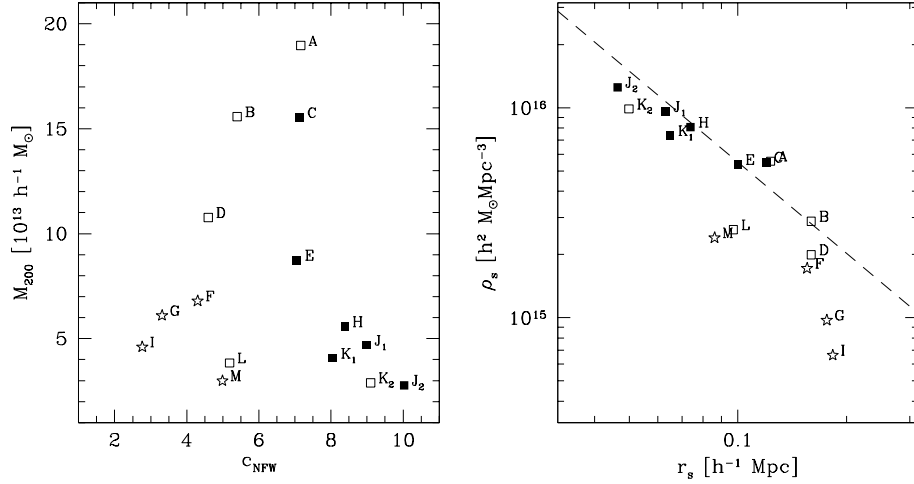


FIGURE 3.3: Relation between  $M_{200}$  and concentration parameter  $c$  (left panel) and characteristic density and radius (right panel). Black squares represent relaxed systems, empty squares show minor mergers and stars are used for major mergers. Observational data from Sato et al. (2000) is indicated by the dashed line.

cent mergers share some similar characteristics, the most remarkable being a power-law profile for more than one decade in radius. At the inner part, the logarithmic slope remains approximately constant. The exact value of  $\alpha_M$  shows some scatter, but the average seems to be slightly lower than 1.5.

A conjecture that deserves further investigation is that violent relaxation and subsequent equipartition of energy drive the inner part of the system into an isothermal state, and thus  $\alpha_M = 1$  immediately after the merger. The cluster would then slowly relax, and the density profile would become increasingly shallow with time until virial equilibrium is reached. This would be consistent with the scenario proposed by Salvador-Sole et al. (1998), in which the halo formation time is defined by the last major merger.

The fact that major mergers rearrange the inner structure of dark matter haloes should leave some common imprint on the radial mass distribution. Apart from the steeper slope of the density profile, one of the features shared by all the merging systems in our sample (already shown in Table 3.1) was that merging haloes tend to be much less concentrated than relaxed ones. This is in agreement with the results of Jing (2000), who concluded that the less virialised haloes (but still fitted by a NFW profile, similar to our ‘minor mergers’), have a mean concentration about 15% smaller than systems in virial equilibrium.

In Figure 3.3, the  $c - M_{200}$  (or, equivalently,  $r_s - \rho_s$ ) relation is shown for our cluster sample. We see a clear dichotomy between the behaviour of the  $c - M_{200}$  relation of relaxed and merging systems. While relaxed

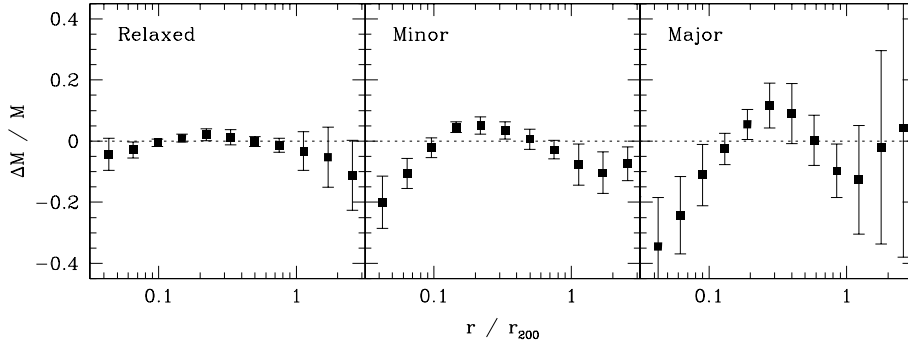


FIGURE 3.4: Accuracy of NFW fit for the simulated clusters

clusters follow the usual trend of bigger concentration for smaller mass, major mergers are so extended that their concentrations are much lower than those of the most massive systems.

Due to the large variations that dark matter haloes experience during a merging event, it seems unlikely that a  $c - M_{200}$  relation can be established during these transient stages of their evolution. A similar situation arises in minor mergers, where the effects on the concentration (on the whole density profile, indeed) depend strongly on the specifics of the encounter, such as the mass ratio of the CDM haloes, their relative velocity, their former concentrations, etc.

The relation seems to be a little tighter in the  $r_s - \rho_s$  plane, shown on the right panel of Figure 3.3. Although major mergers still show a different behaviour than relaxed clusters, their profiles have both larger values of the characteristic radius and lower central densities. This trend agrees well with recent X-ray observational estimates of the mass profiles of objects between  $10^{12}$  and  $10^{15} M_{\odot}$  (Sato et al. 2000, dashed line in Figure 3.3).

### Accuracy of NFW fit

One way to quantify to what extent do clusters follow a given 'universal' profile is plotting the deviations with respect to the proposed form. Since we have fitted our CDM haloes by a NFW function in order to scale both axis in Figure 3.2, we will present our results taking this profile as a reference.

We saw in Table 3.1 that the r.m.s values obtained for the NFW fit indicated accuracies of the order of 5 – 10%. However, we recall that this only applies for the cluster region that has been fitted (i.e. from  $0.05 r_{200}$  to  $r_{200}$ ). Outside this area, the profile of our dark matter haloes is not so well described by the NFW form.

The r.m.s deviation for the whole fit offers only a limited test of the ability of NFW profile to trace the mass distribution found in numerical experiments. We can obtain more information from Figure 3.4, where the

relative difference between this profile and the cumulative mass of our simulated haloes is plotted against clustercentric radius. Excluding major mergers, our clusters do not deviate appreciably from the NFW form throughout most of the radial range  $(0.1 - 1)r_{200}$ . Even in major mergers, the deviation is seldom larger than 20% in this region, although the formula proposed by NFW offers a poor description of the shape (i.e. the logarithmic slope) of the mass distribution in these systems.

However, as pointed out by many authors (e.g. Moore et al. 1999b, see Section 3.1.1), departures from the NFW formula seem to be similar for all clusters, displaying a characteristic 'S' shape. Nonetheless, the mass excess detected at very small radii does not necessarily imply a steeper inner slope of the radial density profile. For example, the form proposed by Taylor and Navarro (2001) (see Section 3.1.3) results in more concentrated CDM distributions, but the asymptotic slope  $\alpha(r \rightarrow 0) \sim 0.7$ . Yet, the fact that our simulated dark matter haloes show *systematic* deviations with respect to the NFW formula hints that it is not a good approximation to the shape of their density profile at the innermost regions.

### 3.2.2 Phase-space structure

In addition to the radial mass distribution, the kinetic structure of simulated CDM haloes can offer interesting insights into the formation of galaxies and galaxy clusters. On cluster scales, rotation is expected to give a negligible amount of support against gravitational collapse because the angular momentum of the system is dominated by the contribution of random motions.

In this section, we will discuss the phase-density structure of our clusters, separating the global and random components and comparing our results with previous work by Bullock et al. (2001) and Taylor and Navarro (2001), respectively (see Section 3.1.3). The details concerning the computation of the angular momentum and velocity dispersion profiles can be found in Section 2.2.3.

#### Velocity Dispersion

As was discussed in Section 3.1.3, the velocity dispersion profile of a collisionless dark matter halo is related to the total mass distribution by virtue of the Jeans equation (3.17). The average radial profile of the spherically-averaged phase-space density  $\rho/\sigma^3$  has been computed for the whole sample of galaxy clusters, and it is plotted in Figure 3.5. Individual profiles display a remarkably low scatter, particularly if we take into account that

1. Major mergers have been included in the average.
2. The profiles have not been normalised.

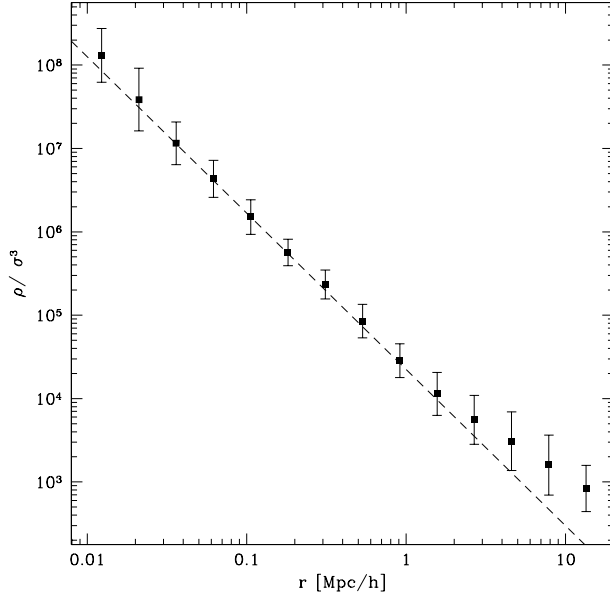


FIGURE 3.5: Phase space density profiles for our haloes (dots) compared to the fit proposed by Taylor and Navarro (2001) ( $\rho/\sigma^3 \propto r^{-1.879}$ )

The phase-space density of our simulated clusters is very well fitted by the simple power-law

$$\rho/\sigma^3 = 2.24 \times 10^4 r^{-1.875} \quad (3.23)$$

where  $\rho$ ,  $\sigma$  and  $r$  are expressed in units of  $h^2 M_\odot \text{ Mpc}^{-3}$ ,  $\text{km s}^{-1}$  and  $h^{-1} \text{ Mpc}$ , respectively. The slope of the power law (-1.875) corresponds to the self-similar solution derived by Bertschinger (1985) for secondary infall onto a spherical perturbation in an otherwise homogeneous Einstein-de Sitter universe, and it has been found to describe also extremely well the phase-space density structure of galactic-size CDM haloes (Taylor and Navarro 2001). An interesting issue which would be worth to investigate is whether the normalisation depends somehow on the scale of the halo, the assumed cosmological model, or any other factor. Unfortunately, the phase-space profiles computed by Taylor and Navarro (2001) have been scaled arbitrarily, so it is impossible to compare with our result (3.23).

This correlation between density and velocity dispersion profiles has been used by Taylor and Navarro (2001) to infer the radial mass distribution of the dark matter from the Jeans equation. Hiotelis (2002b) has generalised this solution for the case of anisotropic velocity tensors, using an approximation for the anisotropy parameter

$$\beta(r) = \beta_1 + 2\beta_2 \frac{r/r_*}{1 + (r/r_*)^2} \quad (3.24)$$



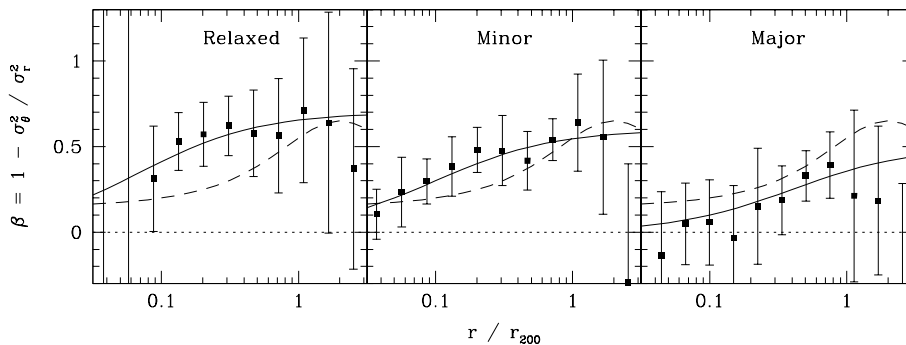


FIGURE 3.6: Anisotropy parameter  $\beta$ . See text for description of curves

where  $\beta_1$  and  $\beta_2$  are free parameters, and  $r_*$  is twice the virial radius (Carlberg et al. 1997; Colín et al. 2000b).

In Figure 3.6, the anisotropy profile of our simulated clusters is compared with expression (3.24), using the best-fit values found by Colín et al. (2000b),  $\beta_1 = 0.15$ , and  $\beta_2 = 0.5$  (dashed lines). Although the average profile of the anisotropy parameter seems to follow a similar trend in all haloes, the assumption of a 'universal' anisotropy profile seems hardly justifiable given the scatter of each individual profile around the mean value<sup>4</sup>.

In any case, the simple formula (3.24) proposed by Carlberg et al. (1997) does not provide a good description of the shape of the anisotropy profiles of our cluster sample. The exception could be the clusters with major mergers, which are much closer to isotropy in velocities than the rest, but we would need to modify the values of  $\beta_1$  and  $\beta_2$  and change  $r_*$  by  $r_{200}$ . Nevertheless, expression (3.24) is a much better approximation to our results than purely isotropic profiles ( $\beta = 0$ , dotted line), which can be ruled out in relaxed clusters and minor mergers at a several sigma confidence level over a broad radial range.

Our numerical results can be better fit by the function (solid lines in Figure 3.6)

$$\beta(r) = \beta_{\max} \frac{r/r_*}{1 + r/r_*} \quad (3.25)$$

where  $\beta_{\max} = (0.7, 0.6, 0.5)$  and  $r_* = (0.07, 0.1, 0.4)r_{200}$  for relaxed clusters, minor and major mergers respectively. We insist, nonetheless, that this fit is a poor approximation to the radial dependence of  $\beta$  in any individual halo, and it could only be applied in a statistical sense, such as in the determination of the *average* mass profile attempted by Hiotelis (2002b).

<sup>4</sup>We note, however, that the numerical derivation of  $\beta$  is not straightforward, since this parameter is extremely sensitive to inaccuracies in the velocity profiles, particularly near the centre.

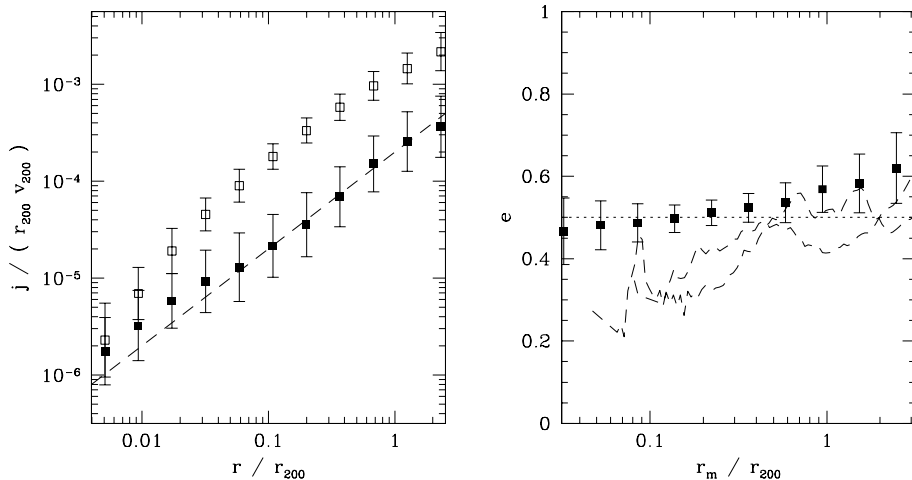


FIGURE 3.7: Angular momentum in the simulated haloes. Left panel: Contribution of bulk rotation (solid squares) and random motions (empty squares).  $j \propto r$  is drawn as a dashed line. Right panel: Eccentricity of the individual orbits (haloes I and J<sub>2</sub> are shown separately).

### Angular momentum

The origin of angular momentum in dark matter haloes can be understood in terms of lineal tidal torque theory, in which protohaloes acquire their angular momentum because of the surrounding shear (Peebles 1969; Doroshkevich 1970; White 1984; Porciani et al. 2002a,b).

In the left panel of Figure 3.7, we plot the angular momentum of our haloes computed in spherical shells around the centre of mass. Solid squares indicate the mean value of  $j$  in each shell (i.e. rigid body rotation). The amount of angular momentum due to random motions (i.e. tangential velocity dispersion) is represented by the open symbols.

The first thing that can be appreciated in Figure 3.7 is that velocity dispersion is the dominant source of kinetic energy in the system. The amount of angular momentum contributed by random motions is higher by approximately one order of magnitude than that corresponding to bulk rotation.

The relative scatter in the radial profiles (when normalised on both axes as indicated in the figure) is larger for the mean angular momentum than for the r.m.s. value. Near the centre, the situation is less clear, since at very small radii the low number of particles (and possible misidentifications of the centre of mass and velocities) makes difficult to disentangle ordered from random motions, as well as radial and tangential directions.

Building upon the pioneering work of Barnes and Efstathiou (1987), the question of a universal angular momentum profile has been recently investigated by several authors (e.g. Bullock et al. 2001; van den Bosch et al. 2002;

Chen and Jing 2002). The spin profiles found in numerical simulations grow approximately linearly with radius (or as  $j \propto r^{1.1}$ , Bullock et al. 2001). Our results are consistent with this behaviour (dashed line in the left panel of Figure 3.7), but they deviate from this simple relation near the centre. However, the discrepancy ( $\sim 2$  over  $j \propto r$  at  $r \sim 0.01r_{200}$ ) is comparable to the scatter in the profiles. We must take into account that, at these radii, the lower number of particles may well lead to an overestimate of the mean angular momentum with respect to the random component.

Once the angular momentum distribution of the dark matter is known, it is interesting to study the structure of the orbits of individual particles around the centre of mass. More precisely, the eccentricity of these orbits has important dynamical consequences, since it controls directly the maximum depth that a dark matter particle is able to reach within the gravitational potential of the dark matter halo. The ideal case  $e = 0$  corresponds to a configuration in which all particles would orbit at constant radius with no mixing between concentric shells, while  $e = 1$  (often assumed in spherical infall models) implies that every dark matter particle goes through the very centre of mass of the cluster. In general, large values of the eccentricity lead to a situation in which the core is mainly composed of particles coming from the outer shells of the halo that happen to be near the pericenter of their orbits.

We plot the the eccentricity profiles of our haloes as a function of the apocentric radius  $r_m$  in the right panel of Figure 3.7. Both quantities have been computed according to the prescriptions given in Section 2.2.3. Haloes I and J<sub>2</sub> are plotted separately as dashed line, since they feature much lower eccentricities than the rest of the sample. Except for these clusters, the rest of the sample exhibits a similar profile (as can be seen from the small scatter). For large apocentres, the eccentricities of different clusters show different behaviours, although the trend is that orbits are in general more radial as we move out to the turn-around radius.

Despite the small dependence of  $e$  on  $r$  seen in Figure 3.7, we will make the approximation  $e \simeq 0.5$  (indicated by the horizontal dotted line) in order to model the orbits of dark matter particles. With this value, the minimum radius reached in the orbit is one third of the apocentric distance, while it would be  $\sim 0.43 r_m$  for  $e = 0.4$  and  $0.25 r_m$  for  $e = 0.6$ . Since the error we make is not large, we will use this simple approximation in our treatment of angular momentum in the spherical collapse formalism (Section 3.3.3).

### 3.3 On the physical origin of dark matter profiles

From the theoretical point of view, a number of plausible arguments have been advanced to try to explain the dynamical structure of dark matter haloes. The controversy regarding the 'universal' density profile and the

asymptotic value of its logarithmic slope at the centre has stimulated a great deal of analytical work attempting to find the physical reasons behind this similarity in the mass distribution, as well as possible correlations with halo size, environment, underlying power spectrum or even the nature of dark matter particles.

The structure of collapsed and virialised objects such as galaxies and clusters poses a real challenge to our understanding of structure formation in the universe. The basic problem of the collisionless collapse of a spherical perturbation in an expanding background was addressed first by the two seminal papers of Gunn and Gott (1972) and Gunn (1977), where the cosmological expansion and the role of adiabatic invariance were first introduced in the context of the formation of individual objects.

The next step was accomplished by Fillmore and Goldreich (1984) and Bertschinger (1985), who found analytical predictions for the density of collapsed objects seeded by scale-free primordial perturbations in a flat universe. Hoffman and Shaham (1985) generalised these solutions to realistic initial conditions in flat as well as open Friedmann models. Modifications of the self-similar collapse model to include more realistic dynamics of the growth process have been attempted (e.g. Avila-Reese et al. 1998; Henriksen and Widrow 1999; Lokas 2000; Kull 1999; Subramanian et al. 2000). Several authors (e.g. Syer and White 1998; Salvador-Sole et al. 1998; Nusser and Sheth 1999) argue that the central density profile is linked to the accretion and merging history of dark matter substructure.

In this section, we will focus on the predictions of spherical collapse theory, showing that this simple model is able to explain the general features of the mass distribution of our simulated haloes described in previous sections. First we explain our numerical implementation of the spherical collapse model and the primordial initial conditions. We then compare the resulting analytical profiles with our simulations. Finally, a brief discussion on the role of hierarchical merging is also included.

### 3.3.1 Spherical collapse

The most simple way of addressing the problem of structure formation is to assume spherical symmetry. For a homogeneous and isotropic universe, General Relativity leads to the Friedmann equation (1.10). Since we are interested on scales much smaller than the horizon, we can restrict our treatment to Newtonian dynamics. In this case, the equation of motion for a Lagrangian shell of mass  $M$  can be derived from energy conservation

$$\epsilon(r) = \frac{E(r)}{m} = \frac{\dot{r}^2}{2} - G \frac{M(r) + \frac{4\pi}{3}\rho_\Lambda r^3}{r} = \epsilon_i(r) \quad (3.26)$$

where  $M(r) = M_i(r_i)$  is the mass contained within the shell,  $\rho_\Lambda$  is the vacuum energy density, and the subscript 'i' denotes initial conditions. If

we assume the universe to be homogeneous,

$$M_i = \frac{4\pi}{3}\Omega_m^i \rho_c^i r_i^3 \quad (3.27)$$

Substituting in (3.26),

$$\frac{\dot{r}^2}{2} - G\frac{4\pi}{3}\rho_c^i \frac{\Omega_m^i r_i^3 + \Omega_\Lambda^i r^3}{r} = \frac{(H_i r_i)^2}{2} - G\frac{4\pi}{3}\rho_c^i \frac{\Omega_m^i r_i^3 + \Omega_\Lambda^i r_i^3}{r_i} \quad (3.28)$$

Since  $\rho_c^i = \frac{3H_i^2}{8\pi G}$ , we can make a coordinate transformation

$$r(t) \equiv r_i \alpha(t) \quad (3.29)$$

and recover the Friedmann equation simply by multiplying both sides of (3.28) by a factor  $\frac{2}{(H_i r_i)^2}$ :

$$\frac{\dot{\alpha}^2}{H_i^2} - \Omega_m^i \alpha^{-1} - \Omega_\Lambda^i \alpha^2 = 1 - \Omega_m^i - \Omega_\Lambda^i \quad (3.30)$$

Now, we introduce a small mass perturbation

$$\Delta_i(r_i) = a_i \Delta(x_i) = \frac{M(r_i)}{\frac{4\pi}{3}\Omega_m^i \rho_c^i r_i^3} - 1 \quad (3.31)$$

at an early epoch  $a_i$ , so that the growth is still in the linear phase. The initial positions and velocities of the spherical shells of matter are slightly modified, keeping only terms to first order in  $\Delta_i(r_i)$ :

$$r'_i \simeq r_i \left(1 - \frac{1}{3}\Delta_i(r_i)\right) \quad ; \quad v'_i \simeq H_i r_i \left(1 - \frac{2}{3}\Delta_i(r_i)\right) \quad (3.32)$$

and the initial specific energy of each shell is thus

$$\begin{aligned} \epsilon'_i(r_i) &\simeq \frac{(H_i r_i)^2}{2} \left[ \left(1 - \frac{2\Delta_i}{3}\right)^2 - \Omega_m^i \left(1 - \frac{\Delta_i}{3}\right)^{-1} - \Omega_\Lambda^i \left(1 - \frac{\Delta_i}{3}\right)^2 \right] \\ &\simeq \frac{(H_i r_i)^2}{2} \left[ (1 - \Omega_m^i - \Omega_\Lambda^i) - \frac{\Delta_i}{3} (4 + \Omega_m^i - 2\Omega_\Lambda^i) \right] \end{aligned} \quad (3.33)$$

Since  $a_i \ll 1$ ,

$$\Omega_m^i = \frac{\Omega_m a_i^{-3}}{\Omega_m a_i^{-3} + \Omega_\Lambda + \Omega_k a_i^{-2}} \simeq 1 \quad ; \quad \Omega_\Lambda^i = \frac{\Omega_\Lambda}{\Omega_m a_i^{-3} + \Omega_\Lambda + \Omega_k a_i^{-2}} \simeq 0 \quad (3.34)$$

and energy conservation (3.26) leads to the equation of motion

$$\frac{2\epsilon_i}{(H_i r_i)^2} \simeq -\frac{5}{3}\Delta_i = \frac{\dot{\alpha}^2}{H_i^2} - \Omega_m^i \alpha^{-1} - \Omega_\Lambda^i \alpha^2 \quad (3.35)$$

valid for a spherical shell enclosing a mass  $M_i$ .

### Before turn-around

According to (3.35), the evolution of a single spherical shell would thus be similar to that of a Friedmann universe. For high enough values of  $\Delta_i$ , the shell reaches a maximum radius  $r_m$  at a *turn-around* time  $t_m$  and re-collapses again to a point singularity. For an Einstein-de Sitter universe, equation (3.35) can be solved analytically, giving

$$r_m = \frac{3r_i}{5\Delta_i} \quad ; \quad t_m = \frac{\pi}{2H_i(5\Delta_i/3)^{3/2}} \quad (3.36)$$

This is also a valid approximation for shells reaching the turn-around radius  $r_m$  before the cosmological constant term starts to dominate the expansion. Since the shells need at least another  $t_m$  to virialise, in the  $\Lambda$ CDM model discussed in Section 1.1, expression (3.36) can be applied to estimate the maximum expansion radius and time for the inner part of a virialised cluster. For the outer shells, however, the equation of motion (3.35) must be integrated numerically in order to find the trajectory up to the maximum radius.

In absence of shell-crossing, gravity would make the shell collapse back in a time-symmetric motion, so that the shell will reach the origin at  $T = 2t_m$ . Since shells are assumed to be composed of collisionless cold dark matter particles, they will simply pass through the centre, describing an oscillatory motion with amplitude  $r_m$  and period  $T$ .

### After turn-around

Equation (3.35) holds as long as the enclosed mass remains constant. However, as a shell re-collapses, it will cross the orbits of the inner shells that are bouncing around the centre. When this happens, the assumption of constant mass breaks down because

1. The mass enclosed by the outer shell decreases
2. The mass enclosed by the inner shells increases

To take into account the first point above, our model assumes that the final mass distribution can be approximated *locally* by a pure power law. Since dark matter particles are expected to spend most of the time in the outermost regions of their orbits (see also Section 3.3.3 on angular momentum), we only need this approximation to be valid over a relatively narrow range below the maximum radius. Near  $r_m$ , the enclosed mass is taken to vary with  $r$  as

$$M(r) = M_i \left( \frac{r}{r_m} \right)^{\alpha_M(r_m)} \quad (3.37)$$

where  $\alpha_M(r_m)$  is the *local* value of the logarithmic slope.

At first sight, this might seem similar to the classical approach followed in early works based on self-similar spherical collapse (e.g. Bertschinger 1985), but in those cases the dark matter distribution was indeed assumed to be a power law, whereas in our model this ansatz is only an approximation to compute the orbits of particles in a given shell. The final mass profile is computed self-consistently as a sum of contributions from all shells, which have different values of  $\alpha_M(r_m)$ .

After turn-around, the particles belonging to a shell will oscillate (or, more generally, *orbit*) in the gravitational potential created by the dark matter halo. Taking the ansatz (3.37), the gravitational potential is approximated as

$$\begin{aligned}\Phi(r) - \Phi(r_m) &= \int_{r_m}^r \frac{GM(r)}{r^2} dr \\ &\simeq \frac{GM_i}{r_m^2[\alpha_M(r_m) - 1]} \left[ \left( \frac{r}{r_m} \right)^{\alpha_M(r_m) - 1} - 1 \right]\end{aligned}\quad (3.38)$$

The probability of finding a particle inside radius  $r$  is just proportional to the fraction of time that it spends within  $r$ :

$$P(r, r_m) = \frac{1}{t_m} \int_0^r \frac{dx}{v_r(x)} = \frac{1}{t_m} \int_0^r \frac{dx}{\sqrt{\Phi(r_m) - \Phi(x)}}\quad (3.39)$$

Note that, in this form, expression (3.39) is valid regardless of the assumed ansatz for  $M(r)$ . Taking different prescriptions to compute the potential, such as an isothermal profile ( $\alpha_M(r_m) = 1$  for every shell, so  $\Phi(r)$  is actually logarithmic) or considering  $M$  constant ( $\alpha_M = 0$ , Keplerian potential  $\Phi(r) = -GM/r$ ) does not lead to significant variations in the probability  $P(r, r_m)$ , and hence in the resulting mass distribution.

If phase mixing is considered to be efficient, particles initially on the same shell will be spread out from  $r = 0$  to  $r = r_m$  a short time after  $t_m$ . For the sake of simplicity, we will consider that phase mixing is instantaneous, so immediately after turn-around the shell is transformed into a density distribution whose cumulative mass is proportional to  $P(r, r_m)$ .

Effect (2) listed above has dramatic influence on the final structure of the dark matter halo. If the recently accreted shells have a non-zero contribution to the mass within  $r$  (i.e.  $P(r, r_m)dM$ ), the mass inside the inner shells whose maximum radius was  $r$  changes from  $M_i(r)$  to

$$M(r) = M_i(r) + M_{\text{add}}(r) \equiv K(r)M_i(r)\quad (3.40)$$

where  $M_{\text{add}}(r)$  accounts for particles belonging to outer shells. To compute  $M_{\text{add}}(r)$  (see Zaroubi and Hoffman 1993), we must integrate the contribution of every shell whose maximum radius is larger than  $r$ , up to the current

turn-around radius  $R_m$ :

$$M_{\text{add}}(r) = \int_r^{R_m} \frac{dM_i(x)}{dx} P(r, x) dx \quad (3.41)$$

Gunn (1977) was the first to apply the concept of adiabatic invariance to the secondary infall problem. If the orbital period of the inner particles is much shorter than the collapse timescale of the outer shells, the dynamics of the inner shell admits an adiabatic invariant

$$J_r = \frac{1}{2\pi} \oint v_r(x) dx \quad (3.42)$$

also known as the radial action. For a potential of the form (3.38), the radial action  $J_r$  is proportional to  $\sqrt{r_m M(r_m)}$ . Therefore, the maximum radius  $r_m$  of the inner shell decreases to a final value given by the implicit equation  $r = F(r)r_m$ , where

$$F(r) = \frac{1}{K(r)} = \frac{M_i}{M_i + M_{\text{add}}(r)} = \frac{M_i}{M_i + M_{\text{add}}(F(r)r_m)} \quad (3.43)$$

and whose solution must be obtained numerically for each shell.

### Summary

To summarise, the numerical procedure to compute the final radius of a Lagrangian shell of matter involves the following steps:

1. Set the initial mass  $M_i$  according to (3.27)
2. Integrate the equation of motion (3.35) up to the maximum radius  $r_m$
3. If  $t_m > t_0$ 
  - The shell is still expanding,  $r = r(t_0)$
4. If  $t_m < t_0$ 
  - Solve (3.43) to compute the new apocenter  $r = F(r)r_m$
  - Add the contribution  $P(r', r)dM$  to  $M_{\text{add}}(r')$
5. Repeat the process for the next shell (closer to the centre).

### 3.3.2 Initial conditions

The spherical collapse model allows us to compute the mass distribution arising from a primordial fluctuation  $\Delta_i(r_i)$ , but does not say anything about the shape of this function or its physical origin. Nevertheless, it is important to note that the final density profile is entirely determined by this initial



condition. In the spherical collapse paradigm, the case for universality in the radial profiles of dark matter haloes can be reformulated in terms of universality in the primordial density fluctuations that fix  $\Delta_i(r_i)$ .

Hoffman and Shaham (1985) suggested that, according to the hierarchical scenario of structure formation, haloes should collapse around local maxima of the *smoothed* density field. The statistics of peaks in a Gaussian random field has been extensively studied in the classical paper by Bardeen et al. (1986, hereafter BBKS). One of the best known results of BBKS is the expression for the radial density profile of a fluctuation centred on a primordial peak of arbitrary height:

$$\frac{\langle \delta_f(r) \rangle}{\sigma_0} = \nu \psi(r) - \frac{\theta(\gamma, \gamma\nu)}{\gamma(1-\gamma^2)} \left[ \gamma^2 \psi(r) + \frac{R_*^2}{3} \nabla^2 \psi(r) \right] \quad (3.44)$$

where  $\sigma_0 \equiv \xi(0)^{1/2}$  is the rms density fluctuation,  $\psi(r) \equiv \xi(r)/\sigma_0$  is the normalised two-point correlation function,  $\nu\sigma_0$  is the height of the peak, and  $\gamma \equiv \sigma_1^2/(\sigma_2\sigma_0)$  and  $R_* \equiv \sqrt{3}\sigma_1/\sigma_2$  are related to the moments of the power spectrum

$$\sigma_j^2 \equiv \frac{1}{2\pi^2} \int_0^\infty P(k) k^{2(j+1)} dk \quad (3.45)$$

The function  $\theta(\gamma, \gamma\nu)$  parameterises the second derivative of the density fluctuation near the peak. BBKS suggest the approximate formula

$$\theta(\gamma, \gamma\nu) \equiv -\frac{\langle \nabla^2 \delta \rangle}{\sigma_2} - \gamma\nu \simeq \frac{3(1-\gamma^2) + (1.216 - 0.9\gamma^4) \exp[-\frac{7}{2}(\frac{\gamma\nu}{2})^2]}{[3(1-\gamma^2) + 0.45 + \frac{\gamma\nu}{2}]^{1/2} + \frac{\gamma\nu}{2}} \quad (3.46)$$

valid to 1% accuracy in the range  $0.4 < \gamma < 0.7$  and  $1 < \gamma\nu < 3$ , which is the scale relevant for both galaxies and galaxy clusters.

Expression (3.44) is often quoted in the literature<sup>5</sup> (e.g. Hoffman 1988; Lokas and Hoffman 2000; Del Popolo et al. 2000; Hiotelis 2002a) as the initial condition  $\Delta_i(r_i)$ , even though BBKS *explicitly* warn in their paper

“Unless the filter is physical (as in pancake models), these profiles cannot be used for hydrodynamic or N-body studies of collapse since substructure must be included”.

Although BBKS referred to a different problem (see our discussion in Section 3.3.4 regarding the effects of merging and substructure), the point we want to stress is that (3.44) describes the *smoothed* density profile around a local maximum of the smoothed density field,

$$\delta_f(\vec{r}) = \int W_f(\vec{r} - \vec{x}) \delta(\vec{x}) d^3\vec{x} \quad (3.47)$$

---

<sup>5</sup>Some authors (Hoffman, private communication) use indeed the prescription described below. Yet (3.44) is stated in their paper to determine the initial conditions.

where the function  $W_f(\vec{r}-\vec{x})$  is a smoothing kernel that depends on a certain filtering scale  $R_f$ .

However, the smoothed density profile  $\langle\delta_f(r)\rangle$ , given by equation (3.44), is *never* equal to the mean value of the local overdensity  $\langle\delta(r)\rangle$  that we need to integrate in order to compute  $\Delta_i(r_i)$ :

$$\Delta_i(r_i) = 4\pi \int_0^{r_i} \langle\delta(\vec{x})\rangle x^2 dx \quad (3.48)$$

Comparing this expression with (3.47), we see that  $\Delta_i(r_i)$  is equivalent to  $\delta_f(0)$  as long as  $W_f$  is taken to be a spherical top hat function of radius  $r_i$ . In phase space, the Fourier transform of this function results in significant oscillations near the cut-off scale, so it is better to choose a Gaussian filter

$$W_f(\vec{r}-\vec{x}) = \frac{1}{(2\pi R_f^2)^{-3/2}} \exp\left(-\frac{|\vec{r}-\vec{x}|^2}{2R_f^2}\right) \quad (3.49)$$

with  $R_f = 0.64r_i$ , such that the enclosed mass is approximately the same as in (3.48).

We are interested in the *physical* density profile around a local maximum of the *smoothed* density field. First, we fix the scale of the fluctuation  $R_f$ . Then, according to (3.48),  $\Delta_i(r_i) = \delta_r(0)$ , where  $\delta_r(0)$  is the central density smoothed on a scale  $r_0 = 0.64r_i$ . Furthermore, we want to impose the condition that  $r = 0$  is a maximum of the density field  $\delta_f(\vec{r})$  smoothed on a scale  $R_f$ . BBKS show that the probability distribution of  $\delta_r(0)$  is a Gaussian with mean

$$\langle\delta_r(0)\rangle = \nu_f \frac{\sigma_{0h}^2}{\sigma_{0f}} - \frac{\gamma_f \theta(\gamma_f, \nu_f)}{1 - \gamma_f^2} \frac{\sigma_{0h}^2}{\sigma_{0f}} \left(1 - \frac{\sigma_{1h}^2 \sigma_{0f}^2}{\sigma_{0h}^2 \sigma_{1f}^2}\right) \quad (3.50)$$

for  $r_0 > R_f$  and

$$\langle\delta_0(0)\rangle = \nu_f \frac{\sigma_{0h}^2}{\sigma_{0f}} \quad (3.51)$$

for  $r_0 < R_f$ . The moments

$$\sigma_{jx}^2 \equiv \frac{1}{2\pi^2} \int_0^\infty P_x(k) k^{2(j+1)} dk \quad (3.52)$$

are computed from

$$P_f(k) \equiv P_{\Lambda\text{CDM}}(k) \exp[-(kR_f)^2] \quad (3.53)$$

and

$$P_h(k) \equiv P_{\Lambda\text{CDM}}(k) \exp\left[-k^2 \frac{R_f^2 + r_0^2}{2}\right] \quad (3.54)$$

Thus, instead of (3.44), we have used (3.50) and (3.51) to set the initial condition  $\Delta_i(r_i)$ , assuming that the cluster collapses from a  $\nu_f \sigma_{0f}$  peak on scale  $R_f$ .

### 3.3.3 Angular momentum

Two decades after the seminal paper by Gunn and Gott (1972), White and Zaritsky (1992) introduced the idea (although see<sup>6</sup> also the pioneering work of Gurevich and Zybin 1988) that angular momentum prevents dark matter particles from reaching the origin.

For pure radial orbits, the mass in the centre is dominated by the contribution  $M_{\text{add}}$  from the outer shells when the profile at turn-around is shallower than isothermal (Fillmore and Goldreich 1984). The final density distribution found by these authors was  $\rho(r) \propto r^{-2}$ , independent on the initial logarithmic slope. More recently, Łokas (2000) and Łokas and Hoffman (2000) found a similar result considering non-self-similar primordial fluctuations based on the peak formalism. Del Popolo et al. (2000) obtains slightly shallower profiles, but they rely on White and Zaritsky (1992) to override the 'crowding effect' associated to radial orbits.

Angular momentum arises in linear theory (White 1984) from the misalignment between the asymmetry of the collapsing region (i.e. the inertia tensor) and the tidal forces it experiences during the lineal regime. Also, violent relaxation (Lynden-Bell 1967) transforms the radial infall energy into random velocity dispersion, due to two-body encounters taking place during shell crossing.

The total amount of angular momentum acquired by the system is, however, an open question. The usual approach (Avila-Reese et al. 1998; Nusser 2001; Hiotelis 2002a) consists in assigning a specific angular momentum at turn-around

$$j \propto \sqrt{GM r_m} \quad (3.55)$$

With this prescription, the orbit eccentricity  $e$  is the same for all particles in the halo (Nusser 2001). As can be seen in Figure 3.7, this is a fair approximation for all but two of our simulated clusters. Therefore, we will assume hereafter a constant eccentricity  $e = 0.5$  for the orbits of every dark matter particle after turn-around. For this value of the eccentricity, the pericenter radius of the orbit will be given by

$$r_{\min} = \frac{1-e}{1+e} r_{\max} = \frac{r_{\max}}{3} \quad (3.56)$$

where  $r_{\max}$  is computed from adiabatic invariance (3.43), following the procedure explained in Section 3.3.1. In this case, angular momentum adds the usual effective term  $j^2/(2r^2)$  to the gravitational potential  $\Phi(r)$  to be substituted in equation (3.39). Although this changes the actual value of the radial action,  $J_r$  is still proportional to  $\sqrt{r_m M(r_m)}$ . Therefore (3.43) still can be used to compute the collapse factor  $F(r)$ . The assumption of spherical symmetry leads to angular momentum conservation, which implies constant  $e$  during the contraction.

---

<sup>6</sup>If you can.

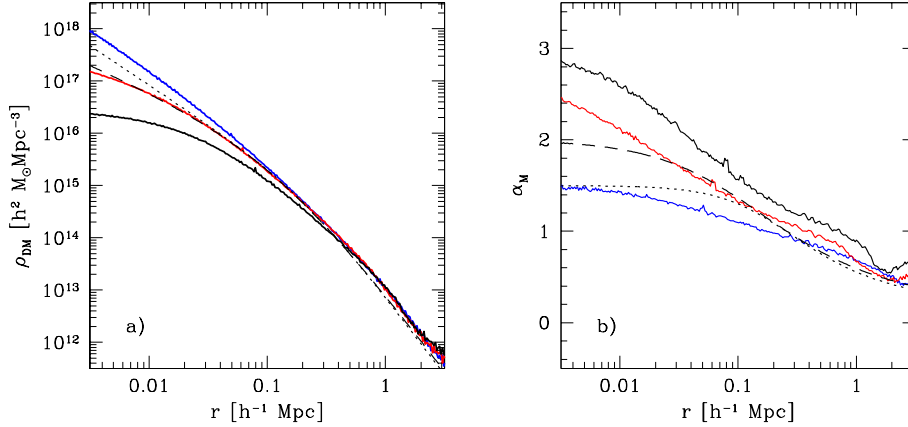


FIGURE 3.8: Mass distribution resulting from a  $3\sigma$  fluctuation on  $1 h^{-1}$  Mpc (solid lines). Black colour is used for  $e = 0.25$ , red for  $e = 0.5$  and blue for pure radial orbits ( $e = 1$ ). NFW (dashed lines) and Moore et al (dotted lines) profiles are shown for comparison. Left panel: Radial density profile. Right panel: Logarithmic slope  $\alpha_M$  of the mass profile.

Moreover, since the radial coordinate of the particle changes only a factor of three (3.56), the approximation  $M(r) \propto r^{\alpha_M}$  provides a reasonable description of the mass profile as long as the local value of the logarithmic derivative of the mass is used to set  $\alpha_M(r)$ .

In Figure 3.8, the final profile obtained for a  $3\sigma$  peak in the primordial density field (smoothed on  $1 h^{-1}$  Mpc scales) is plotted for different values of the orbit eccentricity. As pointed out by White and Zaritsky (1992) and Hiotelis (2002a), angular momentum plays a key role during secondary infall, preventing dark matter particles from reaching the centre of the halo and thus decreasing the amount of mass in the inner regions contributed by recently accreted shells.

As the amount of angular momentum is increased ( $e$  is lowered), we find that the predicted density profile becomes increasingly shallow, in agreement with the results of Hiotelis (2002a). Pure radial orbits give rise to a profile somewhat similar to the form proposed by Moore et al. (1999b), although the exact shape is slightly different (see the right panel of Figure 3.8, where the logarithmic derivative of the cumulative mass is plotted as a function of radius). When the eccentricity is too low (as for example  $e = 0.25$ , represented by solid black lines in the figure), the halo develops a constant density core inconsistent with the results of numerical simulations. A value  $e = 0.5$ , typical of our clusters (see Section 3.2.2), yields a mass distribution almost indistinguishable from the NFW formula up to  $0.02 h^{-1}$  Mpc, where the logarithmic slope predicted by spherical collapse keeps increasing towards the centre while NFW tends to an asymptotic value  $\alpha_M = 2$ .

This is precisely the kind of behaviour we see in the innermost part of

our relaxed clusters (see Figure 3.2). We cannot be totally sure that this is not a spurious effect caused by our finite numerical resolution. Therefore, we suggest that a smoothing length of  $\sim 1 h^{-1}$  kpc would be needed to confidently distinguish between both profiles. We note, however, that this is only marginally beyond the resolution of the numerical experiments presented here. We plan to test this result with simulations from same initial conditions but with another mass refinement level (i.e. effective  $1024^3$  particles and  $\epsilon \sim 200pc$ .)

### 3.3.4 Comparison with simulations

In principle, it is difficult to understand why the spherical collapse picture should be able to predict the density distribution of dark matter haloes, since the assembly of structures in the universe is not expected to proceed by the infall of spherical shells, but rather through a hierarchical series of merging events. Nothing of the symmetric and ordered process envisaged by this simple formalism is actually confirmed by the numerical simulations, in which the collapse of haloes seems to take place in an extremely unordered and random way.

However, Zaroubi et al. (1996) point out that the very complicated coalescence process looks very regular in energy space, where there is a high correlation between the initial and final energies of individual particles. In particular, the ranking in energy space is roughly preserved, an idea already proposed by Quinn and Zurek (1988) and Hoffman (1988).

Furthermore, Moore et al. (1999b) simulated the collapse of a galaxy cluster truncating the power spectrum of primordial fluctuations at a scale  $\sim 4$  Mpc. The lack of small scale power causes the halo to form via a single monolithic collapse rather than through mergers and accretion of smaller haloes. Since the final density profile was very similar to that of the same halo with the standard power spectrum, they concluded that details of the merging history do not affect the final density profiles.

Predictions of spherical infall model have been confronted with numerical simulation in several occasions. Early work by Quinn et al. (1986) found that in general the simple model correctly predicts the structure of bound objects, at least in a statistical sense. Zaroubi et al. (1996) accomplished a series of 'simulations' in which forces were computed assuming spherical symmetry, obtaining the same results as a standard Tree N-body code (but, on the other hand, their analytic predictions did not agree so well with the numerical results). More recently, Lokas and Hoffman (2000), Del Popolo et al. (2000) and Hiotelis (2002a) obtained density profiles comparable to the NFW form using different implementations of the spherical collapse model.

In order to test the validity of the formalism outlined above, we now try to reproduce the individual density profiles of our relaxed and minor

CLUSTER	STATE	$\nu$	$R_f$
A	Minor	3.5	1.3
B	Minor	3.4	1.2
C	Relaxed	3.4	1.3
D	Minor	3.2	0.9
E	Relaxed	2.8	1.4
H	Relaxed	2.5	1.2
J <sub>1</sub>	Relaxed	2.7	1.0
K <sub>1</sub>	Relaxed	2.7	0.9
L	Minor	2.7	0.7
K <sub>2</sub>	Minor	2.5	0.9
J <sub>2</sub>	Relaxed	2.8	0.8

TABLE 3.2: Spherical collapse parameters (peak height  $\nu$  and smoothing scale  $R_f$ ).

merging clusters. Assuming a fixed value of the orbit eccentricity, the model described in this section has two free parameters, which in this case have a clear physical meaning: namely, the smoothing scale  $R_f$  and height  $\nu$  (in units of sigma) of the primordial density peak from which the cluster is formed.

In Table 3.2, we report the best-fit values found for our clusters. Most of them can be described as structures formed from  $\sim 3\sigma$  peaks of the primordial density field, smoothed on  $\sim 1 h^{-1}$  Mpc scales. It is interesting that there exists a certain degeneracy between the parameters  $R_f$  and  $\nu$  for a given mass. However, a higher peak on a smaller smoothed scale corresponds to an earlier formation time. The inner density profile of such peak would be much steeper than that of a similar object formed (at a later redshift) from a lower primordial peak on a larger smoothing scale.

The average accuracy of the mass profiles predicted by our model based on spherical infall is shown in Figure 3.9. Individual profiles for each one of the clusters can be found in Appendix A. Although the overall quality of the fit is only slightly lower than that of the NFW fit (approximately 10%, compared to 5 – 10% reported in Section 3.2.1), there exists a large scatter between different dark matter haloes. This additional uncertainty rises considerably the error in the mass profiles of individual clusters, which can be as large as  $\sim 25\%$ .

Nonetheless, the spherical collapse formalism is able to *predict* the mass distribution from a physically-motivated description, whereas the formulas proposed by NFW or Moore et al. are mere phenomenological fits (valid for a much narrower radial range). Therefore, it constitutes a promising tool to understand the origin of the so-called 'universal' density profile despite the fact that it does not include *explicitly* the merging effects on structure

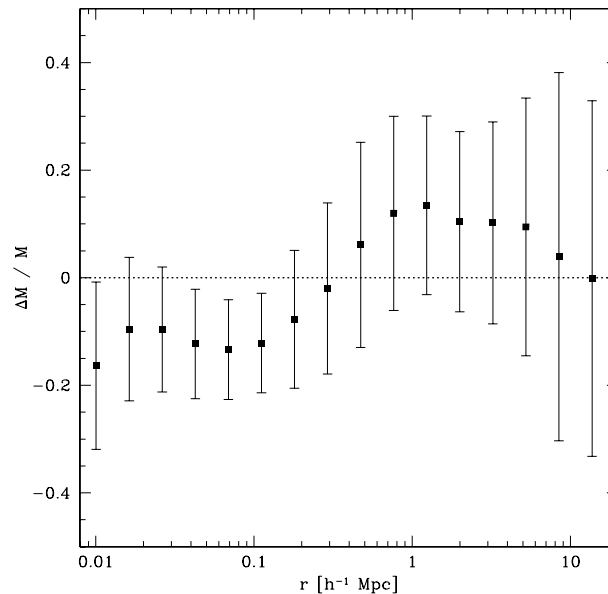


FIGURE 3.9: Accuracy of the spherical collapse prediction

formation.

We conclude that a possible explanation of why the density profiles predicted by the spherical infall model might describe the real (or numerical) dark matter haloes could be that merging is taken into account *implicitly* through the smoothing scale  $R_f$ . Contrary to the common view (see e.g. BBKS), we argue that  $R_f$  has a very precise physical interpretation: dark matter haloes do not form in *local* maxima of the primordial density field. These are the seeds for the very first objects in the universe, which collide amongst themselves and give birth to heavier dark matter clumps. These clumps, in turn, correspond to peaks associated to a very small smoothing scale, below which all the information about the substructure of the primordial density field is lost.

As time goes on, these protohaloes evolve through hierarchical clustering, and the smoothing length corresponding to the resulting objects increases (i.e. all the substructure below this scale is completely erased due to violent relaxation). Our point of view is that the smoothing length associated to a dark matter halo can be interpreted as a measure of the halo formation time or, equivalently, as the scale above which the system still remembers its initial conditions.





# Chapter 4

## Gas

*Too much pressure! Too much pressure!  
The pressure can't stop...  
Too much pressure!*

– The Selecter : *Too Much Pressure* (1980) –

**I**n the hierarchical galaxy formation scenario, cosmic structure grows via gravitational instabilities from small perturbations seeded in an early inflationary epoch. Since most of the mass is assumed to be in the form of collisionless cold dark matter, this yet unidentified component determines the dynamics of baryons on large scales, where hydrodynamic forces are unimportant compared to gravity.

However, if we want our simulations to describe the observable properties of cosmological objects, we must obtain information about the physical state of the baryons, either by resorting to phenomenological relations between the dark and luminous components or by direct self-consistent numerical modelling. The most basic baryonic process to be included in a numerical simulation is gas hydrodynamics, i.e. the presence of a collisional term in the Boltzmann equation representing particle interactions.

In principle, hot gas in clusters of galaxies should be easy to understand. Because of the relatively low ratio of baryons to dark matter, the potential of a cluster should be dark-matter dominated. The dynamical time within a cluster potential is shorter than a Hubble time, so most clusters should be relaxed. Also, the cooling time of vast majority of intracluster gas is longer than a Hubble time. It would appear that cluster structure ought to be scale-free, as long as the shape of a cluster's potential well does not depend systematically on its mass.

If that were the case, then the global properties of clusters, such as halo mass, emission-weighted temperature, and X-ray luminosity, would scale self-similarly (Kaiser 1986). Indeed, numerical simulations that include adi-

abatic gasdynamics produce clusters of galaxies that obey these scaling laws (e.g. Evrard et al. 1996; Bryan and Norman 1998).

Nonetheless, real clusters are not so simple. Even on cluster scales, radiative and feedback processes may not be completely negligible. This is expressed most clearly in the X-ray luminosity-temperature relation, probably due to an increase in entropy of the innermost gas. Observations indicate a much steeper temperature dependence than that expected from pure bremsstrahlung emission, especially for low mass systems (e.g. David et al. 1993; Ponman et al. 1996). The amount of energy injection required depends on the gas density at the time when the heating occurred, either before, during or after the collapse.

In this chapter, we address the reliability of the current numerical implementations of gasdynamics, and then present our results for the sample of galaxy clusters described in Section 2.3.1. The ICM of dynamically relaxed clusters is found to be in hydrostatic equilibrium and can be described by a polytropic equation of state (Ascasibar et al. 2002c). The radial profiles of gas density and temperature are also investigated, as well as the scaling relations between the global properties of our clusters. In most cases, the physical characteristics observed in the simulations show an encouraging agreement with relatively simple analytical predictions.

## 4.1 Numerical gasdynamics

Since the late 1980s a variety of techniques have been developed to simulate gasdynamics in a cosmological context. In part inspired by the success of the N-body scheme, the first gasdynamical techniques were based on a particle representation of Lagrangian gas elements using the smoothed particle hydrodynamics (SPH) technique (Lucy 1977; Gingold and Monaghan 1977).

Soon thereafter, fixed-mesh Eulerian methods were adapted (Cen et al. 1990; Cen 1992) and, more recently, Eulerian methods with sub-meshing (Bryan and Norman 1995), deformable moving mesh (Gnedin 1995; Pen 1995, 1998) or adaptive mesh refinement (AMR, Bryan et al. 1995; Kravtsov et al. 2002) have been developed, as well as extensions of the SPH technique (Shapiro et al. 1996; Springel and Hernquist 2002a; Serna et al. 2002).

These codes are actively being applied to a variety of cosmological problems, ranging to the formation of individual galaxies and galaxy clusters to the evolution of Ly $\alpha$  forest clouds and the large-scale galaxy distribution. Because the inherent complexity of gasdynamics in a cosmological context, such simulations are more difficult to validate than N-body experiments. Standard test cases with known analytical solutions (such as shock tubes) are far from the conditions prevailing in cosmological situations where the gas is coupled to dark matter, and this, in turn, evolves through a hierarchy of mergers.

The Santa Barbara cluster comparison project (Frenk et al. 1999) attempted to assess the extent to which existing modelling techniques gave consistent and reproducible results in a realistic astrophysical application, simulating the formation of a galaxy cluster in a  $\Lambda$ CDM universe with 12 completely independent codes, seven of them based on the SPH technique, while the other five employed grid methods to implement gasdynamics.

The properties of the CDM component in all modes were encouragingly similar, most of the discrepancies being due to small differences in the timing of the final major merger, which happened to be uncomfortably close to  $z = 0$ . There was less agreement in the gas-related quantities, although in most cases they were relatively similar, usually within 10 – 20%. Only the X-ray luminosity showed a strong dependence on the resolution of the different codes, with a spread as high as a factor of 10.

The most remarkable finding was the hint of a systematic trend in the temperature profiles obtained for the inner regions ( $r \leq 100$  kpc). Near the centre, SPH codes generated a flat or slightly declining (inwards) temperature profile, while grid codes produced temperature profiles that are still rising at the resolution limit. The entropy profile in SPH codes decreased continuously towards the centre, while grid codes develop an isentropic core at small radii.

Several authors (e.g. Hernquist 1993; Nelson and Papaloizou 1993, 1994; Serna et al. 1996; Springel and Hernquist 2002a; Serna et al. 2002) have pointed out that an important shortcoming of conventional SPH formulations is the poor conservation of entropy when a low number of particles is used. In this section we intend to test the accuracy of both Eulerian and Lagrangian numerical approaches for integrating the equations of gasdynamics. To this end, we compare results of the adaptive mesh code ART (Kravtsov et al. 2002), (see Section 2.1.2 for a description) with two different implementations of the Lagrangian code GADGET; one of them is the publicly-available version of the code (Springel et al. 2001b), which implements standard SPH gasdynamics, and the other is the explicit entropy-conserving scheme described in Springel and Hernquist (2002a, see also Section 2.1.3).

#### 4.1.1 Santa Barbara cluster

As a first step to test our codes, we have chosen the Santa Barbara cluster initial conditions, corresponding to a  $3\sigma$  peak in the primordial density field smoothed on a 10 Mpc scale. Details concerning the numerical experiments accomplished at different mass and spatial resolutions can be found in Section 2.3.2.

We have plotted in Figure 4.1 the results of all these experiments, using the criterion of 100 gas particles, 200 dark matter particles and  $r > 3\epsilon$  to define the minimum radius in each case. In particular, we compare the results of the Eulerian code ART (Kravtsov et al. 2002, triangles) with the standard

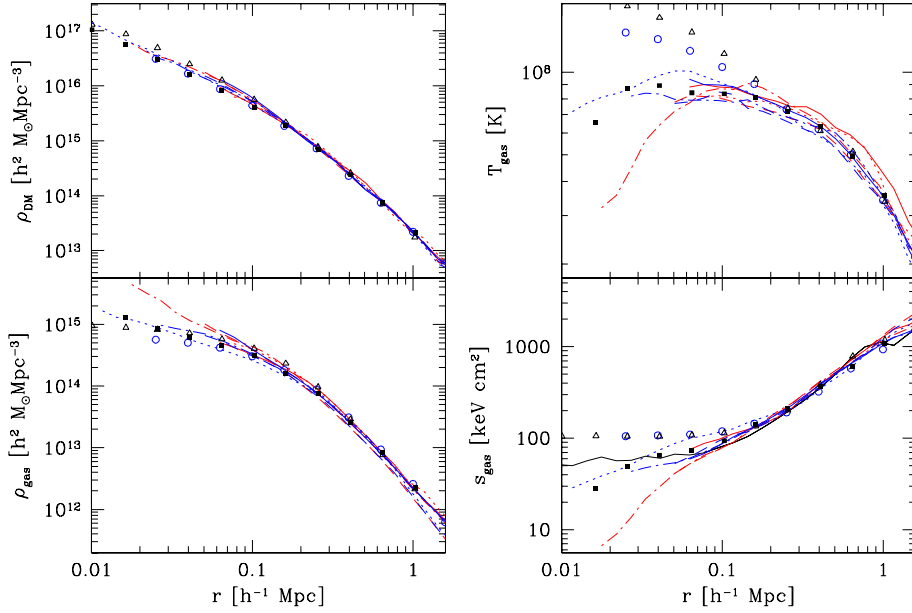


FIGURE 4.1: Simulations of the Santa Barbara Cluster. Top left: Dark matter density. Bottom left: Gas density. Top right: Gas temperature. Bottom right: Gas entropy. Solid squares denote the average of the Santa Barbara experiment (Frenk et al. 1999). Lines represent GADGET results for simulations with different mass resolutions and smoothing (see text), triangles are used for ART and circles for (Bryan et al. 1995).

and entropy-conserving implementations of the SPH algorithm available in GADGET (red and blue lines, respectively). The average of the simulations presented in Frenk et al. (1999) is shown by the solid squares. The results obtained by the adaptive-mesh code of Bryan et al. (1995) are plotted separately (circles).

## Resolution

The profiles for the different numerical experiments of the Santa Barbara cluster reported in Table 2.3 can be seen in Figure 4.1. Blue lines are used to represent the simulations with  $256^3$  particles and  $\epsilon = 2 h^{-1}$  kpc (dotted),  $128^3 - 5 h^{-1}$  kpc (dotted-dashed), and  $128^3 - 20 h^{-1}$  kpc (solid). Red lines (standard SPH) correspond to  $128^3 - 20 h^{-1}$  kpc (solid),  $128^3 - 5 h^{-1}$  kpc (dotted-dashed), and  $64^3 - 20 h^{-1}$  kpc (dotted). The black line on the bottom right panel indicates the entropy profile obtained in the low mass resolution simulation with  $64^3$  particles run with the standard SPH implementation of GADGET, ignoring the resolution limit.

In most cases, all the results are consistent when plotted according to the restrictions prescribed by Klypin et al. (2001). Nonetheless, the two ex-

periments with the highest nominal spatial resolution ( $5 h^{-1}$  kpc and  $256^3$  particles with standard and entropy-SPH) develop a steep decrease in the central temperature. Since we have checked that the centre of mass of both gas and dark matter distributions are approximately coincident (see e.g. the high gas densities obtained for the standard SPH implementation), this effect is probably caused by an artificially low smoothing length, which leads to very compact groups of cold particles that decouple from the surrounding medium. Although Eulerian simulations are not affected by this problem, the unphysical temperature drop described here is often seen in clusters simulated with SPH-based codes at low and medium resolutions (e.g. Eke et al. 1998; Yoshikawa et al. 2000; Mathiesen and Evrard 2001), and in some of the codes reported in Frenk et al. (1999).

If the smoothing scale is not set excessively low, but a small number of particles is used, the resulting cluster displays an extended core of constant density and temperature up to the minimum radius we have used for our plot. This softening-dominated core yields a flat entropy profile at the inner regions (black line in Figure 4.1), pointing to the misleading conclusion that this feature of clusters and groups of galaxies can be reproduced with a fairly low resolution. The same effect has been shown in cluster simulations with variable resolution by Borgani et al. (2002).

### Code comparison

A different issue concerning the entropy profile of galaxy clusters is whether the computations based on different integration schemes give consistent results, for the same numerical resolution. This topic has been previously discussed by Kang et al. (1994), Frenk et al. (1999), Springel and Hernquist (2002a) or Serna et al. (2002), among others.

The maximum number of particles allowed by the Santa Barbara initial conditions was  $256^3$ , which seems insufficient to discern the presence of a physical flattening of the entropy from the effects of numerical smoothing. However, we confirm the trends shown in Frenk et al. (1999): Eulerian codes predict a systematically rising temperature profile near the centre, while SPH algorithms are more consistent with isothermality.

This conclusion is strengthened by the fact that the two completely independent grid-based methods used in this comparison (i.e. ART and Bryan et al. 1995) give very similar results, while both implementations of GADGET show profiles consistent with the average value given in Frenk et al. (1999), which was dominated by SPH experiments.

Nevertheless, it seems that the highest resolution simulations using the entropy-conserving version of GADGET develop a certain tendency towards higher central temperatures, displaying an increasing profile up to  $\sim 60 h^{-1}$  kpc. At this point, there is a sharp break and the temperature drops again in the inner part of the cluster. Quite interestingly, the entropy profile at that

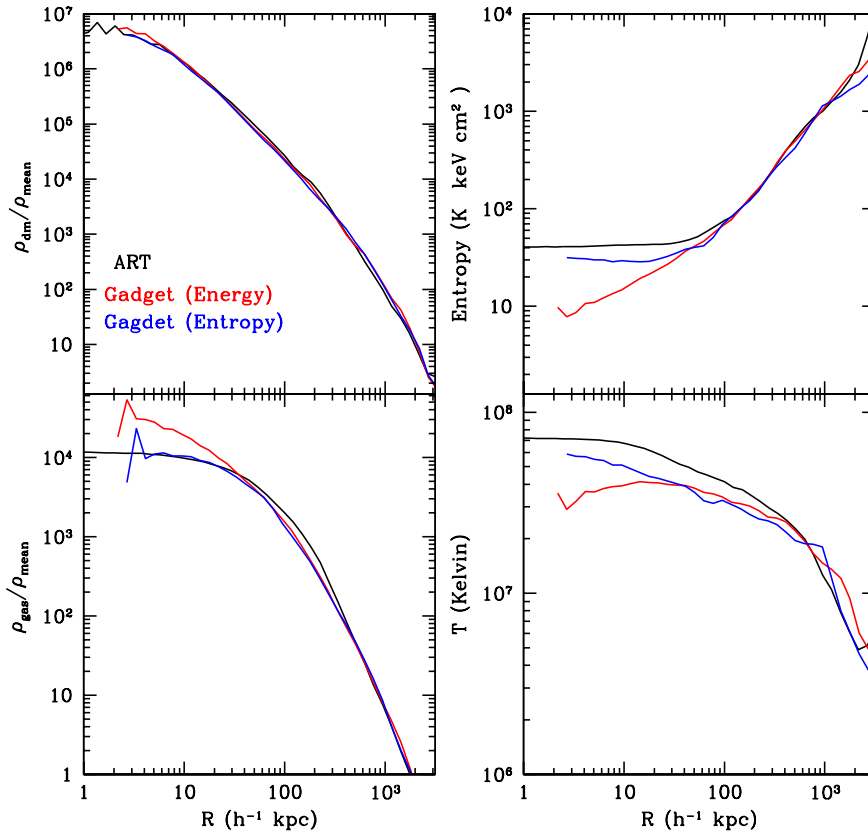


FIGURE 4.2: Simulations of Cluster A

radius shows remarkable signs of flattening (a fact also noted by Serna et al. 2002, who try to overcome the entropy problem by including the so-called  $\nabla h$  terms arising from the spatial dependence of the SPH smoothing length). In any case, more resolution is needed in order to study the structure of the ICM gas at even lower scales and make a reliable assessment on whether the entropy profile produced by these improved formulations of SPH is consistent with the results of Eulerian codes.

#### 4.1.2 Cluster A

Following the spirit of the Santa Barbara Cluster Comparison Project, we have run several numerical experiments from the initial conditions that produced the most massive galaxy cluster of our catalogue, as described in Section 2.3.1. In this case, the number of particles within the virial radius is approximately a factor of 8 larger than in the Santa Barbara cluster. Hence we have been able to resolve scales much deeper into the cluster's potential.

Figure 4.2 shows the results obtained with ART (Nagai and Kravtsov 2002) and both versions of GADGET for the radial profiles of Cluster A. Here, the difference between energy and entropy conservation is mostly evident at low radii (below  $\sim 20 h^{-1}$  kpc). As noted in previous studies (e.g. Serna et al. 2002), the density profile is steeper in the standard formulation of SPH, whereas the temperature is systematically higher when entropy conservation in SPH is enforced.

Consequently, the entropy profile is dramatically dependent on the chosen implementation. In top right panel of Figure 4.2, it can be clearly seen that the entropy profile of the explicit entropy-conserving scheme by Springel and Hernquist (2002a) unambiguously flattens in the central regions of the simulated cluster, while the standard SPH decreases uninterruptedly down to the resolution limit.

Since this effect is already manifest at clustercentric distances that are confidently resolved, we claim that there is a fundamental difference in the predictions based on Eulerian and Lagrangian codes due to the unphysical entropy loss in the latter. The fact that the entropy-conserving version of GADGET produces an entropy floor comparable to that observed in ART gives reassuring support to the idea that this numerical artifact is corrected in this formulation of the SPH algorithm.

## 4.2 Structure of the ICM gas

It has been twenty years since the realization that the extended X-ray emission from clusters (Kellogg et al. 1972) is thermal and arises from optically thin plasma filling the clusters (Mitchell et al. 1976). If this plasma is in hydrostatic equilibrium within the gravitational potential created by the dark matter, the spatial distribution of the ICM density and temperature constitutes an invaluable source of information about the process of structure formation on large scales.

Most importantly, since clusters of galaxies are the largest gravitationally bound structures in the universe, their physical properties have profound cosmological implications, and have often been proposed as a probe to test the values of the cosmological density parameters as well as the validity of the hierarchical CDM scenario (e.g. White et al. 1993). If well calibrated, the slope and evolution of cluster scaling relations, such as size, gas mass or luminosity versus temperature, can be used to constrain cosmological and structure formation models. Temperature profiles are also a fundamental ingredient in the determination of the total mass, as well as the gas entropy distribution, which is a powerful tool to explore non-gravitational processes that could alter the specific thermal energy in the ICM.

It is therefore important to investigate in detail the structure of the intra-cluster medium. Throughout this section, we will assume spherical

symmetry and focus on the radial profiles of several quantities of physical interest: first, we will address the validity of the usual assumptions of hydrostatic equilibrium, isothermality, and polytropic equation of state. Then, the average density and temperature profiles of our galaxy cluster catalogue (whose main properties are described in Section 2.3.1) will be compared with predictions based on the existence of a universal density profile for the dark matter component.

### 4.2.1 Physical state

One of the hypothesis that are often used in the study of galaxy clusters is that gas is in hydrostatic equilibrium with the mass distribution dominated by the dark matter. Allen (1998) suggested that this assumption is only valid for cooling-flow clusters, which has been corroborated by recent observations with *Chandra* and *XMM-Newton*.

Most analytical studies on the radial profiles of the ICM gas rely on hydrostatic equilibrium, in many occasions supplemented by a polytropic or isothermal equation of state for the gas. As we briefly discussed in Section 3.1.2, these prescriptions are used, for example, to estimate the gravitating mass from the observed X-ray emission. It is therefore of crucial importance that the accuracy of these assumptions is investigated by means of direct numerical simulation.

The main difficulty in studying the properties of gas in clusters formed in numerical experiments is the of lack of resolution (e.g. Thacker and Couchman 2001). Recently, Loken et al. (2002) have made a detailed analysis of the gas temperature profile for a sample of 20 clusters simulated with a resolution ( $< 15h^{-1}$  kpc) which is comparable to the present work, using an AMR gasdynamical code.

A completely different problem is the implementation of all the relevant physics involved in cluster formation. Radiative cooling and stellar feedback play a major role on galactic scales, as well as in the dense central parts of galaxy clusters. Outside the core, though, cooling times are longer than a Hubble time, and the effect of cooling on the ICM structure is not expected to be significant, at least on a first approximation.

On the other hand, there are still many open questions regarding the assembly of galaxy clusters even when only adiabatic physics is taken into account (see e.g. the previous section). Before including any radiative process, it is necessary to make sure that the physics associated to gravothermal collapse and shock-wave heating are accurately modelled. This also applies to the many theoretical predictions that can be derived with this 'simple' physics, which are often used as a benchmark to be compared with the observed properties of real clusters of galaxies.



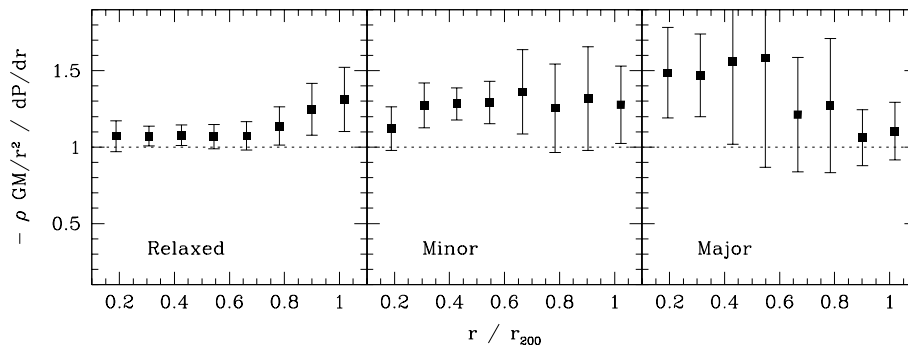


FIGURE 4.3: Test of the hydrostatic equilibrium assumption

### Hydrostatic equilibrium

Assuming that the gravitational potential is counter-balanced by thermal support only (i.e. bulk – infall and/or rotation – and turbulent motions of the gas are negligible with respect to its internal energy), the hydrostatic equilibrium equation for a spherically symmetric system reduces to the simple form

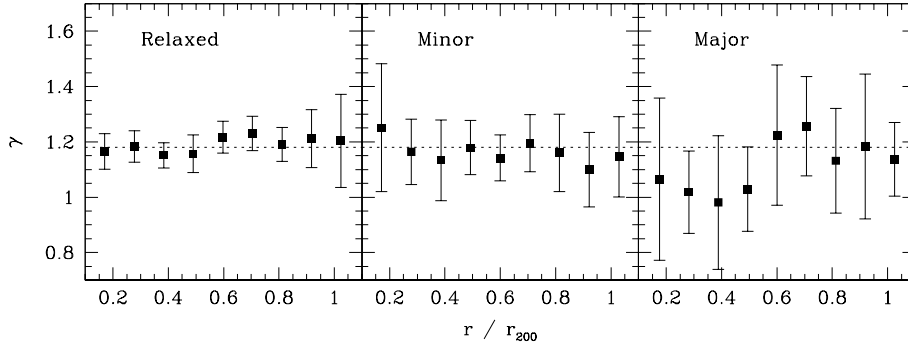
$$\frac{1}{\rho_g} \frac{dP}{dr} = - \frac{GM(r)}{r^2} \quad (4.1)$$

where  $\rho_g(r)$  is the gas density,  $P(r) = \frac{\rho_g(r)kT(r)}{\mu m_p}$  is the pressure and  $M(r)$  is the total (gas + dark matter) mass enclosed within radius  $r$ . Since the dark component dominates the mass of the cluster at all radii, the cumulative mass can be approximated by any of the ‘universal’ profiles described in Section 3.1.1.

We have checked the reliability of the usual assumption of hydrostatic equilibrium in Figure 4.3, where the ratio of the pressure gradient to the gravitational term ( $\rho GM r^{-2}$ ) is plotted as a function of clustercentric radius. If the gas was in thermally-supported hydrostatic equilibrium, this quotient should be equal to unity by virtue of equation (4.1).

For clusters that have been classified as *Relaxed* systems on dynamical grounds (see Section 2.3.1), hydrostatic equilibrium can be applied with a reasonable degree of accuracy ( $\sim 10\%$ ). Deviations from the behaviour predicted by (4.1) are due to the oversimplifying assumption that angular momentum and turbulent motions do not contribute significantly to support the gas against gravity. Besides, near the virial radius ( $r \geq 0.8r_{200}$ ), radial infall cannot be completely neglected.

As can be seen in the middle and right panels of Figure 4.3, the assumption of hydrostatic equilibrium holds only marginally for minor mergers, and not at all for clusters that are undergoing a major merging event. At this point, it is important to recall that non-relaxed systems constitute 60% of our sample. Even if the error is not extremely large (particularly, in the case

FIGURE 4.4: Polytropic index as a function of  $r$ 

of minor mergers), caution must be kept in mind whenever equation (4.1) is applied to a real cluster ensemble.

### Polytropic equation of state

In many occasions, hydrostatic equilibrium is used in combination with a simple equation of state. Usually, the gas is assumed to follow a polytropic law

$$P = \frac{\rho_g k_B T}{\mu m_p} = P_0 \rho_g^\gamma \quad (4.2)$$

where  $\gamma$  is the polytropic index and the normalisation  $P_0$  is an arbitrary constant. The value  $\gamma = 1$  corresponds to the special case of an isothermal gas, and is often seen in the literature, both in analytical and observational studies.

If the ICM gas could be described by the polytropic form (4.2), the radial temperature and the density profiles are related by

$$\frac{T}{T_0} = \left( \frac{\rho_g}{\rho_0} \right)^{\gamma-1} \quad (4.3)$$

where  $\rho_0$  and  $T_0$  are the central values of both magnitudes.

In real clusters, there is no strong physical reason to expect that the gas should be described by a polytropic equation of state. However, the appealing simplicity of equation (4.2) makes it extremely useful in analytical work, and hence it would be interesting to test whether it can be used to interpret the results on a first-order approximation.

The most straightforward way to check whether the ICM follows a polytropic relation is to compute the *local* value of the polytropic index

$$\gamma(r) = 1 + \frac{d \log(T)}{d \log(\rho)} \quad (4.4)$$

Figure 4.4 displays the radial dependence of  $\gamma$  for our sample of simulated galaxy clusters. Albeit some scatter, the radial profiles of the diffuse gas component in relaxed systems and minor mergers seem to be consistent with a polytropic equation of state with  $\gamma \sim 1.18$  (shown by a horizontal dotted line in the figure).

Another important issue is that an isothermal profile ( $\gamma = 1$ ) offers a very poor approximation to our results. In the section below, where the temperature structure of our clusters will be described in more detail, we will see that the constant temperature approximation can be ruled out at a significant level of several sigmas.

### 4.2.2 Radial profiles

In the previous chapter, we thoroughly discussed the possibility that the radial mass distribution of dark matter haloes followed a 'universal' form, finding that relaxed haloes (and even minor mergers, albeit with a lower degree of accuracy) could be described by the simple analytical fits proposed in the literature.

Once we know the dark matter distribution, the hydrostatic equilibrium equation (4.1) relates the gas density and temperature profiles to the cumulative mass, which can be approximated by the dark matter mass.

Several further assumptions must be made in order to compute the gas and temperature profiles. By far, the most common prescription is the so-called  $\beta$ -model, introduced by Cavaliere and Fusco-Femiano (1976) to describe the X-ray surface brightness profiles of galaxy clusters. Assuming that gas is isothermal and in hydrostatic equilibrium with a dark matter potential that follows an analytical King profile (King 1962),

$$\rho(r) = \frac{\rho_0}{(1+x^2)^{3/2}} \quad ; \quad x \equiv \frac{r}{r_c} \quad (4.5)$$

$$M(r) = 4\pi\rho_0r_c^3 \left[ \ln(x + \sqrt{1+x^2}) - \frac{x}{\sqrt{1+x^2}} \right] \quad (4.6)$$

$$\phi(r) = -4\pi G\rho_0r_c^2 \frac{\ln[x + (1+x^2)^{1/2}]}{x} \quad (4.7)$$

one can derive the gas density profile

$$\rho_g(r) = \frac{\rho_0}{[1 + (r/r_c)^2]^{3\beta/2}}, \quad (4.8)$$

where  $\rho_0$  is the central density,  $r_c$  is a core radius and  $\beta \sim kT/(\mu m_p \sigma_{DM}^2)$  relates the thermal energy of the gas to the velocity dispersion of the dark matter component. This form for the density profile  $\rho_g$  has been widely used in the literature (see e.g. Rosati et al. 2002, for a review). More recently, a generalisation of the  $\beta$ -model to account for temperature gradients in the

surface brightness profile of a polytropic gas has been derived by Ettori (2000).

As we have shown in the previous chapter, the King profile is not the model that best fits the cluster gravitational potential of dark matter halos in numerical simulations.

Suto et al. (1998) applied the hydrostatic equilibrium equation to a variety of dark matter density distributions. Assuming a polytropic equation of state for the gas and a NFW profile for the dark component, they find

$$\frac{T(r)}{T_0} = 1 - B \left( 1 - \frac{\ln(1 + \frac{r}{r_s})}{\frac{r}{r_s}} \right) \quad (4.9)$$

and a similar (though more complicated) expression for a Moore et al. formula. The  $B$  parameter gives the normalisation of the temperature profile,  $T_0$ , as a function of cluster dark mass, parametrised in terms of the characteristic density  $\rho_s$  and radius  $r_s$  of the NFW profile:

$$B = \frac{\gamma - 1}{\gamma} \frac{4\pi G \mu m_p \rho_s r_s^2}{k_B T_0} \quad (4.10)$$

Needless to say, the corresponding gas density profiles are given by (4.3).  $B$  fixes not only the central value  $T_0$ , but also the asymptotic behaviour of both gas and temperature profiles ( $T(\infty) \rightarrow 1 - B$ ). If we want the baryon fraction to remain approximately constant at large radii, we must choose  $B = 1$  and  $\gamma \sim 1.2$  in order that  $\rho_g \sim r^{-3}$ .

A similar result for  $B$  and  $\gamma$  has been found by Komatsu and Seljak (2001) from the same assumptions (i.e. NFW profiles, hydrostatic equilibrium, polytropic equation of state and constant baryon fraction at large radii). The normalisation of their temperature profiles is defined as

$$\eta(0) \equiv \frac{3kT_0 R_{200}}{GM_{200} \mu m_p} = 3 \frac{\gamma - 1}{\gamma} \frac{cg(c)}{B} \quad (4.11)$$

where  $g(c) \equiv [\ln(1 + c) - \frac{c}{1+c}]^{-1}$ . However, these authors did not require that  $B = 1$  to have a constant baryon fraction. Instead, they propose a relation between the normalisation  $\eta(0)$ , the polytropic index  $\gamma$  and the concentration parameter  $c$ , which can be fitted by

$$\eta^{-1}(0) = 0.00676\tilde{c}^2 + 0.206\tilde{c} + 2.48 \quad (4.12)$$

and

$$\gamma = 1.15 + 0.01\tilde{c} \quad (4.13)$$

with  $\tilde{c} \equiv c_{\text{NFW}} - 6.5$ . This fit works well for  $c > 3$ , as can be seen in Figure 3 of Komatsu and Seljak (2001), but cannot reproduce the normalisation for less concentrated halos.

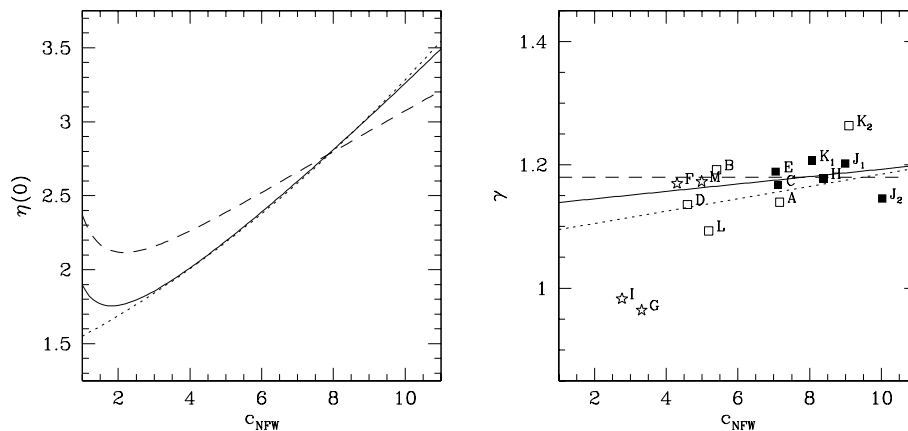


FIGURE 4.5: Left panel: Temperature normalisation  $\eta(0)$ . Right panel: Concentration dependence of the polytropic index. In both cases, solid lines are used for (4.14) and dashed lines for  $\gamma = 1.18$ . Dotted lines represent the results of Komatsu and Seljak (2001).

In Figure 4.5, we compare (4.12) with our prescription  $B = 1$ , equivalent to  $\eta(0) \equiv 3 \frac{\gamma-1}{\gamma} c g(c)$ . Assuming a constant polytropic index,  $\gamma \sim 1.18$ , as our simulations seem to indicate (see Figure 4.4), we obtain a slightly different normalisation. In order to obtain a similar prediction for  $\eta(0)$ , we should use the following dependence of  $\gamma$  on the concentration parameter:

$$\gamma = 1.172 + 0.006\tilde{c} \quad (4.14)$$

As can be seen in the figure, the match with the analytical fit (4.12) is perfect for  $c > 3$ . For lower values of  $c$ , our prescription follows the numerical results of Komatsu and Seljak (2001) (see Figure 3 of their paper).

In any case, both models are compatible with results from our simulated clusters. The most important conclusion drawn from these analyses is that physical properties of the gas are intimately related with the dark matter distribution. As we will show below, the radial temperature and density profiles of the ICM can be unambiguously determined from the parameters of the dark matter halo. Therefore, it is expected that they can also be characterised by 'universal' formulae.

## Temperature

Mass determinations from X-ray emission in clusters usually assume that relaxed clusters (i.e. morphologically symmetric) are isothermal. However, this assumption has been questioned recently by Markevitch et al. (1998), who found evidence of a decreasing temperature profile for nearby clusters observed with ASCA. A large subset of their sample showed a remarkably self-similar temperature profile when properly normalised and rescaled to the

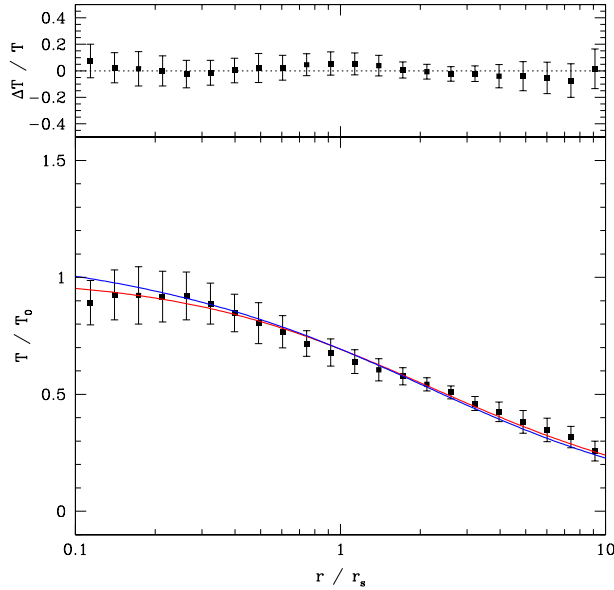


FIGURE 4.6: Average temperature profile (dots) compared to the theoretical predictions based on NFW (red line) and Moore et al. (blue line) profiles for the dark matter, assuming hydrostatic equilibrium and a polytropic equation of state. Accuracy of the NFW-based fit is shown in the top panel.

virial radius. On the contrary, White (2000) and Irwin and Bregman (2000), using data from *BeppoSAX* and *ASCA* satellites, do not find any decrease of the temperature in a large collection of clusters. More recently, the analysis of *BeppoSAX* observations accomplished by De Grandi and Molendi (2002) concluded that temperature profiles of galaxy clusters can be described by an isothermal core followed by a rapid decrease.

In this context, we would like to investigate what can we learn from the temperature profiles obtained in our numerical simulations. Particularly, we will focus on the shape of the radial temperature profiles, compared with both observational data and the simple analytical predictions based on hydrostatic equilibrium and a polytropic equation of state.

The mass-weighted temperature of our sample of galaxy clusters (excluding major mergers) is shown in Figure 4.6 as a function of radius. We see that, with this normalisation, the scatter is low enough ( $\sim 15\%$ ) to hint that the temperature profile can be described by a 'universal' form.

The scale factors in both axis of Figure 4.6 have been chosen to compare with the predictions based on a NFW profile, hydrostatic equilibrium, polytropic equation of state and approximately constant baryon fraction at large radii (i.e.  $B = 1$ ,  $T(\infty) \rightarrow 0$ ):

$$\frac{T(r)}{T_0} = \frac{\ln(1 + \frac{r}{r_s})}{\frac{r}{r_s}} ; \quad k_B T_0 = \frac{\gamma - 1}{\gamma} 4\pi G \mu m_p \rho_s r_s^2 \quad (4.15)$$

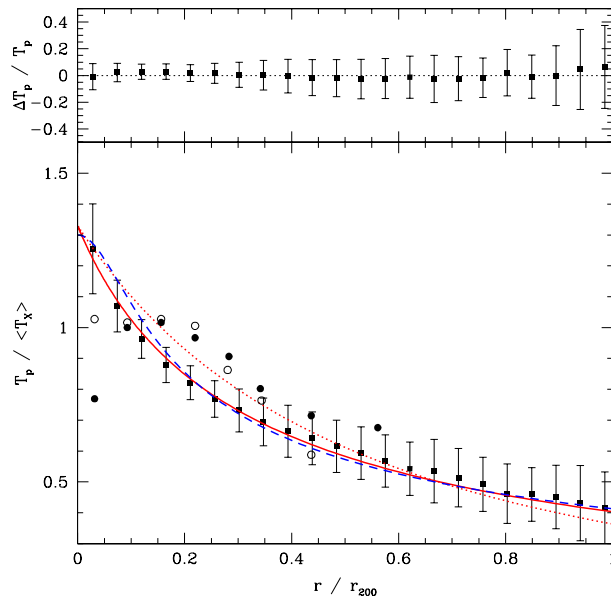


FIGURE 4.7: Averaged projected temperature profile (black squares with error bars) compared to the observational results of De Grandi and Molendi (2002) (solid circles for cooling-flow clusters, empty circles for non-cooling flow) and Markevitch et al. (1998) (dashed blue line). Red lines show the analytical fit proposed by Loken et al. (2002) (see text).

which is shown as a red line in Figure 4.6. In the top panel, we plot deviations from this 'universal' profile. The temperature profile derived from Moore et al. density profile is also shown for comparison (blue line). As can be easily appreciated in the figure, the difference is very small even near the centre.

We would like to remark that equation (4.15) *is not a fit* to the radial temperature profiles of our clusters, but a *prediction* based on the existence of a universal dark matter distribution (in this case, given by NFW expression). The central temperatures  $T_0$  have been computed assuming a polytropic index  $\gamma = 1.18$  for every cluster, so there are no free parameters related to the gas distribution. When only relaxed clusters are considered, the scatter around the predicted profile (determined by the values of  $\rho_s$  and  $r_s$ ) is considerably reduced.

In spite of its physical significance, the radial temperature profile has the disadvantage of not being a direct measurable quantity. In order to make a more reliable comparison with observations, the projected emission-weighted temperature profiles must be computed from our numerical data. More elaborate methods (e.g. Mathiesen and Evrard 2001) could be used to mimic the instrument-dependent observational procedure, simulating annular spectra and estimating the temperature profiles in the same way that is done in real clusters.

Recent results from high resolution AMR gasdynamical simulations of galaxy clusters (Loken et al. 2002) seem to indicate that the projected X-ray temperature profiles have indeed an universal form which decreases significantly with radius. These authors propose, as a best fit to their numerical simulations, the simple analytical formula

$$T(r) = \frac{T_0}{(1 + r/a_x)^\delta} \quad (4.16)$$

where  $T_0$  is the central temperature and  $a_x$  is a core radius. In order to confront this exciting result with our numerical experiments, we compare, Figure 4.7, the averaged temperature profile (once again, excluding clusters with major mergers) projected along the line of sight normalised to the averaged X-ray temperature at the virial radius<sup>1</sup>.

Solid red line shows the best fit we obtain for our data using expression (4.16), whereas the dotted red line indicates the radial dependence found by Loken et al. (2002). Although the results seem to be consistent within the error bars, and the normalisation is similar in both cases ( $T_0 \simeq 1.33 \langle T_X \rangle$ ), the best-fit values of the core radius and the asymptotic exponent are extremely sensitive to the particular details of the profile. While Loken et al. (2002) quote  $a_x = r_{200}/1.5$  and  $\delta = 1.6$  in their study, our clusters are better fit by  $a_x = r_{200}/4.5$  and  $\delta = 0.7$ .

As can be seen in Figure 4.7, our results are almost identical to the observational estimates of Markevitch et al. (1998), who claim that they are well represented by a polytropic  $\beta$ -model. But, as noted by Loken et al. (2002), this is not entirely self-consistent, since gas in the  $\beta$ -model is assumed to be isothermal and the data show a pronounce temperature gradient. Nevertheless, because gas in our cluster do follow a polytropic relation between density and temperature, and we expect the density of gas to be close to the observed one, it is not surprising that the projected profiles agree so well with observations.

However, the agreement is not so good with the temperature profile obtained by De Grandi and Molendi (2002) for a selection of clusters observed with BeppoSax. Our clusters are marginally consistent with their data, but we do not find any evidence of the temperature flattening observed by these authors at the inner regions. This could reflect the need of additional non-adiabatic physics in the simulations, but it could also be a consequence of the observational difficulties involved in the spectral determination of the gas temperature (see the discussion in Mathiesen and Evrard 2001).

---

<sup>1</sup>For a detailed description on the computation of these quantities, the reader is referred to Chapter 2.



### Density

Assuming that the ICM gas can be described by a polytrope, the gas density profile in hydrostatic equilibrium with a NFW dark matter distribution is given by the formula

$$\frac{\rho_g(r)}{\rho_0} = \left( \frac{\ln(1 + \frac{r}{r_s})}{\frac{r}{r_s}} \right)^{\frac{1}{\gamma-1}} \quad (4.17)$$

where we have taken  $B = 1$ , as we did in (4.15) for the temperature. With this prescription, the gas density vanishes as  $r \rightarrow \infty$  and the logarithmic slope is

$$\alpha(r) = \frac{1}{\gamma-1} \left[ -1 + \frac{\frac{r}{r_s}}{(1 + \frac{r}{r_s}) \ln(1 + \frac{r}{r_s})} \right] \quad (4.18)$$

Given the asymptotic behaviour at large radii,  $\alpha \sim \frac{1}{\gamma-1} \left[ -1 + \frac{1}{\ln(\frac{r}{r_s})} \right]$ , it is impossible that the gas density does *exactly* follow the dark matter profile in order to maintain a constant baryon fraction (a fact already noted by Komatsu and Seljak 2001). However, we should recall that NFW is not intended (nor able) to fit the dark matter density much beyond the virial radius, and the assumption of hydrostatic equilibrium is no longer valid in the outer parts of the cluster (see Figure 4.3). Therefore, the only, and necessary, requirement for (4.17) to be a good approximation to the ICM density is that it had a *similar* shape to the NFW profile for a broad radial range around  $r_{200}$ .

This led Komatsu and Seljak (2001) to the constraint (4.13) on the polytropic index of the gas, but no attempt was made to obtain a density normalisation, arguing that the gas mass fraction does not appear in the hydrostatic equilibrium equation, and that there is observational evidence suggesting its dependence on cluster mass (e.g. Arnaud and Evrard 1999). This makes the gas fraction determination uncertain and hence indicates that it should be treated as an additional free parameter.

Although the *global* baryon fraction is not a constant among the different clusters, we propose that a first-guess approximation to the central density  $\rho_0$  may come from the *local* ratio of the gas and dark matter densities.

This quantity is plotted in Figure 4.8 as a function of clustercentric radius, normalised to the cosmic baryon fraction  $\Omega_b/\Omega_{\text{dm}}$ . Not surprisingly, the radial profiles of both dark and gaseous components are very similar throughout most of the cluster<sup>2</sup>, differing only near the origin, where pressure is responsible for the formation of a shallow gas core. A flat baryon fraction profile has also been observed by Allen et al. (2002), who applied this result to the estimation of the mean matter density of the universe.

<sup>2</sup>In fact, this was one of the basic assumptions in the work of Komatsu and Seljak (2001).

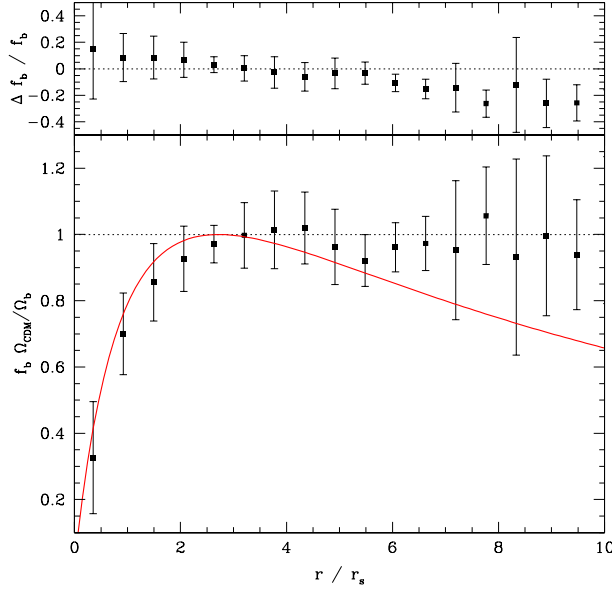


FIGURE 4.8: Radial dependence of the local baryon fraction

The baryon fraction expected from our prescription (4.17), plotted as a red line in Figure 4.8, is simply

$$\frac{\rho_g(r)}{\rho_{DM}(r)} = \frac{\rho_0}{\rho_s} \left( \frac{\ln(1 + \frac{r}{r_s})}{\frac{r}{r_s}} \right)^{\frac{1}{\gamma-1}} \frac{r}{r_s} \left(1 + \frac{r}{r_s}\right)^2 \quad (4.19)$$

Unfortunately, this expression does not tend to a definite asymptotic value, but it varies slowly enough at large radii for the range of polytropic indexes in which we are interested (as  $\gamma = 1.18$  in the figure). Actually, the shape of the gas density profile would be better modelled by slightly higher values ( $\gamma \sim 1.2$ ), resulting in a more constant baryon fraction in the outer parts of the clusters, but we will continue to use same value of  $\gamma$  as in the temperature profiles in order to maintain self-consistency.

The averaged radial density profile of the ICM gas is shown in Figure 4.9, rescaled by  $r_s$  on one axis and the value of  $\rho_0$  inferred from (4.19) in the other. The normalisation  $\rho_0$  has been obtained by imposing the condition that  $\rho_g/\rho_{dm} = \Omega_b/\Omega_{DM}$  at the radius where (4.19) has a maximum. For  $\gamma = 1.18$ , that is

$$\rho_0 \simeq 1.514 \frac{\Omega_b}{\Omega_{dm}} \rho_s \quad (4.20)$$

The quality of this approximation, given in the top panel for the density profile derived from NFW (red line) is significantly poorer ( $\sim 20 - 30\%$  accuracy) than the phenomenological fits for the dark matter. In this plot, we also show the gas density expected from a Moore et al. profile (blue line).

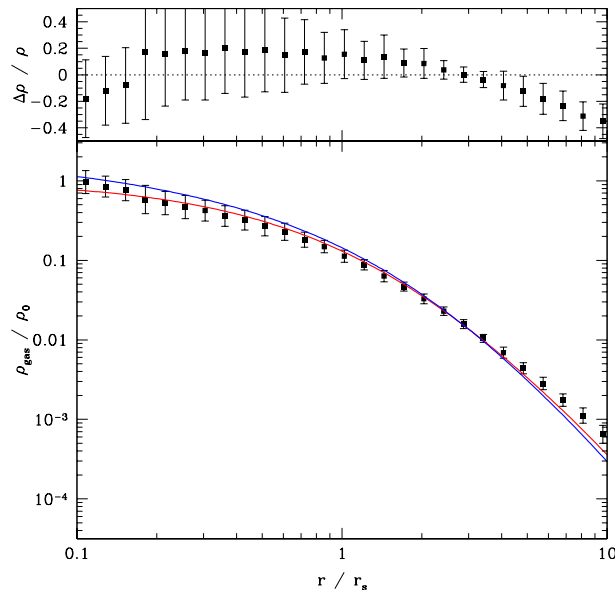


FIGURE 4.9: Average gas density profile

As in the temperature, the difference with NFW is not very large (usually, of the same order as the scatter around the NFW-based prediction). Part of this scatter can be attributed to departures from hydrostatic equilibrium in merging clusters, as well as deviations from purely thermal support that take place even in the outer parts of relaxed clusters.

Apart from self-consistency, another advantage of parametrisation (4.17) over the conventional  $\beta$ -model is due to the instability of the  $\beta$  parameter with respect to changes in the outer radius used to infer its best-fit value. Observational data restricted to radii much smaller than  $r_{200}$  tend to find values close to  $\beta \sim 2/3$ , while wider field cluster images are usually better described by  $\beta \sim 1$  (see e.g. Navarro et al. 1995). Since the profile given in expression (4.17) depends only on the dark matter parameters, and these are much more stable than those of the  $\beta$ -model, we consider this formula to be more reliable in order to extrapolate the gas density up to the virial radius. Moreover, it allows a direct estimate of the total mass if the dark matter halo can be described by a NFW profile, although we have already shown that the accuracy is somewhat limited.

### 4.3 Scaling relations

Before the structure of clusters of galaxies could be resolved by the available observations, they were already realised to exhibit a number of simple correlations between their global properties. These scaling relations could lend insight into the physical nature of clusters when compared with the analyt-

ical predictions expected to hold under the assumption of self-similarity in the formation and evolution of large scale structure (Kaiser 1986).

However, deviations from self-similarity are expected under the effects of, for example, merging (Jing and Suto 2000) and any additional physics acting on the intracluster gas over the simplistic infall in the dark matter potential (e.g. Evrard and Henry 1991; Bryan and Norman 1998; Bialek et al. 2001, and references therein). The latter case is particularly relevant to cool systems, where the extra energy estimated from observed properties is comparable to their thermal energy (e.g. Ponman et al. 1996, 1999; Tozzi and Norman 2001).

In the past 10 years, the advent of space-based X-ray observations of galaxy clusters have revealed that there exist tight correlations between the total gravitating mass, the X-ray luminosity and the temperature of the intracluster medium (e.g. Rosati et al. 2002). A close comparison of theoretical results and observational data can therefore provide valuable constraints on the prevailing cosmological models and even on the nature of the dark matter that dominates the mass distribution and the dynamical evolution of clusters.

### 4.3.1 Mass-temperature

The number density of galaxy clusters as a function of their mass can provide a powerful probe of models of large-scale structure. Since the mass of a cluster is not a directly observable quantity, the abundance of rich clusters of galaxies has been historically measured in terms of some other parameter which is used as an approximation for mass. Several options exist, but much attention has been focused recently on the X-ray temperature.

Cosmological simulations suggest that this magnitude is strongly correlated with mass, showing little scatter (e.g. Evrard et al. 1996; Bryan and Norman 1998). How well simulations agree with observational results is still far from clear, and several issues need to be resolved. Numerical resolution and difficulties to include all the relevant physics are the main sources of uncertainty invariably coupled to cosmological simulations, while instrumental effects and the lack of a reliable method to estimate the mass are the most worrying aspects related to the observational determination of the  $M - T$  relation.

#### Analytical prediction

Within the framework of pure gravitational infall (e.g. Lilje 1992), the cluster mass and the gas temperature should scale simply as  $M \propto T^\alpha$ , where the exponent  $\alpha \simeq 3/2$  is almost unrelated to the particular settings of cosmological parameters. This self-similarity has been later justified by numerical simulations (e.g. Evrard et al. 1996; Bryan and Norman 1998) and is often

used as a reference against which observational results are compared.

There are several ways to obtain this relation. The simplest of them relates the thermal energy of the gas to the potential energy due to self-gravitation of the cluster. By virtue of the virial theorem:

$$\frac{kT_\Delta}{\mu m_p} \simeq \frac{1}{2} \frac{GM_\Delta}{r_\Delta} \quad (4.21)$$

where  $T$  and  $M$  refer to average temperature and cumulative mass. The subscript  $\Delta$  indicates the overdensity threshold at which these quantities are measured. Substituting  $M_\Delta \equiv \frac{4\pi}{3} \Delta \rho_c r_\Delta^3$  and  $\rho_c \equiv \frac{3H_0^2}{8\pi G}$  above we get

$$M_\Delta \simeq \frac{4}{GH_0 \Delta^{1/2}} \left( \frac{kT_\Delta}{\mu m_p} \right)^{3/2} \equiv M_0^{\text{vir}} \Delta^{-1/2} \left( \frac{T_\Delta}{1 \text{ keV}} \right)^{3/2}. \quad (4.22)$$

Therefore, the virial theorem predicts not only the relation between  $M$  and  $T^{1.5}$ , but also the normalisation  $M_0^{\text{vir}} \equiv \frac{4}{(\mu m_p)^{3/2} GH_0} \simeq 6.1210^{14} h^{-1} M_\odot$ .

A similar scaling law can be derived from our assumption of a polytropic equation of state for the gas, in hydrostatic equilibrium with a NFW potential. Using the density profile (4.17), the averaged temperature at overdensity  $\Delta$  is just

$$T_\Delta = T_0 \tau_m(\gamma, r_\Delta/r_s) ; \quad \tau_m(\gamma, r_\Delta/r_s) \equiv \frac{\int_0^{r_\Delta/r_s} \left[ \frac{\ln(1+x)}{x} \right]^{\frac{\gamma}{\gamma-1}} x^2 dx}{\int_0^{r_\Delta/r_s} \left[ \frac{\ln(1+x)}{x} \right]^{\frac{1}{\gamma-1}} x^2 dx} \quad (4.23)$$

and the emission-weighted temperature

$$T_X^\Delta = T_0 \tau_x(\gamma, r_\Delta/r_s) ; \quad \tau_x(\gamma, r_\Delta/r_s) \equiv \frac{\int_0^{r_\Delta/r_s} \left[ \frac{\ln(1+x)}{x} \right]^{\frac{2}{\gamma-1} + \frac{3}{2}} x^2 dx}{\int_0^{r_\Delta/r_s} \left[ \frac{\ln(1+x)}{x} \right]^{\frac{2}{\gamma-1} + \frac{1}{2}} x^2 dx} \quad (4.24)$$

The assumption  $B = 1$  led to the central temperature normalisation given in equation (4.15). Using the definition of  $M_\Delta$ , we recover the scaling relation  $M_\Delta = M_0 \Delta^{-1/2} T_\Delta^{3/2}$ , with  $M_0$  given by

$$M_0 = M_0^{\text{vir}} \left[ \frac{1}{2\tau_{m/x}} \frac{\gamma}{\gamma-1} \frac{\ln(1+r_\Delta/r_s) - \frac{r_\Delta/r_s}{1+r_\Delta/r_s}}{r_\Delta/r_s} \right]^{3/2} \quad (4.25)$$

where the term in brackets depends on the particular values of the polytropic index and 'concentration'  $r_\Delta/r_s$  of each dark matter halo. As we discussed in the previous section, the polytropic index can be taken to be a constant value  $\gamma \simeq 1.18$  for the range of masses covered by our simulated clusters.

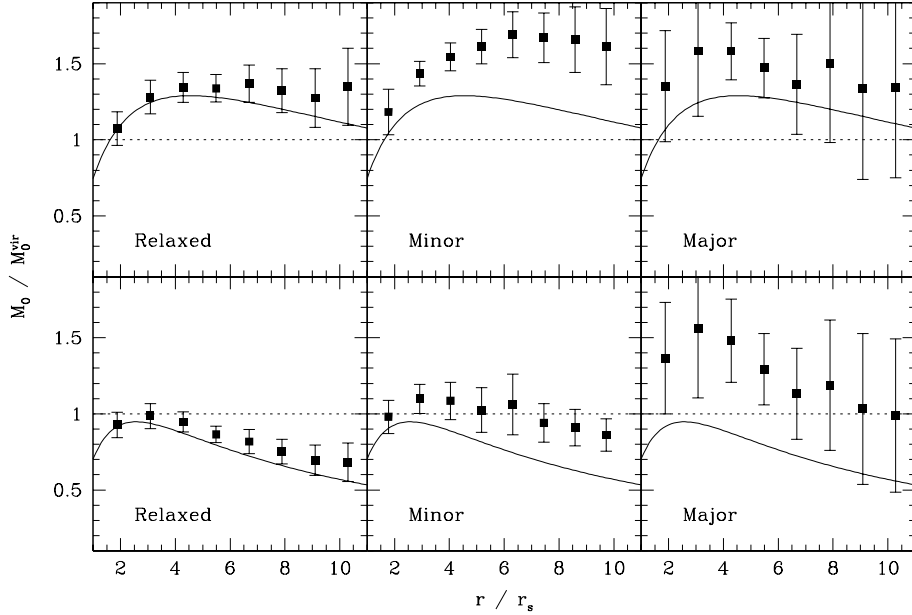


FIGURE 4.10: Analytical  $M - T$  normalisation. Top panel: Mass-weighted temperature. Bottom panel: Emission weighted temperature  $T_X$ .

The validity of this approximation outside this mass range must be tested by independent numerical simulations.

The dependence of  $M_0$  on  $r_\Delta/r_s$  is shown in Figure 4.10, which can be interpreted as a ‘universal profile’ of the ratio between thermal and gravitational energy. The normalisation  $M_0 \equiv M_\Delta \Delta^{1/2} T_\Delta^{-3/2}$  is plotted as a function of radius, in units of the characteristic scale  $r_s$ . For a value of the NFW concentration parameter  $c = 8$ , the radius at which the overdensity is  $\Delta = 2500$  approximately coincides with  $r_s/3$ ,  $r_{1000} \sim r_s/2$  and  $r_{500} \sim 2r_s/3$ . By definition,  $r_{200} = cr_s$ .

As can be seen in Figure 4.10, the normalisation of the  $M - T$  relation predicted by equation (4.25) depends on whether  $T$  or  $T_X$  is used, the difference (which can be up to a factor of 2 near the virial radius) is due to the factor  $\tau_{M/x}^{-3/2}$ . Our formula gives a fair approximation to the mass-temperature relation in relaxed clusters, but it severely overestimates the mean temperature in merging systems (by  $\geq 50\%$  in the outer parts). At high overdensities, though, expression (4.25) is consistent with the results of our simulations within the scatter from halo to halo. The effect of dark halo concentration (which varies between 7 and 10 for our relaxed clusters, 5 and 7 for minor mergers, and 3 – 5 for the major merging subset, see Table 3.1) is always of the order of 10% at all radii.

According to these results, dispersion around the predicted scaling relation between mass and temperature arises mainly due to the excess of gravi-

tational energy present in merging events with respect to the final virialised state. This agrees, at least at a qualitative level, with the deviation from thermally-supported hydrostatic equilibrium that was seen in Figure 4.3.

### Observations

From an observational point of view, several studies have been devoted to test the mass-temperature relation in clusters of galaxies. Horner et al. (1999) claim that the  $M - T$  relation is steeper than the traditional scaling, following a  $M \propto T^{1.8-2.8}$  law when the mass is estimated according to the  $\beta$ -model. Slopes steeper than 1.5 are also observed in high-redshift clusters (Schindler 1999, e.g.) and highly-luminous clusters (Ettori and Fabian 1999), where isothermality has been assumed. Neumann and Arnaud (1999), also using the  $\beta$ -model to estimate the gravitating mass, obtain a  $M - T$  relation consistent with the classical scaling. Allen et al. (2001b), using spatially resolved spectroscopy with *Chandra*, found consistency with the scaling law prediction, but the normalisation was  $\sim 40\%$  lower with respect to numerical simulations.

However, it should be noted that in the above observational analyses, only high-temperature ( $kT > 4 - 5$  keV) clusters are involved. As has been realized in recent studies (e.g. Mohr et al. 1999; Ponman et al. 1999), the input of energy feedback into the ICM can break the self-similarity in the low-temperature clusters and groups. This has been confirmed by Nevalainen et al. (2000), who inferred a slope  $\alpha = 1.79 \pm 0.14$  and a normalisation significantly lower than the one observed in numerical simulations, although the classical relation  $M \propto T^{3/2}$  was recovered when the low-temperature groups are excluded.

Finoguenov et al. (2001) also found that the slope of the  $M - T$  relation for more massive clusters (i.e.  $M_{500} > 5 \times 10^{13} M_{\odot}$ ) was considerably shallower ( $1.58 \pm 0.07$ ) than that obtained for their whole sample ( $1.78 \pm 0.09$ ), the normalisation being more than 50% lower than the value quoted in Evrard et al. (1996). These authors also point out that mass estimates based on isothermality like the  $\beta$ -model result in a steeper scaling relation (a fact already noted by Horner et al. 1999) due to the implicit assumption that the dark matter density scales as  $r^{-2}$ , thus underestimating the mass at low radii and overestimating it at large radii. An additional bias is introduced because the value of  $\beta$ , and hence the asymptotic slope of the gas profile, was a function of temperature.

Xu et al. (2001) compared the mass-temperature relation obtained from the  $\beta$ -model mass estimates and an isothermal distribution in hydrostatic equilibrium with a NFW potential. They found both models to be indistinguishable, giving a slope steeper than the self-similarity prediction unless the clusters at less than 3.5 keV are excluded, in agreement with Finoguenov et al. (2001).

REFERENCE	$\Delta$	$M_0/M_0^{\text{vir}}$	$\alpha$	
Horner et al. (1999)	200	0.92	1.53	velocity dispersion
	200	0.63	1.48	temperature profiles
	200	0.51	1.78	$\beta$ -model
	200	0.47	2.06	$S_X$ deprojection
Ettori and Fabian (1999)	500	0.40(0.97)	1.93	$\beta$ -model
Neumann and Arnaud (1999)	1750	0.75	1.5	$\beta$ -model
Mohr et al. (1999)	1000	1.15	1.5	$\beta$ -model
Nevalainen et al. (2000)	2000	0.58(0.75)	1.77	temperature profiles
	1500	0.57(0.73)	1.77	
	1000	0.52(0.73)	1.79	
	500	0.41(0.74)	1.84	
Finoguenov et al. (2001)	500	0.65	1.68	$\beta$ -model
	500	0.77	1.48	polyt. $\beta$ -model, $T \geq 3$
	500	0.45	1.87	idem. $T \leq 4.5$ keV
Xu et al. (2001)	200	0.67	1.60	$\beta$ -model
	200	0.40	1.81	isothermal NFW
Allen et al. (2001b)	2500	0.97	1.47	$T_{\text{mw}}$ NFW SCDM
	2500	0.93	1.52	$T_{\text{mw}}$ NFW $\Lambda$ CDM
Ettori et al. (2002a)	2500	0.82(1.03)	1.54	$T_{\text{mw}}$ (NFW or King)
	1000	0.78(1.18)	1.76	
	2500	0.88(1.03)	1.51	$T_X$
	1000	0.48(1.06)	1.94	

TABLE 4.1: Observed  $M - T$  relation

Ettori et al. (2002a) have not only studied the slope of the  $M - T$  relation, but they have also extensively investigated the dependency of the scaling relations with the dynamical state of the cluster as well as the outer radius reached by the observational data. The slope at overdensity 2500 is consistent with 1.5, the presence of non-cooling flow clusters significantly increasing the scatter. However, the slope at  $\Delta = 500$  steepened up to  $M \propto T^{2.17 \pm 0.37}$ . Regarding the normalisation, these authors claim that the previously reported lower values (e.g. Horner et al. 1999; Nevalainen et al. 2000) were due to the steeper slopes found in those studies.

Observational data are summarised in Table 4.1, where the reference and overdensity of each study are listed in the first two columns, followed by the best-fit values of the normalisation (rescaled to the self-similar prediction) and the logarithmic slope  $\alpha$ . The number in parentheses corresponds to the best-fit  $M_0$  when the slope is set to  $\alpha = 1.5$ . Particularities of each work, such as the assumptions employed to derive the gravitating mass, are noted on the right margin of the table.



Given the remarkable success of the  $\Lambda$ CDM model in explaining most of the relevant cosmological observations<sup>3</sup>, it is somewhat amazing that observers do show such a tenacious reluctance to accept it as a fact. Except for Allen et al. (2001b), all the mass estimates in Table 4.1 have been made in a  $\Omega = 1$ ,  $\Lambda = 0$ ,  $h = 0.5$  universe. Fortunately, the scaling relation between mass and temperature does not depend on cosmology but through the usual factor  $h^{-1}$  in the mass, which is implicitly taken into account in the units we used for  $M_0^{\text{vir}}$ .

A more worrying concern is raised by the discrepancy found between the masses inferred from different methods and models, as well as that arising from different analysis prescriptions. As can be inferred from the compilation given in Table 4.1, we are far from reaching an acceptable convergence in the observational value neither of the normalisation nor the slope of the scaling relation.

### Simulations

The mass-temperature relation has also been extensively studied by means of cosmological numerical simulations. In most cases, from the early work of Navarro et al. (1995) or Evrard et al. (1996) to the recent high-resolution simulations of Muanwong et al. (2002), slopes consistent with the self-similar value  $\alpha = 1.5$  are found when only adiabatic physics is considered.

The normalisation, however, has a little bit more scatter, although not so much as that present in the different observational estimates. In both cases, this scatter is partly due to the precise value found for the logarithmic slope, since the normalisation of the scaling law is closely related to this parameter (for a given sample, the higher the best-value of  $\alpha$ , the lower the corresponding normalisation  $M_0$ ).

A compilation of different mass-temperature relations found in numerical simulations is given in Table 4.2. The structure of the table is the same of Table 4.1, in which the observational data were presented. Unless otherwise noted, the cumulative mass is compared to the emission-weighted temperature  $T_X$ . Yoshikawa et al. (2000) gives the normalisation referred to both quantities, and Mathiesen and Evrard (2001) also computed a spectral temperature  $T_s$  based on a more detailed model of the line emission of the ICM gas in the soft X-ray band as well as a subsequent fitting procedure closer to the analysis of observational data.

These authors find that the spectral fit temperature is generally lower than the mass or emission-weighted average<sup>4</sup> due to the influence of cooler

---

<sup>3</sup>As well as some others... The  $\Lambda$ CDM model is almost as wonderful as SCDM was ten years ago! (see e.g. Cole et al. 1994a)

<sup>4</sup>Rather surprisingly, their values of  $T_X$  are similar, although slightly lower, than  $T_{\text{mw}}$ , which is reflected in the normalisations quoted in Table 4.2. This is probably due to the presence of cold gas in the most inner part of their clusters.

REFERENCE	$\Delta$	$M_0/M_0^{\text{vir}}$	$\alpha$	
Navarro et al. (1995)	200	1.01	1.5	
Evrard et al. (1996)	2500	1.30	1.5	
	1000	1.38	1.5	
	500	1.30	1.5	
	250	1.15	1.5	
	100	0.89	1.5	
	Bryan and Norman (1998)	200	1.42	1.5
Pen (1998)	200	1.19	1.5	
Eke et al. (1998)	100	1	1.5	
Yoshikawa et al. (2000)	100	1.40	1.5	$T_{\text{mw}}$
		0.91	1.5	$T_X$
Mathiesen and Evrard (2001)	500	1.34	1.52	$T_{\text{mw}}$
	200	1.25	1.54	
	500	1.85	1.38	$T_X$
	200	1.65	1.39	
	500	1.81	1.48	$T_s$ (0.5-9.5)
	200	1.69	1.51	
	500	1.34	1.62	$T_s$ (2.0-9.5)
	200	1.20	1.64	
	Muanwong et al. (2002)	200	2.28	1.5

TABLE 4.2:  $M - T$  relation in previous simulations

	$\Delta$	RELAXED CLUSTERS		WHOLE SAMPLE	
		$M_0/M_0^{\text{vir}}$	$\alpha$	$M_0/M_0^{\text{vir}}$	$\alpha$
$T_{\text{mw}}$	2500	1.20	1.56	1.08	1.71
	1000	1.31	1.59	1.30	1.65
	500	1.34	1.53	1.45	1.54
	200	1.29	1.46	1.57	1.33
$T_{\text{X}}$	2500	0.93	1.61	0.91	1.68
	1000	0.90	1.62	1.04	1.57
	500	0.84	1.57	1.12	1.40
	200	0.71	1.51	1.15	1.17

TABLE 4.3:  $M - T$  relation for our sample

gas being accreted as part of the hierarchical clustering process. Despite significant departures from isothermality, single-temperature models produce acceptable fits for the spectral temperature  $T_s$ . The unusual coincidence that a realistic spectrum has nearly the same shape as an isothermal one was explained by these authors in terms of a lack of spectral resolution.

Although several cosmologies have been assumed in all these works, the results do not seem to be very sensitive to this. As pointed out by Muanwong et al. (2002), the numerical resolution of the simulation is much more important, particularly in those cases where cooling was implemented. Increasing the resolution lowers the emission-weighted temperature due to the presence of cold, dense gas cores that survive in sub-clumps. This has been argued by Mathiesen and Evrard (2001) to explain the lower spectral temperature detected in minor mergers, proposing the deviations from a canonical  $M - T$  relation to distinguish these systems from relaxed clusters.

Table 4.3 summarises our results concerning the mass-temperature relation, where a separate fit has been performed for relaxed clusters (left columns). Our values are consistent with the self-similar prediction in almost every case. Clusters undergoing major merging events are usually responsible for the discrepancies.

The normalisation derived in the present study seems to be in agreement with previous numerical work when the mass-weighted temperature is considered, but is significantly lower when expressed in terms of the emission-weighted temperature. We interpret this result as a resolution effect, maybe related to the numerical implementation of gasdynamics (see Section 4.1). Since  $T_{\text{X}}$  is biased towards the highest-density regions of the cluster, and both our simulated temperature and density profiles seem to increase continuously towards the centre (as expected from the analytical predictions based on hydrostatic equilibrium), the emission-weighted temperature grows as smaller scales are resolved in the cluster cores.

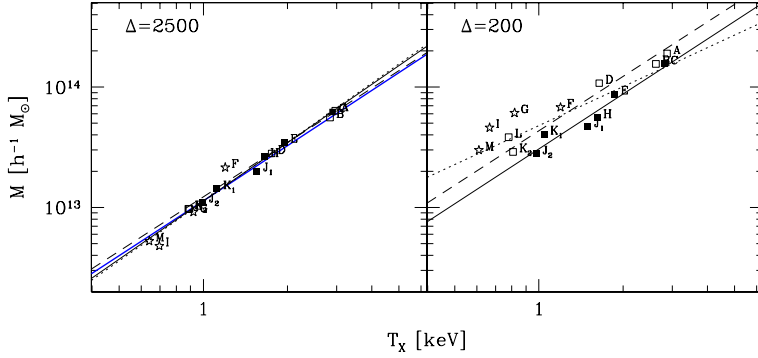


FIGURE 4.11:  $M - T$  relation for our sample at two different overdensities. Solid lines are least-square fits to the relaxed population, dotted lines are used for the whole sample. The analytical prediction is shown by dashed lines and observational data from Allen et al. (2001b) by a blue line.

Indeed, our  $M - T$  relation agrees relatively well with the results of Yoshikawa et al. (2000), as well as those of Mathiesen and Evrard (2001) for the mass-weighted temperature. As noted earlier, the values of  $T_X$  found by these authors are lower than  $T_{\text{mw}}$ . This is only possible if the densest gas is colder than the average. This seems to be the case in their Figure 4, where they plot the phase-space diagram of the gas particles of one of their clusters. As noted in Section 4.1, we attribute the presence of such cold clumps to a numerical artifact associated to SPH softening.

A possible way to overcome the problem posed by the sensitivity of the X-ray related quantities to the detailed structure of the ICM in the central regions is to compute the *local* (instead of average) values at  $r_\Delta$ . Observationally, this has been possible only very recently, thanks to the deprojection of high-resolution maps obtained by space-based observatories (Ettori et al. 2002a). Although it could be in principle a good way to compare numerical and observational results, it is still subject to many uncertainties on the observational side.

Our results at overdensities  $\Delta = 2500$  and  $\Delta = 200$  are compared with both observational data and analytical estimates in Figure 4.11. We see that the virial prediction based on equation (4.22) accurately reproduces our simulated  $M - T$  relation when only relaxed clusters are taken into account. As could be seen in Figure 4.10, merging clusters deviate from the expected normalisation at large radii, being more than 50% heavier for a given temperature. This biases the best-fit slope towards shallower values at  $r_{200}$ , as indicated in Table 4.3, but has an almost negligible effect at higher overdensities.

The best-fit mass-temperature relation found by Allen et al. (2001b) is drawn as a blue line in the left panel of Figure 4.11. Some authors (Ettori et al. 2002a; Mohr et al. 1999) find similar normalisations at high

overdensities, whereas others (Neumann and Arnaud 1999; Nevalainen et al. 2000) quote slightly lower values. The situation is much less clear near the virial radius, but there is a general trend in the sense that observational estimates seem to indicate hotter temperatures for a given virial mass.

### 4.3.2 Luminosity-temperature

A scaling law that is more directly observable is the correlation between bolometric X-ray luminosity and global emission-weighted temperature. It has been known long ago that the slope of the relation appears to fit  $L_X \propto T_X^3$  (e.g. Mitchell et al. 1979; Edge and Stewart 1991; David et al. 1993; Fabian 1994) rather than  $L_X \propto T_X^2$ , as would be expected for a simple self-similar model, and much theoretical work has been devoted to find the reasons for such a discrepancy.

One of the proposed solution involves some *preheating* of the intracluster gas by an agent other than gravity, such as supernova explosions at high redshift (Kaiser 1991; Evrard and Henry 1991). This additional heating would decrease the central density and hence the X-ray luminosity. This view was strengthened by the discovery of an apparent entropy 'floor' in the centres of groups and clusters (Ponman et al. 1999).

However, the amount of heating required is substantial. Although estimates vary, it seems likely that about 1 keV per particle is needed, which may be challenging to explain from supernova heating alone due to an excessive enrichment of the ICM (Kravtsov and Yepes 2000; Valageas and Silk 1999). Another difficulty is that observations of the Ly $\alpha$  forest indicate a much lower temperature for the majority of the intergalactic medium at  $z \sim 2 - 3$  (Bryan and Machacek 2000), a condition that may extend to even low redshifts. Although hardly conclusive, these concerns may be pointing toward another explanation for these observations.

Early on, it was suggested that the steepening of the  $L - T$  relation could be due to systematic variations of the cluster baryon fraction with X-ray temperature (David et al. 1993). Fabian (1994) and Markevitch et al. (1998) also note that the large scatter in the  $L_X - T_X$  plane was mostly due to the strong cooling flows present in more than half the low-redshift clusters (e.g. Edge et al. 1992). It has been argued (Allen and Fabian 1998) that these cooling flows, which can account for up to 70% of the total X-ray luminosity of a cluster (Allen 1998), could be responsible for the observed discrepancy in the slope of this scaling relation.

### Analytical prediction

Simple arguments based on self-similarity predict that the bolometric X-ray luminosity of galaxy clusters should scale with the temperature of the gas according to  $L_X \propto T_X^2$ . Nevertheless, the normalisation of the  $L - T$

relation is often treated as a free parameter. In order to attempt a theoretical prediction, we will calculate the X-ray luminosity of a spherically symmetric cluster of galaxies, assuming that it is dominated by thermal bremsstrahlung emission. With this prescription, the cumulative bolometric luminosity can be computed as

$$L_X(r) = \int_0^r \Lambda_X \left( \frac{\rho_g(x)}{\mu m_p} \right)^2 [kT(x)]^{1/2} 4\pi x^2 dx \quad (4.26)$$

where  $\Lambda_X = 1.2 \times 10^{-24} \text{ erg s}^{-1} \text{ cm}^3 \text{ keV}^{-1/2}$  (Navarro et al. 1995). As explained in Section 2.2.3, this is precisely the definition we use to compute the bolometric luminosity of our numerical clusters.

Although it has already been shown that clusters are definitely *not* isothermal, the term  $T^{1/2}(r)$  varies very slowly compared to  $\rho_g^2(r)$ . Therefore, at a first approximation we can take its mean value out of the integral in (4.26). Since this expression is biased towards the highest-density regions, it would be more accurate to use the emission-weighted average.

After some calculations, we obtain the expression

$$L_X(r) \simeq \frac{\Lambda_X}{(\mu m_p)^2} [kT_X(r)]^{1/2} \frac{\int_0^r \rho_g^2(x) 4\pi x^2 dx / (\frac{4\pi}{3} r^3) M_g^2(r)}{[M_g(r) / (\frac{4\pi}{3} r^3)]^2 \frac{4\pi}{3} r^3} \quad (4.27)$$

which can be simplified using the definitions of cumulative baryon fraction, overdensity and the structure parameter  $Q(r) \equiv \langle \rho_g^2 \rangle / \langle \rho_g \rangle^2$ . The final scaling relation is reduced to the form

$$L_X^\Delta \simeq \frac{\Lambda_X}{(\mu m_p)^2} \Delta \rho_c F_\Delta^2 Q_\Delta M_\Delta [kT_X^\Delta]^{1/2} \equiv L_0 \Delta^{1/2} \left( \frac{\Omega_b}{\Omega_m} \right)^2 \left( \frac{T_X^\Delta}{1 \text{ keV}} \right)^2 \quad (4.28)$$

Proceeding in an analogous manner as we did for the  $M - T$  relation, we express the normalisation  $L_0$  in expression (4.28) in terms of the quantity  $L_0^{\text{vir}} \equiv \frac{\Lambda_X \rho_c}{(\mu m_p)^2} M_0^{\text{vir}} \simeq 2.85 \times 10^{43} h \text{ erg s}^{-1}$ . For the sake of simplicity, we will assume a cosmic baryon fraction  $\Omega_b / \Omega_m = 0.14$  irrespective of the cosmological model. This is approximately the ratio expected for a  $\Lambda$ CDM universe and it is roughly consistent with the value observed in galaxy clusters (e.g. Allen et al. 2002), assuming a low  $\Omega_M$ .

Another difficulty in comparing observational and theoretical results arises from the different scaling with the Hubble constant. Since the observed luminosity is proportional to  $d_L(z)^2$ , it scales as  $h^{-2}$  instead of  $h$ . For nearby clusters, this effect accounts for a factor of 6 in the normalisation depending on whether the comparison is made in units of  $h = 1$ ,  $h = 0.5$  or  $h = 0.7$ . We take  $h = 1$  as the prescription that is more consistent with both observational and numerical methods.

We test the validity of our analytic estimates of the  $L - T$  relation by comparing the values of  $L_X / (f^2 Q)$  and  $MT_X^{1/2}$ . The values of these quantities for all our simulated clusters are plotted in Figure 4.12, as well as the

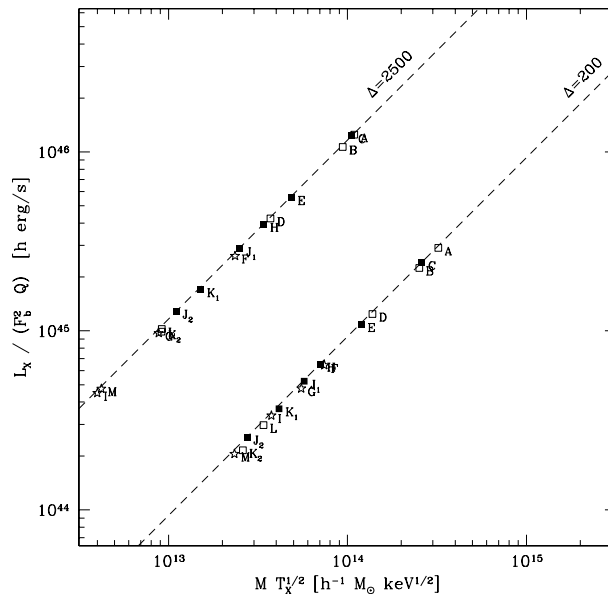


FIGURE 4.12: Normalisation of the  $L - T$  relation, corrected for the effects of baryon fraction and structure parameter.

results of equation (4.28) for two different overdensity values. The agreement is not surprising, since the only assumption we made for deriving the analytical prediction was to consider that  $T^{1/2}$  varied much more slowly than  $\rho_g^2$ , which, as we discussed in Section 4.2.2, is a very good approximation.

### Observations

The luminosity-temperature relation of several cluster catalogs observed with the first generation of X-ray satellites showed a departure from the predicted slope  $\alpha = 2$  (e.g. Edge and Stewart 1991; David et al. 1993) with a measured value of  $\alpha \sim 3$  and a scatter along the mean relation that could be reduced considerably once the effect of the cold cores was taken into account (Fabian 1994).

When the impact of cooling flows on the bolometric luminosity and emission-weighted temperature of the cluster is properly corrected, the  $L - T$  relation is shown to be tighter and closer to (yet not completely consistent) the self-similar scaling prediction (e.g. Allen and Fabian 1998; Ettori et al. 2001). The scatter is significantly reduced in analyses that either excise the core cooling flow regions (Markevitch et al. 1998) or examine samples of clusters defined to possess weak cooling cores (Arnaud and Evrard 1999).

The steeper  $L - T$  dependence found in other studies (e.g. David et al. 1993; Ponman et al. 1996; Cavaliere et al. 1997; Ponman et al. 1999; Xue and Wu 2000; Tozzi and Norman 2001) is often justified by invoking some sort of

REFERENCE	$\Delta$	$L_0/L_0^{\text{vir}}$	$\alpha$	
David et al. (1993)	200	0.084	3.37	
Ponman et al. (1996)	200	0.468	8.20	groups
	200	0.132	3.29	groups+clusters
Allen and Fabian (1998)	200	0.287	3.22	cooling-flow (raw)
	200	1.698	2.13	CF (corrected)
	200	0.191	2.92	non-CF
Markevitch et al. (1998)	200	0.414	2.10	0.1 – 2.4 keV
	200	0.347	2.64	bolometric
Arnaud and Evrard (1999)	200	0.209	2.88	
Xue and Wu (2000)	200	0.017	5.57	groups
	200	0.029	2.79	clusters
Allen et al. (2001b)	2500	0.296	2.17	$T_{\text{mw}}$ SCDM
	2500	0.589	2.08	$T_{\text{mw}}$ $\Lambda$ CDM
Ettori et al. (2002a)	2500	0.055(0.258)	2.79	$T_{\text{mw}}$
	1000	0.347(0.677)	2.37	
	2500	0.076(0.258)	2.64	$T_X$
	1000	0.214(0.551)	2.54	

TABLE 4.4: Observed  $L - T$  relation

pre-heated of the intracluster gas, which would rise the entropy level in the coolest systems.

A compilation on observational estimates of the  $L_X - T_X$  relation is given in Table 4.4. We see that both the normalisation and the logarithmic slope differ considerably from author to author, being extremely sensitive to the details of the data reduction and analysis (e.g. instrumental specifics, treatment of cooling flows, fitting procedure, etc.).

Once again, we see that the parameters  $L_0$  and  $\alpha$  are tightly correlated, reflecting the fact that the typical temperature of most cluster samples is substantially larger than 1 keV. Thus, the normalisations obtained for a self-similar slope  $\alpha = 2$  (quoted between parentheses in Table 4.4) are much higher than those obtained when the slope of the relation is not constrained.

Contrary to the  $M - T$  relation, in this case the assumed cosmological model plays an important role in the exact value of  $L_0$ , while the slope  $\alpha$  is not so affected (see Allen et al. 2001b, the *only* work that included an estimate based on a  $\Lambda$ CDM cosmology).

The effect of differences in individual gas fractions and structure parameters of clusters on the observed logarithmic slope of the  $L - T$  relation has been examined by Arnaud and Evrard (1999), who came to the conclusion that the higher gas concentration in hot clusters is responsible for at least half of the steepening of the  $L - T$  relation. When cluster mass is estimated



REFERENCE	$\Delta$	$L_0/L_0^{\text{vir}}$	$\alpha$	
Navarro et al. (1995)	200	1.46	2	
Bryan and Norman (1998)	200	1.27	2.59	
Eke et al. (1998)	100	1.08	2	
Bialek et al. (2001)	500	3.85	1.56	core included
		1.25	2.02	core excised

TABLE 4.5:  $L - T$  relation in previous simulations

from a  $\beta$ -model, the temperature dependence of the structure factor  $Q$  can explain the observed slope. But if virial theorem is used to derive masses, then the gas fraction increases with cluster temperature, and it contributes as much as  $Q$  to the steepening of the logarithmic slope  $\alpha$ .

### Simulations

Despite the significant amount of observational work regarding normalisation and slope of the  $L_X - T_X$  relation, there are little numerical work done in this regard as compared to works done to study the mass-temperature relation (some of them listed in Table 4.2).

This is a reflection of the difficulty in obtaining reliable estimates of the bolometric X-ray luminosities. While it is reasonable to assume that the results are sensitive to the ICM thermal evolution, it is well known (e.g. Bryan and Norman 1998; Yoshikawa et al. 2000) that they are also affected by the numerical resolution.

When equal mass particles are employed in a given simulation, the smallest clusters have poorer resolution and hence their luminosities tend to be systematically underestimated as compared with more massive ones.

This effect can steepen the slope of the simulated  $L - T$  relation, making it closer to the observed one. Although our numerical experiments seem to have enough resolution to overcome this problem, it is always necessary to keep in mind this consideration when interpreting the results.

Many of the references cited in the present work did not study the  $L - T$  relation at all. Among them, only those reported in Table 4.5 quote the best-fit values found for the parameters  $L_0$  and  $\alpha$ . Bialek et al. (2001) also includes a discussion on the analytical derivation of the scaling laws, highlighting the importance of cluster structure, related to  $F_b$  and  $Q$  parameters.

These authors point out that the slope of the power-law fits can be biased by a few points at one end. In their case, they had two low-temperature systems that appeared to be fortuitously observed mergers. In agreement with our results presented in previous chapter Bialek et al. (2001) remark that these two objects featured steeper density profiles compared to the rest of the sample, and used this fact to justify that their luminosity was a

$\Delta$	RELAXED CLUSTERS		WHOLE SAMPLE	
	$L_0/L_0^{\text{vir}}$	$\alpha$	$L_0/L_0^{\text{vir}}$	$\alpha$
2500	1.34(1.11)	1.89	0.55	2.86
1000	2.35(2.21)	1.90	1.24	2.66
500	3.44(3.13)	1.89	2.23	2.45
200	5.57(4.95)	1.89	4.25	2.28

TABLE 4.6:  $L - T$  relation for our sample

factor of 3 higher than that expected from their gas temperature. Exclusion of the core emission, where the core is defined as a circular area of radius  $0.13r_{200}$ , resulted in a best-fit slope consistent with the analytical scaling (see Table 4.5).

However, this is not what we find in our numerical experiments. In Table 4.6, we show the values of  $L_0$  and  $\alpha$  that best describe the  $L_X - T_X$  relation of our galaxy cluster catalogue. The best-fit parameters are quoted for different overdensity thresholds, making a separate fit for the relaxed subset of the sample. The number in parentheses is the normalisation  $L_0$  when the logarithmic slope is fixed to the canonical value  $\alpha = 2$ .

There is a striking difference between the behaviour of the relaxed clusters and the merging systems in our simulations. Contrarily to the results reported by Bialek et al. (2001), the latter exhibit significantly lower luminosities for a given temperature, mainly due to their lower concentrations (and thus, lower central densities). This is not surprising, since, despite the steeper inner slope of the density profile, the normalisation  $\rho_s$  is significantly reduced with respect to relaxed systems (see e.g. the right panel of Figure 3.3).

We also find, in agreement with Bialek et al. (2001), that the low-mass end of our sample is dominated by the presence of merging systems, but in our case this biases the X-ray luminosity towards *lower* values, and the slope of the  $L - T$  relation steepens considerably when low-mass mergers are included in a least-square fit together with the more massive, relaxed clusters of galaxies.

At high overdensities, merging systems raise the slope of the simulated  $L - T$  relation to values consistent (and sometimes even higher) than those observed. However, since these are the least massive of our clusters, caution must be exercised because of the lower relative resolution (i.e. less particles within the virial radius) in these objects. Nonetheless, a steepening of the luminosity-temperature relation would be expected if

1. Clusters indeed followed a 'universal' baryon fraction profile (as it seems to be the case in Figure 4.8).

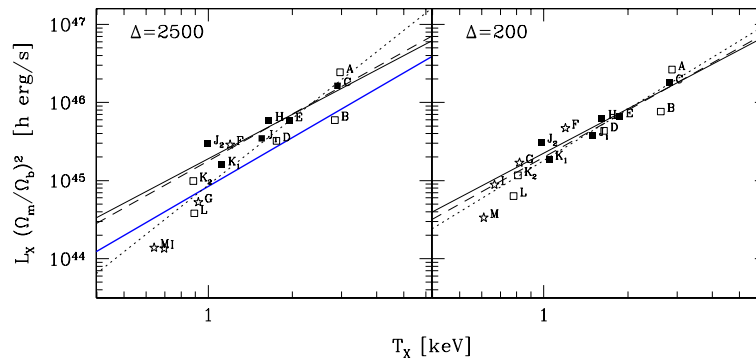


FIGURE 4.13:  $L-T$  relation for our cluster sample. Symbols are as in previous Figures. Observational data from Allen et al. (2001b) are shown as solid blue. Dotted line is the self-similar relation. Dashed line is the unconstrained best fit to relaxed clusters and solid line is the best fit to relaxed clusters for  $\alpha = 2$  (see Table 4.6)

## 2. Low-temperature systems were systematically less concentrated.

In such a case, a dependence of the baryon fraction on temperature would arise and hence the X-ray luminosity of the low-temperature clusters would be significantly depressed with respect to that of the more massive objects. This effect would be more evident at high overdensities. Near the virial radius, the global baryon fraction is expected to be only slightly lower than the cosmic value, since gas and dark matter profiles are observed to be proportional everywhere except in the core regions.

The first hypothesis above can be understood as a consequence of hydrostatic equilibrium and a 'universal' dark matter profile. The second arises from the fact that low-mass systems are more prone to merge (in agreement with the predictions based on the hierarchical scenario). Therefore, we think that this relation between baryon fraction and temperature is not an artifact due to a lack of resolution, but has a physical origin. However, this is not the only mechanism that can alter the observed  $L_X - T_X$  relation. A more detailed discussion is given in the next section.

The steepening of the  $L-T$  scaling law can be clearly seen in Figure 4.13, where the effects of observational 'aperture' (i.e. overdensity) can be appreciated at first sight by comparing the left and right panels. At  $\Delta = 2500$ , our results for the whole sample are perfectly compatible with a power law as steep as  $L_X \propto T_X^3$ .

Observational data from Allen et al. (2001b) have been represented by a blue line in the left panel of Figure 4.13. It is not clear to what extent our results are compatible with this fit, but the disagreement is manifest if we compare with estimates based on a SCDM cosmology. However, such a comparison is not straightforward. These authors, for instance, quote a normalisation which is a factor of 2 lower (as well as a steeper slope) for

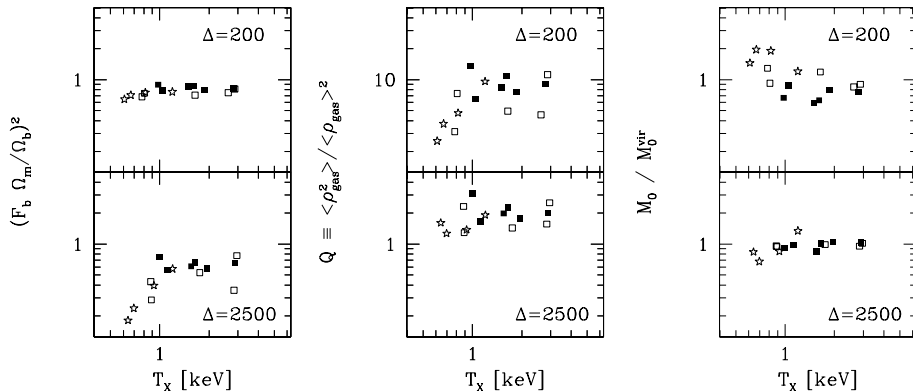


FIGURE 4.14: Deviations from the self-similar  $L - T$  scaling law at different overdensities. Left panel: Baryon fraction. Middle panel: Structure parameter. Right panel: Mass-temperature normalisation.

the same cluster sample if a SCDM cosmological scenario is assumed for the analysis.

Given the many difficulties surrounding the reliable calibration of the  $L_X - T_X$  scaling law from both theoretical and observational grounds, the mass-temperature relation seems to be much more convenient in order to use clusters of galaxies as cosmological probes.

### Departure from self-similarity

We have already shown in Figure 4.12 that our clusters follow quite closely the analytical prediction of the  $L - T$  relation given by expression (4.28) when the effects of substructure are taken into account. However, it is evident from both Figure 4.13 and the slopes quoted in Table 4.6 that the best-fit  $L_X - T_X$  relation deviates significantly from the self-similar scaling law  $L \propto T^2$ , particularly at high overdensities.

Since (4.28) holds, these deviations arise from the factor  $F_b^2 Q M_0$ , where we recall that  $F_b$  denotes the cumulative gas fraction,  $Q \equiv \langle \rho_g^2 \rangle / \langle \rho_g \rangle^2$  is the structure parameter and  $M_0$  is the normalisation of the  $M - T$  relation. It has been often argued that self-similarity implies that these quantities must be the same for all clusters, and hence the normalisation  $L_0$  would be a constant multiple of  $L_0^{\text{vir}}$ .

A systematic dependence of  $L_0$  on temperature would tilt the observed  $L - T$  relation, changing the best-fit value of the logarithmic slope  $\alpha$ . Several authors (e.g. David et al. 1993; Arnaud and Evrard 1999) argued that  $F_b^2 \sim T$  would reconcile the slope  $\alpha \sim 3$  derived from observational data with the self-similar prediction. Some attention has been paid (e.g. Arnaud and Evrard 1999) to the effect of the structure parameter, and almost none to possible variations in  $M_0$ .

Figure 4.14 displays the behaviour of these quantities as a function of temperature and overdensity. In the top panel, we see that the cumulative baryon fraction at  $r_{200}$  is slightly lower than the cosmic value, and does not vary significantly even in clusters undergoing a major merging event. However, these systems are much less concentrated than relaxed structures, which manifests as a factor of  $\sim 3 - 4$  difference in the structure parameter,  $Q$ . However, this variation is anti-correlated with the normalisation of the  $M - T$  relation, since  $M_0$  tends to increase for lower values of  $r_{200}/r_s$  (see Figure 4.10). These two effects compensate each other and the total deviation from the self-similar scaling is relatively small for  $\Delta = 200$ .

As we restrict ourselves to inner radii, both the structure parameter and the normalisation of the  $M - T$  relation tend to more stable values. Now, differences in central concentrations make that smaller systems, whose gas distribution is puffier, get lower baryon fractions than relaxed clusters. Hence, the bolometric X-ray luminosity is suppressed by a factor of 3 with respect to the expected behaviour. As can be seen in Table 4.6, this effect is responsible for a dramatic steepening of the slope of the  $L_X - T_X$  relation.



## Chapter 5

# Stars

*Oh let the sun beat down upon my face  
stars to fill my dream  
I am a traveler of both time and space  
to be where I have been*

– Led Zeppelin : *Kashmir* (1975) –

**S**tar formation and feedback to the interstellar medium (ISM) play a key role in the whole process of structure formation. The cosmological model provides the space-time framework in which the events take place and fixes several key parameters, such as the expansion rate of the universe, the amount of matter and the amplitude of primordial density fluctuations. The large-scale structure of the universe, the clustering properties of matter or the mass distribution in individual objects can be understood in terms of hierarchical growth of dark matter fluctuations. Hydrodynamic simulations have shown to be a valuable tool to understand the physical conditions of the gas at low and moderate densities. Detailed theoretical studies of, e.g. the Lyman-alpha forest (Cen 1992; Hernquist et al. 1996) and the intergalactic medium could be done thanks to them.

At higher densities, radiative cooling and star formation become an essential ingredient in the description of baryons. Unfortunately, our knowledge of the complex physical processes involved in galaxy formation is much less certain. For instance, in the absence of stellar feedback most of the baryonic matter would have cooled into small mini-galaxies (Cole 1991; Blanchard et al. 1992). Photoionization and supernova explosions inhibit cooling and star formation in very low-mass objects, biasing star formation at early times towards high overdensity regions. Feedback has been proposed, as we discussed in the previous chapter, to solve the discrepancy between the observed and theoretical scaling relations of galaxy clusters, as well as the problems of angular momentum in discs (Silk 2001) and the low number of observed dwarf galaxies (Bullock et al. 2000).

Despite the numerous attempts to include star formation in cosmological simulations (e.g. Springel and Hernquist 2002b, and references therein), progress has been comparatively low with respect to gravity or gasdynamics, since the physics involved in star formation and feedback into the interstellar medium is substantially more complex, and also because it acts on scales of a few pc and masses of  $\sim 10^5 M_{\odot}$ , which are well below the resolution limits.

The present chapter describes the results obtained from the model implemented by Yepes et al. (1997, see also Section 2.1.1). The star formation history of the universe (Ascasibar et al. 2002a) is discussed in detail, as well as the main differences between the star formation regimes observed in clusters and field galaxies.

## 5.1 The cosmic star formation history

The star formation history of the universe, i.e. the global star formation rate (SFR) density as a function of redshift, is a crucial test for galaxy formation scenarios. Many measurements of this quantity have been undertaken during the past few years, and the number and accuracy of available observations are still rapidly increasing.

Although there is a large scatter among different indicators at any given redshift, basically all studies find a significant increase (by about one decade) in the cosmic SFR density from the present day to  $z = 1$ . However, it is still a controversial issue (Hopkins et al. 2001) whether it reaches a broad maximum there (e.g. Madau et al. 1996; Gispert et al. 2000) or it declines gradually towards higher redshifts (e.g. Sawicki et al. 1997; Pascarella et al. 1998; Steidel et al. 1999).

From a theoretical point of view, star formation is a highly non-linear process, which precludes any simple analytical treatment. Most efforts towards modeling the star formation history of the universe resort to semi-analytical methods or numerical simulations to tackle the feedback mechanisms that self-regulate the SFR within the hierarchical clustering scenario of structure formation.

Semi-analytical models (see e.g. Kauffmann et al. 1993a; Cole et al. 1994b; Salvador-Sole et al. 1998) construct a large sample of Monte Carlo realizations of halo merging histories, using the Press-Schechter formalism. Hydrodynamics, star formation and feedback are implemented through simple recipes, whose parameters are fixed in order to match the observed properties of real galaxies, specially the luminosity function and the Tully-Fisher relation (Somerville and Primack 1999). Their high computational efficiency allows a fast exploration of the parameter space in search of a viable model, but the number of free parameters asks for supplementary modeling based on more fundamental physics.



Numerical simulations are intended to solve directly the set of differential equations of gravitation and gas hydrodynamics, and hence require much fewer model assumptions than the semi-analytic approach. However, despite the staggering advances in computer technology and numerical algorithms, resolution in large-scale hydrodynamical simulations is severely restricted by computational and data storage requirements. Although gas can be treated self-consistently, some phenomenological recipes are still required in order to model star formation and feedback.

The cosmic SFR density is a direct outcome of semi-analytical methods (Somerville et al. 2001) and hydrodynamical simulations (Tissera 2000; Nagamine et al. 2001; Ascasibar et al. 2002a; Springel and Hernquist 2002c). Both of them predict a significant star formation activity at high  $z$ , favoring the hypothesis of a gradual evolution of the comoving SFR as a function of time.

### 5.1.1 Observations

A variety of observations and observational methods have contributed during the past years to our understanding of the evolution of the star formation rate density on cosmological scales. Nonetheless, different wavelength regimes and estimation prescriptions yield rather discrepant results. In this section, the merits and flaws of each spectral range are reviewed, as well as the usual procedure to construct a consistent diagram of the SFR density as a function of redshift, also known as the 'Madau plot'.

#### Wavelength

Photometric redshift estimates based on Lyman-limit systems (Steidel et al. 1996b,a) stimulated the study of the rest frame UV continuum flux around  $2000 \text{ \AA}$  as a preferred wavelength range for objects in the far universe. This emission traces the presence of massive (and therefore young) stars and can be related directly to the actual star formation rate. It is relatively easy to detect at high  $z$  as it is redshifted into the optical band. However, older stellar populations and AGN can make a significant contribution as well, leading to an overestimation of the total SFR. On the other hand, dust enshrouding star formation regions absorb very efficiently the UV light, re-emitting it in the far IR. Unfortunately, there is still some uncertainty to account for dust extinction and its evolution with redshift (e.g. Adelberger and Steidel 2000).

Recombination lines from HII regions can be in principle a more reliable estimator of the instantaneous SFR, since the ionizing radiation ( $\lambda \leq 912 \text{ \AA}$ ) comes from more massive (younger) stars than the softer UV continuum. These optical lines are less dramatically affected by dust extinction and can be mapped with higher resolution in the local universe, but they require

infrared spectroscopy at moderate redshifts, which has not been possible until very recently due to the faintness of the sources involved (Pettini et al. 1998). For  $H_\alpha$ , this happens at  $z \sim 0.5$ , and for forbidden lines, such as [OII]3727Å, at  $z \sim 1.5$ . There is also a considerable degree of uncertainty in the relation between recombination lines and star formation activity.

Finally, the far infrared (FIR) spectrum of a galaxy can be roughly separated into two components, namely the thermal emission of dust (heated by star formation bursts) around  $\lambda \sim 60 \mu\text{m}$  and an infrared cirrus powered by the global radiation field, which dominates for  $\lambda \geq 100 \mu\text{m}$ . Neglecting cirrus and AGN contamination, the FIR luminosity would also be an excellent tracer, but instrumentation is not as developed in the IR and radio bands as it is in the optical, and the conversion factor between FIR luminosity and SFR is for the moment rather model dependent.

### The Madau plot

The first step to obtain an observational estimate of the cosmic SFR density is the selection of a *complete* sample of galaxies at a given redshift and wavelength. Some authors (e.g. Steidel et al. 1999) claim that the HDF covers a very small area ( $\sim 5 \text{ arcmin}^2$ ), and hence it is not statistically representative of the whole universe. This cosmic variance is difficult to quantify, but the strong clustering of high redshift galaxies (and the fact that most estimates beyond  $z = 2$  are based on the HDF) seems to indicate that this effect could introduce an important systematic bias in the star formation rates inferred for galaxies in the high redshift universe.

Then, the sample must be corrected for incompleteness before constructing the luminosity function, which can be done following the  $V_{\text{max}}$  formalism (Schmidt 1968) or resorting to more elaborate Monte Carlo algorithms (such as that proposed by Steidel et al. 1999). The comoving luminosity density is easily obtained by integration over all magnitudes, extrapolating the faint end as a Schechter function. The last step is to convert the LF to a star formation rate density with the help of a population synthesis model, taking into account the absorption of interstellar dust.

A compilation of recent results is given in Table 5.1, where the first column indicates the bibliographic reference, as well as the survey from which the galaxy sample was extracted. Next columns correspond to the chosen wavelength and redshifts of each analysis, and finally the comoving luminosity and SFR densities.

Conversion factors between the last two quantities differ significantly from author to author, and in some cases only the luminosity density was provided. If there is a SFR estimate in the original paper, then it is quoted in Table 5.1 *corrected by dust extinction*; else, we follow Kennicutt (1998) prescription for an exponential burst and a Salpeter IMF between 0.1 and

SURVEY	ESTIMATOR	$z$	$\log \rho_L^{\text{SCDM}}$	$\log \dot{\rho}_*$	
				SCDM	$\Lambda$ CDM
HDF (Pascarelle et al. (1998)) <sup>d</sup>	1500 Å	0.25 ± 0.25	26.47 <sup>+0.31</sup> <sub>-0.22</sub>	-1.38	-1.36
		0.75 ± 0.25	26.61 <sup>+0.23</sup> <sub>-0.14</sub>	-1.24	-1.26
		1.25 ± 0.25	26.80 <sup>+0.24</sup> <sub>-0.12</sub>	-1.05	-1.10
		1.75 ± 0.25	26.83 <sup>+0.24</sup> <sub>-0.12</sub>	-1.02	-1.08
		2.50 ± 0.50	26.62 <sup>+0.28</sup> <sub>-0.21</sub>	-1.23	-1.30
		3.50 ± 0.50	26.59 <sup>+0.34</sup> <sub>-0.27</sub>	-1.26	-1.34
		4.50 ± 0.50	26.70 <sup>+0.44</sup> <sub>-0.37</sub>	-1.15	-1.23
		5.50 ± 0.50	26.34 <sup>+0.59</sup> <sub>-0.38</sub>	-1.51	-1.59
HDF (Madau et al. (1998)) <sup>d</sup>	1500 Å	2.75 ± 0.75	26.90 ± 0.15	-0.95	-1.02
		4.00 ± 0.50	26.50 ± 0.20	-1.35	-1.43
(Steidel et al. (1999))	1700 Å	3.04 ± 0.35	27.04 ± 0.07	-0.81	-0.89
		4.13 ± 0.35	26.95 ± 0.10	-0.90	-0.98
(Treyer et al. (1998)) <sup>d</sup>	2000 Å	0.15 ± 0.15	26.45 ± 0.15	-1.40	-1.35
CFRS (Lilly et al. (1996)) <sup>d</sup>	2800 Å	0.35 ± 0.15	26.14 ± 0.07	-1.71	-1.68
		0.625 ± 0.125	26.46 ± 0.08	-1.39	-1.39
		0.875 ± 0.125	26.78 ± 0.15	-1.07	-1.10
HDF (Cowie et al. (1999)) <sup>d</sup>	2800 Å	0.35 ± 0.15	25.91 ± 0.12	-1.69	-1.66
		0.625 ± 0.125	26.15 ± 0.12	-1.45	-1.45
		0.875 ± 0.125	26.06 ± 0.12	-1.54	-1.57
		1.25 ± 0.25	26.35 ± 0.10	-1.25	-1.30
HDF (Connolly et al. (1997)) <sup>d</sup>	2800 Å	0.75 ± 0.25	26.77 ± 0.15	-1.08	-1.10
		1.25 ± 0.25	26.94 ± 0.15	-0.91	-0.96
		1.75 ± 0.25	26.84 ± 0.15	-1.26	-1.32
HDF (Sawicki et al. (1997)) <sup>d</sup>	3000 Å	0.35 ± 0.15	26.51 ± 0.47	-1.34	-1.31
		0.75 ± 0.25	26.74 ± 0.06	-1.11	-1.13
		1.50 ± 0.50	26.93 ± 0.05	-0.92	-0.97
		2.50 ± 0.50	27.28 ± 0.06	-0.57	-0.64
		3.50 ± 0.50	26.91 ± 0.10	-0.94	-1.02
(Gallego et al. (1995))	H $\alpha$	0.025 ± 0.025	39.09 ± 0.04	-2.01	-1.89
CFRS (Tresse and Maddox (1998))	H $\alpha$	0.2 ± 0.1	39.44 ± 0.04	-1.66	-1.60
CFRS (Glazebrook et al. (1999))	H $\alpha$	0.875 ± 0.125	40.01 ± 0.15	-0.91	-0.94
(Yan et al. (1999))	H $\alpha$	1.3 ± 0.5	40.21 ± 0.13	-0.89	-0.94
CFRS (Hammer et al. (1997)) <sup>d</sup>	OII 3727 Å	0.35 ± 0.15	38.63 <sup>+0.06</sup> <sub>-0.08</sub>	-1.97	-1.94
		0.625 ± 0.125	39.16 <sup>+0.11</sup> <sub>-0.15</sub>	-1.44	-1.44
		0.875 ± 0.125	39.56 <sup>+0.20</sup> <sub>-0.38</sub>	-1.04	-1.07
CFRS (Flores et al. (1999))	15 $\mu$ m	0.35 ± 0.15	41.97 ± 0.25	-1.46	-1.43
		0.625 ± 0.125	42.20 ± 0.25	-1.15	-1.15
		0.875 ± 0.125	42.53 ± 0.25	-0.82	-0.85
HDF (Hughes et al. (1998))	60 $\mu$ m	3.0 ± 1.0	< 42.26	-0.98	-1.05
(Haarsma et al. (2000))	1.4 GHz	0.28 ± 0.12	26.75 <sup>+0.14</sup> <sub>-0.21</sub>	-1.17	-1.13
		0.46 ± 0.05	27.03 <sup>+0.24</sup> <sub>-0.21</sub>	-0.89	-0.87
		0.60 ± 0.05	27.12 <sup>+0.16</sup> <sub>-0.26</sub>	-0.80	-0.80
		0.81 ± 0.08	27.39 <sup>+0.13</sup> <sub>-0.18</sub>	-0.53	-0.55
		1.60 ± 0.64	27.54 <sup>+0.13</sup> <sub>-0.18</sub>	-0.38	-0.44

TABLE 5.1: Observational estimates of the cosmic SFR density at different epochs.  $\rho_L$  refers to the luminosity density at the appropriate wavelength, expressed in  $\text{erg s}^{-1}\text{Hz}^{-1} \text{Mpc}^{-3}$ .  $\dot{\rho}_*$  represents the comoving SFR density (in  $M_\odot \text{yr}^{-1} \text{Mpc}^{-3}$ ) for our SCDM and  $\Lambda$ CDM cosmologies. <sup>d</sup> Original data has been corrected for dust extinction.

100  $M_{\odot}$ :

$$\dot{\rho}_* [M_{\odot} \text{ yr}^{-1}] = \begin{cases} 1.4 \times 10^{-28} L_{\text{UV}} [\text{erg s}^{-1} \text{Hz}^{-1}] \\ 1.4 \times 10^{-41} L_{3727} [\text{erg s}^{-1} \text{Hz}^{-1}] \end{cases} \quad (5.1)$$

For dust extinction, we have applied a correction of  $A(1500\text{-}2000\text{\AA})=1.2$  mag and  $A(2880\text{\AA},\text{OII})=0.625$  mag, which correspond to factors of 3.02 and 1.78 respectively. All modifications to the original data are noted by a footnote mark on the bibliographic reference in Table 5.1.

### Cosmology

Most observational values given in Table 5.1 were calculated assuming a standard cold dark matter (SCDM) cosmology with dimensionless Hubble parameter  $h = 0.5$  and mean matter density  $\Omega_m = 1$ . Since the conversion factor from luminosity to SFR and the correction for dust extinction are completely independent of the cosmological scenario, the computation of the comoving SFR density in a  $\Lambda$ CDM ( $h = 0.7$ ) model only involves the transformation of the luminosity densities.

In a flat universe, the volume enclosed by a solid angle  $\Delta\omega$  between  $z - \Delta z$  and  $z + \Delta z$  is

$$V(z, \Delta z) = \frac{4\pi}{3} \Delta\omega (d_m^3(z + \Delta z) - d_m^3(z - \Delta z)), \quad (5.2)$$

where  $d_m(z)$  is the comoving distance. Luminosity scales with luminosity distance,  $d_L(z) = (1+z)d_m(z)$ , as  $d_L^2$ . Then, assuming that all galaxies are located at the center of the interval in  $z$ , the luminosity density (and hence the total SFR density) will be proportional to

$$\dot{\rho}_*(z) \propto \frac{L(z)}{V(z, \Delta z)} \propto \frac{d_m^2(z)}{d_m^3(z + \Delta z) - d_m^3(z - \Delta z)} \quad (5.3)$$

The conversion between SFR densities in  $\Lambda$ CDM and variants of the SCDM ( $h = 0.5$ ) cosmologies can be approximated, to first order in  $\Delta z$ , as

$$\frac{\dot{\rho}_*^{\Lambda\text{CDM}}}{\dot{\rho}_*^{\text{SCDM}}} \sim \frac{h^{\Lambda\text{CDM}}}{h^{\text{SCDM}}} \sqrt{\Omega_m + \Omega_{\Lambda}(1+z)^{-3}} \quad (5.4)$$

Figure 5.1 shows this factor, as well as the exact expression for different values of  $\Delta z$ , which requires a numerical evaluation of the luminosity distance in the  $\Lambda$ CDM model. Although the results are very similar, we have chosen to use the exact expression (5.3) to compute the SFRs in Table 5.1 in order to minimize errors.

At low redshifts, the data are consistent for all the independent tracers of the star formation activity once the effect of dust obscuration is taken into account. The steep increase in the cosmic SFR density from the present

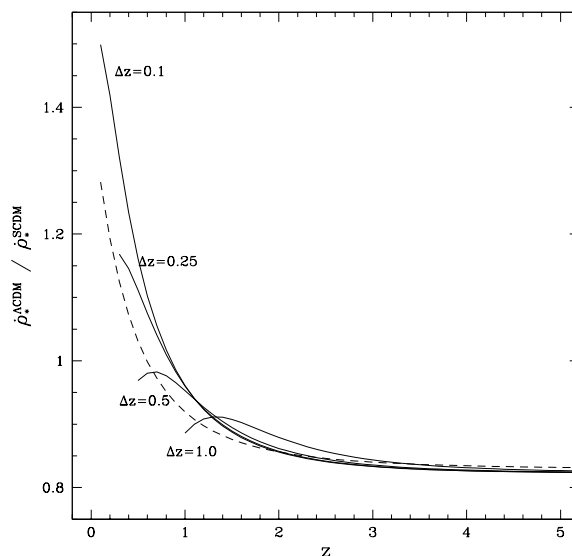


FIGURE 5.1: Conversion factor between star formation densities in SCDM and  $\Lambda$ CDM cosmological models, for several redshift intervals  $\Delta z$ . Dashed line corresponds to the approximation (5.4).

day to  $z \sim 1$  is firmly established. However, there is not yet a full agreement on whether there is a characteristic epoch of star formation in the universe around  $z \sim 1.5$  or, on the contrary, the SFR declines very slowly towards higher  $z$ , as more recent observations seem to point out. The results of ongoing deep surveys will be extremely helpful in order to reach a definitive conclusion from the observational point of view.

### 5.1.2 Simulations

In order to study the cosmic star formation history, several simulations have been accomplished using the Eulerian gasdynamical code YK<sup>3</sup> (succintly described in Section 2.1.1), which incorporates a simple physically motivated model to implement star formation and feedback into the ISM. Our aim was to investigate the separate effects of cosmology, supernova explosions and photoionisation on the self-regulation of the star formation activity. For details on the numerical experiments, the reader is referred to Section 2.3.3.

### Cosmology

Three different cosmological scenarios have been considered in the present study: the currently-favoured  $\Lambda$ CDM universe, the 'old-fashioned' standard CDM model, and a modified version of the latter: The Broken Scale In-

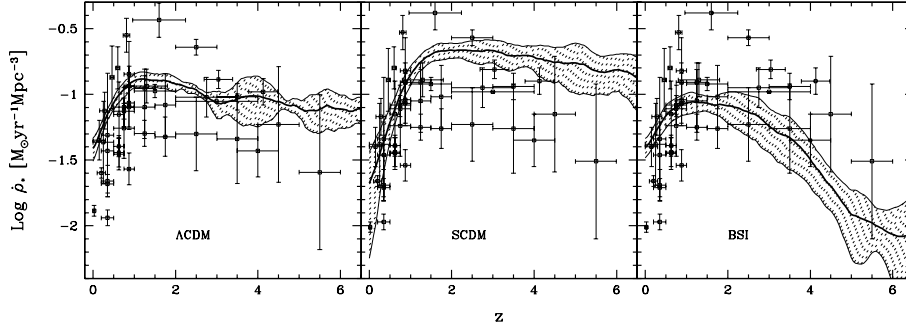


FIGURE 5.2: Evolution of the comoving SFR density in different cosmologies (experiments  $\Lambda$ CDM5, SCDM and BSI). The average value over different realizations is plotted as a thick solid line, while the shaded area represents the  $1\sigma$  deviation from the mean. Dots correspond to the observational data points listed in Ascasibar et al. (2002a)

variance (BSI) model which is based on a double inflation scenario (see e.g. Kates et al. 1995, for a description). The post-recombination power spectrum of the BSI model is similar to that of the  $\tau$ CDM scenario, in which the dark matter consists of a decaying neutrino. The global star formation histories found in our simulations of each one of those three cosmologies are compared in Figure 5.2. A crucial factor is the initial normalisation of the power spectrum, since this parameter sets the amount and evolution of substructure, and therefore represents one of the key ingredients in determining the rate of cooling and subsequent conversion of gas into stars.

Cosmological scenarios with CDM alone cannot explain structure formation on both small and very large scales. However, we have included SCDM as a reference model in our comparison. Due to its large power at small scales, this scenario produces many structures at high redshift, and so it features a flat star formation rate even beyond  $z \sim 6$ , with a plateau about one decade over the observations (Figure 5.2, middle panel). It does not seem very likely that this difference can be explained by dust absorption alone. In this model, too many baryons are transformed into stars, and it happens too early with respect to observations. We claim that the cosmic star formation history poses an additional problem for the SCDM model.

On the contrary, the BSI model leads to a clear maximum in the SFR at  $z \sim 2$ , but the absolute value is too small and the decrease at higher redshifts is clearly too steep (Figure 5.2, right). This model has not enough power at small scales for producing enough stars at high redshift. As a side effect, the cosmic star formation rate density remains too high at low redshifts, since a large part of cold gas remains in high density regions triggering further star formation activity.

A cosmological model with non-zero cosmological constant offers the best agreement with observations (Figure 5.2, left). Both the overall trend and

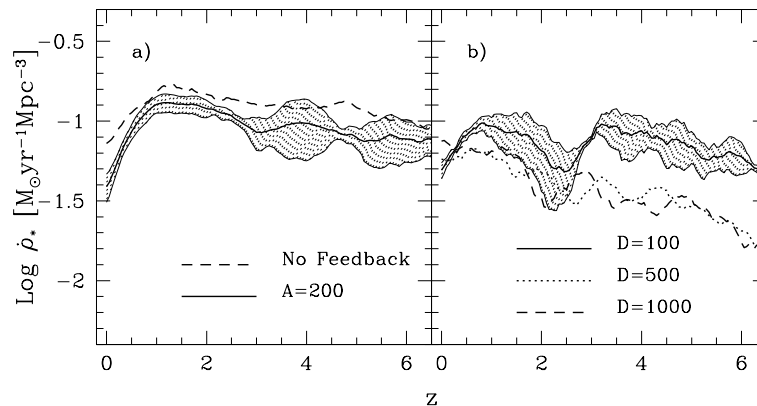


FIGURE 5.3: Effects of stellar feedback on the cosmic SFR density. a)  $\Lambda$ CDM5 simulations with supernova feedback parameter  $A = 200$  (solid line) within  $1\sigma$  error (shaded area) and  $A = 0$  (dashed line). b) Same as (a) but for  $\Lambda$ CDM4 simulations run with different values of the overdensity threshold  $D$  imposed by photoionization.

the height of the plateau fit reasonably well the observational data points. At present, the  $\Lambda$ CDM model fits best all known observational data (see e.g. Bahcall et al. 1999). Our results confirm that this model can also reproduce the observed star formation history of the universe when dust extinction is taken into account, in which case a significant amount of star formation is expected to take place at high redshift.

A further feature, common to all cosmologies, is the smooth redshift dependence of the mean SFR and the small range of scatter. This is in sharp contrast to the evolution of individual baryonic clumps or the behavior of different regions in a single time-step of the simulation. There, we observe huge bursts of star formation (with an increase in activity by a factor of 10 and higher with respect to the average value), as well as a quiescent regime in which the star formation rate remains approximately constant.

In these simulations, the first stars are created around  $z \sim 10$ , which seems to be not too unrealistic, but it may depend on resolution. This was not a primary issue of the present study.

### Feedback

Figure 5.3 shows the results of experiments  $\Lambda$ CDM5 and  $\Lambda$ CDM4, from where the effects of supernova feedback and photoionization were studied. The same trends described in this section were also seen in SCDM and BSI simulations.

Supernovae (left panel of Figure 5.3) play a key role in the slope of the SFR density at low  $z$ . Gas heating and evaporation act as a self-regulating mechanism that inhibits subsequent gas infall when many new stars are

formed. This is specially important in the most massive objects, which show a much higher star formation activity when feedback is not implemented.

In addition, supernova explosions can also blow away the gas reservoirs of dwarf galaxies. The effect on the global star formation rate is more noticeable at high redshift, when there are still very few galaxies massive enough to retain the heated gas within their gravitational potentials. However, photoionization (right panel) is the dominant effect at very early epochs, preventing the gas from cooling and forming stars in low density regions (Efstathiou 1992). As we have discussed in Section 2.1.1, the model implemented in YK<sup>3</sup> takes into account this effect through the overdensity threshold parameter  $\mathcal{D}$  for star formation. Only in regions denser than  $\mathcal{D}$ , molecular clouds will be able to form, and the onset of cosmic star formation activity is thus retarded until objects become dense enough to screen the photoionizing background.

We found a SFR density consistent with observational data for  $\mathcal{D} \sim 100$ . This is in roughly agreement with results from a more detailed theoretical estimate of the same parameter (Muecket and Kates 1997), although in that case the actual value of  $\mathcal{D}$ , as well as the temperature range in which thermal instability is an efficient process, depend on the local gas density and the intensity of the ionizing flux.

### Resolution and volume

Star formation and feedback processes are incorporated in gasdynamical simulations (either SPH or Eulerian) by means of rather simple recipes which pretend to *extrapolate* the effects of local physics acting on scales several orders of magnitude below the resolution limit (often at kpc or even higher, see Table 2.5 for these simulations). In the algorithm implemented in YK<sup>3</sup>, part of this extrapolation is hidden in two parameters: The supernova feedback parameter  $A$  and the overdensity threshold for star formation  $\mathcal{D}$ . Whether this parameterization is a reasonable extrapolation of the underlying sub-grid physics depends on the stability of the results against changes in spatial resolution of the simulations.

On the other hand, when one tries to estimate cosmological averaged quantities, like the SFR density, it is necessary to check for deviations of these quantities due to small number statistics. In the case that matters here, a volume averaged quantity, the *cosmic variance* can have a relatively large contribution in the particular determination of the comoving SFR density. Thus, we have simulated different volumes with similar resolutions, depending on the computational facilities at our disposal.

To check for these two effects we compare in Figure 5.4 our results for  $\Lambda$ CDM simulations with different resolutions and volumes. The most noticeable feature that can be observed in this figure is the steeper slope of the local SFR for larger volume simulations. As we increase the volume, larger



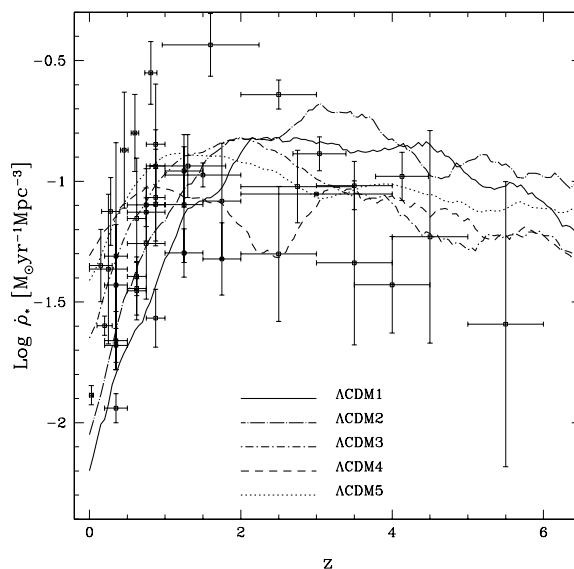


FIGURE 5.4: Comoving SFR in our 5  $\Lambda$ CDM experiments, all with  $A = 200$  and  $\mathcal{D} = 100$ . A significant star formation activity is found at high  $z$  regardless of resolution and volume. This is consistent with the full set of observational data points (Table 5.1).

structures are being simulated (i.e. clusters), in which the star formation activity is significantly reduced during recent epochs. In simulations with smaller volumes, most of the galaxies that form are either isolated or in small groups, and hence have a completely different star formation activity. The effects of environment on the SFR are investigated in more detail in the next section.

If this trend we found in our simulations is indeed real, we can conclude that the effect of cosmic variance might be quite important in the quantitative estimation of the SFR in the nearby universe, and hence it seems very likely that it must be taken into account in the determination (either numerical or observational) of the evolution of the cosmic star formation rate density from  $z \geq 1$  to the present.

Although we do not find significant differences in our estimates of the SFR density from simulations with different spatial resolutions, there is a general trend to have more SFR density at early times in the highest resolution experiments. This is a consequence of the overcooling problem (see e.g. Balogh et al. 2001, for a recent review), and it is directly related to the increasing number of low-mass halos resolved in these simulations, particularly at high redshift. A detailed analysis of this question would require a more realistic treatment of photoionization than the simplistic prescription of an overdensity threshold for star formation.

EXPERIMENT	$\rho_*(z = 0)$	$\rho_*(z = 3)/\rho_*(0)$
$\Lambda$ CDM1	6.50	0.252
$\Lambda$ CDM2	8.60	0.243
$\Lambda$ CDM3	9.51	0.115
$\Lambda$ CDM4	9.01	0.116
$\Lambda$ CDM5	10.9	0.119
SCDM	12.3	0.115
BSI	7.37	0.041

TABLE 5.2: Present star density (in  $10^8 h M_\odot \text{Mpc}^{-3}$ ) and fraction of stars older than  $z = 3$  for the different numerical experiments.

Keeping all these considerations in mind, we should be extremely cautious when making *quantitative* estimates of the cosmic SFR density at any given  $z$ . However, this quantity shows a similar behavior in all  $\Lambda$ CDM experiments. This is a very promising result indicating that its *qualitative* evolution (i.e. the shape of the curve) is a robust prediction of our simulations. More precisely, we claim that no characteristic epoch of cosmic star formation is found for a  $\Lambda$ CDM universe. The comoving SFR density increases with lookback time until it reaches a nearly constant mean plateau beyond  $z = 2$ . Stars probably formed gradually at high redshift, according to most recent observations and taking dust extinction into account. At some point around  $z \sim 1$ , the global star formation activity would have declined sharply until the present day, although individual SFRs of active galaxies are kept approximately constant.

The star density  $\rho_*(z)$  shows a similar behavior for both CDM and  $\Lambda$ CDM models. The most remarkable difference is found in the present value of  $\rho_*(0)$  (see Table 5.2), which can be observationally deduced from the local luminosity density, assuming a constant mass-to-light ratio (e.g. Madau et al. 1996; Fukugita et al. 1998):

$$\rho_*^{\text{obs}}(0) \sim 7 \times 10^8 h M_\odot \text{Mpc}^{-3} \quad (5.5)$$

Based on the fraction of stars in bulges, ellipticals and S0s, Renzini (1998) estimated that about 30% of the stellar content of the universe should have already been formed by  $z = 3$ , regardless of the cosmological model. The amount of stars produced in experiments  $\Lambda$ CDM1 and 2 (Table 5.2), both at  $z = 3$  and  $z = 0$ , are in fair agreement with the observationally derived values for these quantities. For the other experiments, the fraction of stars older than  $z = 3$  is significantly lower, not only because of a low star formation activity at high redshift, but also due to a higher SFR in the local universe, as well as to the cosmic bias towards low-density regions introduced by the small simulated volumes.

These results have been recently confirmed by Springel and Hernquist (2002c) who estimated the cosmic star formation history in the  $\Lambda$ CDM model using a similar prescription for star formation and feedback in the GADGET code. Through a series of simulations with different resolutions and volumes, they claim to have found stable results from the numerical point of view. The general features of the cosmic star formation history found by these authors are similar to those reported in Ascasibar et al. (2002a). Although systematically lower, their SFR density is marginally consistent with observational estimates. The reason for this discrepancy could be attributed to the extreme feedback model they have used in their simulations.

## 5.2 Star formation in clusters of galaxies

In the hierarchical scenario of structure formation, the first cosmological objects are expected to collapse around the highest overdensity peaks, merging until they eventually form the giant ellipticals in the centers of clusters and the bulges of the most massive isolated galaxies. These objects contain the vast majority of stars older than  $z = 3$ , and hence their star formation history must be completely different from that of galaxies living in less dense environments.

The strong morphology segregation observed in rich galaxy clusters (e.g. Dressler 1980) testifies the fundamental role played by the environment on the evolution of galaxies. Yet, the physical mechanisms responsible for such transformations are still a matter of debate. Several processes might alter the star formation conditions in cluster galaxies. Some are related to the interaction with the intracluster medium (a fact already pointed out by Gunn and Gott 1972) and others account for the effects of tidal forces due to the gravitational potential of the cluster (Merritt 1983) or galaxy-galaxy interactions (Moore et al. 1996, 1998b, 1999a). All these mechanisms can produce strong perturbations in the galaxy morphology, which include the formation of tidal tails, dynamical disturbances that appear as asymmetries in the rotation curves (Dahle et al. 2001) and significant removal of the diffuse gas (Giovanelli and Haynes 1985; Valluri and Jog 1990; Quilis et al. 2000)<sup>1</sup>.

Most of these processes are expected to change significantly the star formation activity of galaxies in clusters. Several studies have addressed the

---

<sup>1</sup>In this regard, our simulations of clusters of galaxies described in previous chapters give also an indication that gas stripping is a very important phenomenon to inhibit star formation in cluster galaxies. We do observe that most of the small halos that orbit the cluster potential do lose their gas very fast. A visual impression of this phenomenon can be seen from a series of animations done from one of our SPH cluster simulations. They can be accessed from the following web page <http://pollux.ft.uam.es/gustavo/VIDEOS/LCDM80/clustervideo.html> We plan to do a detailed quantitative study of this effect in the near future.

issue of the influence of the cluster environment on the SFR of disk galaxies, but no agreement has been established so far: whereas some authors proposed similar or even enhanced star formation in cluster spirals than in the field, some others claim quenched SFRs in cluster spirals. This discrepancy could arise from non-uniformity of the adopted methods and wavelengths or from real differences in the studied clusters.

If the star formation rates are reduced when galaxies are accreted into larger groups or clusters, the cosmological implications could be profound, since approximately 30–40% of the present-day galaxies are observed not to be isolated (e.g. Carlberg et al. 2001, and references therein), in agreement with the results found in numerical models (e.g. Gottlöber et al. 2001). As structure builds up in the universe, more and more galaxies can be found in groups and, if these environments serve to terminate star formation, it will be clearly reflected in the evolution of the universe as a whole, explaining part of the observed decline in the global SFR at recent epochs.

### 5.2.1 Observations

The effect of local environment on galaxy evolution in general is not well understood. Many observational studies of environmental effects have been devoted to the study of galaxies in the cores of rich clusters, which differ so dramatically from more common galaxies (e.g. Dressler 1980; Dressler et al. 1985; Couch and Sharples 1987; Balogh et al. 1997, 1999; Poggianti et al. 1999; Moss and Whittle 2000; Couch et al. 2001; Solanes et al. 2001). In particular, Balogh et al. (1997, 1998) showed that the mean cluster galaxy star formation may be suppressed as far as twice the virial radius from the cluster center, relative to a field sample with similar bulge-to-disk ratios, physical disk size, and luminosity, which suggests that the observed decrease in the SFR may not be fully explained by the morphology-density relation.

This conclusion has also been suggested by (Hashimoto et al. 1998), who studied the relation between local galaxy density and star formation activity in the Las Campanas Redshift Survey, and similar results have been obtained in more recent studies based on the 2dF Galaxy Redshift Survey (Lewis et al. 2002b) and the Early Data Release of the Sloan Digital Sky Survey (Gomez et al. 2002).

From a wide field photometric survey using the SUBARU telescope, Kodama and Smail (2001) reported the detection of an abrupt change in the colours of galaxies at a 'critical' projected surface density of  $\sim 200 h_{75}^{-2}$  gal. Mpc $^{-2}$ . This corresponds to a radial distance of  $\sim 1 h_{75}^{-1}$  Mpc from the cluster center. Such a 'break' has been confirmed by the SFRs derived from the SDSS Gomez et al. (2002), although it occurs at an order of magnitude lower surface density, i.e. at a larger clustercentric radius. Further observations are needed in order to discern whether this difference is physical (i.e. due to the differences in redshift or luminosity limits of both studies) or an

artifact due to the specifics of the analysis techniques.

In any case, the 'critical' density (or radius) where the star formation rate of galaxies is found to change from that of the field seems to be well beyond the virialised regions of clusters of galaxies. Since the mechanisms that alter the SFR in the cores of rich clusters, e.g. ram-pressure stripping (Gunn and Gott 1972; Quilis et al. 2000), galaxy harassment (Moore et al. 1999a), or tidal disruption (Byrd and Valtonen 1990), are unlikely to be important at low overdensities, these results point in the direction that the SFR is significantly reduced due to close interactions in less massive groups within the infall region of clusters (Zabludoff et al. 1996; Zabludoff and Mulchaey 1998; Gomez et al. 2002, e.g.).

In this scenario, environmental effects associated to hierarchical structure formation could be responsible for some of the observed decline in the cosmic SFR from  $z \sim 1$  to the present. Results from the SDSS (Gomez et al. 2002) seem to support this view, indicating that the break in the SFR-density relation corresponds approximately to the turn-around radius of the studied clusters (a few times  $r_{200}$ ), which roughly marks the limit of the gravitational influence of the dark matter halo, but is too large for the ICM gas to have any significant influence on the infalling galaxies.

Although Lewis et al. (2002b) found that the relation between SFR and local density was independent on the cluster velocity dispersion and presumably mass, a spectral analysis of galaxy groups in the 2dFGRS accomplished by Martínez et al. (2002) concludes that even the environment of low mass-systems ( $M \sim 10^{13} M_{\odot}$ ) is effective in diminishing the process of star formation in their member galaxies, but the fraction of spectral types associated to star forming galaxies decreases with group virial mass. Furthermore, Balogh et al. (2002) have also found some evidence that the morphology-density relation is correlated with the cluster X-ray luminosity.

To evaluate the contribution of clusters of galaxies to the current star formation rate density, Iglesias-Páramo et al. (2002) computed the  $H\alpha$  luminosity function of the central regions of two nearby clusters, obtaining the total SFR per unit volume of the member galaxies. Multiplying by the cluster density in the universe (Bramel et al. 2000), these authors conclude that the SFR in type 2 and type 1 clusters can account for approximately 0.25% and 10.8% of the cosmic stellar production at  $z = 0$ , respectively.

### 5.2.2 Simulations

The environmental effects on the star formation activity that can be seen in numerical experiments are due to differences in merging history and removal of the hot gas reservoir that surrounds every isolated galaxy. In semi-analytical models (e.g. Kauffmann et al. 1993b; Somerville and Primack 1999; Cole et al. 2000), it is assumed that this supply of fresh fuel for star formation is lost when galaxies are accreted into larger haloes. Therefore, in this

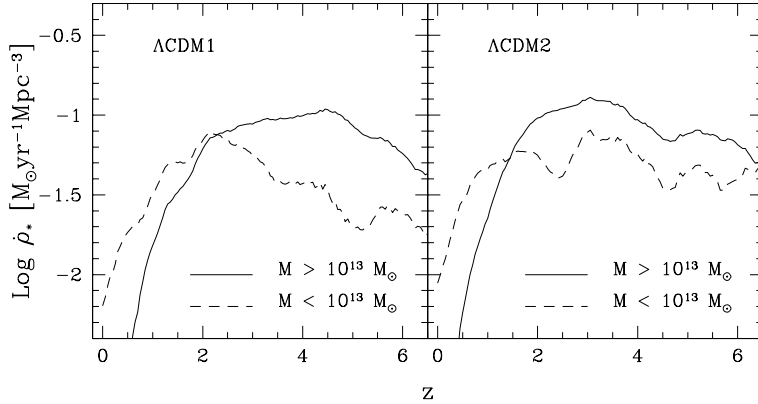


FIGURE 5.5: Star formation rate densities in models  $\Lambda$ CDM1 and  $\Lambda$ CDM2 due to halos more (solid lines) and less (dashed lines) massive than  $10^{13} M_{\odot}$  at  $z = 0$ .

simple scheme, star formation rates begin to decline for any satellite galaxy, whether in a poor group or in a rich cluster.

Although these models are able to successfully match some of the observed trends, such as the radial gradients in SFR within the virial radius of clusters (Balogh et al. 2000; Diaferio et al. 2001; Okamoto and Nagashima 2001), they lack at present the capability to explore how galaxies lose their gas (see e.g. Bekki et al. 2002). One strength of numerical simulations is that they address the problem from first principles, making it possible to constrain the contribution of the proposed mechanisms acting on the SFR, as well as the role played by different environments in galaxy formation and evolution.

Gottlöber et al. (2001) have studied the merging history of dark matter halos as a function of their environment, finding that haloes located inside clusters have formed earlier than isolated objects of the same mass. Moreover, they showed that at higher redshifts ( $z \sim 1 - 4$ ), progenitors of cluster and group galaxies have 3–5 times higher merger rates than isolated galaxies. Mergers of galaxies are thought to play a crucial role in the evolution of the SFR. In particular, the inflow of material may serve as a source of high-density gas and therefore increase the star formation activity.

Amongst all the numerical experiments we have accomplished with YK<sup>3</sup>, only  $\Lambda$ CDM 1 and 2 sample a volume large enough to contain clusters and groups of galaxies.

In Figure 5.5 we plot the contribution to the cosmic SFR density due to the progenitors of present-day objects, according to the mass at  $z = 0$ . The stellar production of objects that end up in haloes more massive than  $10^{13} M_{\odot}$  at present (clusters, large groups) are plotted as solid lines, whereas the SFR density of those that are in less massive objects at the end of the simulation (isolated galaxies or small groups) is shown by the dashed lines.

The most massive objects have their peaks of star formation activity around  $z \sim 3$ , undergoing passive evolution since  $z \sim 2$ . This is in excellent agreement with the merging history found by Gottlöber et al. (2001) from N-body simulations. The progenitors of these objects were responsible for the bulk of star formation at high redshift, and could be very likely associated with the Lyman Break Galaxy population.

On the other hand, galaxies that are isolated at  $z = 0$  or galaxies residing in small groups tend to be much younger. In agreement with the results of Iglesias-Páramo et al. (2002), these objects are responsible for most of the current stellar production. In these low-density areas, halos massive enough to retain their gas content display a nearly constant SFR with sporadic burst episodes.

Unfortunately, the simulated volume in these numerical experiments is too small to be cosmologically representative. In fact, the larger volume covered by  $\Lambda$ CDM1 contains only one galaxy cluster of approximately  $3 \times 10^{14} M_{\odot}$ , whereas the simulation  $\Lambda$ CDM2 contains four massive groups of about  $5 \times 10^{13} M_{\odot}$ . Comparing the solid lines in the left and right panels of Figure 5.5, we find qualitatively the expected scenario: the peak of star formation in the progenitors of the more massive cluster happened earlier (at  $z \sim 4.5$ ) than for the less massive groups ( $z \sim 3$ ). This lends some support to the claim that the effect of environment on the SFR of infalling galaxies is related to the group mass (Martínez et al. 2002) or luminosity (Balogh et al. 2002).

As we have seen in Section 5.1.2, photoionization and supernova explosions inhibit cooling and star formation in very low-mass objects, providing a physical mechanism to suppress the over-cooling of gas at very early epochs. Thus, the formation of the first stars is biased towards high overdensity regions that will collapse later to form the cores of the present-day galaxy clusters. As their hierarchical assembly proceeds, the gas component of these objects is heated by shock waves produced during mergers, and the cooling times become too long for efficient star formation to take place. Consequently, the SFR drops drastically once the initial reservoir of cold gas has been exhausted.

At the same time, new galaxies will form and produce stars. Some of them will remain in rather isolated areas until present (dashed lines in Figure 5.5) and some others will fall recently into the potential wells of the clusters. It seems very likely that tidal interactions trigger intense star formation bursts in these infalling galaxies (e.g. Lavery and Henry 1988).

Observations and simulations coincide in pointing out that star formation activity in galaxies located in dense cluster environments decays (or even stops). Thus, their colours become redder, giving rise to the Butcher and Oemler (1978) effect. Moreover, these objects are expected to experience many close encounters and sometimes mergers with neighbouring cluster galaxies, which could explain their morphological transformation

from an initial spiral Hubble type into the S0 population that is observed to dominate the inner regions of clusters (Dressler et al. 1997). In fact, our high resolution simulations of cluster formation done with GADGET show that dark matter sub-haloes orbit many times in the cluster potential, losing most of their gas envelope, but with keeping most of their dark matter content<sup>2</sup>.

---

<sup>2</sup>see <http://pollux.ft.uam.es/gustavo/VIDEOS/LCDM80/clustervideo.html> for detailed animation of dark subhalo orbiting within the cluster potential



## Chapter 6

# Conclusions and future prospects

*So here we are again to experience the bitter, scalding end  
and we're the only ones who can perceive it  
But others sing of beauty and the story that's unfolded  
as one that deserves praise and ritual*

– Bad Religion : *Pessimistic Lines* (1988) –

### 6.1 Conclusions

**F**rom a set of numerical experiments, using different codes and initial conditions, we have been able to compile a database of numerical galaxy clusters. High resolution (spatial and mass) has been achieved in selected areas of the computational box by means of refinement techniques. The simulations were carried out within the framework of the  $\Lambda$ CDM cosmological scenario, which is the most favoured by current observational data. The initial realisation was equivalent to a set-up with  $1024^3$  homogeneous particles.

From our cluster database, we have been able to study the physical properties of both the dark and baryonic components. Most of the work accomplished for the present thesis focuses on the analysis of the simulated clusters at  $z = 0$ . Below we summarise the major conclusions that can be derived from the results of this analysis.

#### 6.1.1 Dark matter

1. Numerical predictions about the dark matter distribution are robust within the resolution limits. ART and GADGET give consistent results. Perturbations to the dark matter potential due to the presence of

baryons are negligible on cluster scales when only adiabatic physics is taken into account.

2. From a sample of 15 clusters, 6 have been catalogued as relaxed systems, 4 as minor mergers and 5 as major mergers. The amount of dynamical activity is significantly higher in the low-mass end of the sample, in agreement with the expectation from hierarchical assembly.
3. There are systematic differences between the inner profiles of our numerical clusters according to their dynamical state. Relaxed clusters are better described by the profile proposed by Navarro et al. (1997), while minor mergers are closer to the form advocated by Moore et al. (1999b). Major mergers follow a pure power-law distribution for more than one order of magnitude in radius; their profiles are even steeper than  $\rho \propto r^{-1.5}$ .
4. The logarithmic slope of the mass profile of relaxed haloes does not reach any asymptotic slope at our resolution limit. Indeed, it seems to increase above the NFW value for small enough radii. More resolution is needed in order to verify this conclusion.
5. Merging systems are systematically more extended than relaxed clusters. This effect completely disrupts the usual  $c - M_{200}$  relation, although some correlation is still found in the  $\rho_s - r_s$  plane. The best-fit values of these parameters are consistent with those inferred from observations.
6. The phase-space density of our clusters is well fitted a power-law  $\rho/\sigma^3 = 2.24 \times 10^4 r^{-1.875}$ , similar to that found by Taylor and Navarro (2001) for galaxy-size haloes.
7. We find no clear evidence of a 'universal' profile of the anisotropy parameter  $\beta \equiv 1 - \sigma_\theta^2/\sigma_r^2$ . Although there are hints of some average trend, the scatter shown by individual profiles is extremely high. An isotropic velocity field ( $\beta = 0$ ) can be confidently ruled out in relaxed clusters and minor mergers.
8. Angular momentum grows roughly proportional to  $r$  in our clusters, in agreement with previous numerical work. Rotational support from bulk rotation is negligible with respect to the contribution of random motions. The eccentricity of individual particle orbits is approximately  $e = 0.5$  throughout the whole cluster, but two of our objects deviate from this behaviour.
9. The inclusion of angular momentum and the choice of the initial conditions are the most delicate issues concerning the spherical infall model. Our clusters are very well described by  $\sim 3\sigma$  peaks of the density field,

smoothed on  $\sim 1 h^{-1}$  Mpc scales, when the eccentricity of the orbits is fixed to  $e = 0.5$ .

### 6.1.2 Gas

1. We find additional evidence of non-physical entropy losses in the standard implementation of the SPH algorithm. This effect can be of critical importance in the computation of the entropy profiles in groups and clusters of galaxies. The new formulation of SPH proposed by Springel and Hernquist (2002a) seems to overcome this problem; high-resolution simulations accomplished with this code are consistent with the results of the Eulerian code ART. An excessively low number of particles can produce an isentropic core due to numerical effects.
2. The assumption of hydrostatic equilibrium is justified for the clusters classified as 'relaxed' on dynamical grounds, although some deviations occur in the outer parts of the cluster. It holds only marginally for minor mergers, and not at all for systems undergoing a major merging event.
3. A polytropic equation of state with  $\gamma \sim 1.18$  provides a good description of the ICM gas. Only major mergers deviate from a polytropic relation.
4. Under the assumptions of hydrostatic equilibrium, polytropic equation of state, a universal profile for the dark matter, and constant baryon fraction at large radii, the temperature profile is *determined* by the underlying dark matter distribution. Our results are consistent with Komatsu and Seljak (2001), who follow a slightly different prescription. The temperature profile derived from a NFW profile provides an excellent fit to the simulation data.
5. Projected X-ray temperature profiles are very similar to those observed in real clusters. Although the situation is less clear in the inner regions, probably in connection with non-adiabatic phenomena, an isothermal temperature profile can be ruled out both on observational and theoretical grounds. Our data is very well fitted by the formula proposed by Loken et al. (2002), but no agreement is found regarding the best-fit values of the free parameters.
6. The density profile of the ICM gas can also be derived by the procedure outlined above (4). Again, it is *entirely* determined once the parameters describing the dark matter halo are known. Nevertheless, the agreement with numerical data is considerably poorer than for the temperature profile.

7. The relationship between dark and baryonic profiles is reflected also in the scaling relations between global quantities. The  $M - T_X$  relation is predicted to follow the self-similar scaling relation, particularly at high overdensities. As we go to larger radii, the density of merging systems is significantly higher. This adds to the fact that our prescription severely underestimates the gas density at large radii.
8. Our mass-temperature relation agrees relatively well with previous independent numerical experiments. However, some discrepancies are found in the emission-weighted temperature due to differences in the inner shape of the profile. We claim that this is probably a resolution effect. The agreement with observational estimates based on the  $\Lambda$ CDM model and a NFW profile is good; other observational methods tend to predict slightly lower normalisations, but the scatter is rather large.
9. The  $L_X - T_X$  relation can be derived from the definition of X-ray luminosity, substituting the appropriate profiles for the gas density and temperature. The scaling law so obtained is *not* expected to follow the self-similar prediction  $L_X \propto T_X^2$ , since it depends on three additional factors: the square of the baryon fraction,  $F^2$ , the structure parameter,  $Q$ , and the exact normalisation of the  $M - T$  relation,  $M_0$ . When these factors are taken into account, the agreement between predicted and simulated scaling laws is extremely good.
10. At low overdensities (e.g.  $\Delta = 200$ ), the baryon fraction is close to the cosmic value for all clusters, the structure parameter  $Q$  increases dramatically with  $T_X$  (i.e. low-mass haloes are much less concentrated due to merging), but  $M_0$  is a decreasing function of temperature. The last two effects roughly compensate, so they simply introduce some scatter in the  $L_X - T_X$  relation observed at the virial radius.
11. At high overdensities (e.g.  $\Delta = 2500$ ), both the structure factor and the normalisation of the  $M - T$  relation are almost the same for every cluster, but the baryon fraction is lower in the less-concentrated low-temperature clusters. Hence, the X-ray luminosity of these systems is suppressed with respect to that of the massive clusters, and the observed  $L_X - T_X$  relation steepens considerably.
12. Our normalisation of the  $L_X - T_X$  relation is significantly higher than that found in previous numerical studies. This could well be a numerical artifact due to our higher resolution. Low-resolution studies would not be able to solve the high-density regions near the centre of the cluster, and hence the bolometric luminosity would be underestimated. This issue must be investigated in more detail.

13. Observational estimates also yield lower luminosities for a given temperature. The discrepancy amounts to a factor of 2 for the only estimate based on a  $\Lambda$ CDM cosmology, and it is much worse for SCDM estimates. However, the comparison between different cosmologies is not straightforward.

### 6.1.3 Stars

1. A  $\Lambda$ CDM cosmology shows the best agreement with observations of the cosmic star formation history. Standard CDM tends to overpredict the cosmic star formation rate density, while BSI fails to form enough stars at high  $z$  due to its reduced power at small scales.
2. Photoionisation fixes the onset of star formation in the universe, suppressing star formation in low-mass objects at high  $z$ . Supernovae feedback is very efficient to self-regulate the process of converting gas into stars, preventing the most massive halos to form too many stars at later times.
3. In contrast to the first observational estimates (Madau et al. 1996), but in agreement with more recent data (Steidel et al. 1999), the  $\Lambda$ CDM model predicts almost no drop in the cosmic SFR for  $2 < z < 5$ . Star formation seems to be a gradual process with no characteristic epoch.
4. The comoving simulated volumes in our experiments are comparable to those covered by observations. Thus, a non-negligible error is expected in the observational measurements due to cosmic variance associated with small volume statistics. This is most important when one wants to determine the steep slope of the SFR density from  $z \sim 1$  to the present time.
5. Star formation histories are very different for objects that end up in the cores of clusters and isolated galaxies. Galaxies in cluster cores have much older stellar populations, and their activity is drastically reduced when they lose their cold gas reservoirs.
6. In agreement with recent observations, we find that the mechanism quenching the star formation in infalling galaxies is efficient in low-mass groups ( $M \sim 10^{13} M_{\odot}$ ) as well as in clusters.

## 6.2 Future prospects

Our database still has a lot of *juice* to be squeezed from it. In particular, we have restricted our analysis to the present epoch, and there is a lot of

work that can be done regarding the study of the evolutionary trends of both dark matter and gas properties.

These numerical simulations are also very interesting to investigate realistic cluster mergers. All our objects have experienced a major merging event since  $z=0.6$ . With an appropriate time resolution, we will be able to study in detail the physics of mergers and put constraints in the relaxation time-scale as a function of the merger characteristics. Moreover, we can simultaneously compare the X-ray properties of the system with the dark matter distribution before, during and after the merger. Then, an unbiased tracer of the dynamical state of a cluster could be applied to real systems in order to understand the combined observations in X-ray and optical wavelengths.

On the other hand, new high-resolution simulations are being carried out at the present time. Their aim is to add more clusters to the present sample, not only to improve statistics, but also to enlarge the mass coverage. This is particularly important for the study of the scaling relations found between dark matter and gas properties, as well as to test the validity of our prescription relating the structure of both components.

Finally, the implementation of cooling and star formation would offer new insights on the process of galaxy formation and evolution. Some steps are also being taken in this direction. In the long term, we would like to self-consistently model photoionisation and chemical enrichment, computing the intensity of the ionising background at each timestep, as well as metal production and advection.

From the point of view of analytical modelling, we would like to extend our treatment of spherical collapse in order to predict the evolution of the dark matter profiles. It would be also extremely interesting to study the multiplicity function of dark matter haloes in combination with the statistics of Gaussian random peaks. Regarding the gas, taking into account infall and rotational motions into the hydrostatic equilibrium equation will surely improve our theoretical estimations of the ICM density and temperature profiles, as well as the normalisation of the scaling relations.

## 6.3 Conclusiones y perspectivas futuras

### 6.3.1 Materia oscura

1. Las predicciones numéricas sobre la distribución de materia oscura son robustas dentro de los límites de resolución. ART y GADGET dan resultados consistentes. Las perturbaciones del potencial de materia oscura debido a la presencia de bariones son despreciables a la escala de los cúmulos, al menos cuando sólo se considera la física adiabática.
2. De una muestra de 15 cúmulos, 6 han sido catalogados como sistemas relajados, 4 como fusiones' menores y 5 como fusiones mayores. La magnitud de la actividad dinámica es significativamente mayor en el extremo de baja masa de la muestra, como se podía esperar debido a la organización jerárquica.
3. Hay diferencias sistemáticas entre los perfiles internos de nuestros cúmulos numéricos dependiendo de su estado dinámico. Los cúmulos relajados se describen mejor con el perfil propuesto por Navarro et al. (1997), mientras que las fusiones menores están más próximos a la forma defendida por Moore et al. (1999). Los fusiones mayores siguen una ley de potencias pura para más de un orden de magnitud en el radio; sus perfiles tienen una pendiente incluso mayor que  $\rho \propto r^{-1.5}$ .
4. La pendiente logarítmica del perfil de masas de los halos relajados no alcanza ninguna pendiente asintótica para nuestro límite de resolución. De hecho, parece aumentar por encima del valor de "NFW" para radios suficientemente pequeños. Se necesita mayor resolución para verificar esta conclusión.
5. La extensión de los sistemas fusionados es sistemáticamente mayor que la de los cúmulos relajados. Este efecto distorsiona completamente la relación  $c - M_{200}$  usual, aunque todavía se puede encontrar algo de correlación en el plano  $\rho_s - r_s$ . Los valores que mejor ajustan estos parámetros son consistentes con los inferidos a partir de las observaciones.
6. La densidad del espacio de fase de nuestros cúmulos se ajusta bien con la ley de potencias  $\rho/\sigma^3 = 2.24 \times 10r^{-1.875}$ , similar a la encontrada por Taylor y Navarro (2001) para halos del tamaño de galaxias.
7. No encontramos una evidencia clara de un perfil universal en el parámetro de anisotropía,  $\beta \equiv 1 - \sigma_\theta^2/\sigma_r^2$ . Aunque hay indicaciones de una tendencia promedio, la variabilidad de los perfiles individuales es extremadamente alta. Podemos descartar con seguridad la existencia de un campo de velocidades isótropo ( $\beta = 0$ ) en los cúmulos relajados y en los fusiones menores.

8. El momento angular crece aproximadamente de forma proporcional a  $r$ , consistentemente con trabajo numérico previo. El soporte rotacional es despreciable con respecto a las contribuciones debidas al movimiento aleatorio. La excentricidad de las órbitas de partículas individuales es aproximadamente  $e = 0.5$  para todo el cúmulo. Dos cúmulos se desvían de este comportamiento.
9. La inclusión del momento angular y la elección de las condiciones iniciales son los elementos más delicados en lo que respecta al modelo de caída esférico. Nuestros cúmulos se describen muy bien con picos  $\approx 3\sigma$  del campo de densidades, suavizados en las escalas  $\approx 1h^{-1}$  Mpc, cuando se fija la excentricidad de las órbitas a  $e = 0.5$ .

### 6.3.2 Gas

1. Encontramos evidencia adicional de pérdidas de entropía no físicas en la implementación estandar del algoritmo SPH. Este efecto puede tener una importancia crítica en el cálculo del perfil de entropía en grupos y cúmulos de galaxias. La nueva formulación de SPH propuesta parece solucionar este problema; Las simulaciones de alta resolución realizadas con este código son consistentes con los resultados del código Euleriano ART. Un número excesivamente bajo de partículas puede producir un núcleo “isentrópico” debido a efectos numéricos.
2. La hipótesis de equilibrio hidrostático está justificada para los cúmulos relajados desde un punto de vista dinámico, aunque se tienen algunas desviaciones en las partes externas del cúmulo. Es válida sólo de forma marginal para fusiones menores y falla completamente para sistemas en proceso claro de fusión.
3. La ecuación de estado del gas intracumular se puede describir bien mediante un politrópico de índice  $\gamma \approx 1.18$ . Sólo las fusiones mayores se desvían de una relación politrópica.
4. Bajo las hipótesis de equilibrio hidrostático, una ecuación de estado politrópica, un perfil universal para la materia oscura y una fracción bariónica constante a radios grandes, el perfil de temperatura queda *determinado* por la distribución de materia oscura subyacente. Nuestros resultados son consistentes con los de Komatsu y Seljak (2001), que tienen un modelo ligeramente diferente. El perfil de temperatura obtenido a partir de un perfil de NFW proporciona un ajuste excelente de los resultados de la simulación.
5. Los perfiles de temperatura de rayos X proyectados son muy similares a los observados en cúmulos reales. Aunque la situación es menos clara en las regiones internas, lo que está probablemente relacionado con



fenómenos no adiabáticos, se puede descartar un perfil de temperaturas isotérmico por razones tanto teóricas como observacionales. Nuestros datos se ajustan muy bien con la fórmula propuesta por Loken et al. (2002), pero no se encuentra concordancia según los valores de mejor ajuste de los parámetros libres.

6. El perfil de densidad del gas ICM se puede obtener también con el procedimiento descrito más arriba. De nuevo, queda *completamente* determinado una vez que se conocen los parámetros que describen el halo de materia oscura. De todas formas, la concordancia con los datos numéricos es considerablemente peor que con el perfil de temperatura.
7. La relación entre los perfiles oscuro y bariónico se refleja también en las relaciones de escala entre los promedios globales. Se predice que la relación  $M - T_x$  sigue una relación de escala de autosimilaridad, en particular, para sobredensidades altas. Cuando incrementamos el radio, la densidad de los sistemas que se fusionan se incrementa significativamente por encima del valor esperado por su temperatura. Esto se acumula con el hecho de que nuestro modelo infraestima severamente la densidad del gas para radios grandes.
8. Nuestra relación temperatura-masa concuerda relativamente bien con experimentos numéricos previos independientes. Sin embargo, se encuentran algunas discrepancias en la temperatura pesada con las emisiones debido a diferencias en la forma interna del perfil. Pensamos que es probablemente un efecto de la resolución. La concordancia con estimaciones observacionales basadas en el modelo  $\Lambda$ CDM y el perfil NFW es buena; otros métodos observacionales tienden a predecir normalizaciones ligeramente menores, aunque con una variabilidad significativa.
9. La relación  $L_x - T_x$  puede obtenerse de la definición de la luminosidad de rayos X, substituyendo los perfiles adecuados de densidad de gas y temperatura. No se espera que la ley de potencias que se obtiene así siga la predicción autosimilar  $L_x \propto T_x^{-2}$ , porque depende de tres factores adicionales: el cuadrado de la fracción bariónica,  $F^2$ , el parámetro de estructura,  $Q$ , y la normalización exacta de la relación  $M - T$ ,  $M_0$ . Cuando estos factores se toman en cuenta, la concordancia entre las leyes de escala predichas y simuladas es extremadamente buena.
10. Para sobredensidades bajas (e.j.  $\Delta = 200$ ), la fracción bariónica es cercana al valor cósmico para todos los cúmulos, el parámetro  $Q$  de estructura crece dramáticamente con  $T_X$  (es decir, los halos poco masivos están mucho menos concentrados debido a la fusión), pero  $M_0$  es una función decreciente de la temperatura. Los dos últimos efectos se

compensan aproximadamente, así que introducen alguna variabilidad en la relación  $L_x - T_x$  observada en el radio virial.

11. A grandes sobredensidades (e.j.  $\Delta = 2500$ ) el factor de estructura y la normalización de la relación  $M - T$  son la misma para todos los cúmulos pero la fracción bariónica es más baja en los cúmulos menos concentrados y con baja temperatura. Por lo tanto, la luminosidad en rayos X de estos sistemas es menor respecto de la de los cúmulos masivos, y la relación  $L_x - T_x$  observada aumenta su pendiente considerablemente.
12. Nuestra normalización de la relación  $L_x - T_x$  es significativamente mayor que la encontrada en estudios numéricos previos. Esto se podría deber a un artefacto numérico de nuestra mayor resolución. Los estudios a baja resolución podrían ser incapaces de resolver las regiones de alta densidad cerca del centro del cúmulo, y por lo tanto la luminosidad volumétrica podría estar infravalorada. Esta cuestión debe ser investigada en mayor detalle.
13. Estimaciones observacionales también dan luminosidades menores a temperatura dada. La discrepancia es de un factor 2 para la estimación basada sólo en la cosmología  $\Lambda$ CDM, y es mucho peor para las estimaciones SCDM. Sin embargo, la comparación entre las diferentes cosmologías no es trivial.

### 6.3.3 Estrellas

Hemos realizado 66 simulaciones numéricas agrupadas en siete experimentos diferentes, con el fin de obtener una predicción teórica de la historia de la formación estelar cósmica. Comparamos nuestras predicciones con estimaciones observacionales publicadas. Resumimos nuestros resultados:

1.  $\Lambda$ CDM muestra el mejor acuerdo con las observaciones. El modelo CDM Estándar tiende a sobreestimar la densidad cósmica  $SFR$ , mientras que la  $BSI$  falla al formar suficientes estrellas a gran corrimiento hacia el rojo debido a su fuerza reducida a escalas pequeñas.
2. La fotoionización fija el comienzo de la formación estelar en el universo, suprimiendo la formación estelar de objetos masivos a alto  $z$ . La retroalimentación de las supernovas es muy eficiente para autoregular el proceso de convertir gas en estrellas, previniendo así que los halos mas masivos formen demasiadas estrellas en épocas tardías.
3. Al contrario de las primeras estimaciones observacionales, pero de acuerdo con los datos más recientes, el modelo  $\Lambda$ CDM predice que no existe decaimiento en el  $SFR$  cósmico para  $2 < z < 5$ . La formación estelar parece ser un proceso gradual sin ninguna época característica.

4. Los volúmenes comóviles en los experimentos son comparables con las observaciones. Por lo tanto se puede esperar un error apreciable en las medidas observacionales debidas a la variancia cósmica asociada a la estadística de volúmenes pequeños. Esto es lo más importante cuando se quiere determinar el salto de pendiente de la densidad  $SFR$  para  $z \sim 1$  en el momento actual.
5. La historia de la formación estelar es muy diferente en objetos que acaban en los centros de los cúmulos de las galaxias de campo. Las galaxias de los centros de los cúmulos tienen una población estelar mucho más vieja y su actividad se reduce drásticamente cuando pierden la reserva de gas frío a partir de la que se forman las estrellas.
6. En concordancia con las observaciones más recientes, encontramos que los mecanismos que inhiben la formación estelar en cúmulos de galaxias son también eficientes en entornos correspondientes a grupos más pequeños ( $M \sim 10^{13} M_{\odot}$ ).

Los efectos de selección, extinción por polvo y conversión de luminosidades a tasas de formación estelar son las principales fuentes de incertidumbre de las estimaciones observacionales. así mismo el pequeño volumen estudiado por el *HDF* también podría introducir algún tipo de sesgo estadístico en las observaciones a alto redshift.

Las incertidumbres en los experimentos numéricos provienen fundamentalmente de la resolución espacial y de la modelización de la formación estelar y de los procesos de realimentación. El uso de códigos eulerianos con malla adaptativa será muy útil para conseguir un aumento significativo de la resolución espacial en volúmenes cosmológicos que sean estadísticamente significativos.

El enriquecimiento químico y los procesos de fotoionización han sido tenidos en cuenta de forma fenomenológica en el código que hemos utilizado. Sería extremadamente interesante realizar un modelo autoconsistente de ambos procesos simultáneamente, calculando la intensidad del fondo ionizante ultravioleta, no sólo proveniente de quásares y *AGN*, sino también de las estrellas generadas en la simulación en cada paso de tiempo, así como la producción de metales en las mismas y su tratamiento hidrodinámico como otra variable más.



# Appendix A

## Cluster Atlas

*Is this the real life? Is this just fantasy?  
Caught in a landslide, no escape from reality  
Open your eyes, look up to the skies and see!*  
– Queen : *Bohemian Rhapsody* (1975) –

**T**hroughout this work, the sample of galaxy clusters described in Section 2.3.1 has been analysed in a statistical way. The present appendix is devoted to test whether the theoretical considerations that have been discussed in the previous chapters can be applied to *predict* the structure of individual clusters.

### A.1 Figure description

We have been plotted two figures per cluster. The first one is divided into two columns, which in turn have been sub-divided into three panels. The second one contains a contour plot overlaid on a colour map.

The left column of the first figure is devoted to the dark matter distribution, while the right column is used to display the radial properties of the ICM gas. In both cases, the numerical results are indicated by dots, while solid lines are used to represent the theoretical predictions.

**DARK MATTER:** Dark matter density is plotted on the top panel, normalised to the mean cosmic value. In the middle panel, the cumulative mass is shown, and the lower panel is used to display its logarithmic slope  $\alpha_M$ . The solid lines show the predictions based on the spherical collapse formalism, as discussed in Section 3.3.4. The values of the peak height and smoothing scale appropriate for each cluster can be found in Table 3.2. We recall that major mergers have not been fit by the spherical infall model.

**GAS:** Top panel shows the gas density, also normalised to mean cosmic value. Solid line corresponds to the prediction (4.17) based on hydrostatic

equilibrium with a NFW-like potential, a polytropic equation of state and constant baryon fraction at large radii. Middle panel is used for the temperature, which has been compared with our prescription (4.15). The lower panel shows the entropy profile of the cluster, computed as  $S = kTn_e^{-2/3}$  both for the experimental and theoretical profiles. As has been shown in Section 4.1, the entropy-conserving version of GADGET is able to produce isentropic cores in many of our clusters. For details on the computation of the theoretical predictions of the gas profiles, the reader is referred to Section 4.2.2.

COLOUR PLOT: This image represents the a map of the dark matter density, projected along the three axes. As can be appreciated in some figures, the cluster might look more or less 'relaxed' (where, in this context, we understand 'relaxed' as 'spherically symmetric') depending on the projection observed. If we assume that light traces mass, this colour plots can be thought of as a coarse approximation to an observational image of the cluster in an optical band.

CONTOUR PLOT: These contours correspond to the projected X-ray luminosity of the clusters. Although they approximately trace the observed shape of the dark mater distribution, it is evident that the gas has much less substructure than the dark matter. This is due to the gas stripping that galaxies experience as they orbit through the cluster. Most of the infalling haloes lose their gas reservoir during the first pericentre passage.

## A.2 Individual clusters

## Cluster A

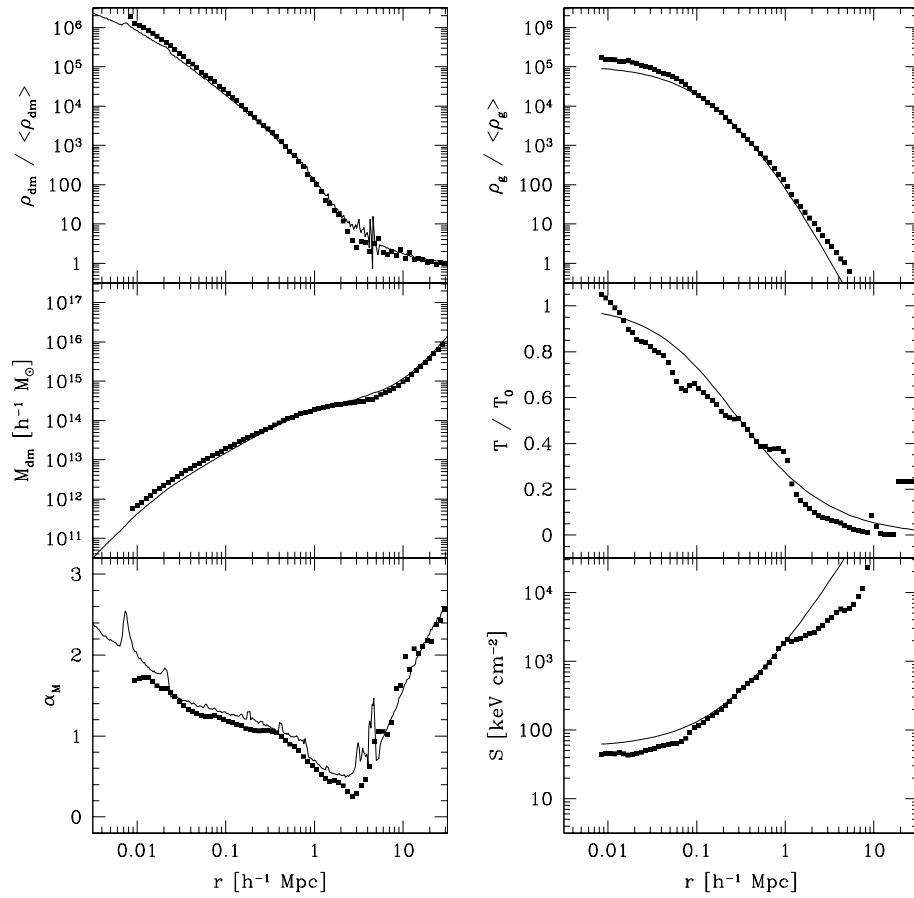


FIGURE A.1: Cluster A





## Cluster B

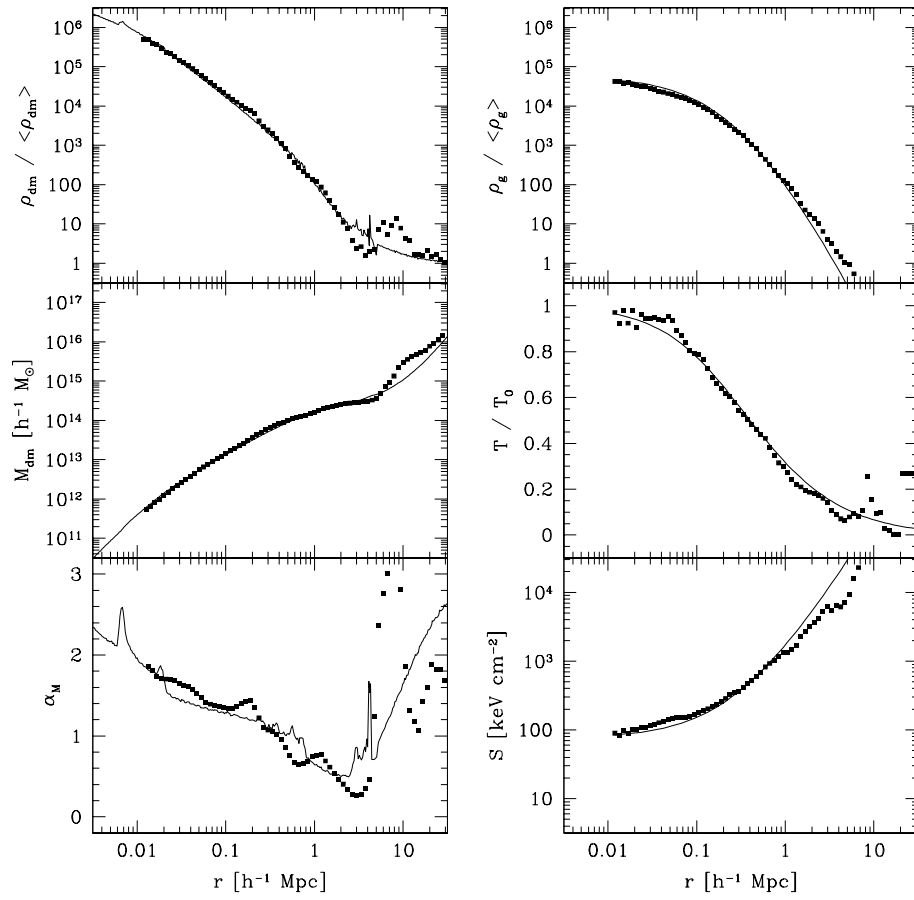


FIGURE A.2: Cluster B



## Cluster C

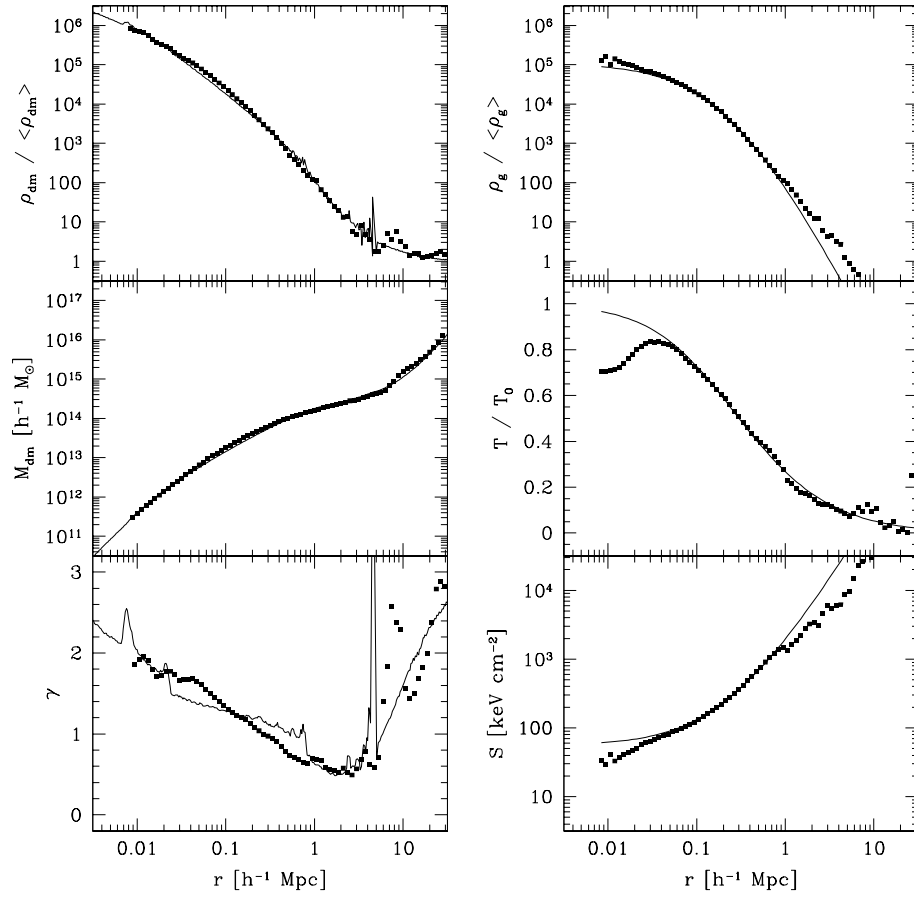


FIGURE A.3: Cluster C



## Cluster D

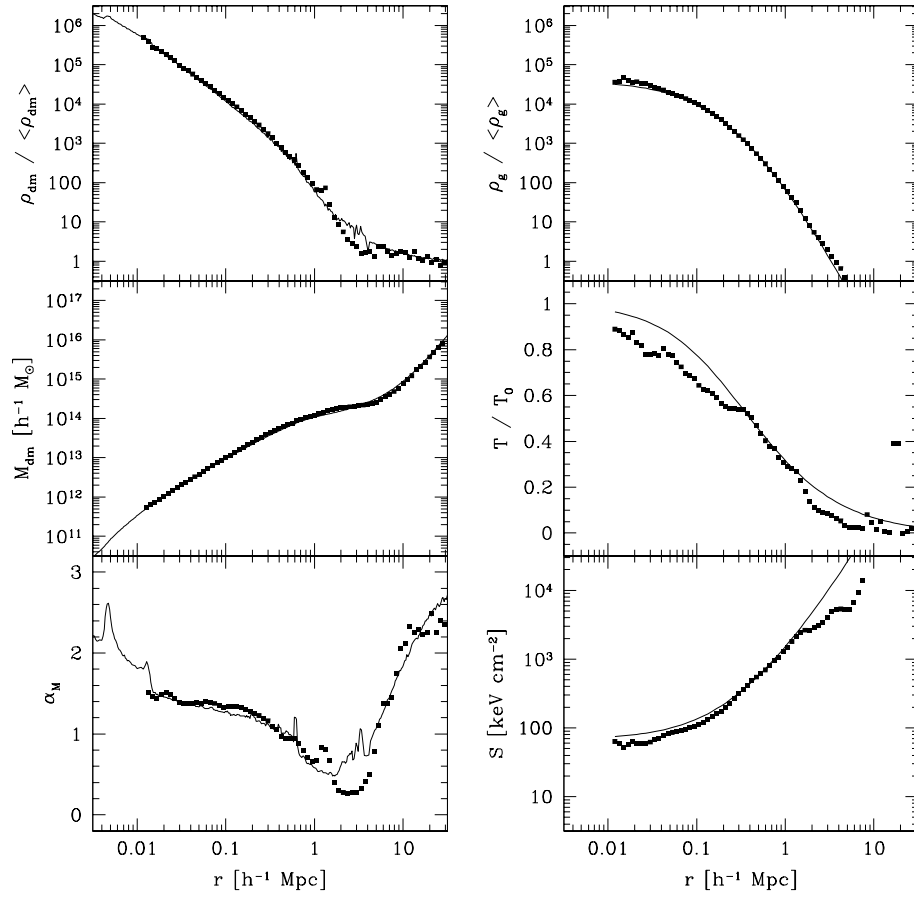


FIGURE A.4: Cluster D



## Cluster E

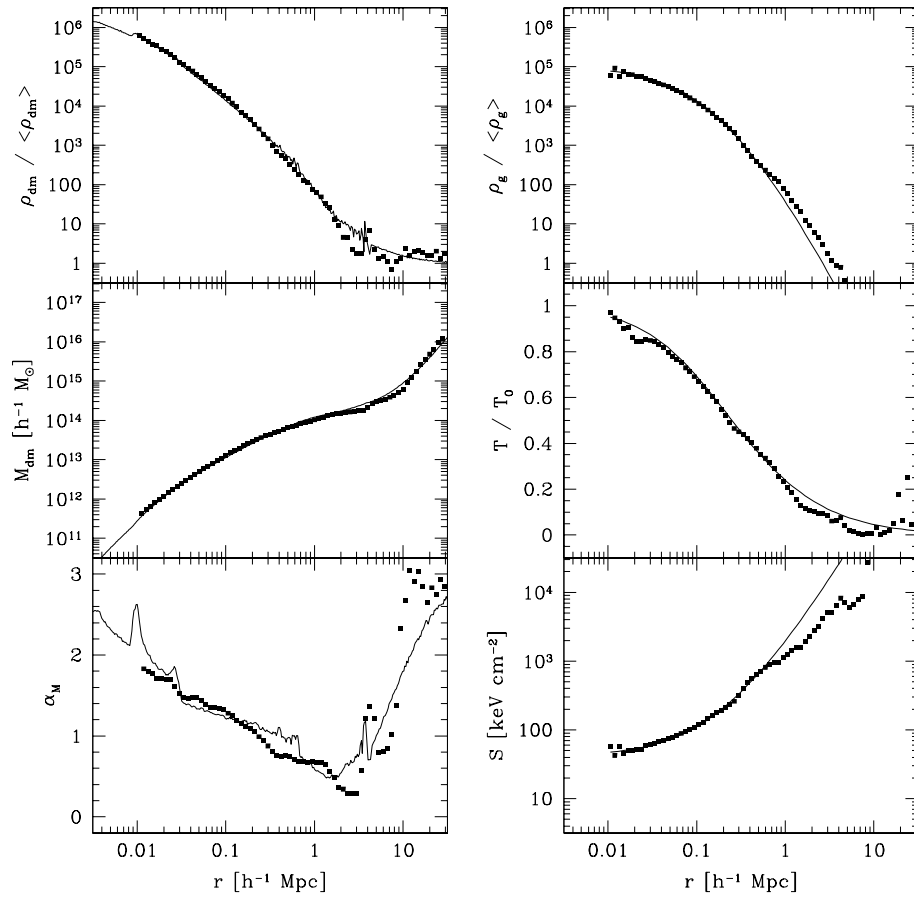


FIGURE A.5: Cluster E





## Cluster F

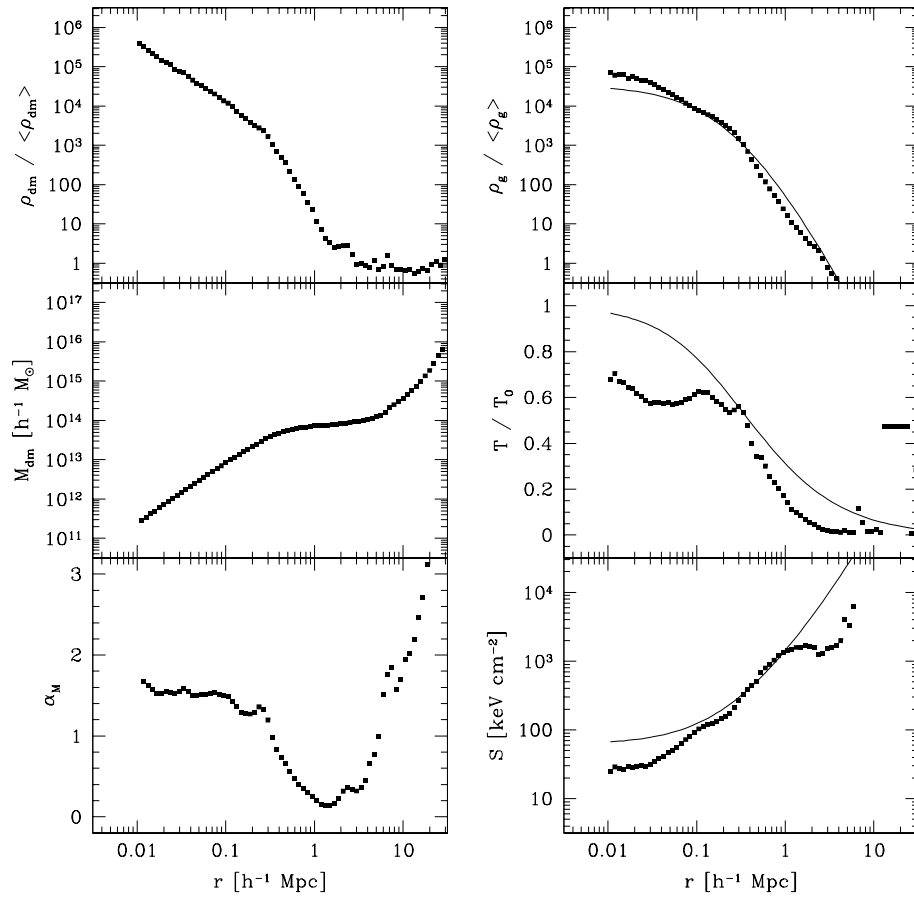


FIGURE A.6: Cluster F



Cluster G

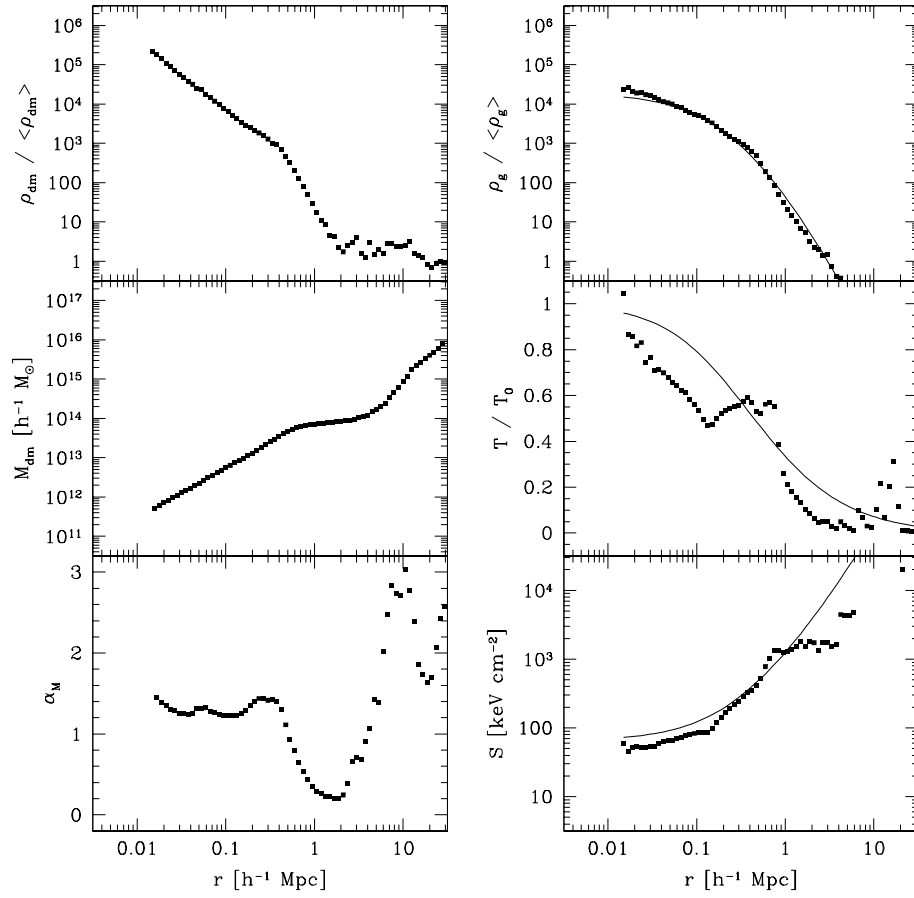


FIGURE A.7: Cluster G



## Cluster H

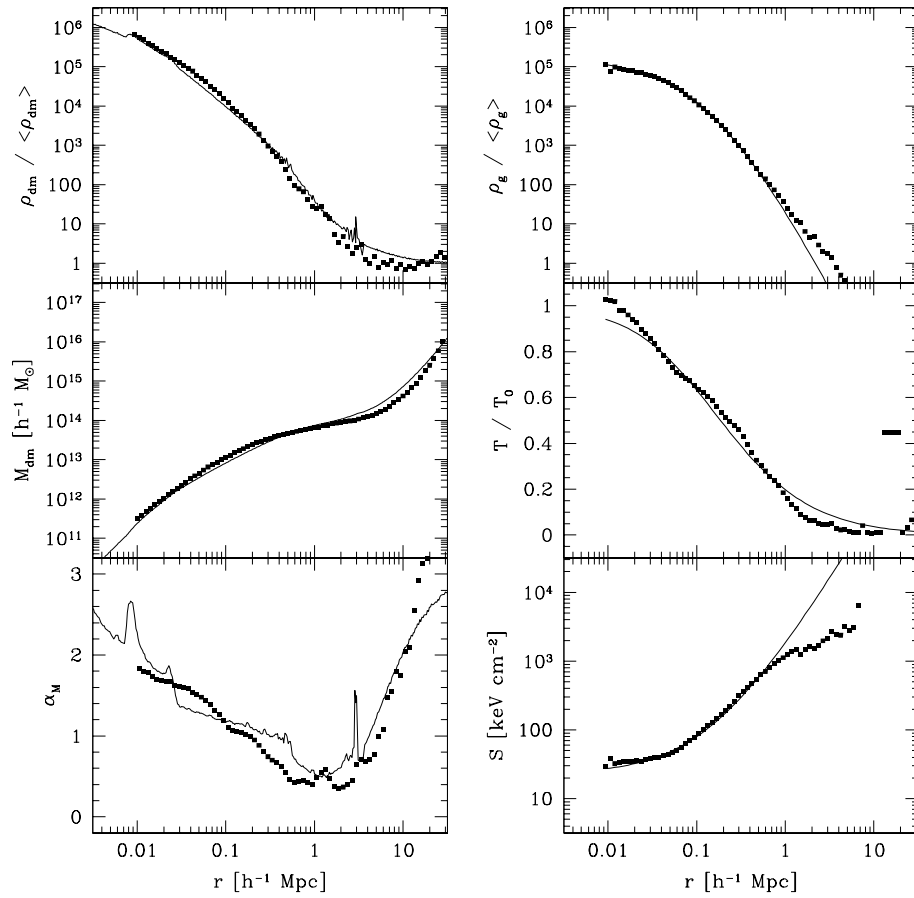


FIGURE A.8: Cluster H



Cluster I

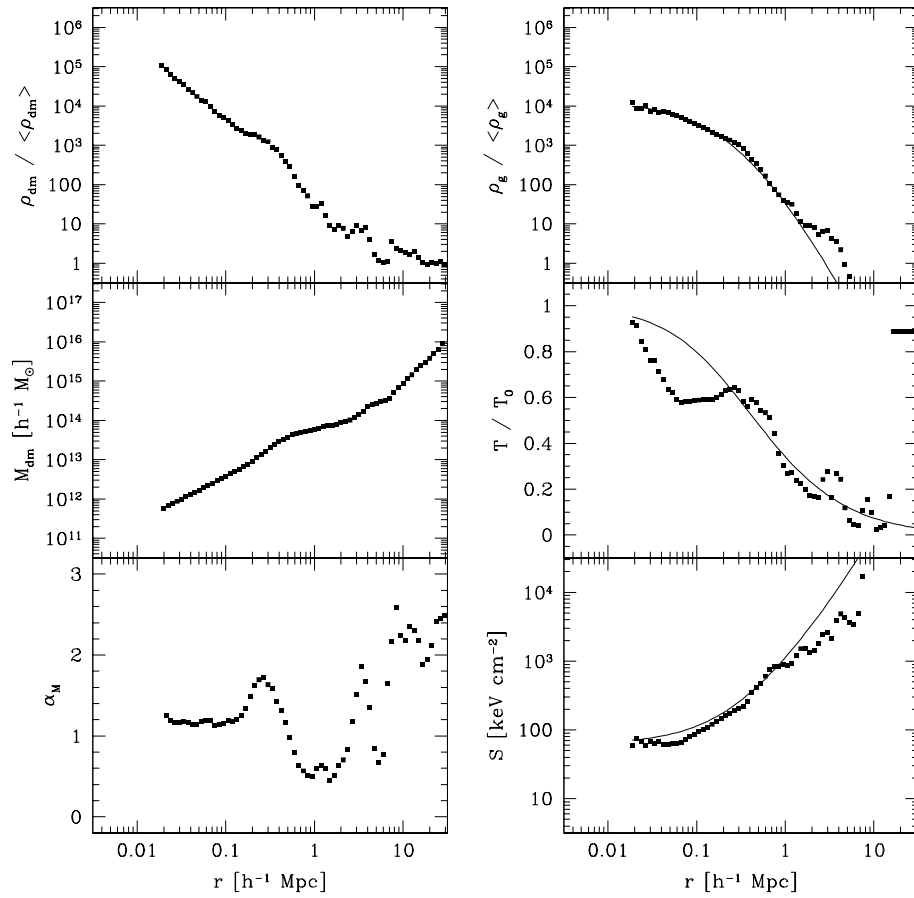
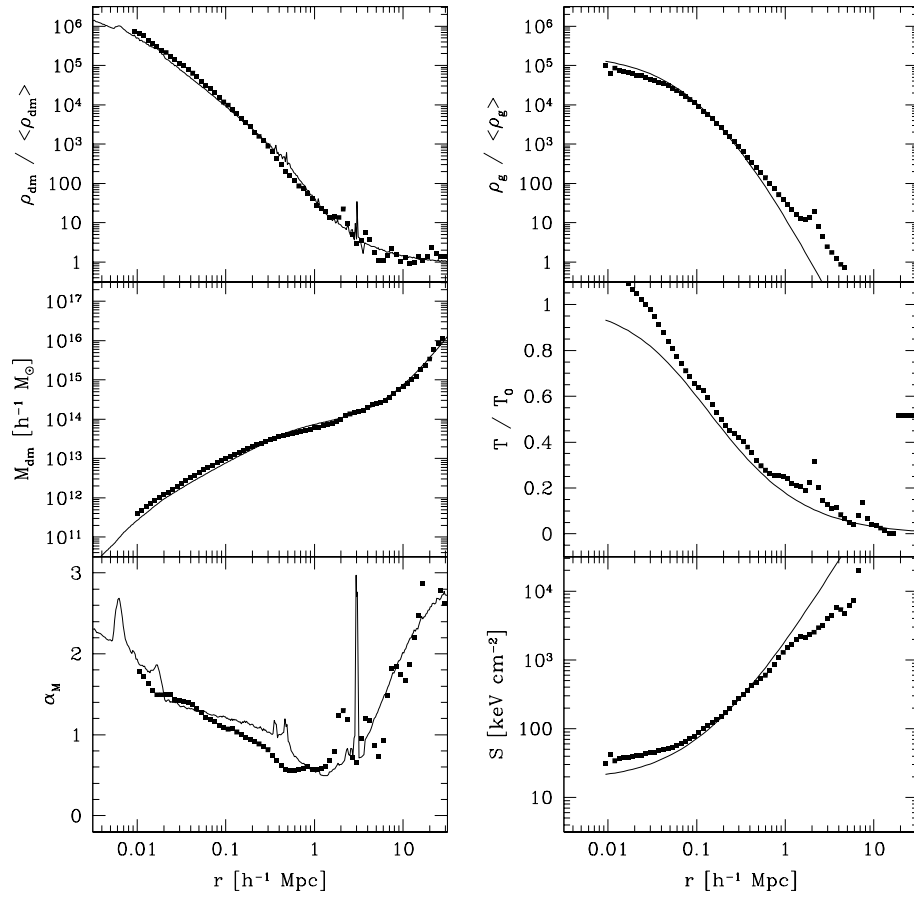


FIGURE A.9: Cluster I





Cluster J<sub>1</sub>FIGURE A.10: Cluster J<sub>1</sub>



Cluster  $K_1$

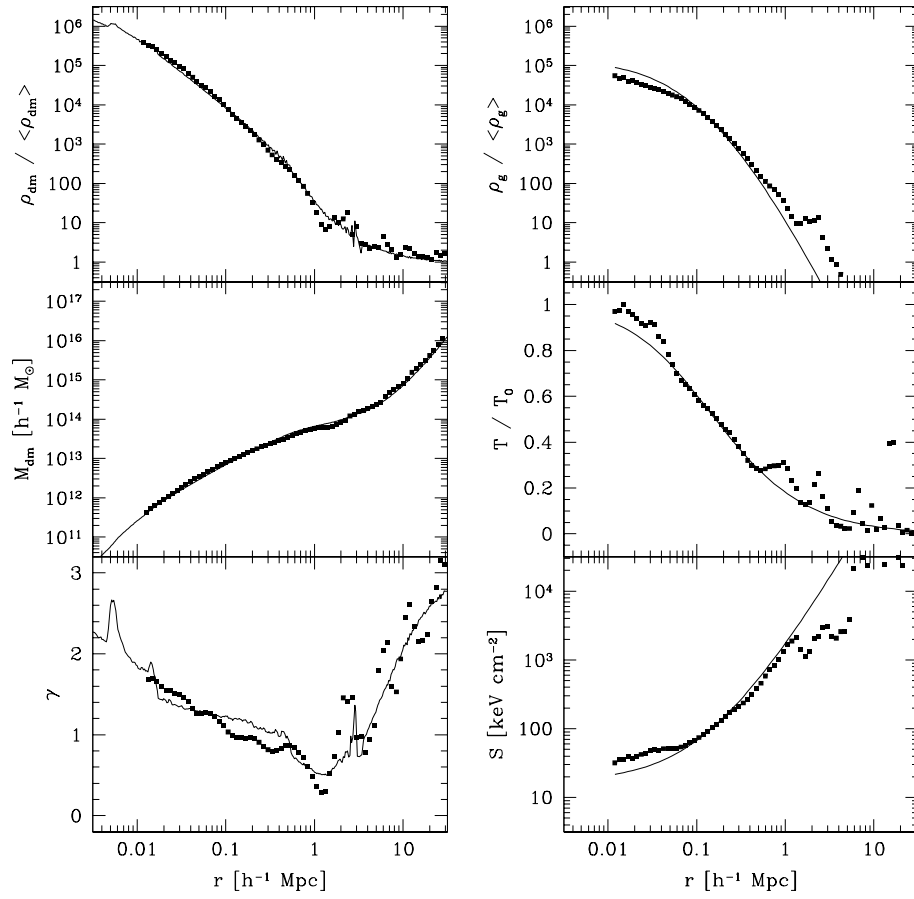


FIGURE A.11: Cluster  $K_1$



Cluster L

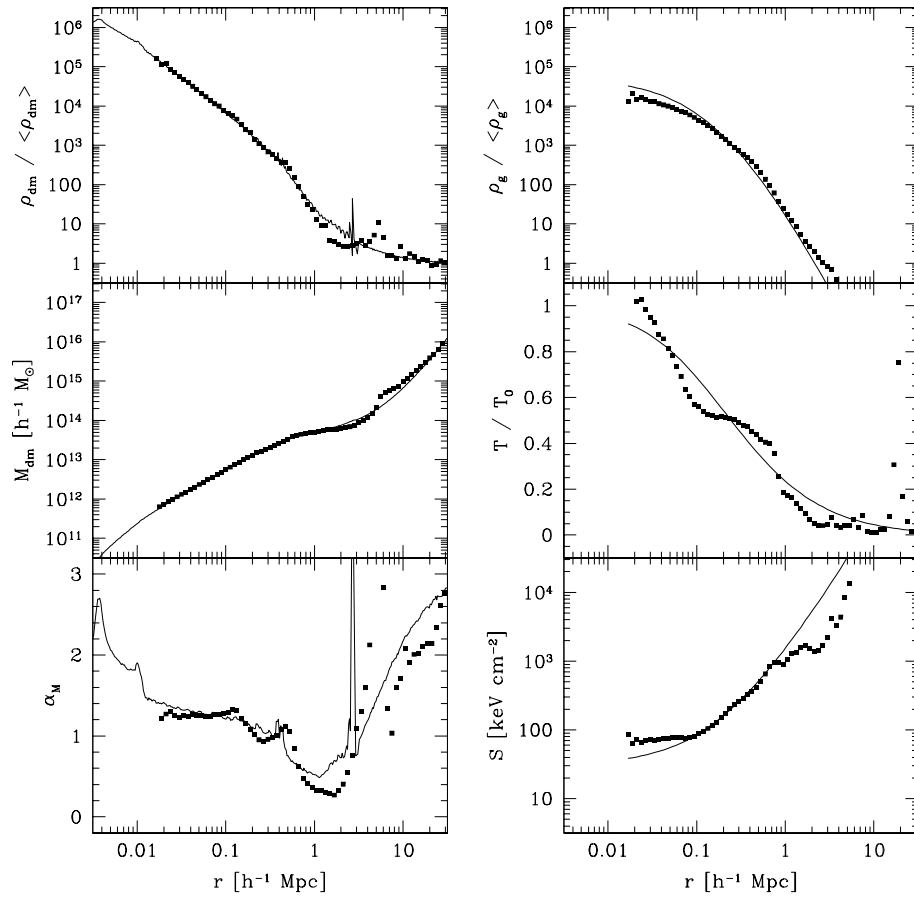


FIGURE A.12: Cluster L



Cluster M

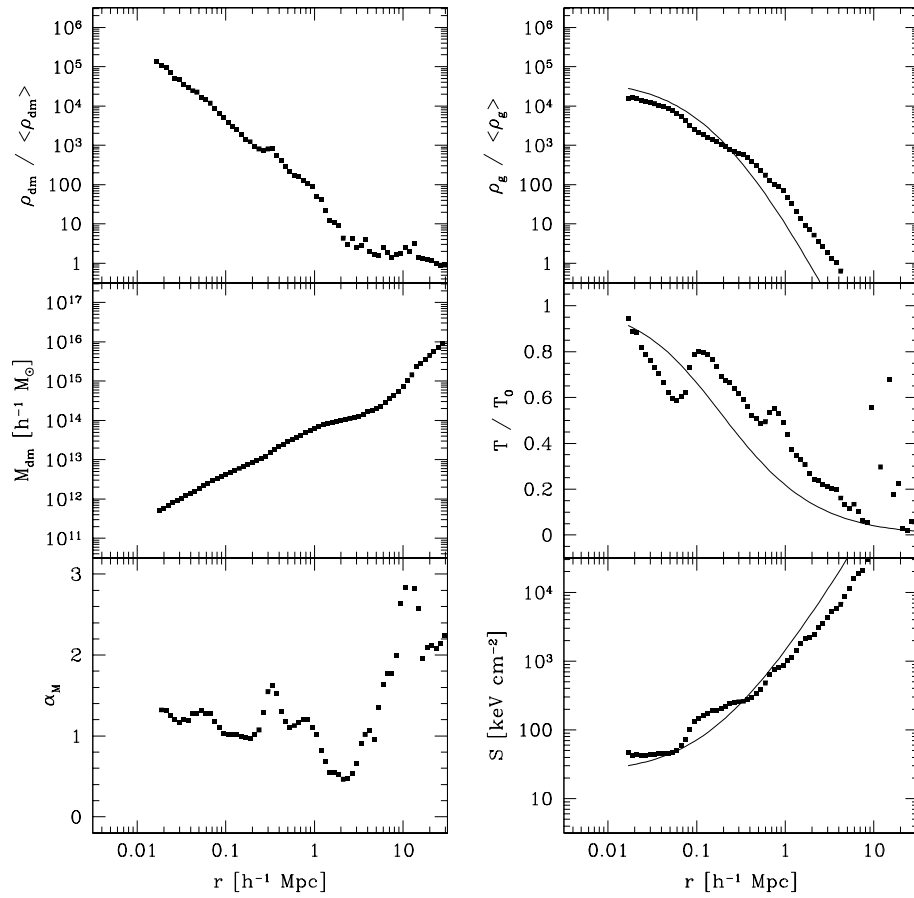


FIGURE A.13: Cluster M





Cluster  $K_2$

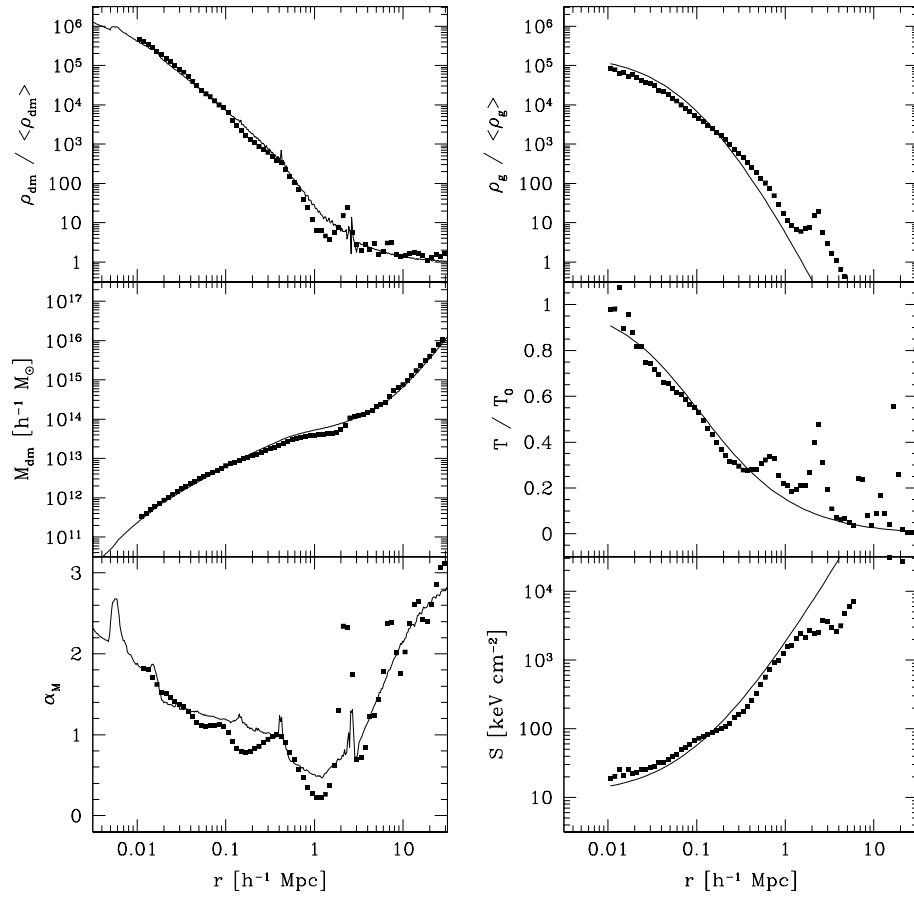


FIGURE A.14: Cluster  $K_2$



Cluster J<sub>2</sub>

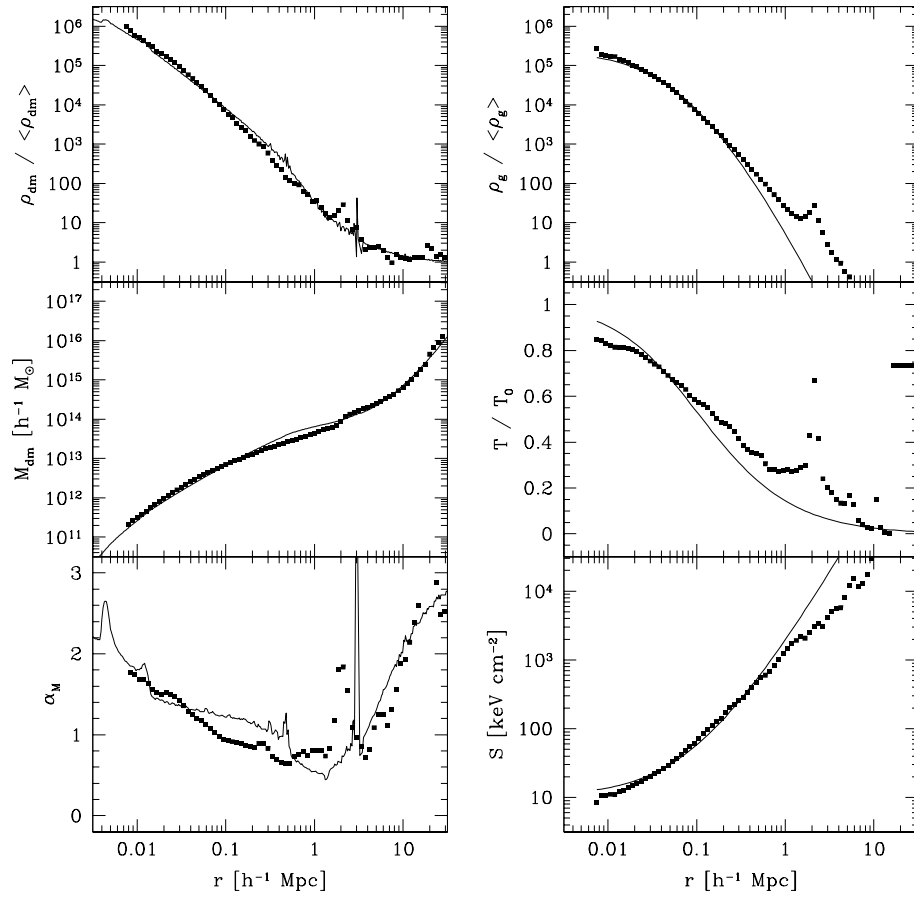


FIGURE A.15: Cluster J<sub>2</sub>



# Bibliography

*Words get written. Words get twisted.  
Old meanings move in the drift of time.  
Lift the flickering torches. See gentle shadows change  
the features of the faces cut in unmoving stone.*  
– Jethro Tull : *Roots to Branches* (1995) –

- Aarseth, S. J., Turner, E. L., and Gott, J. R. (1979).  
N-body simulations of galaxy clustering. I - Initial conditions and galaxy  
collapse times.  
*ApJ*, 228:664–683.
- Adams, T. F. (1976).  
The detectability of deuterium Lyman alpha in QSOs.  
*A&A*, 50:461.
- Adelberger, K. L. and Steidel, C. C. (2000).  
Multiwavelength Observations of Dusty Star Formation at Low and High  
Redshift.  
*ApJ*, 544:218–241.
- Allen, S. W. (1998).  
Resolving the discrepancy between X-ray and gravitational lensing mass  
measurements for clusters of galaxies.  
*MNRAS*, 296:392–406.
- Allen, S. W., Ettori, S., and Fabian, A. C. (2001a).  
Chandra measurements of the distribution of mass in the luminous lensing  
cluster Abell 2390.  
*MNRAS*, 324:877–890.
- Allen, S. W. and Fabian, A. C. (1998).  
The impact of cooling flows on the  $T_X$ - $L_{\text{Bol}}$  relation for the most luminous  
clusters.  
*MNRAS*, 297:L57–L62.

- Allen, S. W., Schmidt, R. W., and Fabian, A. C. (2001b).  
The X-ray virial relations for relaxed lensing clusters observed with Chandra.  
*MNRAS*, 328:L37–L41.
- Allen, S. W., Schmidt, R. W., and Fabian, A. C. (2002).  
Cosmological constraints from the X-ray gas mass fraction in relaxed lensing clusters observed with Chandra.  
*MNRAS*, 334:L11–L15.
- Arabadjjs, J. S., Bautz, M. W., and Garmire, G. P. (2002).  
Chandra Observations of the Lensing Cluster EMSS 1358+6245: Implications for Self-interacting Dark Matter.  
*ApJ*, 572:66–78.
- Arnaud, M. and Evrard, A. E. (1999).  
The L<sub>X</sub>-T relation and intracluster gas fractions of X-ray clusters.  
*MNRAS*, 305:631–640.
- Ascasibar, Y., Yepes, G., Gottlöber, S., and Müller, V. (2002a).  
Numerical simulations of the cosmic star formation history.  
*A&A*, 387:396–405.
- Ascasibar, Y., Yepes, G., Gottlöber, S., and Müller, V. (2002b).  
The structure of cold dark matter haloes.  
*in preparation*.
- Ascasibar, Y., Yepes, G., Müller, V., and Gottlöber, S. (2002c).  
The Universal Density and Temperature Profile of Galaxy Clusters.  
*ApJ*, *in preparation*.
- Avila-Reese, V., Firmani, C., and Hernández, X. (1998).  
On the Formation and Evolution of Disk Galaxies: Cosmological Initial Conditions and the Gravitational Collapse.  
*ApJ*, 505:37–49.
- Bahcall, N. A., Ostriker, J. P., Perlmutter, S., and Steinhardt, P. J. (1999).  
The Cosmic Triangle: Revealing the State of the Universe.  
*Science*, 284:1481.
- Balbi, A., Ade, P., Bock, J., Borrill, J., Boscaleri, A., De Bernardis, P., Ferreira, P. G., Hanany, S., Hristov, V., Jaffe, A. H., Lee, A. T., Oh, S., Pascale, E., Rabii, B., Richards, P. L., Smoot, G. F., Stompor, R., Winant, C. D., and Wu, J. H. P. (2000).  
Constraints on Cosmological Parameters from MAXIMA-1.  
*ApJ*, 545:L1–L4.

- Balogh, M. L., Morris, S. L., Yee, H. K. C., Carlberg, R. G., and Ellingson, E. (1997).  
Star Formation in Cluster Galaxies at  $0.2 < z < 0.55$ .  
*ApJ*, 488:L75.
- Balogh, M. L., Morris, S. L., Yee, H. K. C., Carlberg, R. G., and Ellingson, E. (1999).  
Differential Galaxy Evolution in Cluster and Field Galaxies at  $z \sim 0.3$ .  
*ApJ*, 527:54–79.
- Balogh, M. L., Navarro, J. F., and Morris, S. L. (2000).  
The Origin of Star Formation Gradients in Rich Galaxy Clusters.  
*ApJ*, 540:113–121.
- Balogh, M. L., Pearce, F. R., Bower, R. G., and Kay, S. T. (2001).  
Revisiting the cosmic cooling crisis.  
*MNRAS*, 326:1228–1234.
- Balogh, M. L., Schade, D., Morris, S. L., Yee, H. K. C., Carlberg, R. G., and Ellingson, E. (1998).  
The Dependence of Cluster Galaxy Star Formation Rates on the Global Environment.  
*ApJ*, 504:L75.
- Balogh, M. L., Smail, I., Bower, R. G., Ziegler, B. L., Smith, G. P., Davies, R. L., Gaztelu, A., Kneib, J.-P., and Ebeling, H. (2002).  
Distinguishing Local and Global Influences on Galaxy Morphology: A Hubble Space Telescope Comparison of High and Low X-Ray Luminosity Clusters.  
*ApJ*, 566:123–136.
- Bardeen, J. M., Bond, J. R., Kaiser, N., and Szalay, A. S. (1986).  
The statistics of peaks of Gaussian random fields.  
*ApJ*, 304:15–61.
- Barnes, J. and Efstathiou, G. (1987).  
Angular momentum from tidal torques.  
*ApJ*, 319:575–600.
- Barnes, J. and Hut, P. (1986).  
A Hierarchical  $O(N \log N)$  Force-Calculation Algorithm.  
*Nature*, 324:446–449.
- Bekki, K., Couch, W. J., and Shioya, Y. (2002).  
Passive Spiral Formation from Halo Gas Starvation: Gradual Transformation into S0s.  
*ApJ*, 577:651–657.

- Benoit, A., Ade, P., Amblard, A., Ansari, R., Aubourg, E., Bargout, S., Bartlett, J. G., Bernard, J.-P., Bhatia, R. S., Blanchard, A., Bock, J. J., Boscaleri, A., Bouchet, F. R., Bourrachot, A., Camus, P., Couchot, F., de Bernardis, P., Delabrouille, J., Desert, F. X., Dore, O., Douspis, M., Dumoulin, L., Dupac, X., Filliatre, P., Fosalba, P., Ganga, K., Gannaway, F., Gautier, B., Giard, M., Giraud-Heraud, Y., Gispert, R., Guglielmi, L., Hamilton, J.-C., Hanany, S., Henrot-Versille, S., Kaplan, J., G., L., Lamarre, J.-M., Lange, A. E., Macias-Perez, J. F., Madet, K., Maffei, B., Magneville, C., Marrone, D. P., Masi, S., Mayet, F., Murphy, A., Naraghi, F., Nati, F., Patanchon, G., Perrin, G., Piat, M., Ponthieu, N., Prunet, S., Puget, J.-L., Renault, C., Rosset, C., Santos, D., Starobinsky, A., Strukov, I., Sudiwala, R. V., Teyssier, R., Tristram, M., Tucker, C., (2002).  
Cosmological constraints from Archeops.  
(astro-ph/0210306).
- Bertschinger, E. (1985).  
Self-similar secondary infall and accretion in an Einstein-de Sitter universe.  
*ApJS*, 58:39–65.
- Bialek, J. J., Evrard, A. E., and Mohr, J. J. (2001).  
Effects of Preheating on X-Ray Scaling Relations in Galaxy Clusters.  
*ApJ*, 555:597–612.
- Binney, J. and Tremaine, S. (1987).  
*Galactic dynamics*.  
Princeton, NJ, Princeton University Press, 1987, 747 p.
- Blais-Ouellette, S., Carignan, C., and Amram, P. (2001).  
Mass Distribution in Spiral Galaxies: Multiwavelength Rotation Curves to Test Dark Halos.  
In *Galaxies: the Third Dimension*.
- Blanchard, A., Valls-Gabaud, D., and Mamon, G. A. (1992).  
The origin of the galaxy luminosity function and the thermal evolution of the intergalactic medium.  
*A&A*, 264:365–378.
- Blumenthal, G. R., Faber, S. M., Primack, J. R., and Rees, M. J. (1984).  
Formation of galaxies and large-scale structure with cold dark matter.  
*Nature*, 311:517–525.
- Borgani, S., Girardi, M., Carlberg, R. G., Yee, H. K. C., and Ellingson, E. (1999).  
Velocity Dispersions of CNOC Clusters and the Evolution of the Cluster Abundance.



- ApJ*, 527:561–572.
- Borgani, S., Governato, F., Wadsley, J., Menci, N., Tozzi, P., Quinn, T., Stadel, J., and Lake, G. (2002).  
The effect of non-gravitational gas heating in groups and clusters of galaxies.  
*MNRAS*, 336:409–424.
- Borgani, S. and Guzzo, L. (2001).  
X-ray clusters of galaxies as tracers of structure in the Universe.  
*Nature*, 409:39–45.
- Borriello, A. and Salucci, P. (2001).  
The dark matter distribution in disc galaxies.  
*MNRAS*, 323:285–292.
- Bramel, D. A., Nichol, R. C., and Pope, A. C. (2000).  
The Local Space Density of Optically Selected Clusters of Galaxies.  
*ApJ*, 533:601–610.
- Bryan, G. L. and Machacek, M. E. (2000).  
The B Distribution of the Ly $\alpha$  Forest: Probing Cosmology and the Inter-galactic Medium.  
*ApJ*, 534:57–68.
- Bryan, G. L. and Norman, M. L. (1995).  
Simulating X-ray Clusters with Adaptive Mesh Refinement.  
*Bulletin of the American Astronomical Society*, 27:1421.
- Bryan, G. L. and Norman, M. L. (1998).  
Statistical Properties of X-Ray Clusters: Analytic and Numerical Comparisons.  
*ApJ*, 495:80.
- Bryan, G. L., Norman, M. L., Stone, J. M., Cen, R., and Ostriker, J. P. (1995).  
*Comput. Phys. Comm.*, 89:149.
- Bullock, J. S., Dekel, A., Kolatt, T. S., Kravtsov, A. V., Klypin, A. A., Porciani, C., and Primack, J. R. (2001).  
A Universal Angular Momentum Profile for Galactic Halos.  
*ApJ*, 555:240–257.
- Bullock, J. S., Kravtsov, A. V., and Weinberg, D. H. (2000).  
Reionization and the Abundance of Galactic Satellites.  
*ApJ*, 539:517–521.

- Burkert, A. (1995).  
The Structure of Dark Matter Halos in Dwarf Galaxies.  
*ApJ*, 447:L25.
- Burles, S. and Tytler, D. (1998a).  
The Deuterium Abundance toward Q1937-1009.  
*ApJ*, 499:699.
- Burles, S. and Tytler, D. (1998b).  
The Deuterium Abundance toward QSO 1009+2956.  
*ApJ*, 507:732–744.
- Butcher, H. and Oemler, A. (1978).  
The evolution of galaxies in clusters. II - The galaxy content of nearby clusters.  
*ApJ*, 226:559–565.
- Byrd, G. and Valtonen, M. (1990).  
Tidal generation of active spirals and S0 galaxies by rich clusters.  
*ApJ*, 350:89–94.
- Carlberg, R. G., Yee, H. K. C., Ellingson, E., Abraham, R., Gravel, P., Morris, S., and Pritchet, C. J. (1996).  
Galaxy Cluster Virial Masses and Omega.  
*ApJ*, 462:32.
- Carlberg, R. G., Yee, H. K. C., Ellingson, E., Morris, S. L., Abraham, R., Gravel, P., Pritchet, C. J., Smecker-Hane, T., Hartwick, F. D. A., Hesser, J. E., Hutchings, J. B., and Oke, J. B. (1997).  
The Average Mass Profile of Galaxy Clusters.  
*ApJ*, 485:L13.
- Carlberg, R. G., Yee, H. K. C., Morris, S. L., Lin, H., Hall, P. B., Patton, D. R., Sawicki, M., and Shepherd, C. W. (2001).  
Galaxy Groups at Intermediate Redshift.  
*ApJ*, 552:427–444.
- Cavaliere, A. and Fusco-Femiano, R. (1976).  
X-rays from hot plasma in clusters of galaxies.  
*A&A*, 49:137–144.
- Cavaliere, A., Menci, N., and Tozzi, P. (1997).  
The Luminosity-Temperature Relation for Groups and Clusters of Galaxies.  
*ApJ*, 484:L21.

- Cen, R. (1992).  
A hydrodynamic approach to cosmology - Methodology.  
*ApJS*, 78:341–364.
- Cen, R. (2001).  
Decaying Cold Dark Matter Model and Small-Scale Power.  
*ApJ*, 546:L77–L80.
- Cen, R. Y., Ostriker, J. P., Jameson, A., and Liu, F. (1990).  
The universe in a box - Thermal effects in the standard cold dark matter scenario.  
*ApJ*, 362:L41–L45.
- Chen, D. N. and Jing, Y. P. (2002).  
The Angular Momentum Distribution within Halos in Different Dark Matter Models.  
(astro-ph/0201520).
- Cole, S. (1991).  
Modeling galaxy formation in evolving dark matter halos.  
*ApJ*, 367:45–53.
- Cole, S., Aragon-Salamanca, A., Frenk, C. S., Navarro, J. F., and Zepf, S. E. (1994a).  
A Recipe for Galaxy Formation.  
*MNRAS*, 271:781.
- Cole, S., Aragon-Salamanca, A., Frenk, C. S., Navarro, J. F., and Zepf, S. E. (1994b).  
A Recipe for Galaxy Formation.  
*MNRAS*, 271:781.
- Cole, S., Lacey, C. G., Baugh, C. M., and Frenk, C. S. (2000).  
Hierarchical galaxy formation.  
*MNRAS*, 319:168–204.
- Colella, P. and Woodward, P. R. (1984).  
Hydrodynamical simulations of galaxy formation: effects of supernova feedback.  
*J.Comp.Phys*, 54:174–.
- Colella, P. and Woodward, P. R. (1985).  
*J.Sci. Stat. Comp.*, 6:85.
- Colín, P., Avila-Reese, V., and Valenzuela, O. (2000a).  
Substructure and Halo Density Profiles in a Warm Dark Matter Cosmology.  
*ApJ*, 542:622–630.

- Colín, P., Klypin, A. A., and Kravtsov, A. V. (2000b).  
Velocity Bias in a  $\Lambda$  Cold Dark Matter Model.  
*ApJ*, 539:561–569.
- Colín, P., Klypin, A. A., Kravtsov, A. V., and Khokhlov, A. M. (1999).  
Evolution of Bias in Different Cosmological Models.  
*ApJ*, 523:32–53.
- Connolly, A. J., Szalay, A. S., Dickinson, M., Subbarao, M. U., and Brunner, R. J. (1997).  
The Evolution of the Global Star Formation History as Measured from the Hubble Deep Field.  
*ApJ*, 486:L11.
- Couch, W. J., Balogh, M. L., Bower, R. G., Smail, I., Glazebrook, K., and Taylor, M. (2001).  
A Low Global Star Formation Rate in the Rich Galaxy Cluster AC 114 at  $z=0.32$ .  
*ApJ*, 549:820–831.
- Couch, W. J. and Sharples, R. M. (1987).  
A spectroscopic study of three rich galaxy clusters at  $Z = 0.31$ .  
*MNRAS*, 229:423–456.
- Couchman, H. M. P. (1991).  
Mesh-refined P3M - A fast adaptive N-body algorithm.  
*ApJ*, 368:L23–L26.
- Cowie, L. L., Songaila, A., and Barger, A. J. (1999).  
Evidence for a Gradual Decline in the Universal Rest-Frame Ultraviolet Luminosity Density for  $z < 1$ .  
*AJ*, 118:603–612.
- Crone, M. M., Evrard, A. E., and Richstone, D. O. (1994).  
The cosmological dependence of cluster density profiles.  
*ApJ*, 434:402–416.
- Dahle, H., Hannestad, S., and J., S. (2002).  
The Density Profile of Cluster-scale Dark Matter Halos.  
*ApJ*, *submitted* ([astro-ph/0206455](https://arxiv.org/abs/astro-ph/0206455)).
- Dahle, H., Kaiser, N., Squires, G., and Broadhurst, T. J. (2001).  
Weak Lensing Analysis of a WFPC2 Mosaic of Abell 1689.  
In *ASP Conf. Ser. 237: Gravitational Lensing: Recent Progress and Future Go*, page 311.

- Davé, R., Spergel, D. N., Steinhardt, P. J., and Wandelt, B. D. (2001).  
Halo Properties in Cosmological Simulations of Self-interacting Cold Dark Matter.  
*ApJ*, 547:574–589.
- David, L. P., Slyz, A., Jones, C., Forman, W., Vrtillek, S. D., and Arnaud, K. A. (1993).  
A catalog of intracluster gas temperatures.  
*ApJ*, 412:479–488.
- Davis, M., Efstathiou, G., Frenk, C. S., and White, S. D. M. (1985).  
The evolution of large-scale structure in a universe dominated by cold dark matter.  
*ApJ*, 292:371–394.
- de Bernardis, P., Ade, P. A. R., Bock, J. J., Bond, J. R., Borrill, J., Boscaleri, A., Coble, K., Crill, B. P., De Gasperis, G., Farese, P. C., Ferreira, P. G., Ganga, K., Giacometti, M., Hivon, E., Hristov, V. V., Iacoangeli, A., Jaffe, A. H., Lange, A. E., Martinis, L., Masi, S., Mason, P. V., Maukkopf, P. D., Melchiorri, A., Miglio, L., Montroy, T., Netterfield, C. B., Pascale, E., Piacentini, F., Pogosyan, D., Prunet, S., Rao, S., Romeo, G., Ruhl, J. E., Scaramuzzi, F., Sforna, D., and Vittorio, N. (2000).  
A flat Universe from high-resolution maps of the cosmic microwave background radiation.  
*Nature*, 404:955–959.
- de Blok, W. J. G. and Bosma, A. (2002).  
High-resolution rotation curves of low surface brightness galaxies.  
*A&A*, 385:816–846.
- de Blok, W. J. G., McGaugh, S. S., Bosma, A., and Rubin, V. C. (2001).  
Mass Density Profiles of Low Surface Brightness Galaxies.  
*ApJ*, 552:L23–L26.
- De Grandi, S. and Molendi, S. (2002).  
Temperature Profiles of Nearby Clusters of Galaxies.  
*ApJ*, 567:163–177.
- Del Popolo, A., Gambera, M., Recami, E., and Spedicato, E. (2000).  
Density profiles of dark matter halos in an improved secondary infall model.  
*A&A*, 353:427–434.
- den Hartog, R. and Katgert, P. (1996).  
On the dynamics of the cores of galaxy clusters.  
*MNRAS*, 279:349–388.

- Diaferio, A., Kauffmann, G., Balogh, M. L., White, S. D. M., Schade, D., and Ellingson, E. (2001).  
The spatial and kinematic distributions of cluster galaxies in a  $\Lambda$ CDM universe: comparison with observations.  
*MNRAS*, 323:999–1015.
- Doroshkevich, A. G. (1970).  
*Astrofisika*, 6:581.
- Dressler, A. (1980).  
Galaxy morphology in rich clusters - Implications for the formation and evolution of galaxies.  
*ApJ*, 236:351–365.
- Dressler, A., Oemler, A. J., Couch, W. J., Smail, I., Ellis, R. S., Barger, A., Butcher, H., Poggianti, B. M., and Sharples, R. M. (1997).  
Evolution since  $Z = 0.5$  of the Morphology-Density Relation for Clusters of Galaxies.  
*ApJ*, 490:577.
- Dressler, A., Thompson, I. B., and Shectman, S. A. (1985).  
Statistics of emission-line galaxies in rich clusters.  
*ApJ*, 288:481–486.
- Dubinski, J. (1996).  
A parallel tree code.  
*New Astronomy*, 1:133–147.
- Dubinski, J. and Carlberg, R. G. (1991).  
The structure of cold dark matter halos.  
*ApJ*, 378:496–503.
- Edge, A. C. and Stewart, G. C. (1991).  
EXOSAT Observations of Clusters of Galaxies - Part Two - X-Ray to Optical Correlations.  
*MNRAS*, 252:428.
- Edge, A. C., Stewart, G. C., and Fabian, A. C. (1992).  
Properties of cooling flows in a flux-limited sample of clusters of galaxies.  
*MNRAS*, 258:177–188.
- Efstathiou, G. (1992).  
Suppressing the formation of dwarf galaxies via photoionization.  
*MNRAS*, 256:43P–47P.
- Efstathiou, G., Bond, J. R., and White, S. D. M. (1992).  
COBE background radiation anisotropies and large-scale structure in the universe.

- MNRAS*, 258:1P–6P.
- Efstathiou, G., Moody, S., Peacock, J. A., Percival, W. J., Baugh, C., Bland-Hawthorn, J., Bridges, T., Cannon, R., Cole, S., Colless, M., Collins, C., Couch, W., Dalton, G., de Propris, R., Driver, S. P., Ellis, R. S., Frenk, C. S., Glazebrook, K., Jackson, C., Lahav, O., Lewis, I., Lumsden, S., Maddox, S., Norberg, P., Peterson, B. A., Sutherland, W., and Taylor, K. (2002).  
Evidence for a non-zero  $\Lambda$  and a low matter density from a combined analysis of the 2dF Galaxy Redshift Survey and cosmic microwave background anisotropies.  
*MNRAS*, 330:L29–L35.
- Eke, V. R., Navarro, J. F., and Frenk, C. S. (1998).  
The Evolution of X-Ray Clusters in a Low-Density Universe.  
*ApJ*, 503:569.
- Ettori, S. (2000).  
Note on a polytropic  $\beta$ -model to fit the X-ray surface brightness of clusters of galaxies.  
*MNRAS*, 311:313–316.
- Ettori, S., Allen, S. W., and Fabian, A. C. (2001).  
BeppoSAX observations of three distant, highly luminous clusters of galaxies: RXJ1347-1145, Zwicky 3146 and Abell 2390.  
*MNRAS*, 322:187–194.
- Ettori, S., De Grandi, S., and Molendi, S. (2002a).  
Gravitating mass profiles of nearby galaxy clusters and relations with X-ray gas temperature, luminosity and mass.  
*A&A*, 391:841–855.
- Ettori, S. and Fabian, A. C. (1999).  
ROSAT PSPC observations of 36 high-luminosity clusters of galaxies: constraints on the gas fraction.  
*MNRAS*, 305:834–848.
- Ettori, S., Fabian, A. C., Allen, S. W., and Johnstone, R. M. (2002b).  
Deep inside the core of Abell 1795: the Chandra view.  
*MNRAS*, 331:635–648.
- Evrard, A. E. and Henry, J. P. (1991).  
Expectations for X-ray cluster observations by the ROSAT satellite.  
*ApJ*, 383:95–103.
- Evrard, A. E., Metzler, C. A., and Navarro, J. F. (1996).  
Mass Estimates of X-Ray Clusters.  
*ApJ*, 469:494.

- Fabian, A. C. (1994).  
Cooling Flows in Clusters of Galaxies.  
*ARA&A*, 32:277–318.
- Fabian, A. C. (2002).  
Cluster cores and cooling flows.  
(astro-ph/0210150).
- Fadda, D., Girardi, M., Giuricin, G., Mardirossian, F., and Mezzetti, M. (1996).  
The Observational Distribution of Internal Velocity Dispersions in Nearby Galaxy Clusters.  
*ApJ*, 473:670.
- Fall, S. M. (1978).  
On the evolution of galaxy clustering and cosmological N-body simulations.  
*MNRAS*, 185:165–178.
- Fillmore, J. A. and Goldreich, P. (1984).  
Self-similar gravitational collapse in an expanding universe.  
*ApJ*, 281:1–8.
- Finoguenov, A., Reiprich, T. H., and Böhringer, H. (2001).  
Details of the mass-temperature relation for clusters of galaxies.  
*A&A*, 368:749–759.
- Flores, H., Hammer, F., Thuan, T. X., Césarsky, C., Desert, F. X., Omont, A., Lilly, S. J., Eales, S., Crampton, D., and Le Fèvre, O. (1999).  
15 Micron Infrared Space Observatory Observations of the 1415+52 Canada-France Redshift Survey Field: The Cosmic Star Formation Rate as Derived from Deep Ultraviolet, Optical, Mid-Infrared, and Radio Photometry.  
*ApJ*, 517:148–167.
- Flores, R. A. and Primack, J. R. (1994).  
Observational and theoretical constraints on singular dark matter halos.  
*ApJ*, 427:L1–L4.
- Freedman, W. L., Madore, B. F., Gibson, B. K., Ferrarese, L., Kelson, D. D., Sakai, S., Mould, J. R., Kennicutt, R. C., Ford, H. C., Graham, J. A., Huchra, J. P., Hughes, S. M. G., Illingworth, G. D., Macri, L. M., and Stetson, P. B. (2001).  
Final Results from the Hubble Space Telescope Key Project to Measure the Hubble Constant.  
*ApJ*, 553:47–72.



- Frenk, C. S., White, S. D. M., Bode, P., Bond, J. R., Bryan, G. L., Cen, R., Couchman, H. M. P., Evrard, A. E., Gnedin, N., Jenkins, A., Khokhlov, A. M., Klypin, A., Navarro, J. F., Norman, M. L., Ostriker, J. P., Owen, J. M., Pearce, F. R., Pen, U.-L., Steinmetz, M., Thomas, P. A., Villumsen, J. V., Wadsley, J. W., Warren, M. S., Xu, G., and Yepes, G. (1999).  
The Santa Barbara Cluster Comparison Project: A Comparison of Cosmological Hydrodynamics Solutions.  
*ApJ*, 525:554–582.
- Frenk, C. S., White, S. D. M., Davis, M., and Efstathiou, G. (1988).  
The formation of dark halos in a universe dominated by cold dark matter.  
*ApJ*, 327:507–525.
- Frenk, C. S., White, S. D. M., Efstathiou, G., and Davis, M. (1990).  
Galaxy clusters and the amplitude of primordial fluctuations.  
*ApJ*, 351:10–21.
- Fukugita, M., Hogan, C. J., and Peebles, P. J. E. (1998).  
The Cosmic Baryon Budget.  
*ApJ*, 503:518.
- Fukushige, T. and Makino, J. (1997).  
On the Origin of Cusps in Dark Matter Halos.  
*ApJ*, 477:L9.
- Fukushige, T. and Makino, J. (2001).  
Structure of Dark Matter Halos from Hierarchical Clustering.  
*ApJ*, 557:533–545.
- Gallego, J., Zamorano, J., Aragon-Salamanca, A., and Rego, M. (1995).  
The Current Star Formation Rate of the Local Universe.  
*ApJ*, 455:L1.
- Gamow, G. (1946).  
*Phys. Rev.*, 70:572–573.
- Geller, M. J., Diaferio, A., and Kurtz, M. J. (1999).  
The Mass Profile of the Coma Galaxy Cluster.  
*ApJ*, 517:L23–L26.
- Ghigna, S., Moore, B., Governato, F., Lake, G., Quinn, T., and Stadel, J. (1998).  
Dark matter haloes within clusters.  
*MNRAS*, 300:146–162.
- Ghigna, S., Moore, B., Governato, F., Lake, G., Quinn, T., and Stadel, J. (2000).

- Density Profiles and Substructure of Dark Matter Halos: Converging Results at Ultra-High Numerical Resolution.  
*ApJ*, 544:616–628.
- Gingold, R. A. and Monaghan, J. J. (1977).  
Smoothed particle hydrodynamics - Theory and application to non-spherical stars.  
*MNRAS*, 181:375–389.
- Giovanelli, R. and Haynes, M. P. (1985).  
Gas deficiency in cluster galaxies - A comparison of nine clusters.  
*ApJ*, 292:404–425.
- Gispert, R., Lagache, G., and Puget, J. L. (2000).  
Implications of the cosmic infrared background for light production and the star formation history in the Universe.  
*A&A*, 360:1–9.
- Glazebrook, K., Blake, C., Economou, F., Lilly, S., and Colless, M. (1999).  
Measurement of the star formation rate from H $\alpha$  in field galaxies at  $z=1$ .  
*MNRAS*, 306:843–856.
- Gnedin, N. Y. (1995).  
Softened Lagrangian hydrodynamics for cosmology.  
*ApJS*, 97:231–257.
- Gomez, P., Nichol, R., Miller, C., Balogh, M., Goto, T., Zabludoff, A., Romer, K., Bernardi, M., Sheth, R., Hopkins, A., Castander, F., Connolly, A., Schneider, D., Brinkmann, J., Lamb, D., SubbaRao, M., and York, D. (2002).  
Galaxy Star-Formation as a Function of Environment in the Early Data Release of the Sloan Digital Sky Survey.  
In *Accepted for publication in ApJ, 24 pages in emulateapj.sty*, page 10193.
- Goodman, J. (2000).  
Repulsive dark matter.  
*New Astronomy*, 5:103–107.
- Gottlöber, S., Klypin, A., and Kravtsov, A. V. (2001).  
Merging History as a Function of Halo Environment.  
*ApJ*, 546:223–233.
- Gottlöber, S., Müller, V., and Starobinsky, A. A. (1991).  
Analysis of inflation driven by a scalar field and a curvature-squared term.  
*Phys. Rev. D*, 43:2510–2520.

- Greengard, L. F. (1988).  
*The rapid evaluation of potential fields in particle systems.*  
MIT Press, 1988.
- Gunn, J. E. (1977).  
Massive galactic halos. I - Formation and evolution.  
*ApJ*, 218:592–598.
- Gunn, J. E. and Gott, J. R. I. (1972).  
On the Infall of Matter Into Clusters of Galaxies and Some Effects on  
Their Evolution.  
*ApJ*, 176:1.
- Gurevich, A. V. and Zybin, K. P. (1988).  
Nondissipative gravitational turbulence.  
*Zhurnal Eksperimental noi i Teoreticheskoi Fiziki*, 94:3–25.
- Haarsma, D. B., Partridge, R. B., Windhorst, R. A., and Richards, E. A.  
(2000).  
Faint Radio Sources and Star Formation History.  
*ApJ*, 544:641–658.
- Halverson, N. W., Leitch, E. M., Pryke, C., Kovac, J., Carlstrom, J. E.,  
Holzapfel, W. L., Dragovan, M., Cartwright, J. K., Mason, B. S., Padin,  
S., Pearson, T. J., Readhead, A. C. S., and Shepherd, M. C. (2002).  
Degree Angular Scale Interferometer First Results: A Measurement of the  
Cosmic Microwave Background Angular Power Spectrum.  
*ApJ*, 568:38–45.
- Hammer, F., Flores, H., Lilly, S. J., Crampton, D., Le Fevre, O., Rola, C.,  
Mallen-Ornelas, G., Schade, D., and Tresse, L. (1997).  
Canada-France Redshift Survey. XIV. Spectral Properties of Field Galax-  
ies up to  $z=1$ .  
*ApJ*, 481:49.
- Hanany, S., Ade, P., Balbi, A., Bock, J., Borrill, J., Boscaleri, A., de  
Bernardis, P., Ferreira, P. G., Hristov, V. V., Jaffe, A. H., Lange, A. E.,  
Lee, A. T., Mauskopf, P. D., Netterfield, C. B., Oh, S., Pascale, E., Rabi,  
B., Richards, P. L., Smoot, G. F., Stompor, R., Winant, C. D., and Wu,  
J. H. P. (2000).  
MAXIMA-1: A Measurement of the Cosmic Microwave Background  
Anisotropy on Angular Scales of  $10' - 5\text{deg}$ .  
*ApJ*, 545:L5–L9.
- Hancock, S., Rocha, G., Lasenby, A. N., and Gutierrez, C. M. (1998).  
Constraints on cosmological parameters from recent measurements of cos-  
mic microwave background anisotropy.

*MNRAS*, 294:L1–L6.

Hashimoto, Y., Oemler, A. J., Lin, H., and Tucker, D. L. (1998).

The Influence of Environment on the Star Formation Rates of Galaxies.  
*ApJ*, 499:589.

Henriksen, R. N. and Widrow, L. M. (1999).

Relaxing and virializing a dark matter halo.  
*MNRAS*, 302:321–336.

Hernquist, L. (1993).

Some cautionary remarks about smoothed particle hydrodynamics.  
*ApJ*, 404:717–722.

Hernquist, L., Katz, N., Weinberg, D. H., and Jordi, M. (1996).

The Lyman-Alpha Forest in the Cold Dark Matter Model.  
*ApJ*, 457:L51.

Hiotelis, N. (2002a).

Density profiles in a spherical infall model with non-radial motions.  
*A&A*, 382:84–91.

Hiotelis, N. (2002b).

Density profiles of dark matter halos with anisotropic velocity tensors.  
(astro-ph/0207628).

Hockney, R. W. and Eastwood, J. W. (1981).

*Computer Simulation Using Particles*.  
Computer Simulation Using Particles, New York: McGraw-Hill, 1981.

Hockney, R. W., Goel, S. P. ., and Eastwood, J. W. (1974).

Quiet high-resolution computer simulations.  
*J. Comp. Phys*, 14:148.

Hoffman, Y. (1988).

On the formation and structure of galactic halos.  
*ApJ*, 328:489–498.

Hoffman, Y. and Shaham, J. (1985).

Local density maxima - Progenitors of structure.  
*ApJ*, 297:16–22.

Hopkins, A. M., Connolly, A. J., Haarsma, D. B., and Cram, L. E. (2001).

Toward a Resolution of the Discrepancy between Different Estimators of Star Formation Rate.  
*AJ*, 122:288–296.

- Horner, D. J., Mushotzky, R. F., and Scharf, C. A. (1999).  
Observational Tests of the Mass-Temperature Relation for Galaxy Clusters.  
*ApJ*, 520:78–86.
- Hu, W., Barkana, R., and Gruzinov, A. (2000).  
Observational Evidence for Self-Interacting Cold Dark Matter.  
*Physical Review Letters*, 85:1158–1161.
- Hubble, E. (1929).  
A Relation between Distance and Radial Velocity among Extra-Galactic Nebulae.  
*Proceedings of the National Academy of Science*, 15:168–173.
- Hughes, D. H., Serjeant, S., Dunlop, J., Rowan-Robinson, M., Blain, A., Mann, R. G., Ivison, R., Peacock, J., Efstathiou, A., Gear, W., Oliver, S., Lawrence, A., Longair, M., Goldschmidt, P., and Jenness, T. (1998).  
High-redshift star formation in the Hubble Deep Field revealed by a submillimetre-wavelength survey.  
*Nature*, 394:241–247.
- Iglesias-Páramo, J., Boselli, A., Cortese, L., Vílchez, J. M., and Gavazzi, G. (2002).  
A deep H $\alpha$  survey of galaxies in the two nearby clusters Abell 1367 and Coma. The H $\alpha$  luminosity functions.  
*A&A*, 384:383–392.
- Irwin, J. A. and Bregman, J. N. (2000).  
Radial Temperature Profiles of 11 Clusters of Galaxies Observed with BEPOSAX.  
*ApJ*, 538:543–554.
- Jansen, F., Lumb, D., Altieri, B., Clavel, J., Ehle, M., Erd, C., Gabriel, C., Guainazzi, M., Gondoin, P., Much, R., Munoz, R., Santos, M., Schartel, N., Texier, D., and Vacanti, G. (2001).  
XMM-Newton observatory. I. The spacecraft and operations.  
*A&A*, 365:L1–L6.
- Jernigan, J. G. and Porter, D. H. (1989).  
A tree code with logarithmic reduction of force terms, hierarchical regularization of all variables, and explicit accuracy controls.  
*ApJS*, 71:871–893.
- Jimenez, R., Verde, L., and Oh, S. P. (2002).  
Dark halo properties from rotation curves.  
*MNRAS*, submitted (astro-ph/0201352).

- Jing, Y. P. (2000).  
The Density Profile of Equilibrium and Nonequilibrium Dark Matter Halos.  
*ApJ*, 535:30–36.
- Jing, Y. P. and Suto, Y. (2000).  
The Density Profiles of the Dark Matter Halo Are Not Universal.  
*ApJ*, 529:L69–L72.
- Kaiser, N. (1986).  
Evolution and clustering of rich clusters.  
*MNRAS*, 222:323–345.
- Kaiser, N. (1991).  
Evolution of clusters of galaxies.  
*ApJ*, 383:104–111.
- Kang, H., Ostriker, J. P., Cen, R., Ryu, D., Hernquist, L., Evrard, A. E., Bryan, G. L., and Norman, M. L. (1994).  
A comparison of cosmological hydrodynamic codes.  
*ApJ*, 430:83–100.
- Kaplinghat, M., Knox, L., and Turner, M. S. (2000).  
Observational Evidence for Self-Interacting Cold Dark Matter.  
*Physical Review Letters*, 85:3335–3338.
- Kates, R., Muller, V., Gottlober, S., Mucket, J. P., and Retzlaff, J. (1995).  
Large-scale structure formation for power spectra with broken scale invariance.  
*MNRAS*, 277:1254–1268.
- Kauffmann, G., White, S. D. M., and Guiderdoni, B. (1993a).  
The Formation and Evolution of Galaxies Within Merging Dark Matter Haloes.  
*MNRAS*, 264:201.
- Kauffmann, G., White, S. D. M., and Guiderdoni, B. (1993b).  
The Formation and Evolution of Galaxies Within Merging Dark Matter Haloes.  
*MNRAS*, 264:201.
- Kellogg, E., Gursky, H., Tananbaum, H., Giacconi, R., and Pounds, K. (1972).  
The Extended X-Ray Source at M87.  
*ApJ*, 174:L65.

- Kennicutt, R. C. (1998).  
Star Formation in Galaxies Along the Hubble Sequence.  
*ARA&A*, 36:189–232.
- Khokhlov, A. M. (1998).  
Fully Threaded Tree Algorithms for Adaptive Refinement Fluid Dynamics Simulations.  
*J.Comp.Phys*, 143:239–267.
- King, I. (1962).  
The structure of star clusters. I. an empirical density law.  
*AJ*, 67:471.
- Klypin, A., Gottlöber, S., Kravtsov, A. V., and Khokhlov, A. M. (1999).  
Galaxies in N-Body Simulations: Overcoming the Overmerging Problem.  
*ApJ*, 516:530–551.
- Klypin, A., Kravtsov, A. V., Bullock, J. S., and Primack, J. R. (2001).  
Resolving the Structure of Cold Dark Matter Halos.  
*ApJ*, 554:903–915.
- Klypin, A., Primack, J., and Holtzman, J. (1996).  
Small-Scale Power Spectrum and Correlations in Lambda + Cold Dark Matter Models.  
*ApJ*, 466:13.
- Klypin, A. A. and Shandarin, S. F. (1983).  
Three-dimensional numerical model of the formation of large-scale structure in the Universe.  
*MNRAS*, 204:891–907.
- Knebe, A., Green, A., and Binney, J. (2001).  
Multi-level adaptive particle mesh (MLAPM): a c code for cosmological simulations.  
*MNRAS*, 325:845–864.
- Knebe, A., Kravtsov, A. V., Gottlöber, S., and Klypin, A. A. (2000).  
On the effects of resolution in dissipationless cosmological simulations.  
*MNRAS*, 317:630–648.
- Kodama, T. and Smail, I. (2001).  
Testing the hypothesis of the morphological transformation from field spiral to cluster S0.  
*MNRAS*, 326:637–642.
- Kolb, E. W. and Turner, M. S. (1990).  
*The early universe*.  
Frontiers in Physics, Reading, MA: Addison-Wesley, 1988, 1990.

- Komatsu, E. and Seljak, U. (2001).  
Universal gas density and temperature profile.  
*MNRAS*, 327:1353–1366.
- Koranyi, D. M. and Geller, M. J. (2000).  
Kinematics and Mass Profile of AWM 7.  
*AJ*, 119:44–58.
- Kravtsov, A. V., Klypin, A., and Hoffman, Y. (2002).  
Constrained Simulations of the Real Universe. II. Observational Signatures of Intergalactic Gas in the Local Supercluster Region.  
*ApJ*, 571:563–575.
- Kravtsov, A. V., Klypin, A. A., Bullock, J. S., and Primack, J. R. (1998).  
The Cores of Dark Matter-dominated Galaxies: Theory versus Observations.  
*ApJ*, 502:48.
- Kravtsov, A. V., Klypin, A. A., and Khokhlov, A. M. (1997).  
Adaptive Refinement Tree: A New High-Resolution N-Body Code for Cosmological Simulations.  
*ApJS*, 111:73.
- Kravtsov, A. V. and Yepes, G. (2000).  
On the supernova heating of the intergalactic medium.  
*MNRAS*, 318:227–238.
- Kull, A. (1999).  
A Model for the Density Distribution of Virialized Cold Dark Matter Halos.  
*ApJ*, 516:L5–L8.
- Lacey, C. and Cole, S. (1994).  
Merger Rates in Hierarchical Models of Galaxy Formation - Part Two - Comparison with N-Body Simulations.  
*MNRAS*, 271:676.
- Lange, A. E., Ade, P. A., Bock, J. J., Bond, J. R., Borrill, J., Boscaleri, A., Coble, K., Crill, B. P., de Bernardis, P., Farese, P., Ferreira, P., Ganga, K., Giacometti, M., Hivon, E., Hristov, V. V., Iacoangeli, A., Jaffe, A. H., Martinis, L., Masi, S., Mauskopf, P. D., Melchiorri, A., Montroy, T., Netterfield, C. B., Pascale, E., Piacentini, F., Pogosyan, D., Prunet, S., Rao, S., Romeo, G., Ruhl, J. E., Scaramuzzi, F., and Sforna, D. (2001).  
Cosmological parameters from the first results of Boomerang.  
*Phys. Rev. D*, 63:42001.



- Lavery, R. J. and Henry, J. P. (1988).  
Evidence for galaxy-galaxy interactions as an active agent of the 'Butcher-Oemler' effect at a redshift of 0.2.  
*ApJ*, 330:596–600.
- Lee, A. T., Ade, P., Balbi, A., Bock, J., Borrill, J., Boscaleri, A., de Bernardis, P., Ferreira, P. G., Hanany, S., Hristov, V. V., Jaffe, A. H., Mauskopf, P. D., Netterfield, C. B., Pascale, E., Rabii, B., Richards, P. L., Smoot, G. F., Stompor, R., Winant, C. D., and Wu, J. H. P. (2001).  
A High Spatial Resolution Analysis of the MAXIMA-1 Cosmic Microwave Background Anisotropy Data.  
*ApJ*, 561:L1–L5.
- Lewis, A. D., Buote, D. A., and Stoke, J. T. (2002a).  
Chandra Observations of Abell 2029: The Dark Matter Profile at  $< 0.01R_{vir}$  in an Unusually Relaxed Cluster.  
*ApJ*, *submitted* (astro-ph/0209205).
- Lewis, I., Balogh, M., De Propris, R., Couch, W., Bower, R., Offer, A., Bland-Hawthorn, J., Baldry, I. K., Baugh, C., Bridges, T., Cannon, R., Cole, S., Colless, M., Collins, C., Cross, N., Dalton, G., Driver, S. P., Efstathiou, G., Ellis, R. S., Frenk, C. S., Glazebrook, K., Hawkins, E., Jackson, C., Lahav, O., Lumsden, S., Maddox, S., Madgwick, D., Norberg, P., Peacock, J. A., Percival, W., Peterson, B. A., Sutherland, W., and Taylor, K. (2002b).  
The 2dF Galaxy Redshift Survey: the environmental dependence of galaxy star formation rates near clusters.  
*MNRAS*, 334:673–683.
- Lia, C. and Carraro, G. (2001).  
Parallel Tree-SPH: A Tool for Galaxy Formation.  
*Ap&SS*, 276:1049–1056.
- Lilje, P. B. (1992).  
Abundance of rich clusters of galaxies - A test for cosmological parameters.  
*ApJ*, 386:L33–L36.
- Lilly, S. J., Le Fevre, O., Hammer, F., and Crampton, D. (1996).  
The Canada-France Redshift Survey: The Luminosity Density and Star Formation History of the Universe to  $z$  approximately 1.  
*ApJ*, 460:L1.
- Lineweaver, C. H., Barbosa, D., Blanchard, A., and Bartlett, J. G. (1997).  
Constraints on  $h$ ,  $\Omega_b$  and  $\Omega_c$  from cosmic microwave background observations.  
*A&A*, 322:365–374.

- Lokas, E. L. (2000).  
Universal profile of dark matter haloes and the spherical infall model.  
*MNRAS*, 311:423–432.
- Lokas, E. L. and Hoffman, Y. (2000).  
Formation of Cuspy Density Profiles: A Generic Feature of Collisionless  
Gravitational Collapse.  
*ApJ*, 542:L139–L142.
- Lokas, E. L. and Mamon, G. A. (2001).  
Properties of spherical galaxies and clusters with an NFW density profile.  
*MNRAS*, 321:155–166.
- Loken, C., Norman, M. L., Nelson, E., Burns, J., Bryan, G. L., and Motl,  
P. (2002).  
A Universal Temperature Profile for Galaxy Clusters.  
*ApJ*, 579:571–576.
- Lucey, J. R. (1983).  
An assessment of the completeness and correctness of the Abell catalogue.  
*MNRAS*, 204:33–43.
- Lucy, L. B. (1977).  
A numerical approach to the testing of the fission hypothesis.  
*AJ*, 82:1013–1024.
- Lynden-Bell, D. (1967).  
Statistical mechanics of violent relaxation in stellar systems.  
*MNRAS*, 136:101.
- Macfarland, T., Couchman, H. M. P., Pearce, F. R., and Pichlmeier, J.  
(1998).  
A new parallel  $P^3M$  code for very large-scale cosmological simulations.  
*New Astronomy*, 3:687–705.
- Madau, P., Ferguson, H. C., Dickinson, M. E., Giavalisco, M., Steidel, C. C.,  
and Fruchter, A. (1996).  
High-redshift galaxies in the Hubble Deep Field: colour selection and star  
formation history to  $z \sim 4$ .  
*MNRAS*, 283:1388–1404.
- Madau, P., Pozzetti, L., and Dickinson, M. (1998).  
The Star Formation History of Field Galaxies.  
*ApJ*, 498:106.
- Makino, J. (2002).  
An efficient parallel algorithm for  $O(N^2)$  direct summation method and  
its variations on distributed-memory parallel mac.

- New Astronomy*, 7:373–384.
- Marchesini, D., D’Onghia, E., Chincarini, G., Firmani, C., Conconi, P., Molinari, E., and Zacchei, A. (2002).  
H $\alpha$  Rotation Curves: The Soft Core Question.  
*ApJ*, 575:801–813.
- Markevitch, M., Forman, W. R., Sarazin, C. L., and Vikhlinin, A. (1998).  
The Temperature Structure of 30 Nearby Clusters Observed with ASCA:  
Similarity of Temperature Profiles.  
*ApJ*, 503:77.
- Martel, H. and Shapiro, P. R. (1998).  
A convenient set of comoving cosmological variables and their application.  
*MNRAS*, 297:467–485.
- Martínez, H. J., Zandivarez, A., Domínguez, M., Merchán, M. E., and Lambas, D. G. (2002).  
Galaxy groups in the 2dF Galaxy Redshift Survey: effects of environment  
on star formation.  
*MNRAS*, 333:L31–L34.
- Mathiesen, B. F. and Evrard, A. E. (2001).  
Four Measures of the Intracluster Medium Temperature and Their Relation  
to a Cluster’s Dynamical State.  
*ApJ*, 546:100–116.
- Mazure, A., Katgert, P., den Hartog, R., Biviano, A., Dubath, P., Escalera,  
E., Focardi, P., Gerbal, D., Giuricin, G., Jones, B., Le Fevre, O., Moles,  
M., Perea, J., and Rhee, G. (1996).  
The ESO Nearby Abell Cluster Survey. II. The distribution of velocity  
dispersions of rich galaxy clusters.  
*A&A*, 310:31–48.
- Mellier, Y. (1999).  
Probing the Universe with Weak Lensing.  
*ARA&A*, 37:127–189.
- Merritt, D. (1983).  
Relaxation and tidal stripping in rich clusters of galaxies. I - Evolution of  
the mass distribution.  
*ApJ*, 264:24–48.
- Miralda-Escude, J. and Babul, A. (1995).  
Gravitational Lensing in Clusters of Galaxies: New Clues Regarding the  
Dynamics of Intracluster Gas.  
*ApJ*, 449:18.

- Mitchell, R. J., Culhane, J. L., Davison, P. J. N., and Ives, J. C. (1976).  
Ariel 5 observations of the X-ray spectrum of the Perseus Cluster.  
*MNRAS*, 175:29P–34P.
- Mitchell, R. J., Dickens, R. J., Burnell, S. J. B., and Culhane, J. L. (1979).  
The X-ray spectra of clusters of galaxies and their relationship to other  
cluster properties.  
*MNRAS*, 189:329–361.
- Mohr, J. J., Mathiesen, B., and Evrard, A. E. (1999).  
Properties of the Intracluster Medium in an Ensemble of Nearby Galaxy  
Clusters.  
*ApJ*, 517:627–649.
- Monaghan, J. J. (1992).  
Smoothed particle hydrodynamics.  
*ARA&A*, 30:543–574.
- Moore, B. (1994).  
Evidence against Dissipationless Dark Matter from Observations of  
Galaxy Haloes.  
*Nature*, 370:629.
- Moore, B., Governato, F., Quinn, T., Stadel, J., and Lake, G. (1998a).  
Resolving the Structure of Cold Dark Matter Halos.  
*ApJ*, 499:L5.
- Moore, B., Katz, N., Lake, G., Dressler, A., and Oemler, A. (1996).  
Galaxy harassment and the evolution of clusters of galaxies.  
*Nature*, 379:613–616.
- Moore, B., Lake, G., and Katz, N. (1998b).  
Morphological Transformation from Galaxy Harassment.  
*ApJ*, 495:139.
- Moore, B., Lake, G., Quinn, T., and Stadel, J. (1999a).  
On the survival and destruction of spiral galaxies in clusters.  
*MNRAS*, 304:465–474.
- Moore, B., Quinn, T., Governato, F., Stadel, J., and Lake, G. (1999b).  
Cold collapse and the core catastrophe.  
*MNRAS*, 310:1147–1152.
- Moss, C. and Whittle, M. (2000).  
An H $\alpha$  survey of eight Abell clusters: the dependence of tidally induced  
star formation on cluster density.  
*MNRAS*, 317:667–686.

- Mould, J. R., Huchra, J. P., Freedman, W. L., Kennicutt, R. C., Ferrarese, L., Ford, H. C., Gibson, B. K., Graham, J. A., Hughes, S. M. G., Illingworth, G. D., Kelson, D. D., Macri, L. M., Madore, B. F., Sakai, S., Sebo, K. M., Silbermann, N. A., and Stetson, P. B. (2000a).  
The Hubble Space Telescope Key Project on the Extragalactic Distance Scale. XXVIII. Combining the Constraints on the Hubble Constant.  
*ApJ*, 529:786–794.
- Mould, J. R., Huchra, J. P., Freedman, W. L., Kennicutt, R. C., Ferrarese, L., Ford, H. C., Gibson, B. K., Graham, J. A., Hughes, S. M. G., Illingworth, G. D., Kelson, D. D., Macri, L. M., Madore, B. F., Sakai, S., Sebo, K. M., Silbermann, N. A., and Stetson, P. B. (2000b).  
Erratum: The Hubble Space Telescope Key Project on the Extragalactic Distance Scale. XXVIII. Combining the Constraints on the Hubble Constant.  
*ApJ*, 545:547–547.
- Muanwong, O., Thomas, P. A., Kay, S. T., and Pearce, F. R. (2002).  
The effect of cooling and preheating on the X-ray properties of clusters of galaxies.  
*MNRAS*, 336:527–540.
- Muecket, J. P. and Kates, R. E. (1997).  
Evolution of a hot primordial gas in the presence of an ionizing ultraviolet background: instabilities, bifurcations, and the formation of Lyman limit systems.  
*A&A*, 324:1–10.
- Nagai, D. and Kravtsov, A. V. (2002).  
Cold Fronts in CDM clusters.  
*ApJ*, *submitted* (astro-ph/0206469).
- Nagamine, K., Fukugita, M., Cen, R., and Ostriker, J. P. (2001).  
Star Formation History and Stellar Metallicity Distribution in a Cold Dark Matter Universe.  
*ApJ*, 558:497–504.
- Navarro, J. F., Frenk, C. S., and White, S. D. M. (1995).  
Simulations of X-ray clusters.  
*MNRAS*, 275:720–740.
- Navarro, J. F., Frenk, C. S., and White, S. D. M. (1996).  
The Structure of Cold Dark Matter Halos.  
*ApJ*, 462:563.
- Navarro, J. F., Frenk, C. S., and White, S. D. M. (1997).  
A Universal Density Profile from Hierarchical Clustering.

*ApJ*, 490:493.

Nelson, R. P. and Papaloizou, J. C. B. (1993).

Three-Dimensional Hydrodynamic Simulations of Collapsing Prolate Clouds.

*MNRAS*, 265:905.

Nelson, R. P. and Papaloizou, J. C. B. (1994).

Variable Smoothing Lengths and Energy Conservation in Smoothed Particle Hydrodynamics.

*MNRAS*, 270:1.

Netterfield, C. B., Ade, P. A. R., Bock, J. J., Bond, J. R., Borrill, J., Boscaleri, A., Coble, K., Contaldi, C. R., Crill, B. P., de Bernardis, P., Farese, P., Ganga, K., Giacometti, M., Hivon, E., Hristov, V. V., Iacoangeli, A., Jaffe, A. H., Jones, W. C., Lange, A. E., Martinis, L., Masi, S., Mason, P., Mauskopf, P. D., Melchiorri, A., Montroy, T., Pascale, E., Piacentini, F., Pogosyan, D., Pongetti, F., Prunet, S., Romeo, G., Ruhl, J. E., and Scaramuzzi, F. (2002).

A Measurement by BOOMERANG of Multiple Peaks in the Angular Power Spectrum of the Cosmic Microwave Background.

*ApJ*, 571:604–614.

Netterfield, C. B., Devlin, M. J., Jarolik, N., Page, L., and Wollack, E. J. (1997).

A Measurement of the Angular Power Spectrum of the Anisotropy in the Cosmic Microwave Background.

*ApJ*, 474:47.

Neumann, D. M. and Arnaud, M. (1999).

Regularity in the X-ray surface brightness profiles of galaxy clusters and the M-T relation.

*A&A*, 348:711–727.

Nevalainen, J., Markevitch, M., and Forman, W. (2000).

The Cluster M-T Relation from Temperature Profiles Observed with ASCA and ROSAT.

*ApJ*, 532:694–699.

Norman, M. L. and Bryan, G. L. (1999).

Cosmological Adaptive Mesh Refinement  $\hat{\{CD\}}$ .

In *ASSL Vol. 240: Numerical Astrophysics*, page 19.

Nusser, A. (2001).

Self-similar spherical collapse with non-radial motions.

*MNRAS*, 325:1397–1401.

- Nusser, A. and Sheth, R. K. (1999).  
Mass growth and density profiles of dark matter haloes in hierarchical clustering.  
*MNRAS*, 303:685–695.
- Oguri, M., Taruya, A., and Suto, Y. (2001).  
Probing the Core Structure of Dark Halos with Tangential and Radial Arc Statistics.  
*ApJ*, 559:572–583.
- Okamoto, T. and Nagashima, M. (2001).  
Morphology-Density Relation for Simulated Clusters of Galaxies in Cold Dark Matter-dominated Universes.  
*ApJ*, 547:109–116.
- O’Meara, J. M., Tytler, D., Kirkman, D., Suzuki, N., Prochaska, J. X., Lubin, D., and Wolfe, A. M. (2001).  
The Deuterium to Hydrogen Abundance Ratio toward a Fourth QSO: HS 0105+1619.  
*ApJ*, 552:718–730.
- Pascarelle, S. M., Lanzetta, K. M., and Fernández-Soto, A. (1998).  
The Ultraviolet Luminosity Density of the Universe from Photometric Redshifts of Galaxies in the Hubble Deep Field.  
*ApJ*, 508:L1–L4.
- Pearce, F. R., Thomas, P. A., Couchman, H. M. P., and Edge, A. C. (2000).  
The effect of radiative cooling on the X-ray properties of galaxy clusters.  
*MNRAS*, 317:1029–1040.
- Pearson, T. J., Mason, B. S., Readhead, A. C. S., Shepherd, M. S., Sievers, J., Udomprasert, P. S., Cartwright, J. K., Farmer, A., Padin, S., Myers, S. T., Bond, J. R., Contaldi, C. R., Pen, U., Prunet, S., Pogosyan, D., Carlstrom, J. E., Kovac, J., Leitch, E. M., Pryke, C., Halverson, N. W., Holzzapfel, W. L., Altamirano, P., Bronfman, L., Casassus, S., May, J., and Joy, M. (2002).  
The Anisotropy of the Microwave Background to  $l = 3500$ : Mosaic Observations with the Cosmic Background Imager.  
*ApJ*, *submitted* (astro-ph/0205388).
- Peebles, P. J. E. (1969).  
Origin of the Angular Momentum of Galaxies.  
*ApJ*, 155:393.
- Peebles, P. J. E. (1982).  
Large-scale background temperature and mass fluctuations due to scale-invariant primeval perturbations.

- ApJ*, 263:L1–L5.
- Peebles, P. J. E. (2000).  
Fluid Dark Matter.  
*ApJ*, 534:L127–L129.
- Pen, U. (1995).  
A Linear Moving Adaptive Particle-Mesh N-Body Algorithm.  
*ApJS*, 100:269.
- Pen, U. (1998).  
A High-Resolution Adaptive Moving Mesh Hydrodynamic Algorithm.  
*ApJS*, 115:19.
- Penzias, A. A. and Wilson, R. W. (1965).  
A Measurement of Excess Antenna Temperature at 4080 Mc/s.  
*ApJ*, 142:419–421.
- Perlmutter, S., Aldering, G., Goldhaber, G., Knop, R. A., Nugent, P., Castro, P. G., Deustua, S., Fabbro, S., Goobar, A., Groom, D. E., Hook, I. M., Kim, A. G., Kim, M. Y., Lee, J. C., Nunes, N. J., Pain, R., Pennypacker, C. R., Quimby, R., Lidman, C., Ellis, R. S., Irwin, M., McMahon, R. G., Ruiz-Lapuente, P., Walton, N., Schaefer, B., Boyle, B. J., Filippenko, A. V., Matheson, T., Fruchter, A. S., Panagia, N., Newberg, H. J. M., Couch, W. J., and The Supernova Cosmology Project (1999).  
Measurements of Omega and Lambda from 42 High-Redshift Supernovae.  
*ApJ*, 517:565–586.
- Pettini, M., Kellogg, M., Steidel, C. C., Dickinson, M., Adelberger, K. L., and Giavalisco, M. (1998).  
Infrared Observations of Nebular Emission Lines from Galaxies at  $Z \sim 3$ .  
*ApJ*, 508:539–550.
- Plionis, M. and Basilakos, S. (2002).  
The cluster substructure-alignment connection.  
*MNRAS*, 329:L47–L51.
- Poggianti, B. M., Smail, I., Dressler, A., Couch, W. J., Barger, A. J., Butcher, H., Ellis, R. S., and Oemler, A. J. (1999).  
The Star Formation Histories of Galaxies in Distant Clusters.  
*ApJ*, 518:576–593.
- Ponman, T. J., Bourner, P. D. J., Ebeling, H., and Bohringer, H. (1996).  
A ROSAT survey of Hickson’s compact galaxy groups.  
*MNRAS*, 283:690–708.



- Ponman, T. J., Cannon, D. B., and Navarro, J. F. (1999).  
The thermal imprint of galaxy formation on X-ray clusters.  
*Nature*, 397:135–137.
- Porciani, C., Dekel, A., and Hoffman, Y. (2002a).  
Testing tidal-torque theory - I. Spin amplitude and direction.  
*MNRAS*, 332:325–338.
- Porciani, C., Dekel, A., and Hoffman, Y. (2002b).  
Testing tidal-torque theory - II. Alignment of inertia and shear and the characteristics of protohaloes.  
*MNRAS*, 332:339–351.
- Power, C., Navarro, J. F., Jenkins, A., Frenk, C. S., White, S. D. M., Springel, V., Stadel, J., and Quinn, T. (2002).  
The Inner Structure of  $\Lambda$ CDM Halos I: A Numerical Convergence Study.  
*MNRAS*, *submitted* (astro-ph/0201544).
- Pratt, G. W. and Arnaud, M. (2002).  
The mass profile of  $j$ ASTROBJ $_i$ A1413 $_i$ /ASTROBJ $_i$  observed with XMM-Newton: Implications for the M-T relation.  
*A&A*, 394:375–393.
- Press, W. H., Flannery, B. P., and Teukolsky, S. A. (1986).  
*Numerical recipes. The art of scientific computing.*  
Cambridge: University Press, 1986.
- Quilis, V., Moore, B., and Bower, R. (2000).  
Gone with the Wind: The Origin of S0 Galaxies in Clusters.  
*Science*, 288:1617–1620.
- Quinn, P. J., Salmon, J. K., and Zurek, W. H. (1986).  
Primordial density fluctuations and the structure of galactic haloes.  
*Nature*, 322:329–335.
- Quinn, P. J. and Zurek, W. H. (1988).  
The angular momentum distribution in galactic halos.  
*ApJ*, 331:1–18.
- Renzini, A. (1998).  
The Main Epoch of Metal Production in the Universe.  
In *ASP Conf. Ser. 146: The Young Universe: Galaxy Formation and Evolution at Intermediate and High Redshift*, page 298.
- Ricker, P. M., Dodelson, S., and Lamb, D. Q. (2000).  
COSMOS: A Hybrid N-Body/Hydrodynamics Code for Cosmological Problems.  
*ApJ*, 536:122–143.

- Riess, A. G., Filippenko, A. V., Challis, P., Clocchiatti, A., Diercks, A., Garnavich, P. M., Gilliland, R. L., Hogan, C. J., Jha, S., Kirshner, R. P., Leibundgut, B., Phillips, M. M., Reiss, D., Schmidt, B. P., Schommer, R. A., Smith, R. C., Spyromilio, J., Stubbs, C., Suntzeff, N. B., and Tonry, J. (1998).  
Observational Evidence from Supernovae for an Accelerating Universe and a Cosmological Constant.  
*AJ*, 116:1009–1038.
- Rogstad, D. H. and Shostak, G. S. (1972).  
Gross Properties of Five Scd Galaxies as Determined from 21 cm Observations.  
*ApJ*, 176:315.
- Rosati, P., Borgani, S., and Norman, C. (2002).  
The Evolution of X-ray Clusters of Galaxies.  
*ARA&A*, 40:539–577.
- Rubin, V. C. and Ford, W. K. J. (1970).  
Rotation of the Andromeda Nebula from a Spectroscopic Survey of Emission Regions.  
*ApJ*, 159:379.
- Sadat, R. and Blanchard, A. (2001).  
New light on the baryon fraction in galaxy clusters.  
*A&A*, 371:19–24.
- Salvador-Sole, E., Solanes, J. M., and Manrique, A. (1998).  
Merger versus Accretion and the Structure of Dark Matter Halos.  
*ApJ*, 499:542.
- Sand, D. J., Treu, T., and Ellis, R. S. (2002).  
The Dark Matter Density Profile of the Lensing Cluster MS 2137-23: A Test of the Cold Dark Matter Paradigm.  
*ApJ*, 574:L129–L133.
- Sarazin, C. L. (1988a).  
*X-ray emission from clusters of galaxies*.  
Cambridge Astrophysics Series, Cambridge: Cambridge University Press, 1988.
- Sarazin, C. L. (1988b).  
*X-ray emission from clusters of galaxies*.  
Cambridge Astrophysics Series, Cambridge: Cambridge University Press, 1988.

- Sato, S., Akimoto, F., Furuzawa, A., Tawara, Y., Watanabe, M., and Kumai, Y. (2000).  
The Observed Mass Profiles of Dark Halos and the Formation Epoch of Galaxies.  
*ApJ*, 537:L73–L76.
- Sawicki, M. J., Lin, H., and Yee, H. K. C. (1997).  
Evolution of the Galaxy Population Based on Photometric Redshifts in the Hubble Deep Field.  
*AJ*, 113:1–12.
- Schindler, S. (1999).  
Distant clusters of galaxies: X-ray properties and their relations.  
*A&A*, 349:435–447.
- Schmidt, B. P., Suntzeff, N. B., Phillips, M. M., Schommer, R. A., Clocchiatti, A., Kirshner, R. P., Garnavich, P., Challis, P., Leibundgut, B., Spyromilio, J., Riess, A. G., Filippenko, A. V., Hamuy, M., Smith, R. C., Hogan, C., Stubbs, C., Diercks, A., Reiss, D., Gilliland, R., Tonry, J., Maza, J. ., Dressler, A., Walsh, J., and Ciardullo, R. (1998).  
The High-Z Supernova Search: Measuring Cosmic Deceleration and Global Curvature of the Universe Using Type IA Supernovae.  
*ApJ*, 507:46–63.
- Schmidt, M. (1968).  
Space Distribution and Luminosity Functions of Quasi-Stellar Radio Sources.  
*ApJ*, 151:393.
- Schmidt, R. W., Allen, S. W., and Fabian, A. C. (2001).  
Chandra observations of the galaxy cluster Abell 1835.  
*MNRAS*, 327:1057–1070.
- Scott et al. (2002).  
First results from the Very Small Array – III. The CMB power spectrum.  
*MNRAS*, *submitted* (astro-ph/0205380).
- Seljak, U. and Zaldarriaga, M. (1996).  
A Line-of-Sight Integration Approach to Cosmic Microwave Background Anisotropies.  
*ApJ*, 469:437.
- Serna, A., Alimi, J.-M., and Chieze, J.-P. (1996).  
Adaptive Smooth Particle Hydrodynamics and Particle-Particle Coupled Codes: Energy and Entropy Conservation.  
*ApJ*, 461:884.

- Serna, A., Domínguez-Tenreiro, R., and Sáiz, A. (2002).  
Conservation Laws in Smoothed Particle Hydrodynamics: the DEVA Code.  
*MNRAS*, page submitted.
- Shapiro, P. R., Martel, H., Villumsen, J. V., and Owen, J. M. (1996).  
Adaptive Smoothed Particle Hydrodynamics, with Application to Cosmology: Methodology.  
*ApJS*, 103:269.
- Silk, J. (2001).  
The formation of galaxy discs.  
*MNRAS*, 324:313–318.
- Smith, S. (1936).  
The Mass of the Virgo Cluster.  
*ApJ*, 83:23–30.
- Sofue, Y. and Rubin, V. (2001).  
Rotation Curves of Spiral Galaxies.  
*ARA&A*, 39:137–174.
- Solanes, J. ., Manrique, A., García-Gómez, C., González-Casado, G., Giovanelli, R., and Haynes, M. P. (2001).  
The H I Content of Spirals. II. Gas Deficiency in Cluster Galaxies.  
*ApJ*, 548:97–113.
- Somerville, R. S. and Primack, J. R. (1999).  
Semi-analytic modelling of galaxy formation: the local Universe.  
*MNRAS*, 310:1087–1110.
- Somerville, R. S., Primack, J. R., and Faber, S. M. (2001).  
The nature of high-redshift galaxies.  
*MNRAS*, 320:504.
- Sommer-Larsen, J. and Dolgov, A. (2001).  
Formation of Disk Galaxies: Warm Dark Matter and the Angular Momentum Problem.  
*ApJ*, 551:608–623.
- Spergel, D. N. and Steinhardt, P. J. (2000).  
Observational Evidence for Self-Interacting Cold Dark Matter.  
*Physical Review Letters*, 84:3760–3763.
- Springel, V. and Hernquist, L. (2002a).  
Cosmological smoothed particle hydrodynamics simulations: the entropy equation.  
*MNRAS*, 333:649–664.

- Springel, V. and Hernquist, L. (2002b).  
Cosmological SPH simulations: A hybrid multi-phase model for star formation.  
In *submitted to MNRAS*, 25 pages, version with high-resolution figures available at [http://www.mpa-garching.mpg.de/volker/paper\\_multiphase/](http://www.mpa-garching.mpg.de/volker/paper_multiphase/), page 6393.
- Springel, V. and Hernquist, L. (2002c).  
The history of star formation in a LCDM universe.  
In *submitted to MNRAS*, 25 pages, version with high-resolution figures available at [http://www.mpa-garching.mpg.de/volker/paper\\_sfr/](http://www.mpa-garching.mpg.de/volker/paper_sfr/), page 6395.
- Springel, V., White, S. D. M., Tormen, G., and Kauffmann, G. (2001a).  
Populating a cluster of galaxies - I. Results at  $z=0$ .  
*MNRAS*, 328:726–750.
- Springel, V., Yoshida, N., and White, S. D. M. (2001b).  
GADGET: a code for collisionless and gasdynamical cosmological simulations.  
*New Astronomy*, 6:79–117.
- Steidel, C. C., Adelberger, K. L., Giavalisco, M., Dickinson, M., and Pettini, M. (1999).  
Lyman-Break Galaxies at  $z > 4$  and the Evolution of the Ultraviolet Luminosity Density at High Redshift.  
*ApJ*, 519:1–17.
- Steidel, C. C., Giavalisco, M., Dickinson, M., and Adelberger, K. L. (1996a).  
Spectroscopy of Lyman Break Galaxies in the Hubble Deep Field.  
*AJ*, 112:352.
- Steidel, C. C., Giavalisco, M., Pettini, M., Dickinson, M., and Adelberger, K. L. (1996b).  
Spectroscopic Confirmation of a Population of Normal Star-forming Galaxies at Redshifts  $z > 3$ .  
*ApJ*, 462:L17.
- Subramanian, K., Cen, R., and Ostriker, J. P. (2000).  
The Structure of Dark Matter Halos in Hierarchical Clustering Theories.  
*ApJ*, 538:528–542.
- Suto, Y., Sasaki, S., and Makino, N. (1998).  
Gas Density and X-Ray Surface Brightness Profiles of Clusters of Galaxies from Dark Matter Halo Potentials: Beyond the Isothermal beta-Model.  
*ApJ*, 509:544–550.

- Swaters, R. A., Madore, B. F., van den Bosch, F. C., and Balcells, M. (2002).  
The Central Mass Distribution in Dwarf and Low Surface Brightness Galaxies.  
*ApJ*, *in press* (astro-ph/0210152).
- Syer, D. and White, S. D. M. (1998).  
Dark halo mergers and the formation of a universal profile.  
*MNRAS*, 293:337.
- Taylor, J. E. and Navarro, J. F. (2001).  
The Phase-Space Density Profiles of Cold Dark Matter Halos.  
*ApJ*, 563:483–488.
- Tegmark, M. (1996).  
The Angular Power Spectrum of the Four-Year COBE Data.  
*ApJ*, 464:L35.
- Teyssier, R. (2002).  
Cosmological hydrodynamics with adaptive mesh refinement. A new high resolution code called RAMSES.  
*A&A*, 385:337–364.
- Thacker, R. J. and Couchman, H. M. P. (2001).  
Star Formation, Supernova Feedback, and the Angular Momentum Problem in Numerical Cold Dark Matter Cosmogony: Halfway There?  
*ApJ*, 555:L17–L20.
- Tissera, P. B. (2000).  
Analysis of Star Formation in Galaxy-like Objects.  
*ApJ*, 534:636–649.
- Tissera, P. B. and Dominguez-Tenreiro, R. (1998).  
Dark matter halo structure in CDM hydrodynamical simulations.  
*MNRAS*, 297:177–194.
- Tozzi, P. and Norman, C. (2001).  
The Evolution of X-Ray Clusters and the Entropy of the Intracluster Medium.  
*ApJ*, 546:63–84.
- Tresse, L. and Maddox, S. J. (1998).  
The H alpha Luminosity Function and Star Formation Rate at Z approximately 0.2.  
*ApJ*, 495:691.
- Treyer, M. A., Ellis, R. S., Milliard, B., Donas, J., and Bridges, T. J. (1998).  
An ultraviolet-selected galaxy redshift survey: new estimates of the local star formation rate.

- MNRAS*, 300:303–314.
- Tyson, J. A., Kochanski, G. P., and dell’Antonio, I. P. (1998).  
Detailed Mass Map of CL 0024+1654 from Strong Lensing.  
*ApJ*, 498:L107.
- Tytler, D., Fan, X.-M., and Burles, S. (1996).  
Cosmological baryon density derived from the deuterium abundance at redshift  $Z = 3.57$ .  
*Nature*, 381:207–209.
- Valageas, P. and Silk, J. (1999).  
The entropy history of the universe.  
*A&A*, 350:725–742.
- Valluri, M. and Jog, C. J. (1990).  
Collisional removal of H I from the inner disks of Virgo Cluster galaxies.  
*ApJ*, 357:367–372.
- van den Bosch, F. C., Abel, T., Croft, R. A. C., Hernquist, L., and White, S. D. M. (2002).  
The Angular Momentum of Gas in Proto-Galaxies I. Implications for the Formation of Disk Galaxies.  
(astro-ph/0201095).
- van den Bosch, F. C. and Swaters, R. A. (2001).  
Dwarf galaxy rotation curves and the core problem of dark matter haloes.  
*MNRAS*, 325:1017–1038.
- van Haarlem, M. P., Frenk, C. S., and White, S. D. M. (1997).  
Projection effects in cluster catalogues.  
*MNRAS*, 287:817–832.
- van Leer, B. (1977).  
Towards the ultimate conservative difference scheme: IV. A new approach to numerical convection.  
*Journal of Computational Physics*, 23:276–299.
- Weinberg, S. (1972).  
*Gravitation and cosmology: Principles and applications of the general theory of relativity*.  
New York: Wiley, —c1972.
- Weisskopf, M. C., Tananbaum, H. D., Van Speybroeck, L. P., and O’Dell, S. L. (2000).  
Chandra X-ray Observatory (CXO): overview.

- In *Proc. SPIE Vol. 4012, p. 2-16, X-Ray Optics, Instruments, and Missions III*, Joachim E. Truemper; Bernd Aschenbach; Eds., volume 4012, pages 2–16.
- West, M. J., Jones, C., and Forman, W. (1995).  
Substructure: Clues to the Formation of Clusters of Galaxies.  
*ApJ*, 451:L5.
- White, D. A. (2000).  
Deconvolution of ASCA X-ray data - II. Radial temperature and metallicity profiles for 106 galaxy clusters.  
*MNRAS*, 312:663–688.
- White, S. D. M. (1976).  
The dynamics of rich clusters of galaxies.  
*MNRAS*, 177:717–733.
- White, S. D. M. (1984).  
Angular momentum growth in protogalaxies.  
*ApJ*, 286:38–41.
- White, S. D. M., Davis, M., Efstathiou, G., and Frenk, C. S. (1987).  
Galaxy distribution in a cold dark matter universe.  
*Nature*, 330:451–453.
- White, S. D. M. and Frenk, C. S. (1991).  
Galaxy formation through hierarchical clustering.  
*ApJ*, 379:52–79.
- White, S. D. M., Frenk, C. S., and Davis, M. (1983).  
Clustering in a neutrino-dominated universe.  
*ApJ*, 274:L1–L5.
- White, S. D. M., Navarro, J. F., Evrard, A. E., and Frenk, C. S. (1993).  
The Baryon Content of Galaxy Clusters - a Challenge to Cosmological Orthodoxy.  
*Nature*, 366:429.
- White, S. D. M. and Rees, M. J. (1978).  
Core condensation in heavy halos - A two-stage theory for galaxy formation and clustering.  
*MNRAS*, 183:341–358.
- White, S. D. M. and Zaritsky, D. (1992).  
Models for Galaxy halos in an open universe.  
*ApJ*, 394:1–6.



- Xu, H., Jin, G., and Wu, X. (2001).  
The Mass-Temperature Relation of 22 Nearby Clusters.  
*ApJ*, 553:78–83.
- Xue, Y. and Wu, X. (2000).  
The  $L_X-T$ ,  $L_X-\sigma$ , and  $\sigma-T$  Relations for Groups and Clusters of Galaxies.  
*ApJ*, 538:65–71.
- Yan, L., McCarthy, P. J., Freudling, W., Teplitz, H. I., Malumuth, E. M., Weymann, R. J., and Malkan, M. A. (1999).  
The H $\alpha$  Luminosity Function and Global Star Formation Rate from Redshifts of 1-2.  
*ApJ*, 519:L47–L50.
- Yepes, G. (2001).  
Cosmological numerical simulations: past, present and future.  
In *The Restless Universe*, page 217.
- Yepes, G., Kates, R., Khokhlov, A., and Klypin, A. (1997).  
Hydrodynamical simulations of galaxy formation: effects of supernova feedback.  
*MNRAS*, 284:235–256.
- Yoshida, N., Springel, V., White, S. D. M., and Tormen, G. (2000).  
Weakly Self-interacting Dark Matter and the Structure of Dark Halos.  
*ApJ*, 544:L87–L90.
- Yoshikawa, K., Jing, Y. P., and Suto, Y. (2000).  
Cosmological Smoothed Particle Hydrodynamic Simulations with Four Million Particles: Statistical Properties of X-Ray Clusters in a Low-Density Universe.  
*ApJ*, 535:593–601.
- Zabludoff, A. I. and Mulchaey, J. S. (1998).  
The Properties of Poor Groups of Galaxies. I. Spectroscopic Survey and Results.  
*ApJ*, 496:39.
- Zabludoff, A. I., Zaritsky, D., Lin, H., Tucker, D., Hashimoto, Y., Sackett, S. A., Oemler, A., and Kirshner, R. P. (1996).  
The Environment of “E+A” Galaxies.  
*ApJ*, 466:104.
- Zaroubi, S. and Hoffman, Y. (1993).  
Gravitational Collapse in an Expanding Universe: Asymptotic Self-similar Solutions.  
*ApJ*, 416:410.

- Zaroubi, S., Naim, A., and Hoffman, Y. (1996).  
Secondary Infall: Theory versus Simulations.  
*ApJ*, 457:50.
- Zwicky, F. (1937).  
On the Masses of Nebulae and of Clusters of Nebulae.  
*ApJ*, 86:217–246.

Y sobre todo, a Pilar y a Petri.